# *Ordering phenomena in iron-containing spinels*

*Giuditta Perversi*

For the degree of Doctor of Philosophy

School of Chemistry

University of Edinburgh

June 2018

# ABSTRACT


The spinel structure (general formula $AB_2O_4$) is widely occurring in natural and synthetic materials, and has a marked technological and scientific significance due to its magnetic, electric and multiferroic behaviours. The presence of transition metal cations with multiple oxidation state and the resulting charge, orbital and spin degrees of freedom of the partially occupied *d*-orbitals lead to uniquely ordered ground states.

The coupling of all the three degrees of freedom can result in a structurally distorted ground state where the direct metal-metal interaction forms atomic clusters, or "orbital molecules". The Verwey phase of magnetite ($Fe_3O_4$), occurring below $T_V$ ~ 125 K, is driven by a cooperative bond distortion that forms linear $Fe^{3+}$-$Fe^{2+}$-$Fe^{3+}$ arrangement (trimeron). The effect of non-stoichiometry and chemical modification on this complex structure has been investigated with a variety of samples through microcrystal synchrotron XRD. A mineral sample (Al, Si, Mg and Mn impurities, $T_V$ = 119 K) confirms the Verwey phase as the most complex long-range electronic order known to occur naturally; its relevance in space sciences is discussed. Moreover, the structural analysis of two synthetic magnetites ($Fe_{3(1-\delta)}O_4$ with $3\delta = 0.012$ and $T_V$ = 102 K, $Fe_{3-x}Zn_xO_4$ with x = 0.03 and $T_V$ = 90 K) univocally confirmed the persistence of the transition, and its first order, at doping level > 1 %, contrary to previous reports. Moreover, the temperature evolution of the trimerons and their persistence above $T_V$ was probed through X-ray Pair Distribution Function analysis on pure $Fe_3O_4$: the data analysis between 90 K < T < 923 K show that the Verwey phase goes from long-range ordered (T < 125 K) to short-range ordered (T > 850 K). Magnetite can thus only be considered to have a regular cubic spinel structure above the Curie temperature ($T_C$ = 858 K).

The pyrochlore lattice of B cations in a spinel gives the structure the potential for frustration upon antiferromagnetic ordering. $Fe_2GeO_4$ and $\gamma$-$Fe_2SiO_4$ were synthesised through conventional solid state routes, with the use of high-pressure synthesis for the latter. Magnetometry and heat capacity measurements highlighted two transitions ($T_{m1}$ =

8.6 K and $T_{m2}$ = 7.2 K, and $T_{m1}$ = 11.2 K and $T_{m2}$ = 7.5 K respectively). Powder neutron diffraction data between 2 K < T < 25 K showed that both materials stay undistorted below $T_N$. Magnetic Rietveld refinement led to two highly unconventional magnetic structures, with incommensurate propagation vectors and modulation of the moment magnitude. γ-$Fe_2SiO_4$ also shows a spin-ice order below $T_{m2}$. The results are unique and unusual for transition metal oxides; the models are systematised by proposing a "frustration wave" model, in which the degree of frustration is a spatial quantity that can be distributed through the structure in order to stabilise the ground state.

# LAY SUMMARY

The spinel structure is widely occurring in natural and synthetic materials. The oxides of this family exhibit the general formula $AB_2O_4$, where the oxygen forms a *ccp* arrangement, the B cation coordinates in edge-sharing octahedra and the A cation occupies tetrahedra. The technological and scientific significance of these materials has risen in the last few decades, reflecting their broad range of magnetic, electric and multiferroic behaviours. The chemical flexibility of these systems allows for the presence of transition metal cations with multiple oxidation states; the charge, orbital and spin degrees of freedom of the partially occupied *d*-orbitals lead to the occurrence of unique ordered ground states.

The coupling of all the three degrees of freedom can result in a structurally distorted ground state where the direct metal-metal interaction forms atomic clusters, or "orbital molecules". The most significant example of orbital molecule behaviour is in the Verwey phase of magnetite ($Fe_3O_4$). Upon cooling below $T_V$ ~ 125 K, the material becomes a semi-conductor and the crystal symmetry lowers from cubic *Fd-3m* to monoclinic *Cc*; this transition is driven by cooperative bond distortion that delocalizes one electron between three neighbouring Fe sites in a linear $Fe^{3+}$-$Fe^{2+}$-$Fe^{3+}$ arrangement (trimeron).
The complexity of this ground state makes it highly susceptible to effects of non-stoichiometry and chemical modification: the influence of these parameters on the ground state structure was investigated on natural (inherently impure) and synthetic ($Fe_{3(1-\delta)}O_4$ with $3\delta = 0.012$, $Fe_{3-x}Zn_xO_4$ with $x = 0.03$) samples through single crystal synchrotron XRD. Moreover, the temperature evolution of the trimerons and their persistence above $T_V$ as a short-range distortion is proven through X-ray Pair Distribution Function analysis on pure $Fe_3O_4$ performed on a wide range of temperatures (90 K < T < 923 K).

The 3D arrangement of the B cations in a spinel outlines a pyrochlore lattice. As such, upon antiferromagnetic ordering of the spins, the structure has the potential for frustration, which in transition metal oxides is usually resolved through distortion. The ground states of $Fe_2GeO_4$ and γ-$Fe_2SiO_4$ are investigated through magnetometry and heat capacity measurements and their magnetic orders are probed with powder neutron diffraction data. Both materials are antiferromagnetic and remain structurally cubic down to 2 K, and can be associated with two highly unconventional magnetic structures. The results are discussed as a notable exception to the norm, and framed to advance state-of-the-art understanding of magnetic frustration in transition metals.

# DECLARATION

I declare that this thesis has been composed by me alone, and that the work presented in this thesis is my own, or where it is the work of another they are duly credited. Furthermore I confirm that this work has not been submitted for any other degree or professional qualification than this doctorate. Some of the research herein has already been published as detailed in the Publications section.

*Giuditta Perversi*

# ACKNOWLEDGEMENTS

I would like to start by thanking my supervisor, Professor J. Paul Attfield, who set the foundations for all the projects I had the pleasure to work on during the course of my Ph.D. Thank you for giving me the freedom to explore science confidently and autonomously, and for showing me how to turn an idea in a rigorous investigation. Your down-to-Earth approach combined with brilliant leaps of faith has been incredibly inspiring and it was a privilege to work under your supervision.

All the work in this thesis was funded by the European Research Council, to which I am very grateful.

My warmest gratitude goes of course to the Attfield Research group. My Ph.D. experience was priceless because of your presence, both personal and professional.

Thank you to Dr James Cumby, Dr Elise Pachoud and Dr Angel Arevalo Lopez, who will be acknowledge in several chapters of this thesis for their contributions. I wish to thank Angel for teaching me high-pressure synthesis and magnetic neutron refinement, and for every time he sat next to me for hours and days until issues were solved. Thank you, James, for your patience even when subjected to the most random questions, for the amount of knowledge you shared with me in the course of three years. Thank you, Elise, for making very frustrating syntheses and refinements work at the end of the day, you have been crucial for a lot of my work.

Thank you to my fellow Ph.D. colleagues, for every crazy trip, beamtime, conference and office banter. Thank you to Alex Browne, who started this adventure together with me and Graham McNally; you have been a constant presence and this degree would not be the same without you as a friend and fellow scientist. Thank you to Jacky Hong, for being the social glue of the PhDs, fuelled by crazy questions and even crazier amount of cake. Thank you to Paul Sarte, who is unfailing kind and supporting and always sees the best in your work even when you're not so sure, and for being a bottomless well of knowledge. I cherish every happy memory that involves you and I hope we will make much more in the future.

I am also grateful to all the colleagues in the Open Plan Office, especially Dr Xiao Wang for managing the Mag Lab and its instrumentation.

This work would not have been possible without Central Facilities, and I am grateful to the ILL and the ESRF facilities for granting me time to carry on my work. Thank you to Dr Jon Wright of ID11 at ESRF, for being the local contact in most of my experiments there; you were incredibly helpful and insightful and your technical expertise was very inspiring. Thank you to Dr Clemens Ritter of D20 and D2B at ESRF, for his unwavering support and knowledge during the experiment.
On a similar note, thank you to Dr Mark Senn for all the interesting chats we had together.

I also wish to thank the School of Chemistry, from Admin to Postgradutate services, for offering a constant support during my four years at Edinburgh and helping me to improve as a scholar and as a person. Thank you to Prof Simon Parsons, my second supervisor, and Dr Caroline Kirk in particular for their presence and help. A special thank you goes to the Public Engagement team, for showing me another side of science and allowing me to contribute extensively to it. Thank you to Dr Jenny Bos and Dr Anna-Maria Maciejuk, for having faith in me and for coordinating all the School's efforts.

This thesis has been thoroughly read by a number of people: my supervisor Prof Attfield, Dr Cumby, Alex Browne, thank you for your scientific insight, for spotting a number of typos and helping me straighten up the English.

On a more personal note, Bianka Michaylova and Amelia Bain, thank you for proofreading my obscure research topics and catching even more typos, and for your unwavering support while I was writing this and for your friendship in these years.
Thank you to the LAMPS society, for showing me the beauty of these university organisations and welcoming a chemist among medievalists of various extractions. Callum, Joanna, Stephenie, Morgan, Danielle, and all the others, thank you for every castle trip and movie night.
Thank you to Jacopo, Cristina, Maria, and Rossana who are far away at home but always ready to welcome me back. Thank you to Eleonora, for being here at my best and at my worst. And finally thank you to my brother and my Mum, for believing in this and believing in me, always, and for doing their best to support me in any way they possibly could.

# PUBLICATIONS

The following publications have been made as a result of the work carried out in this thesis:

- "The Verwey structure of a natural magnetite", G. Perversi, J. Cumby, E. Pachoud, J. P. Wright, and J. P. Attfield. *Chem. Commun*. **52**, 4864-4867. (2016)

- "Frustration wave order in iron(II) oxide spinels", G. Perversi, A. M. Arevalo-Lopez, C. Ritter, and J. P. Attfield. *Communication Physics* – under review

- "Persistence of trimeron distortion in the high-temperature phase of magnetite", G. Perversi, E. Pachoud, J. P. Wright, and J. P. Attfield. – in preparation

- "Evolution of the Verwey structure in substituted magnetite", G. Perversi, J. C. Cumby, E. Pachoud, J. P. Wright, and J. P. Attfield – in preparation

# TABLE OF CONTENTS

# 2. Experimental Methods

# *3. The Verwey Structure of Magnetite*

# *4. Unconventional Magnetism in Fe(II) Spinels*

# *5. Conclusions and future directions*

# 1. INTRODUCTION

## 1.1 Transition Metal Oxides

Transition metal oxides (TMO) are a class of materials of unique interest in solid state chemistry, representing a widely occurring compound form involving *d*-block metals. Their natural abundance grants them direct relevance for Earth Sciences, as they are key to understanding the geology and geophysics of our planet. However, it is the broad range of interesting physical properties they exhibit that accounts for their scientific popularity. Some famous examples include highly insulating or highly conductive behaviours (e.g. $SrTiO_3$ [1] or $LaNiO_3$ [2] respectively), ferroelectricity (e.g. $BaTiO_3$ [3]), colossal magnetoresistance (e.g. $Sr_2FeMoO_6$ [4]), permanent magnetism (e.g. $SrFe_{12}O_{19}$ [5]) and high temperature superconductivity (e.g. $HgBa_2Ca_2Cu_3O_8$ and other cuprates[6]).
All these properties can be ascribed to the presence of outer *d*-orbitals and the nature of the bond between transition metal and oxygen. There is no unambiguous definition for these features: the behaviour of cations and anions in TMO can range from full localisation (ionic behaviour) to complete delocalisation (band behaviour), depending on the actual orbital overlap and mobility of the electrons. These systems are therefore broadly defined as highly correlated electron systems.

Cations from the *d*-block range widely in terms of dimensions and allowed electronic configurations: several of them can access multiple oxidation states (i.e. Mn, Fe, V, etc.) and add additional complexity to the electron-electron/electron-phonon correlations that are key to understanding their properties. As such, predicting TMO behaviour from first-principles calculations is challenging and experimental work can often unveil different answers.
The above-mentioned variability also means that, under normal conditions, TMO occur in a variety of crystal structures and compositions. Over the last few decades, several lines of experimental work in chemistry were dedicated to exploring the possibility of tuning

properties with careful changes of the composition of synthetically pure TMO. Additionally, the nature of the bonds in these compounds opens their lattices to physical modification: within the same composition, several crystal structures might be present with variation of temperature and/or pressure, and a transition to a different symmetry often modifies the physical properties. [7]

Within this framework, iron-containing oxides are renowned for their magnetic behaviour, which allows for a variety of applications in transformers [8], magnetic recording [9] and microwave antennas [10]. These technologies are usually dominated by "soft ferrites", common members of the spinel family with low coercivity, suitable for an energy-efficient switching of the direction of magnetisation, and high energy losses at high frequencies, ideal for inductors. Hard ferrites, by contrast, are characterised by high coercivity and magnetic remanence, and are thus suitable for permanent magnets; these materials are usually hexaferrites ($XFe_{12}O_{19}$ with X = Ba, Sr) and are commonly employed in all applications that require high performance but do not explicitly require neodymium and samarium alloys. [11] The ready availability of the chemical components combined with the ceramic processing capabilities makes these materials highly applicable and the flexibility of the features as a function of chemical substitution, microstructuring, and bulk processing has kept research active in this field over the last decades.

A better comprehension of the structure-to-property relationship in transition metal oxides is undoubtedly needed to widen our understanding of how their electronic, magnetic, mechanical, and thermal behaviours work, and possibly open new paths of application for modern technological challenges.

In this work, the physical chemistry of TMO will be taken into consideration and applied to iron-containing oxides belonging to the spinel structural family. The relevant basis for these systems will be outlined accordingly in the following chapters.

# 1.2 Ferrite Materials

## 1.2.1. Specifics on the spinel structure

Materials that crystallize in the spinel structure follow the general formula $AB_2X_4$, with X = S, Se, O. Only oxygen-based compounds will be considered for the rest of this study. The two cations may be different oxidation states of the same element (binary spinels) or two altogether different elements (ternary spinels); to ensure the electroneutrality of the compound the most common pairs of oxidation states are $A^{2+}/B^{3+}$, in a 1:2 ratio between A and B, and $A^{4+}/B^{2+}$.

The $O^{2-}$ anions form a cubic close-packed lattice, whose interstices can be either tetrahedral (⅛ occupancy) or octahedral (½ occupancy). In a "normal" spinel the B cations are confined to octahedral interstices, whereas an "inverse" spinel has partial site mixing with half the B cations in octahedral and half in tetrahedral positions. Solid solutions allow for partial modification of this composition and arrangement, following the $(A_{1-x}B_x)_T[A_xB_{2-x}]_O O_4$ formula where the degree of inversion *x* can vary from 1 (fully inverse) to 0 (fully normal). The resulting lattice has face-centred cubic symmetry (spacegroup *Fd-3m*) and has $BO_6$ octahedra and $AO_4$ tetrahedra as the key structural units. The octahedra are edge-sharing and create interconnected chains along the plane diagonal directions, equivalent by cubic symmetry; the tetrahedra are located in the space left vacant by the arrangement of the B sites (Fig. 1). [12]

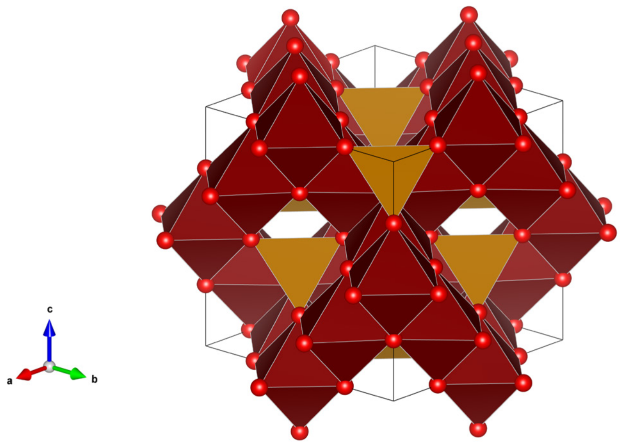


**Figure 1 – Spinel crystal structure, where the $BO_6$ octahedra are depicted in red and the $AO_4$ tetrahedra are depicted in yellow. Oxygen atoms are represented with red spheres.**

The strong connectivity of the structural units is a key feature in the spinel structure: it is the main facilitator for interactions exceeding the first coordination sphere and it provides the foundation for the very rich properties of this family of materials. By considering just A cations, it is possible to outline a diamond sublattice within the cubic cell (Fig. 2A); the second coordination shell of B cations, on the other hand, forms a tridimensional sublattice of corner-sharing tetrahedra (pyrochlore lattice, Fig. 2B) that can also be visualized as a planar triangular arrangement alternated with a kagomè lattice along the body diagonal (Fig. 2C).

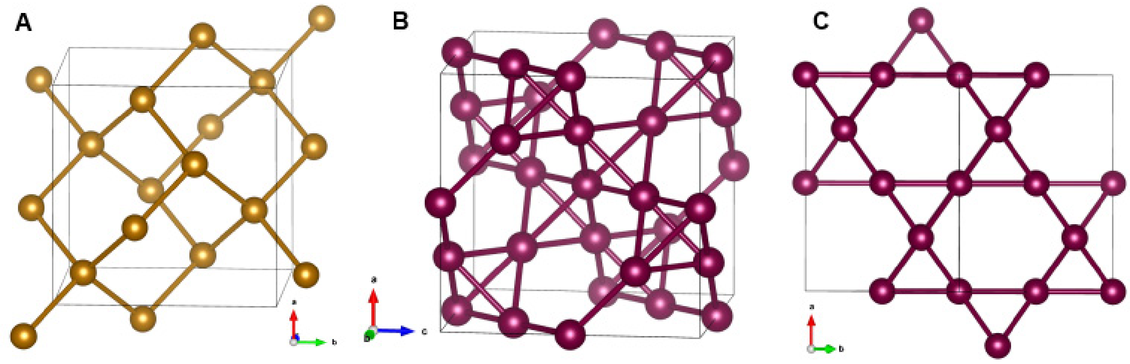


**Figure 2 – Different sublattices within the spinel structure. A) Diamond sublattice of A-site cations; B) 3D corner-sharing tetrahedral sublattice of B-site cations; C) Different projection of b, to show the kagomè lattice.**

In an ideal spinel, normal or inverse, the confinement of cations in their assigned sites with the appropriate ratio is perfect and oxygen bonds have equal lengths dictated by the cubic symmetry. In reality, site mixing is one of the major sources of disorder within spinel crystals and can only be avoided in some cases with proper synthetic conditions. Oxygen bonds, instead, are heavily influenced by the nature of the cation located in octahedral coordination and routinely subjected to trigonal distortion; crystal field considerations dictate the elongation or compression of bonds.

These effects will be outlined in more depth in Section 1.3.

## 1.2.2. Introduction to magnetite

Magnetite is the common name of $Fe_3O_4$, and represents one of the most abundant forms of iron in combination with oxygen available in the Earth's crust, along with $Fe_2O_3$ (α, hematite and γ, maghemite) and $Fe_{1-x}O$ (wüstite). As such, it has been known as a mineral since ancient times and it was one of the spinels to have its structure solved by W. H. Bragg in 1915. [13]

As introduced, the spinel structure family is highly populated by synthetic and natural materials; among them, however, the occurrence of a binary spinel ($AB_2O_4$ where A = B) is fairly rare, and, apart from $Fe_3O_4$ , only $Co_3O_4$ [14] and $Mn_3O_4$ [15] fit the requirements. Moreover, magnetite is the only inverse binary spinel: the extended formula is $(Fe^{3+})_T[Fe^{3+}, Fe^{2+}]_OO_4$ and charge balance is satisfied by taking advantage of the multiple valences available to iron cations. The net result is that tetrahedral sites host a $3d^5$ cation only, but octahedral sites have a mixture of $3d^5$ and $3d^6$, making magnetite a semivalent inverse spinel with a net configuration of $d^{5.5}$, high spin.
Due to this electronic arrangement, magnetite has a net magnetism with a very high ordering temperature ($T_C \approx 856$ K) associated with a ferrimagnetic ordering of moments along the cubic [1 1 1] body diagonal; the ferrimagnetism arises from the arrangement of $Fe^{3+}$ and $Fe^{2+}$ in a 2:1 ratio, leaving a residual magnetic moment that is not counterbalanced by any antiparallel aligned spin (Fig. 3A). This structure was first proposed by Néel in 1948 [16] and confirmed by neutron diffraction in 1951. [17] The combination of ferrimagnetism and conductivity can be rationalised in terms of double-exchange between A and B sites and superexchange of the minority spin of $Fe^{2+}$ among the octahedral B sites (Fig. 3B).

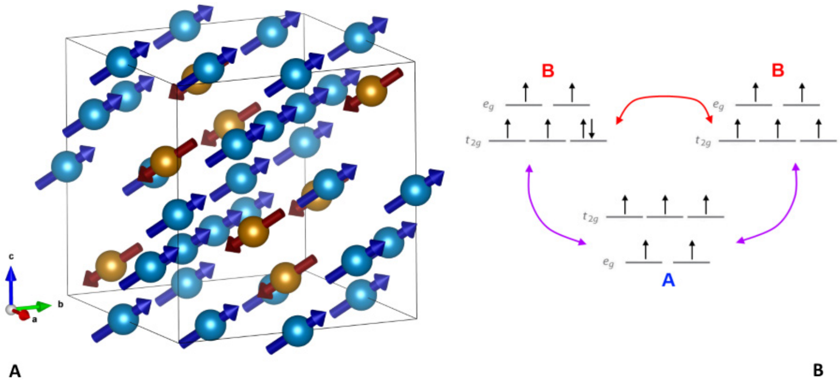


**Figure 3 – A) Magnetic structure of magnetite, showing the ferrimagnetic spin arrangement for one unit cell. Tetrahedral atoms are in gold, with ordered moments in red (8 per formula unit); octahedral atoms are in light blue, with ordered moment in blue (16 per formula unit). Oxygen atoms are not displayed. As a result, $Fe_3O_4$ has a net ferromagnetic moment of ~ 4 $\mu_B$ per unit cell. [18] B) Superexchange (red arrow) and double-exchange (purple arrow) mechanisms for A and B sites in a spinel structure, exemplified for $d^6/d^5$ cations (i.e. $Fe^{2+}/Fe^{3+}$).**

The mobility of the minority spin electron is also responsible for the remarkable conductivity of $10^2$-$10^3$ $\Omega^{-1}m^{-1}$, several orders of magnitude higher than the $Fe^{3+}$-only $Fe_2O_3$.[19] The semi-metallic behaviour of magnetite is also consistent with its low bandgap (0.1 eV), which explains the black colour of this mineral in contrast with the red of the α-$Fe_2O_3$ (rust).[20]

Much of the historical popularity of $Fe_3O_4$ is related to the possibility of permanently magnetising mineral magnetite with the application of a magnetic field. Interestingly, there are permanently-magnetised pieces of magnetite, known as lodestone, that are naturally occurring, even though there is no consensus on the source of the magnetic field that managed to create this property. A lodestone can attract pieces of metallic iron and was involved in early evidence of the concept of magnetism, hence the mineral name; moreover, the magnetisation is strong enough to actually use small cuts of this mineral in compasses, which is the source of the secondary name for $Fe_3O_4$ (*lode* is archaic English for *path, journey*). [21] [22]

In recent years, it has been discovered that magnetite can also be biosynthesised by some bacteria in the form of nanoparticles, whose alignment under electrical or magnetic stimulation will act as a navigation prompt for bacteria. There are even instances of human-biosynthesised magnetite nanoparticles, but their precise role in human biology has yet to be perfectly understood. [23]

In normal conditions these properties are fairly consistent in their temperature dependence, making magnetite an easy choice for technological applications like magnetic recording. In recent years, however, it has been substituted by more powerful hard ferrites, with higher saturation magnetisation when permanently magnetised.

The discontinuities that arise in this simple but versatile material at more extreme temperature conditions, however, are incredibly interesting and have been the focus of extended studies.
The low-temperature behaviour of $Fe_3O_4$ is characterized by the onset of the so-called "Verwey transition": first reported by Evert J. W. Verwey in 1939 [24] with resistivity measurements at $T < 120$ K, this phase transition is associated with discontinuities in electrical, magnetic and heat capacity properties. The prominence of these physical changes made the Verwey transition the routine method of detection and quantification of magnetite content in rock sample of unknown composition,[25] but, apart from the popularity among the geologists, a rationalisation for this physical behaviour remained elusive for several decades. The reason behind this long-standing problem in solid state science is associated with the complexity of the low-temperature structure. Only recently a complex cooperative distortion leading to the formation of linear $Fe^{3+}$-$Fe^{2+}$-$Fe^{3+}$ clusters was unveiled as the driving force of the transition. [26]
Full details on the history of the Verwey transition in magnetite and further work on influencing it through chemical modifications and tracking its features as a function of temperature will be provided in Chapter 3.

### 1.2.3. Other ferrites

Given the very high natural abundance of oxygen and iron in the Earth's crust, accounting for more than 50% of all the naturally available elements, it is intuitive that iron-containing oxides are a common occurrence and that the spinel ferrites family is richly populated.

Apart from $Fe_3O_4$, there are other iron-containing minerals that assume the spinel structure in a variety of conditions. In these minerals, the oxidation state of iron can be mixed between 2+ and 3+ or exclusively 2+, depending on whether the spinel is inverse or normal respectively. Interestingly, however, a clear distinction can be drawn between spinels with another transition metal to accompany iron (e.g. $Fe_2NiO_4$, $Fe_2CoO_4$, $Fe_2MnO_4$, $Fe_2CuO_4$) and spinels with a non-magnetic cation on the A site (e.g. $Fe_2TiO_4$, $Fe_2ZnO_4$, $Fe_2GeO_4$): in the first case, the spinels are actually soft ferrites with a spontaneous onset of ferromagnetism at very high temperatures ($T_C > 700$ K); in the second case, the spinels remain paramagnetic down to at least 140 K and tend to assume an antiferromagnetic ordering only upon cooling. This fundamental difference can be systematised in terms of magnetic exchange interactions (cfr. Chapter 2.3) between cations in the B positions among themselves and with the A-site cations: in order to have the minority spin electron swapped among octahedral B sites (double-exchange), the B sites must be ferromagnetically aligned with each other; the interaction between A and B sites is mediated by the corner-sharing oxygen, and in order for the sites to interact with the paired spins of the oxygen without spin flipping the two sites need to be antiferromagnetically ordered. [27]

The net result from a technological point of view is that the hard ferrites are under extensive investigation for the influence of chemical substitution, nanostructuring and microstructuring to enhance the magnetic properties and widen the applicability in common devices. [28] Soft ferrites, instead, are generally just used for the mechanical properties, common to all ceramics, and have only recently been investigated for catalytic and electronic effects at the interface with other materials. [29] [30]

On the other hand, the extensive natural occurrence of both classes makes them undoubtedly relevant from a geological point of view, and several of the ferrite systems have been investigated under high pressures and high temperatures in order to properly model the inner layers of the Earth. It is also notable that most of the spinels of the second class have $Fe^{2+}$ as the only transition metal cation. Since the spinel structure outlines a uniformly frustrated lattice of B sites (pyrochlore lattice), all the nearest neighbour interactions are equivalent and these systems are magnetically frustrated upon antiferromagnetic ordering. Frustration can lead to unconventionally ordered states below the onset of the transition, and the results are generally regarded as highly interesting for the fundamental physical chemistry of magnetic interactions. However, since the magnetic ordering tends to occur at liquid helium temperatures, some of these phases have never been characterised from a structural point of view.
The investigation of two of these systems, $Fe_2GeO_4$ and $\gamma$-$Fe_2SiO_4$, will be the subject of Chapter 4.

# 1.3 Charge, Orbital and Spin Ordering in TMO

## 1.3.1. Degrees of freedom and examples of ordering

Understanding the very rich physics of highly correlated electron systems usually entails solving the ground state of the material, which in experimental terms can be approximated to the most stable “frozen” state that can be found upon lowering the temperature. Removing thermal energy from the system stabilises the most fundamental interactions in the crystal: charge (potentially mobile *d*-electrons), orbital (crystal field splitting of energies) and spin (ordered magnetic states) degrees of freedom. The high connectivity of spinels, which have cubic symmetry, or perovskites, which have which often have distortions in the cubic symmetry (tetragonal, orthorhombic), makes these degrees of freedom susceptible to the formation of ordered ground states.

### *1.3.1.1. Charge ordering*

The occurrence of charge ordering is associated with systems that contain a given cation in multiple oxidation states, either as a starting feature of the structure or as an effect of a disproportionation transition. Following a charge ordering transition, the random distribution of the disordered phase shifts towards the localisation of a given cation with a set oxidation state in a certain crystallographic site. As a result of this rearrangement, this change can usually be tracked through crystallography since the ordering inherently modifies the symmetry of the lattice; moreover, the localisation of charges highly affects the conductivity of TMO, usually leading to a metal/semiconductor to insulator transition with marked features in the resistivity profile as a function of temperature.

Disproportionation spontaneously occurs in structures like the perovskite $CaCu_3Fe_4O_{12}$, a product of high pressure synthesis, where the octahedral position goes from $Fe^{4+}$ valence to $Fe^{3+}$+$Fe^{5+}$ upon cooling below 210 K. [31] The transition is accompanied by structural, conductivity and magnetisation changes. Despite its appeal, charge ordering by disproportionation will not be the subject of this thesis.

Semi-valent structures are exemplified by $Fe_3O_4$, which has B sites with a semi-valent charge of 2.5+ coming from the average of $Fe^{2+}$ and $Fe^{3+}$ cations, randomly distributed in its spinel high-temperature phase. Verwey himself postulated that the transition at T ~ 125 K was driven by a charge ordering of the two different cations in given sites, breaking both the symmetry of the structure and the double exchange/superexchange mechanism of its conductivity. However, the true nature of the ground state is more complicated and a detailed description will be provided in Chapter 3.

A more classic example of charge ordering is perovskite manganites with general formula $Ln_{1-x}A_xMnO_3$, where Ln is a rare earth, A is a divalent cation and Mn is tetravalent; depending on the ionic radius of A, these compounds can undergo a charge-ordering metal to insulator transition which can be tuned with a magnetic field. As such, they are of key importance for colossal magnetoresistance (CMR) applications. [32]

Semivalence is also present in the triangular oxide $LuFe_2O_4$, which charge-orders in a pattern of alternating $Fe^{2+}$ and $Fe^{3+}$ octahedra upon cooling below 330 K, causing ferroelectricity and ferromagnetic ordering in the incommensurably distorted structure (Fig. 4).[33]

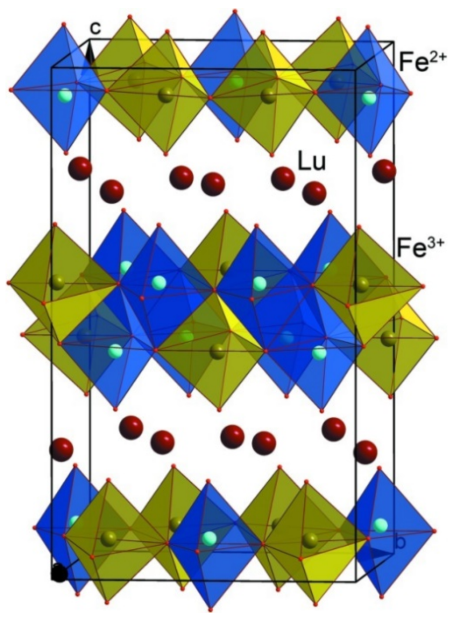


**Figure 4 – Crystal structure of $LuFe_2O_4$ in its charge-ordered ground state. Lu atoms are in red, $Fe^{2+}O_6$ octahedra are in blue and $Fe^{3+}O_6$ octahedra are in yellow, oxygen atoms are involved in the coordination but not displayed. Within bilayers of octahedra, the charges are evenly localised from the average 2.5+ valence of the high-temperature phase.[34]**

A state of semi-valence is relatively common in transition metal oxides, in light of the high degree of chemical substitutions achievable in the flexible structural framework. Charge ordering as outlined above, however, tends to occur most commonly with cations from the first row of the *d*-block. It is beyond the scope of this work to fully review the entire charge-ordered structure landscape, as the materials that most commonly undergo this type of transitions are perovskites rather than spinels.

#### *1.3.1.2. Orbital ordering*

In an ideal spinel, normal or inverse, the coordination around the transition metal cations, usually defined in terms of M-O bonds, is perfectly symmetrical as dictated by the cubic symmetry. However, the nature of the cation located in octahedral or tetrahedral coordination requires the consideration of crystal field effects, as a distortion of these arrangements is likely to occur in the ground state in response to energy considerations.

Placing a transition metal cation in an octahedral or tetrahedral coordination causes a crystal field splitting of the five-fold degenerate *d*-orbitals: three $t_{2g}$ orbitals at lower energy and two $e_g$ orbitals at higher energy in the octahedral case, and *vice versa* in the tetragonal case. A depiction of this effect for an octahedral crystal field is provided in Fig. 5. [35]

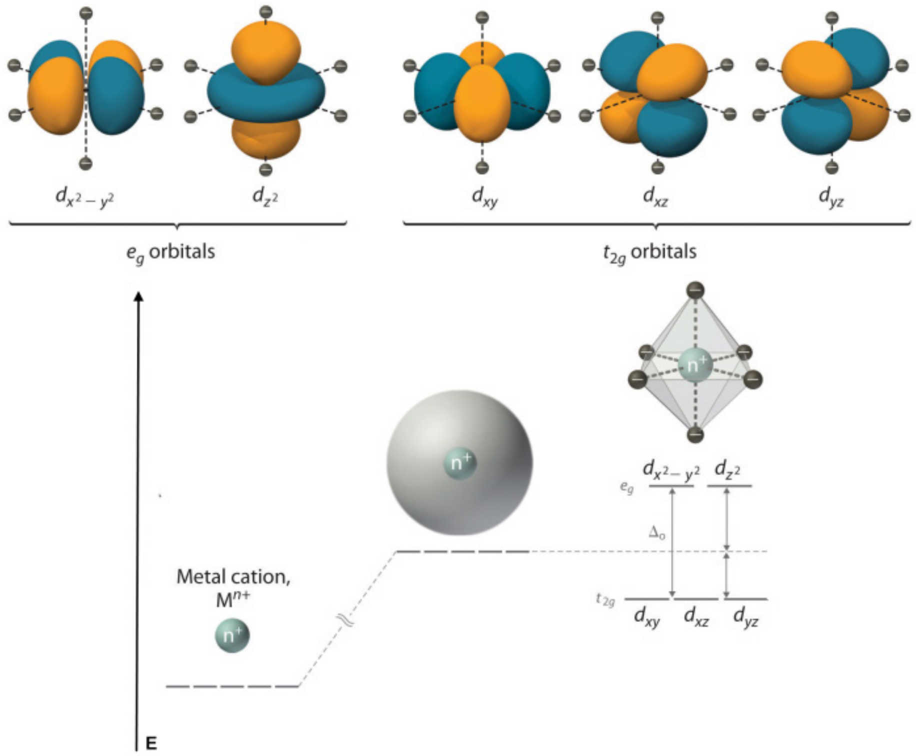


**Figure 5 – (Top) Valence *d*-orbitals of a transition metal with the distribution of negative charges associated with an octahedral crystal field; their directionality and the separation of labels is indicated. (Bottom) Split in energy for a metal cation $M^{n+}$ in the vacuum, compared with the same cation surrounded by a uniform sphere of negative charges, compared with the splitting when the charges are located at the corners of an octahedron. $\Delta_O$ is the crystal field energy split, the two $e_g$ orbitals increase in energy of $+0.6\Delta_O$, the three $t_{2g}$ orbitals decrease in energy of $-0.4\Delta_O$. This effect is reversed in a tetrahedral field, with the three $t_{2g}$ orbitals at higher energy and the two $e_g$ orbitals at lower energy, due to poor orbital overlap between metal and ligand orbitals (in tetrahedral coordination the ligands are directed on the axes).[36]**

Crystal field splitting reduces the degeneracy of the five orbitals, but there is still degeneracy within the two $t_{2g}$ and $e_g$ subsets. When the occupancy of the *d* orbitals is appropriate, the octahedra can be prone to distortion of the B-O bonds in order to remove the additional degeneracy and obtain a further energy gain. The configurations liable to benefit from a further removal of degeneracy are depicted in Fig. 6.

Systems with $d^0/d^{10}$, $d^3$ and $d^8$ configurations would not have any energy gain from a further splitting of the $e_g/t_{2g}$ orbitals; the same is true for $d^5$ in high-spin arrangement and $d^6$ in low-spin arrangement. These degenerate configurations may be subjected to pseudo (or second order) Jahn-Teller effects involving excited states at sufficiently low energy; this mechanism is favoured when the distorted configuration would improve the covalence bonding between the atoms and thus gain energy.

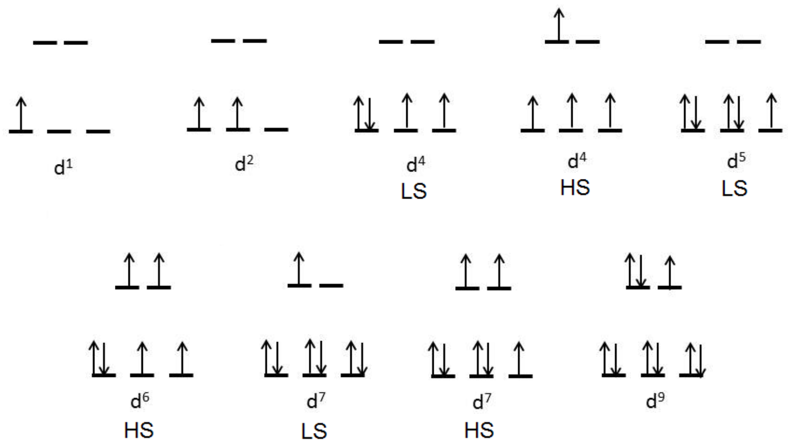


**Figure 6 – Electronic configurations in octahedral *d*-orbitals that lead to Jahn-Teller activity. Configurations labelled as low-spin (LS) happen in systems in which the splitting energy between the $t_{2g}$ and $e_g$ states is greater than the paring energy; in the opposite case, the standard Hund's rule is followed and the high-spin (HS) configuration is achieved. The stability rules for the spinel system rely on both dimensions of the cation and oxidation state, so not all these configurations are accessible.**

This leads to a direct solid-state application of the Jahn-Teller theorem, according to which every non-linear molecule with a partially filled set of degenerate orbitals will be unstable with respect to distortion.[37] A Jahn-Teller effect in the $BO_6$ unit splits the triply degenerate $t_{2g}$ orbitals in two $e'_g$ orbitals one $a_{1g}$ pointing towards the centre of the B-tetrahedron (trigonal distortion), or the doubly-degenerate $e_g$ into two nondegenerate orbitals and the triply degenerate $t_{2g}$ into one separate orbital and a doubly-degenerate pair (tetragonal distortion) (Fig. 7).

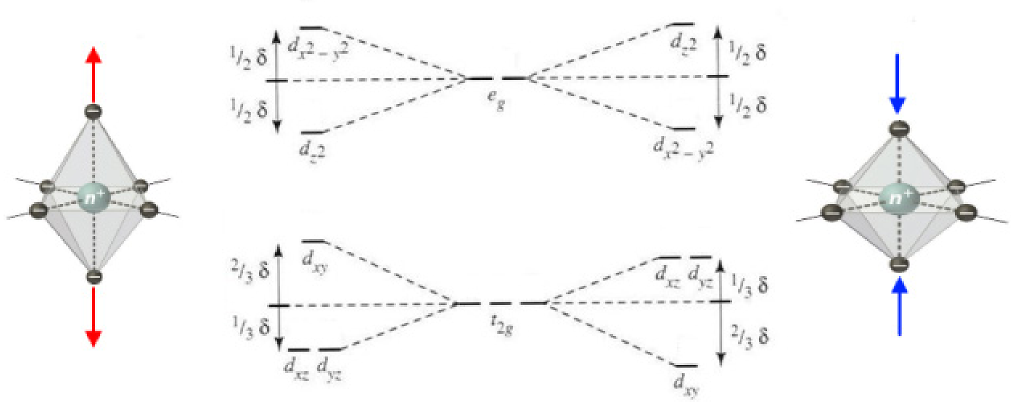


**Figure 7 – Removal of the degeneration of the $t_{2g}$ and $e_g$ orbitals in an octahedral crystal field as a result of Jahn-Teller elongation (left) or compression (right) of an $M^{n+}$-O bond (conventionally considered as being the one in the z direction), with relative shifts in energy. In a given system, the favourability of compression over elongation or *vice versa* depends on the electronic configuration of the metal cation.[35]**

In molecular complexes the flexibility of the structures allows for dynamism in bond contraction and elongation without disrupting the general symmetry. In solid state there are a number of competing interactions, from electrostatic to strain, that need to be balanced upon onset of the Jahn-Teller effect. The overall result is that the distortion in this highly-interconnected framework is always cooperative, and can lead to symmetry breaking and changes of structure at low temperature, when the thermal vibration of the lattice cannot compensate for the energy gained from a breaking of the degeneracy.[38]
The balanced outcome of these cooperative distortions can be defined as orbital ordering, and the resulting ground states tend to have a specific arrangement of orbitals. It is quite a common occurrence in perovskite structures and can often be paired with charge ordering interactions. [39] A usual example of this behaviour is $LaMnO_3$: this compound has an antiferromagnetic ground state in which the inherent degeneracy of the $Mn^{3+}$ cations ($d^4$, $t_{2g}^3e_g^1$) is removed by cooperative Jahn-Teller distortion in the lattice (Fig. 8). [40]

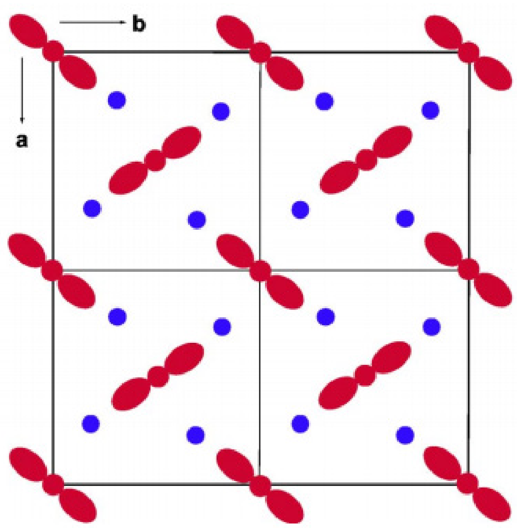


**Figure 8 – Orbital ordered ground state of $LaMnO_3$. La ions are indicated in purple, Mn in red, oxygen atoms are not shown but are octahedrally coordinated around the manganese. The staggered ordering of *d* orbitals in the *ab* plane is also repeated along the *c* direction. [40]**

### *1.3.1.3 Spin ordering*

With the exception of closed-shell configurations such as $d^0/d^{10}$ and $d^6$ LS, all transition metal oxides with unpaired electrons arranged in the orbitals carry an intrinsic magnetic moment. When inserted in an interconnected environment such as a crystal structure, magnetic moments can interact with each other, giving rise to the spin degree of freedom.

At high temperature, the thermal energy can overcome the magnetic interaction, leading to a paramagnetic phase with random orientation of the spins; upon lowering the temperature, the spin degree of freedom gains relevance and structures commonly undergo a magnetic ordering.
Magnetic ordering effects are complex and can give rise to a number of exotic arrangements of spins. A comprehensive outline of magnetic interactions and magnetic ordering will be provided in Chapter 2.3.
As introduced in the previous subsections, the presence of spin ordering does not rule out orbital or charge ordering transitions, even though a change in the structure can lead to a rearrangement of already ordered spins or can induce ordering in a paramagnetic structure.

## 1.3.2. Cooperative ordering and "orbital molecules"

Spin, orbital and charge degrees of freedom are often coupling or interacting when present at the same time in a material. Systems with these interactions are usually characterised by multiple ordering: $La_{0.5}Ca_{0.5}MnO_3$, for example, has $Mn^{4+}$ and $Mn^{3+}$ ordered in layers, a staggered ordering of *d*-orbitals from the $e_g^1$ states of the Jahn-Teller active $Mn^{3+}$ sites and magnetic ordering of the manganese spins (Fig. 9).[41]

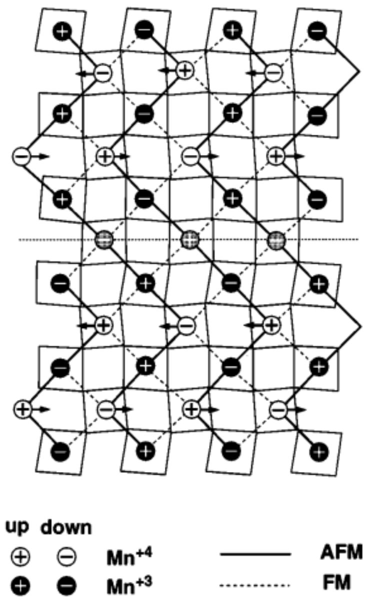


**Figure 9 – Projection on the *ac* plane of the structure of $La_{0.5}Ca_{0.5}MnO_3$ at T = 1.5 K. $Mn^{3+}$ is in filled circles, $Mn^{4+}$ in empty circles, the direction of the ordered spins are indicated by + and – signs. The type of magnetic coupling is indicated by bold and dotted lines. Orbital ordering (equivalent to Fig. 8) is not depicted.[41]**

The spinel structure has a unique place in the analysis of ordering phenomena of transition metal oxides, since it has a variety of examples with concurrent ordering features. The relevance of their influence can be readily modified upon changing the environment: pressure, temperature, magnetic field and level of doping are all external stimuli that introduce, modify or suppress one or more of these orderings. Moreover, in contrast with manganites, the metal-metal distances in spinels are close enough to allow direct interactions between cations.

In one of the most interesting cases of this behaviour, the coupling of charge, orbital and spin degrees of freedom leads to the formation of self-organised states as a result of cooperative ordering. At the onset of the phase transition, usually accompanied by a change in crystal structure, two or more transition metals can form clusters with a shared electron density, resembling a weak covalent bond, which can be formed and disrupted reversibly by changing the system's temperature. These clusters are called "orbital molecules" and are relevant to the understanding of the ground state of the spinels in which they occur.

The most basic orbital molecule observed is a dimer, in which two adjacent B centres pair their electrons to form a spin singlet. An example of this behaviour is the ground state of the normal spinel $MgTi_2O_4$, where the $Ti^{3+}$ has a $d^1$ configuration, metallic conduction from the orbitals left free for electron hopping and *Fd-3m* space group at high temperature. Upon cooling below 260 K, the structure distorts to a $P4_12_12$ (or $P4_32_12$) space group and the material becomes insulating, due to the formation of Ti-Ti dimers where the two spins are paired in the same $t_{2g}$ orbital. These short bonds alternate with longer metal-metal distances, giving rise to a chiral ordered ground state (Fig. 10) [42]. Spin-singlet dimers are a relatively common occurrence in several systems with edge-sharing and face-sharing octahedra, even outside of the spinel structure family. Apart from several other $Ti^{3+}$ oxides, they can be found in ruthenium metal oxides with $Ru^{4+}$ and $Ru^{5+}$ oxidation state ($Li_2RuO_3$ [43], $Ba_3CaRu_2O_9$ [44], and $Ba_3NaRu_2O_9$ [45]) and in rhodium metal oxides with $Rh^{4+}$ oxidation state ($LiRh_2O_4$ [46]).

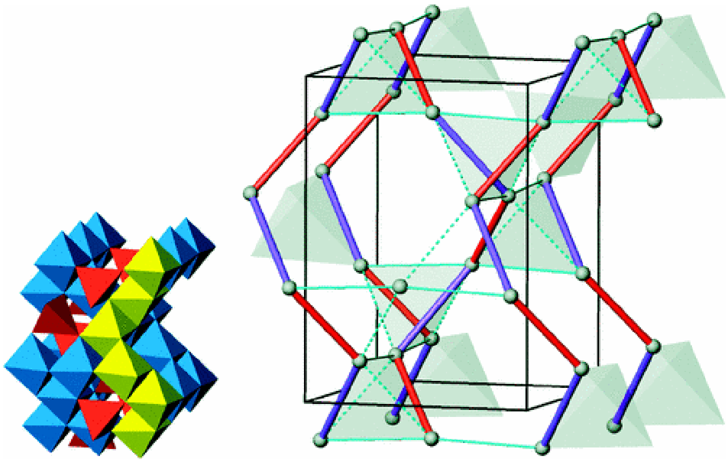

**Figure 10 – Tetragonal structure of $MgTi_2O_4$ at 200 K, with the Ti-Ti bond connectivity outlined. The red bonds are the short, dimerised Ti-Ti distances, the purple bonds by contrast are the longest, whereas the dashed lines are intermediate bonds. The inset to the left shows the full 3D structure of the spinel, and the B sites involved in a helix are coloured in yellow.[42]**

In contrast with several examples of dimers, orbital molecules involving three or more metal centres are a rarer occurrence and have not been widely reported for spinel structures. There are several examples involving trimers of vanadium cations ($LiVO_2$ [47], $Na_{0.5}VO_2$ [48] and $BaV_{10}O_{15}$ [49]), not all definitely confirmed by crystallography, and one case with a linear arrangement of three face- sharing $Ru^{4+}$ octahedra in $Ba_4Ru_3O_{12}$ [50]. Spinel materials only have two definitively reported cases of large orbital molecules: linear arrangement of $Fe^{3+}$-$Fe^{2+}$-$Fe^{3+}$ cations (“trimerons”) in the low-temperature phase of $Fe_3O_4$[26] and large clusters of seven vanadium cations in $AlV_2O_4$. [51] Orbital molecules formation and their evolution as a function of temperature and chemical pressure will be the subject of Chapter 3, where a more detailed introduction to the trimeron discovery and description will be provided. The ordered phase of $AlV_2O_4$ has recently been subject to PDF studies and the findings show that it could involve clusters of tetramers and trimers rather than one single heptamer over seven sites;[52] this ordering has a perfect equivalent in $GaV_2O_4$.[53]

Overall, orbital molecules can be described as a new class of quantum electronic state arising through the amplification of the charge, orbital and spin degrees of freedom in transition metal oxides. These clusters tend to be highly anisotropic and can result in structures with low symmetry and interesting properties such as multiferroism, but their inherent directionality can lead to specific crystallographic planes or atomic chains where novel physical interactions can be influenced and be exploited.

Discovering and characterizing more of these ordered states could be a key step to not only better understand these fundamental interactions, but also to find new technological applications for TMO. The use of spin and charge coupling in TMO is already widespread in spintronics and has contributed to significantly advancing our information storage capabilities. In the foreseeable future, an "orbitronics" analogue, where the angular momentum of the orbitals is put to use, could be available for the creation of high-performance devices.[54]

## *1.4 Aims of Research*

The present study is designed to examine the low-temperature ordering effects of ferrite materials. The main results will be derived by a variety of structural methods, but physical methods will be presented as the necessary foundation before further characterisation.

After this brief introduction on spinel ferrites and the significance of possible ordering features, Chapter 2 will present the experimental methods used in this research. Starting from the synthesis of the materials, it will continue to the necessary elements of crystallography to understand the formalism of crystal structures. Diffraction will then be described in its general physics, and then detailed in its use with X-ray and neutron sources. A description of the data collection procedures will be provided for each of the diffraction techniques used, the instrumentation that supported the studies, and the software available for the analysis. Moreover, details on the relevant physical properties of ferrite materials and how they were characterised in this study will be outlined.

The experimental Chapter 3 will be completely focused on studies of the ground state of magnetite. After a brief background on the research efforts that led to the first solution of the Verwey phase and the trimeron discovery, two features that were not previously reported will be explored. The first study will be on the variability of the transition with chemical composition, through single crystal synchrotron X-ray diffraction studies on a natural sample (~ 0.5% impurities), an oxygen deficient sample ($Fe_{3(1-\delta)}O_4$ with ~1% impurities) and a Zn-doped sample ($Fe_{3-x}Zn_xO_4$ with ~ 3% impurities); the results of the structural analysis, and their significance will be provided. The second study will explore the possible persistence of trimerons on a locally ordered scale even in the high-temperature phase of magnetite, reportedly cubic and undistorted over the long range; a Pair Distribution Function (PDF) study of synchrotron powder diffraction data between 90 and 923 K will be outlined and the conclusions will be linked with the existing literature on the subject.

The experimental Chapter 4 will be focused on the previously unknown magnetic structures of two normal spinels, $Fe_2GeO_4$ and γ-$Fe_2SiO_4$. Details on the synthesis of both samples, their physical characterisation and preliminary structural data will be provided, before focusing on the results of neutron powder diffraction studies. Both structures undergo an unconventional magnetic ordering that has never previously been observed in this type of material. Details on the magnetic structure solution will be provided, and the results will be systematised in the bigger picture of frustrated magnetism with a novel take of ordering through “frustration waves”.

Chapter 5 will draw the overall conclusion of the work and outline some future prospects of the research.

# 2. EXPERIMENTAL METHODS

## *2.1 Solid State Synthesis*

### 2.1.1. High temperature route

In laboratory conditions, transition metal oxides are commonly synthesised through high temperature solid-state synthesis. In this synthetic route, precursors are powdered materials, often commercially available, weighted in stoichiometric quantity to ensure the right ratio of elements for the desired final product; no dissolution in solvents or conventional chemical reaction is involved. Proper mixing of components is ensured purely through diffusion processes, which are a thermally activated and in normal ambient condition would not occur on a kinetically relevant scale. Diffusion can be enhanced through fine grinding of precursor powders and compaction in pellet form to increase the contact between the particles, followed by an appropriate rising of the temperature, usually above at least 400°C. The net result of this general protocol is the formation of a new solid, in most cases within one or two days of reaction.

The standard equipment to perform this type of synthesis is a laboratory furnace, routinely spanning temperatures between 300°C and 1600°C. In a box furnace heating elements are placed on the sides of a cube and the easy access through a front door makes it appropriate for quenching synthesis, where the temperature of the sample needs to be promptly lowered (Fig. 11A). In a tubular furnace the heating elements are placed around an alumina tube; two accesses on the sides of the working cylinder make this furnace appropriate to add different atmospheres (inert, reducing or oxidizing) as part of the reaction environment (Fig. 11B).

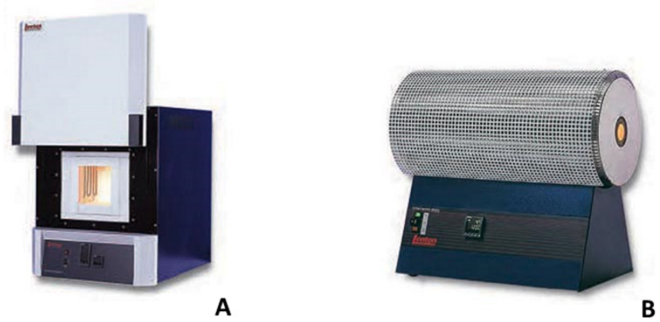


Figure 11 – A) Box furnace, with front access to the heating chamber. B) Tubular furnace, with side access to the alumina tube. The optimal heating position is considered to be the centre of the tube, which is surrounded by heating elements. With the appropriate fitting, the tube can be put under gas atmosphere.

Different syntheses have different requirements and conditions need to be optimised on chemical bases and tuned with experience. In particular, transition metals have a plethora of accessible oxidation states, thus making the change of reaction atmosphere a useful tool to control the reaction product. Common methods of obtaining oxidizing atmospheres are with air and oxygen flow, hydrogen can be used in various percentages to create a reducing atmosphere, and inert atmospheres are nitrogen and argon. If the stabilisation of certain oxidation states (e.g. $Fe^{2+}$ rather than $Fe^{3+}$) requires a very precise control on the oxygen content of the reaction environment, a quartz tube sealed under vacuum and placed in a box furnace is the preferred route. The quartz tube method has been employed for most of the syntheses featured in this thesis. [55]

A more precise control of temperature and atmosphere is usually necessary to influence the growth and the stoichiometry of single crystals, in comparison to powders. The work on $Fe_3O_4$ has employed complex processes of annealing in controlled oxygen atmosphere that will be described in Chapter 3.

### 2.1.2. High-pressure/high-temperature route

Materials can be influenced by pressure in terms of composition, reactivity and symmetry. Application of pressure in combination with temperature increases the diffusion of atoms between different powdered precursors, making reactions faster; on the other hand, high-pressure phases tend to form structures with higher symmetry and higher coordination numbers of the cations, sometimes stabilizing unconventional oxidation states and neighbouring interactions.

Applying the Le Chatelier's Principle of Equilibrium to crystalline systems can provide reasoning behind this behaviour: if we consider our material to be a system in chemical equilibrium, application of pressure favours a decrease in volume; the $\Delta PV$ for the system is negative, resulting in an overall lowering of energy of the system. In the solid state, a reduction of the volume can be obtained through a more efficient packing of atoms, inherently related with a more symmetrical crystal. Adding temperature of course helps the breaking and reforming of the bonds and can accelerate the reaction significantly.[56]

Exploring high-pressure may help in obtaining structures and properties that would not be accessible at normal conditions. However, reaching pressures capable of influencing crystal lattices is a technological challenge that took several decades to overcome and is still in demand of further optimization.

The apparatus currently used at the University of Edinburgh and employed for some of the syntheses in this thesis is a Walker-type multi-anvil module, capable of reaching pressures up to 25 GPa and temperatures up to 2500°C.

A simple anvil design is the archetype of the high pressure apparatus, as designed by Percy W. Bridgman in the early 1900s. It applies the principle of maximizing the achievable pressure by reducing the application area of an increasingly large force: the point of contact with the sample needs to be extremely small, but the anvil needs to be designed with a material and a shape that can withstand the application of a large loading weight without deforming or breaking. In the Bridgman design these requirements are met by placing the sample between the circular cut faces of two tungsten carbide anvils (Fig. 12). [57]

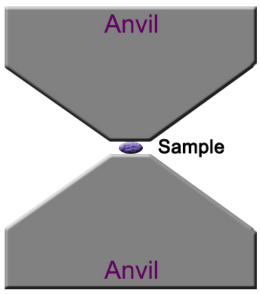


**Figure 12 – Schematic depiction of a Bridgman-type cell design, with two anvils pressing on a sample.**

The Bridgman design is limited in working temperature and uniaxial pressure (10 GPa, 500°C), but adding multiple anvils can overcome these constraints. The Voggenreiter Walker-type model has two-stage multi-anvil settings: a first, bigger set of six anvils made of tooled steel fits eight tungsten carbide cubes with a triangular cut between its six faces (Fig. 13A). The tungsten carbide cubes enclose an octahedral pressure cell and the adequate spacing to obtain an overall perfect cube is achieved with pyrophilite gaskets as separators (Fig. 13B). This whole assembly is enclosed in a stainless steel cylinder, on top of which a hydraulic press imposes incremental loads to increase the resulting pressure on the sample while water-cooling the chamber (Fig. 13C). The result of this geometry is uniform pressure, which is maximised by imposing large loads on the compressible steel cylinder and first anvil, in comparison to the rigid tungsten carbide cubes.

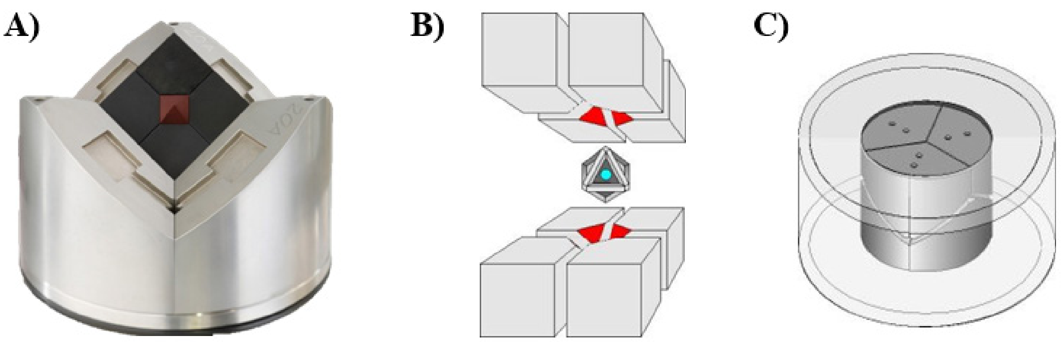


**Figure 13 – Components of the multi-anvil apparatus: A) three of the six tooled steel anvils, with a model cube in its designed position; B) Model of the eight tungsten carbide cube arrangement around the octahedral pressure cell, the gaskets displayed around the octahedron are spacers for the correct line up of the cube and in real experimental setting are glued around the cut of the cubes. The space for the sample is highlighted in blue; C) Model of the positioning of the six steel anvils (containing the cube) within the steel cylinder chamber that encloses the whole setup. Both the inside of the chamber and the sides of the six anvils are lined up with insulating layers of plastic to avoid short-circuiting.** [58]

The octahedral pressure cell is made of MgO ceramic and hollowed to fit several components together to ensure the right environment for the sample. The sample is packed in a boron-nitrate capsule, which is surrounded, in order, by two graphite sleeves and a $ZrO_2$ cylinder; the upper part of the zirconia cylinder is capped on each side with an MgO lid and a ring containing a polished molybdenum disc (Fig. 14). The molybdenum disc is a conductor and is suited for bringing current to the graphite sleeves, which will act as heaters during the reaction. The path for the electric current through the six tungsten carbide cubes is provided by two Cu electrodes placed on two diametrically opposed cubes in the anvil, allowing the current to flow through and out of the system. To avoid short-circuiting, half of the cubes have PTFE tape on their faces, so that they are insulated from the adjacent ones; the overall shape of the 8-anvils cube is insulated from the 6-anvil cylinder through six squares of fiberglass; finally, the 6-anvil cylinder is insulated from the containment ring with two layers of mylar film of different thickness. [59]

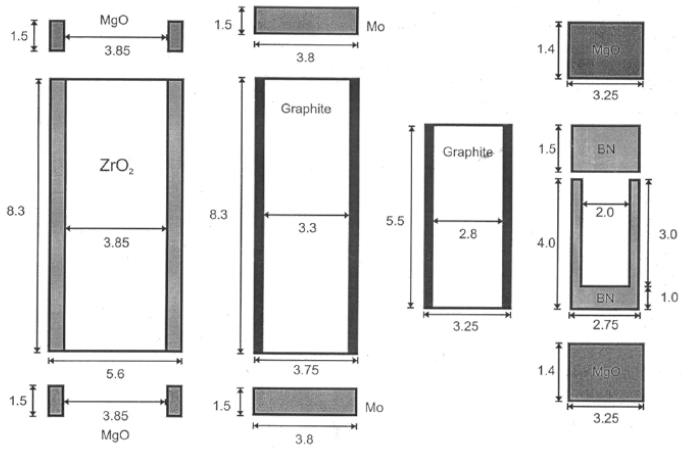


**Figure 14 – Schematic depiction of concentric assembly for the high-pressure sample. Dimensions are given in millimetres, and the fully packed cylinder is inserted in the octahedral pressure cell.**

In this type of apparatus, values for both pressure and temperature are established through a calibration procedure. Calibrating pressure requires assembling the whole set up with bismuth as a sample and a resistometer connected to the set up; the load from the press in tons can then be correlated to pressure by following discontinuities in resistivity associated with the well-established pressure-induced phase transitions in Bi (2.55, 3.15 and 7.70 GPa, Fig. 15A). Conversely, temperature is calibrated through a Pt-Rh thermocouple connected to the setup; readings in °C are correlated with the power of the current through the graphite heaters and interpolated to provide the parameters for future experiments. [60] Calibration measurements were performed by Dr Elena Solana Madruga.

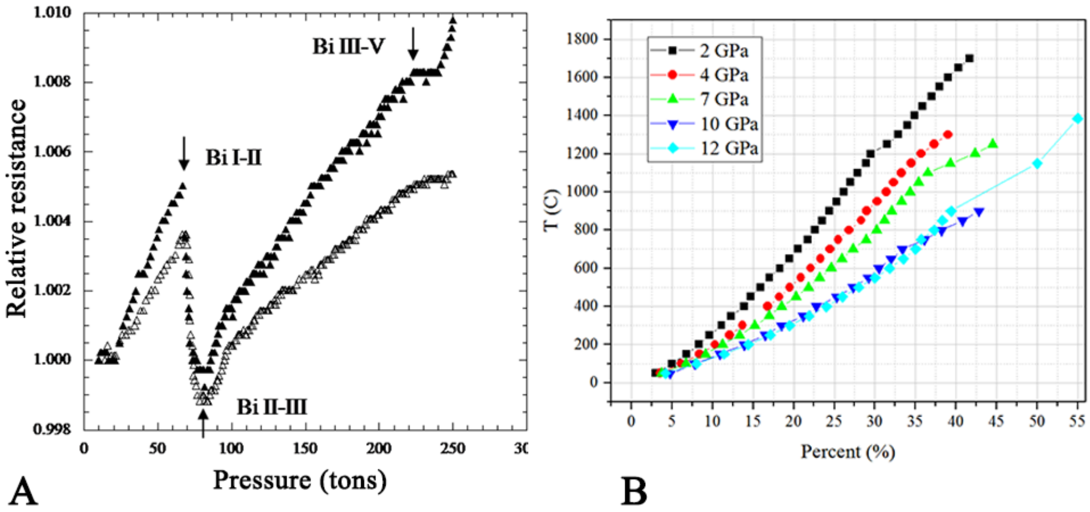


**Figure 15 – A) Measured resistance from bismuth as a function of applied load of the hydraulic press in tons. The three phase transitions of the element are noted on the graph. B) Measured temperature as a function of percentage of input power, at different loading pressures.**

The outlined procedures are applicable to pressures up to 15 GPa and temperatures up to 2000°C, as they are the only ones relevant for the purpose of this thesis. These performances are achievable with a set of tungsten carbide cubes with a truncation edge length of 8 mm,  an octahedral cell with edge length of 14 mm (known as 14/8 set) and a graphite heater. Lowering the dimension of the truncation and octahedral edges to 7/3 and substituting the graphite for a rhenium capsule to act as an heater, the setting can withstand pressures up to 25 GPa and temperatures up to 2200°C. Changing heating element is a necessity at higher pressures, since carbon enters the field of stability of diamond and the conductor-to-insulator transition would cause a short-circuiting of the pressure cell.

The dimensions of the octahedral pressure cell limits the BN capsule diameter to 2 mm of internal diameter. As such, the high-pressure high-temperature synthesis route performed with this apparatus has a hard limit on the sample dimensionality: syntheses with the 14/8 set routinely yield 7-10 mg of sample per run, syntheses with the 7/3 set have a maximum yield of 3-5 mg per run. However, in contrast with *in situ* high-pressure experiments with apparatus like the Diamond-Anvil Cell, samples recovered from a multi-anvil Walker-type press are actual high-pressure products, which remain metastable at room temperatures and pressure. The yield of one high-pressure run is sufficient to perform X-Ray diffraction with laboratory and synchrotron sources, various physical measurements and several complementary techniques (i.e. Mossbauer, Electron Microscopy, etc.); moreover, results

are remarkably reproducible and for experiments requiring more samples these can be obtained from different high-pressure runs  (i.e. neutron powder diffraction).
This makes the high-pressure high-temperature synthesis an incredibly interesting tool that has led to the discovery of new materials and new polymorphs in the last decades.

Details on the synthesis of a geologically relevant high-pressure high-temperature phase will be provided in Chapter 4.3.

# 2.2 Structural Characterisation

## 2.2.1 Introduction to crystallography

### *2.2.1.1. Symmetry and space groups*

All materials studied in this thesis are crystalline, which means that atoms in the solid phase are arranged in a pattern that repeats with at least some degree of order in three dimensions.

Given a fundamental group of atoms, enclosed in a unit cell with metric *a, b, c* and related angles α, β, γ, the entirety of the solid can be reproduced by periodically propagating it with at least translational symmetry. Every crystal can be ascribed to one of the fourteen Bravais Lattices, which define all the possible relationships between dimensions and angles and also take into account centring within the cell (face, body and base centring); the lattices are shown in Fig. 16.

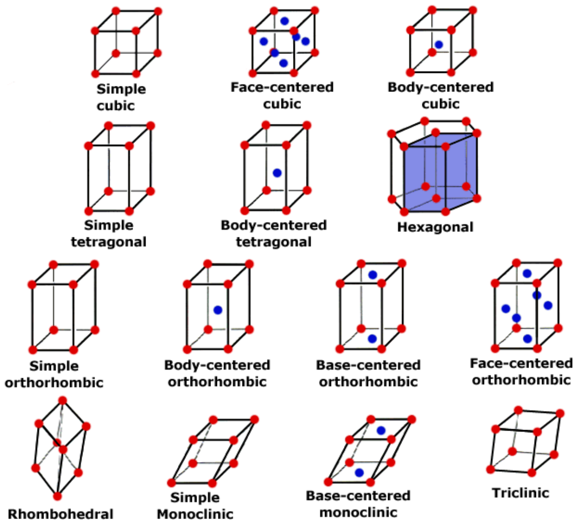


**Figure 16 – Schematic depiction of the 14 Bravais lattices, with the associated standard naming.[61]**

The requirement for translational symmetry means that two adjacent cells will be perfectly equal. However, it is common for a unit cell to have an additional symmetry relationship within the atoms inside it: symmetry elements can be a simple relationship (inversion, rotation, mirroring) or a composition of multiple movements (glide planes, screw axes). In this way, a whole crystal can be described through the application of all the symmetry operations, including translation, to a fundamental group of atoms not initially related by any symmetry (asymmetric unit).

The number of finite combinations of symmetry operators is unique and after crossing them with the 14 Bravais Lattices only 230 possible crystal symmetries can be derived. The 230 crystal symmetries strictly obey group theory, and can therefore be called space groups. The list can be constructed by pure mathematical knowledge and does not require any empirical consideration. A detailed description of each space group is tabulated in the International Tables of Crystallography, Volume A.[62] [63]

#### *2.2.1.2. Distortions and phase transitions*

As introduced in Chapter 1, crystals can undergo ordering phenomena involving a change and coupling between the degrees of freedom. Whilst spin ordering does not inherently change position or disposition of atoms, both charge localisation and modification in bond lengths in response to crystal field effects usually result in a change of symmetry of the structure. From a crystallographic point of view, this is caused by a loss of one or more symmetry elements that defined the starting, or "parent", space group. The mathematics of group theory dictates that, if a group in itself exists and is self-consistent, a subset of its components will be a group in itself; the distorted structure will therefore have the characteristics of a different space group.

Any change of symmetry provoked by a distortion will relate two crystals, characterised by two space groups, by the so-called "group-subgroup" relationship. The sequential loss of symmetry elements and the resulting space groups can be depicted as a subgroup tree, exemplified in Fig. 17 for *Fd-3m*, as the spinel structure will be the starting point of any structural work in this thesis.

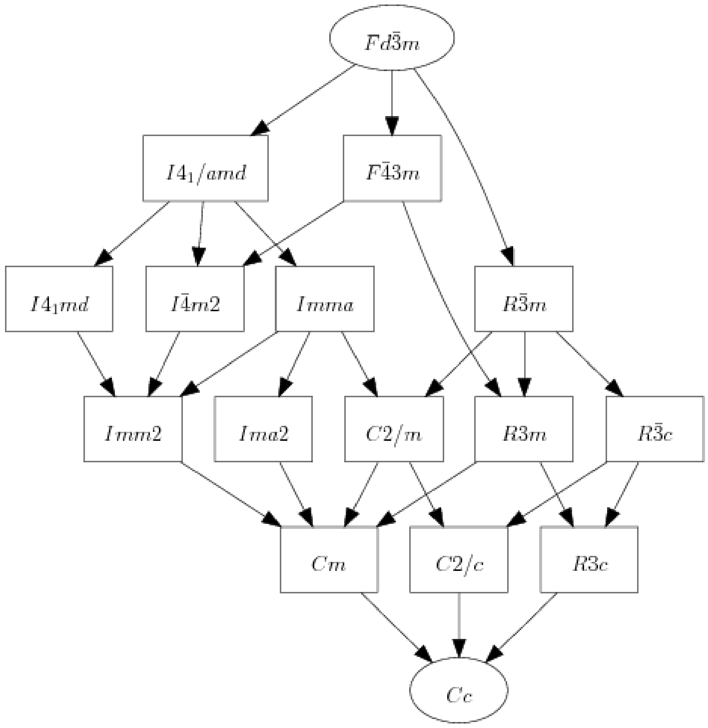


**Figure 17 – Sequence of group-subgroup relationships from the parent structure (*Fd-3m*) to a lower symmetry structure (*Cc*). The whole path can be covered through a sequential removal of symmetry elements from the parent, and it can be expanded to a further group by removing constraints on the cell metric. *Fd-3m* is the structure of a cubic spinel, *Cc* will be discussed as the symmetry of the low temperature structure in magnetite, *$I4_1/amd$* is a common distortion of antiferromagnetic spin ordered spinels. The graph was generated through the Bilbao Crystallographic Sever.** [64]

Phase transitions that make direct use of these diagrams are usually first order, on the account that there is no way to reach a symmetry at the bottom of the diagram without going through the sequential steps that compose it. Conversely, the requirement for a second order phase transition is the presence of a continuous process, and for the nature of distortions in solids and their relationship with symmetry their occurrence is possible within a group-subgroup framework only if it involves a one-step process (e.g. a transition from *Fd-3m* to *$I4_1/amd$*, *F-43m* and *R-3m* can be second order).[65] [66]

An additional factor that can accompany this type of transitions is the presence of twinning. Twinning occurs when two crystal grains grow from a shared origin in a way that is in itself symmetrical in space. Some twinning processes are related to crystal growth or mechanical processes, but first order phase transition can produce twins as an effect of symmetry loss: crystals that undergo cooperative distortions severely modifying the space group tend to compensate the strain imposed by the change in lattice metric with the formation of twin domains. In this case, every symmetry element lost from the parent structure can become a twin generator, relating two grains through a symmetry that is not really present in the structure itself in its distorted state. [67]

Twinning represents a problem in the analysis of phase transitions because it adds complexity to data. Chapter 2.2.5 will introduce the way twinning can be incorporated in the studies of crystal structures, as it will be relevant for the ground state of magnetite discussed in Chapter 3.

### *2.2.1.3. Representation analysis*

The periodic lattice of a crystalline material can be described as a set with a given modulation and characterised by a given symmetry, propagating through 3D space with a propagation vector, ***k***. For any given space group, this periodicity will be commensurate, but there could be more complex crystal structures that are subtly shifting in modulation and are incommensurate.

This is particularly useful for symmetry lowering transitions: the lower symmetry space group can be described as the parent group *G* to which we apply a propagation vector ***k***, defined in reciprocal space. A propagation with indexes (1 1 1) would leave the modulation, and thus the parent group, invariant; by contrast, a propagation with fractional indexes in any of the three directions would describe a cell with lowered symmetry and can only mathematically apply to a subset of operators of the parent group. The subset of operators is a group in itself, which we can call $G_k$, or little group of *G*.

The description of how the structure changes under the relevant symmetry elements, simplified in sets of a sum of orthogonal matrixes, is called the Irreducible Representation (Irreps) of $G_k$. With this capability, it is also possible to model distortions or symmetry changes that are only relevant for certain atoms in a cell of a given symmetry (e.g. magnetic ordering, by definition only influencing magnetic atoms), keeping the invariant part of the description fixed.

Irreducible representations are usually labelled as $\Gamma$, and are composed by a number of basis vectors $\psi$. In a simple case, these bases would just describe the influence of the symmetry on an atom *a* in the $j^{th}$ cell as a function of ***k***:

$$a_j = \psi_j \exp -2\pi\, ik \cdot r$$

In a very simplified case, an irreducible representation could be composed like this:

$$\Gamma_i = \begin{pmatrix} 1 & 0 & 0 \\ 0 & 1 & 0 \\ 0 & 0 & 1 \end{pmatrix} \begin{pmatrix} \psi_1 \\ \psi_2 \\ \psi_3 \end{pmatrix}$$

This approach is very flexible and can be applied to a variety of cases, from purely structural to purely magnetic or a combination of thereof. [68] An overview of the Irreps analysis for studies of ordered magnetic moments in crystal structures will be provided in Chapter 2.2.5 and applied to the data analysis of Chapter 4.

## 2.2.2 Fundamentals of diffraction

A thorough analysis of transition metal oxides and the various features they exhibit requires a tool capable of detecting atomic arrangements in the solid state and their changes. While several techniques fit this requirement, diffraction is the most widespread and preferred in the work presented.

In physics, diffraction is generally defined as a scattering from a small aperture whose dimension is comparable with the wavelength of the particle/radiation passing through it. An incoming plane wave passing through two slits will diffract from them as two new point sources; a detector placed at a suitable distance will see the effect of the diffraction as an interference pattern, with point of maxima given by constructing interference and point of lack of signal given from destructive interference (Fig. 18).

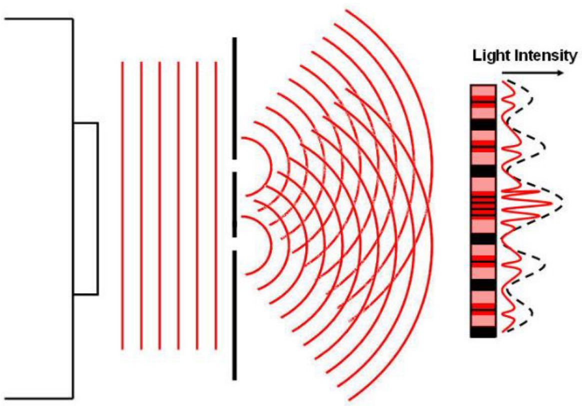


**Figure 18 – Double slit diffraction of a planar wave of photons. Each slit acts as a single source for diffracted spherical waves that overlap and interfere with each other in the propagation. The image on the right side is an imaginary detector, getting peaks of constructive interference intensities and dark spots when the interference is destructive.** [69]

This effect can be readily applied by comparing spacing between atoms arranged in a one-dimensional chain to the effect of several slits for the radiation: provided that the wavelength and interatomic distance are comparable, the resulting interference pattern allows to infer the distance between two "point sources" of diffracted radiation.[70]

In the solid state, applying diffraction requires to take into account the presence of a multi-dimensional arrangement of atoms. For detection of constructive interference from a crystalline lattice, the diffracted radiation must follow the Bragg's Law, formulated by W. L. Bragg and W. H. Bragg in 1913 on the basis of empirical evidence:

$$n\lambda = 2d\sin\vartheta$$

The equation states the interdependencies for a monochromatic radiation $\lambda$ diffracted at an angle $\vartheta$ after scattering from planes at a distance $d$. $n$ is the order or the interference, usually simplified to 1, and for the law to be satisfied it must be integer and positive. Given that the distance between atomic planes in a crystal is usually in the order of 0.25 nm, diffraction from a crystal can be performed with X-rays or other particles with a wavelength of propagation smaller than 10 nm. [71]

Every crystal will have multiple planes in diffraction conditions at the same time, in a way that is dictated by the symmetry of the atomic lattice. Regardless of the specific space group, the diffracting crystal will have a series of equivalent planes that will reach constructive interference at the same time. These planes are labelled with the Miller indexes, *hkl*, and represent an easy way to refer to specific subsections of a unit cell: for instance, a plane crossing the body diagonal of a cubic cell will be labelled as 111. Any generalized plane will intercept the unit cell in positions *a/h*, *b/k*, *c/l*. If the cell parameters are orthogonal, every equivalent set of planes will follow the relationship:

$$\frac{1}{{d_{hkl}}^2} = \frac{h^2}{a^2} + \frac{k^2}{b^2} + \frac{l^2}{c^2}$$

The Miller indexes are directly correlated with the reciprocal lattice, a useful tool to ascertain the diffraction conditions of a set of planes. For any given cell of metric vectors ***a, b, c***, it is possible to define a reciprocal cell with metric ***a*, b*, c**** according to the following relationships:

$$\boldsymbol{a}^* = \frac{\boldsymbol{b} \times \boldsymbol{c}}{\boldsymbol{a} \cdot \boldsymbol{b} \times \boldsymbol{c}} \qquad \boldsymbol{b}^* = \frac{\boldsymbol{c} \times \boldsymbol{a}}{\boldsymbol{b} \cdot \boldsymbol{c} \times \boldsymbol{a}} \qquad \boldsymbol{c}^* = \frac{\boldsymbol{a} \times \boldsymbol{b}}{\boldsymbol{c} \cdot \boldsymbol{a} \times \boldsymbol{b}}$$

As such, each reciprocal vector is perpendicular to the plane defined by the remaining vectors (i.e. $\boldsymbol{a} \cdot \boldsymbol{a}^* = 1, \boldsymbol{a} \cdot \boldsymbol{b}^* = \boldsymbol{a} \cdot \boldsymbol{c}^* = 0$). The reciprocal equivalent of the interplanar distance $d_{hkl}$ is defined as:

$$\frac{1}{d_{hkl}} = H_{hkl} = h\boldsymbol{a}^* + k\boldsymbol{b}^* + l\boldsymbol{c}^*$$

which is equivalent to saying that the vector $H_{hkl}$, of length equivalent to the reciprocal of the interplanar spacing, is normal to any given set of *hkl* planes in the lattice. The equivalence with the diffraction conditions of a set of planes is depicted in Fig. 19.

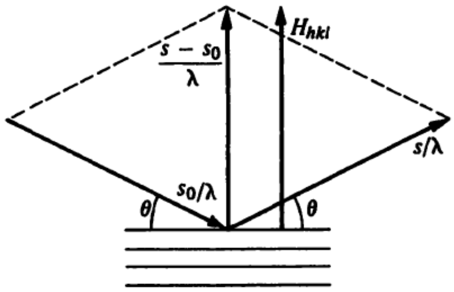


**Figure 19 – Schematic of diffraction conditions for a general incident beam $s_0/\lambda$ and diffracted beam $s/\lambda$, incoming with an angle θ. The drawing is in scale to show the equivalence between the diffracted vector $(s-s_0)/\lambda$ with the reciprocal vector $H_{hkl}$. [70]**

An equivalently useful tool to determine the presence or absence of diffraction from a given set of *hkl* planes is the so-called Ewald sphere of reflection, which can be drawn as a sphere of radius 1/λ centred on the end of an incident beam vector $s_0/\lambda$ and crossing the origin of the reciprocal lattice. The Bragg's law is satisfied for any given *hkl* point that falls on the surface of this sphere. A simplified scheme of the Ewald sphere in two dimensions is provided in Fig. 20.[72]

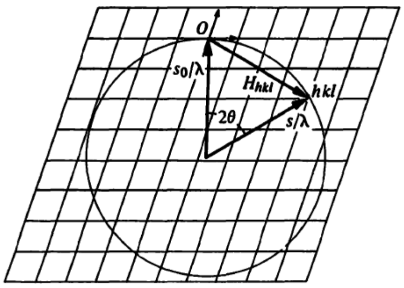


**Figure 20 – Sphere of reflection on a two-dimensional reciprocal lattice. The relationship between incident beam (*$s_0/\lambda$*), diffracted beam (*$s/\lambda$*), angle of diffraction (2θ) and reciprocal lattice vector ($H_{hkl}$) is shown in graphical form. A set of *hkl* planes will be in diffraction conditions if an *hkl* point falls on the outlined circumference/sphere. [70]**

For a given volume, a triclinic crystal with a primitive cell and only translational symmetry (equivalent to the *P1* space group) will have the highest number reflections in its diffraction pattern. Any additional symmetry element is accompanied by more conditions of destructive interferences, called "systematic absences", which can help identify the symmetry of the diffracting crystal experimentally.

The most concise way to express the scattering behaviour of a crystal is through the structure factor, accounting for both symmetry and atomic composition:

$$F_{hkl} = \sum_i f_i \exp[2\pi i(hx_i + ky_i + lz_i)]$$

where, for every atom *i* in *x, y, z* coordinates, the scattering beam phase and intensity are determined in relationship to the scattering function. This scattering function *f* depends not only on characteristics of the atom itself, but also on the type of incident radiation. [60]

The outlined formalism is applicable to any scattering event arising from coherent domains, which is also known as "coherent scattering". It is however worth noting that the total detected intensity during a real diffraction experiment is composed of incoherent (IC), multiple scattering (MC) and background (BG) intensity:

$$I_{TOT} = I_C + I_{IC} + I_{MC} + I_{BG}$$

Incoherent intensity arises from events that are not perfectly elastic, such as fluorescence, Compton scattering or even magnetic contributions in the case of neutron beams. Multiple scattering generally refers to a scattered beam that incurs in a new elastic event while propagating through the sample, and it can be particularly prominent for complex samples with large dimensions. Background scattering is the most controversial component: apart from contributions from air, sample holder and instrumental components, it may consists of broad and low intensities between and underneath Bragg diffraction peaks; this diffuse intensity can arise from amorphous impurities, or from structural effects of local disorder that are not on a sufficiently large scale to give rise to long-range coherent scattering. [73]

In most of the modelling procedures associated with diffraction experiments, only coherent scattering is considered and the background is arbitrarily fitted with a smooth curve. However, the merit of a more thorough analysis of total scattering will be explored in Section 2.2.5.

In this thesis, only X-ray diffraction and neutron diffraction were employed, so a more detailed description of their mechanics will be provided.

### 2.2.3. X-Ray diffraction

X-ray diffraction takes advantage of short-wavelength photons (0.01 to 10 nm) to analyse crystal lattices with comparable *d*-spacing. Electromagnetic radiation does not interact directly with the atomic nuclei composing the crystal: X-rays scatter from the electronic clouds surrounding each atom. Therefore, the scattering power of an atom and its X-ray scattering function *f* are a function of its number of electrons (*Z*), making X-ray diffraction particularly well-suited for heavy atoms with a dense electronic cloud.

It is necessary to point out that diffraction is not the only mechanism for interaction between X-Rays and matter: because of their high energy, X-rays tend to have a small penetration depth inside of a material (~ 5 µm), are susceptible to backscattering effects, and can lose some energy in inelastic interactions like ionization and fluorescence of the material. These effects are secondary for the diffraction purpose but tend to become more prominent at high incident angle; the scattering function decreases rapidly as a function of the resolution ($sin\theta/\lambda$, for a given wavelength) in addition to the mentioned variation with $Z$ (Fig. 21).

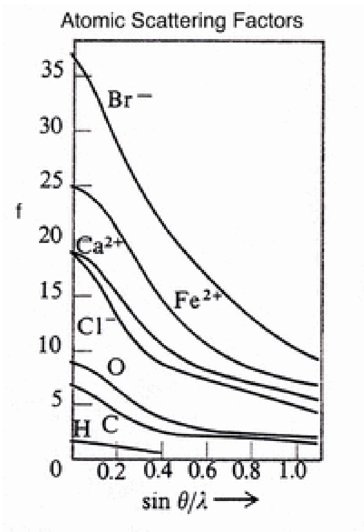


**Figure 21 – Scattering function as a function of the resolution for a series of different atoms and cations. It can be noticed that the scattering power is consistently low at high scattering angle, and that the exact shape of the curve of decay is quite atom dependent.** [74]

All of these effects will influence whether or not the diffraction signal from a sample is strong enough to appear clearly. The way a diffraction pattern presents itself and how much information can be extracted from it will strongly depend on the specific diffraction technique used.

### *2.2.3.1. Single crystal diffraction*

In single crystal X-ray diffraction the sample is a single coherent domain. The amount of diffraction spots appearing and their distribution is not only related to the symmetry of the crystal, but also to its orientation in comparison to the incident beam of radiation. If the structure is already known and the crystal is accurately grown, there can be merit in aligning the crystal in a definite direction to the beam and obtaining a very specific set of diffraction spots; however, if the aim is to determine the crystal structure, the best approach is collecting the largest number of reflections possible and rotating the sample in comparison to the beam.

In order to deal with these experimental requirements, single crystal X-ray diffraction can be collected with a point detector and a four-angle goniometer or with an area detector and a single axis of rotation (Fig. 22). Given their sensitivity and response time, in modern days almost every single crystal diffraction experiment is done with CCD or CMOS area detectors.

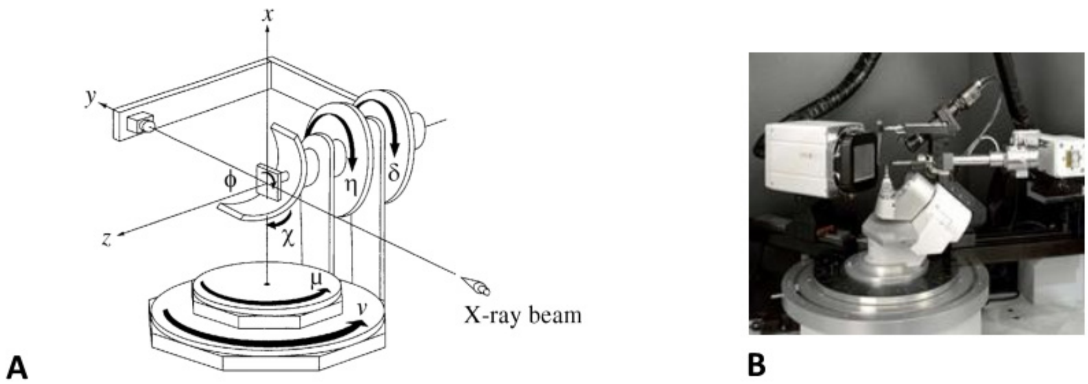


**Figure 22 – A) Schematic of a four-angle goniometer diffractometer, the four angles 2θ, ϕ, χ and Ω define the geometry of the crystal in relationship with the incident beam and the diffracted beam. B) Schematic of a single crystal diffractometer with area detector. This setting has a single axis of rotation to turn the axis on itself.**

A complete diffraction signal from a single crystal appears as a tridimensional sphere of spots, reflecting the *hkl* positions on the reciprocal lattice in a way that is dictated by the structure factor. From a theoretical point of view, the full data set should constitute a reciprocal space picture of the electron density distribution in the crystal; structure factor $F_{hkl}$ and electron density $\rho_{xyz}$ can be related through Fourier transform:

$$\rho_{xyz} = \frac{1}{V} \sum_{hkl=-\infty}^{+\infty} |F_{hkl}| \cdot \exp[-2\pi i(hx + ky + lz - \varphi_{hkl})]$$

Where the summation runs for any *hkl* point of the reciprocal lattice in diffraction conditions, and $\varphi_{hkl}$ is the phase of the diffracted waves that constitute the structure factor. In a real case, however, not only the extent of the collected reflections is finite, but the intensity of the collected diffracted beam is only proportional to the structure factor squared:

$$I_{hkl} = A \cdot p \cdot L \cdot k \cdot |F_{hkl}|^2$$

Where A is the absorption factor, p is the correction for the polarisation of the incident beam ($p = (1 + \cos^2 2\theta)/2$), *L* the Lorentz factor that corrects for aberration given by the moving instrument and k is a scaling for the various measured structure factors. The squaring is equivalent to a loss of the phase information, in what is known as "the phase problem" of X-ray crystallography. As a result, the solution of a completely unknown crystal requires modelling and minimisation procedures, and single crystal X-ray diffraction cannot be considered a perfect reproduction of the lattice.

However, with a proper collection of intensities as a function of angles, this technique is incredibly precise in providing an indication of the atomic positions in the sample, and as such it can be used, for instance, to changes in symmetry as a function of the change in environment, even when involving closely related space groups.[60 75]

#### *2.2.3.2. Powder diffraction*

By contrast, a powder sample is defined as being composed of a significant number of small crystallites aligned randomly in respect to the incident beam. Diffraction from powder is an extremely popular method due to the complexity associated with growing crystals and for the flexibility it allows in the investigation of the crystal structures. This technique is used more routinely than single crystal diffraction and it can be performed in reflection geometry, with the sample levelled on a flat plate, or transmission geometry, with the sample on a tape or packed inside a capillary.

Single *hkl* reflections are not visible in powder diffraction, and the collected signal from randomly oriented crystallites is the angular average of a single crystal diffraction pattern (Fig. 23).

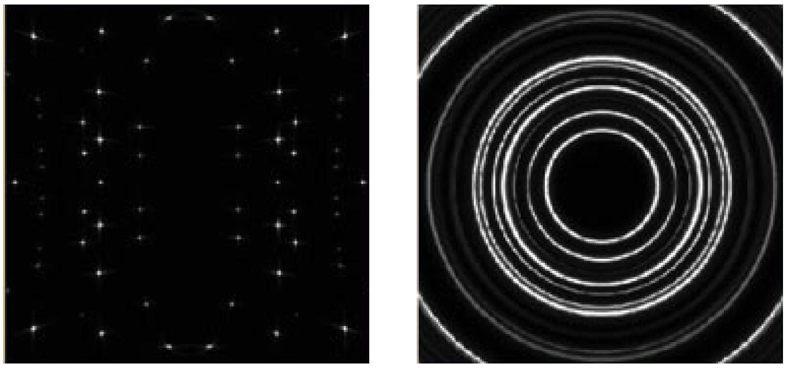

**Figure 23 – Diffraction from single crystal (left) and powder (right) of the same compound, collected from an area detector. It can be inferred how the powder diffraction pattern can be obtained with a random rotation in every possible direction of the single crystal diffraction, keeping the same origin.** [76]

A 2D detector will show concentric rings arising from the sample at different angles, with a spacing that can be related to the interplanar *d*-spacing through the Bragg's Law; an angular detector will show a series of intensities as a function of angle, which can also be obtained by integrating diffraction rings. As a result of the loss of single *hkl* reflection intensities, it can be challenging to derive the space group of a completely unknown lattice: the amount of reflections present and their positions can often guide towards a symmetry class, but some subtle systematic absences can be lost. On the other hand, a powder diffractogram offers a very accurate picture of the average structure, since it arises from a big number of crystallites of the same material, and it gains a very precise metric of the unit cell. [77]

The quality of a diffraction pattern and the complexity of the experimental settings heavily depend on the quality of the incident radiation and the geometry of the instrument. As such, it is worth discussing the sources of radiation employed in this thesis.

### *2.2.3.3. X-ray sources*

Diffraction in laboratories is routinely performed with X-ray tubes as a source of radiation. X-rays are generated in an evacuated glass tube, containing a water-cooled metal target; upon getting hit by high-voltage electrons, the target can generate a spectrum of X-rays. Depending on the metal composing the target, however, this spectrum will have one or more peaks associated with the K-shell emissions of the element. The addition of filters with the right absorption edge and monochromating crystals can reduce the amount of radiation to a single wavelength, at the cost of its intensity.

Every product of solid-state synthesis in this thesis was checked with the Bruker D2 Phaser diffractometer, in order to assure the formation of the desired structure. In the D2 Phaser, the target is made of copper, yielding a $K\alpha_1$ = 1.5405 Å and $K\alpha_2$ = 1.5431 Å; most of the $K\beta$ = 1.3923 Å is filtered out through a Ni foil, but collection times longer than 4 h can make the signal prominent enough for detection. This instrument works in a $\vartheta$-$\vartheta$ Bragg-Brentano geometry and centres a flat plate sample holder within a goniometric circle of modest diameter; with samples as small as 5 mg dispersed on a thin layer with the aid of some volatile solvent, this geometry requires a divergent beam hitting the surface of the holder (glass or silicon for low background). The diffracted beams are detected by a Si Lynxeye detector, placed on the moving arm of the instrument; routine collections were performed between 5 and 140 deg.[78]

Even though this instrument is suitable to obtain preliminary confirmation of the successful and complete reaction, the quality of the data is fairly limited in resolution and experiments can only be performed in ambient conditions. Additionally, since only Cu radiation is available, samples containing iron will incur in strong fluorescence effects that will hinder the quality of the data further, since the Cu Kα falls on the absorption edge of Fe.

The acquisition of data suitable for analysis of subtle structural effects requires a stronger source of radiation and high-performing instruments, for both powder diffraction and single crystal experiments.

The highest performance for challenging experiments and a wide range of equipment is available at synchrotron sources, internationally funded to provide access to the whole scientific community; machine time on these instruments is awarded on the basis of biannual proposal rounds. The work of this thesis relied heavily on the European Synchrotron Radiation Facility (ESRF) in Grenoble, France.

The basic concept behind a synchrotron is that any beam of electrons, while changing direction, emits radiation in tangent to the curvature of their path. The ESRF generates bunches of electrons with an electron gun and first accelerates them to 200 million eV in a Linac. A further increase in energy up to 6 GeV is achieved in a 300 m booster synchrotron. The resulting highly energetic electrons are sent into the storage ring, where they travel in a 844 m circumference circle under high vacuum (Fig. 24).

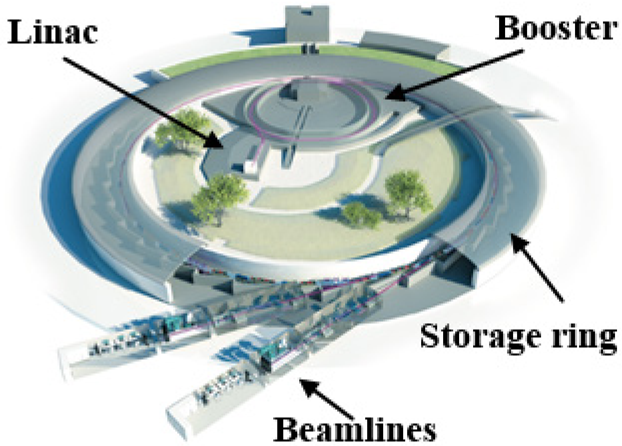


**Figure 24 – Outline of a synchrotron radiation source, with the main parts essential for its performance highlighted.[77]**

In a large-scale facility like ESRF, the circular path is achieved through a series of 32 linear sections, alternated with 32 curvatures. The curving of the path is achieved with Bending Magnets: passing through them, the electrons change the direction of their path in reaction to the strong magnetic field, and emit a broad radiation from microwave to hard X-rays in tangent to the plane of the orbit.
The linear sections employ focusing magnets, to keep electrons as close as possible to an ideal flat orbit, and an Undulator. The Undulator consists of a series of small magnets that make the electron beam wiggle in its path, producing radiation at each twist; in contrast with the Bending Magnet, the radiation produced in this section is remarkably bright and intensely focused, with an energy that can be tuned in a specific region of the spectrum by using the distance between the magnets to control the propagation width of the wiggles. Depending on the type of radiation preferred for a specific beamline, the beam can be

directed after a Bending Magnet or after an Undulator; further fine-tuning and focusing ensues to achieve the desired dimension and energy of X-rays. [79]

Two of the Beamlines used in this work were ID11 and ID22.
The first experimental hutch (EH1) of ID11 was used both for single crystal and for powder diffraction experiments. This hutch is equipped with a Huber diffractometer and has a large working area ideal for complex sample environments. The stage can withstand heavy loads and and moves in *x, y, z* and *Ω* directions within 2 µm of uncertainty and 1 arcsec of angular resolution. Hot air blowers and nitrogen steam blowers can be mounted to perform experiments away from ambient temperatures. This hutch is situated 41 m away from the storage ring and is optimized for high-energy experiments with a highly coherent and intensely focused beam; in the course of this work, a beam of 75 keV ($\lambda$ = 0.15815 Å) and 50x50 µm of size has been employed. The dimension of the beam matches the pixel size of the FReLoN camera detector, which is a phosphor fluorescence CCD with fast readout times. The capabilities of this instrument make it ideal for small single crystals and fast *in situ* studies; moreover, it is a highly-customizable setup and the addition of detectors and change in sample geometry can always be discussed and arranged with the scientist in charge. [80]
ID22 is optimised for high-resolution powder diffraction and has been used for collection of powder rings at 65 keV of energy. The sample stage is stable within 1 arcsec and is optimized for diffraction from capillary. In the experiment performed, the diffracted beam is detected by a flat panel Perkin Elmer XRD 1611CP3 detector, with CsI scintillator arranged in a 41 x 41 $cm^2$ plate and aligned with the sample stage to collect the highest possible 2$\theta$ range (equal to a high momentum transfer *Q*). This instrument is one of the few X-ray beamline that can perform experiments at liquid helium temperature through a custom-built helium cryostat with a Be window sized appropriately for the 2D detector. [81]
Technical specifications on the various experiments performed will be given in the relevant sections.

## 2.2.4 Neutron diffraction

### *2.2.4.1. Nuclear and magnetic neutron diffraction*

Whereas X-rays scatter via interaction with the electron density in the crystalline lattice, a neutron is a particle and interacts directly with the atomic nuclei. Following the de Broglie relationship ($\lambda = \frac{h}{mv}$), a neutron with an appropriate velocity will have a wavelength < 3 Å, which makes it suitable for investigation of long-range ordered crystals.

Even though the rules of diffraction remain fundamentally the same in an elastic scattering experiment, two key factors need to be considered: the interactions of neutron-nuclei does not scale with just the dimension of the atom and neutrons inherently possess a magnetic moment.[82]

Neutrons are weakly interacting with matter and most of them will pass unscattered through the solid, whose dimensions need to be bigger in comparison to X-rays; collection times of the diffraction signal are also at least an order of magnitude longer. As a result, only a fraction of the incoming neutrons will be detected after diffraction; the number of neutrons with wavevector *k* scattered elastically by a system in every given direction per second is given by the total scattering cross-section $\sigma_{tot}$, which can be corrected for a given direction (i.e. the one of the detector) as a differential scattering cross section $\frac{d\sigma}{d\Omega}$ in a given solid angle $\frac{d\Omega}{\Phi d\Omega}$ (Fig. 25).

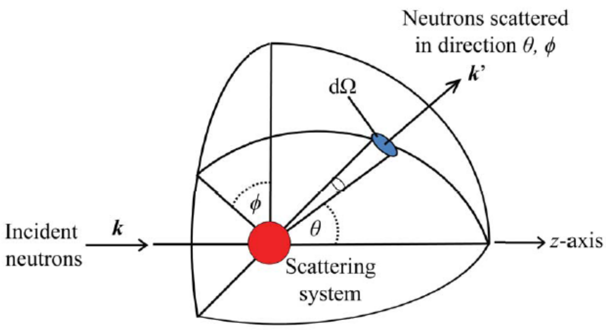


**Figure 25 – Outline of the scattering process of a wavevector *k*, with the depiction of the solid angle dΩ to clarify the meaning of the differential scattering cross section.**

The fraction of neutrons that actually interact with an atomic nucleus in the lattice get scattered in a spherical symmetrical wave that can be expressed as:

$$\psi = -\frac{b}{r}\exp(ikr)$$

where *k* is the incoming wavevector, *r* is the distance from the nucleus and *b* is the neutron scattering length. The *b* parameter relates to the fact that the impact of a neutron with an atom transiently forms a nucleus-neutron compound, the characteristics of which depend on the isotopic abundance of the atom and the possible pairing of spins. When the potential of a neutron approaching a nucleus is repulsive, *b* has positive value, and *vice versa*. The scattering length influences the total scattering cross-section following $\sigma_{tot} = 4\pi b^2$; it can be divided further in coherent scattering cross-section, $\sigma_{coh} = 4\pi \bar{b}^2$, arising from the interference between the scattered wavefunction, and incoherent scattering cross-section, $\sigma_{inc} = 4\pi\left(\overline{b^2} - \bar{b}^2\right)$, arising from spin and isotope disorder that make *b* deviate from an average value. [83]

In a neutron-scattering experiment, the *b* parameter is equivalent to the scattering function *f* in X-rays; as such, $\sigma_{coh}$ and $\sigma_{inc}$ can be used to give an estimation of the contrast obtainable from different atoms. The strength of the coherent scattering cross-section does not have a linear dependency with the dimension of the nuclei: hydrogen, almost invisible to X-rays, is an incredibly strong scatterer of neutrons and two elements that are relatively close on the periodic table (i.e. Fe, Z = 26 $b_{coh}$ = 9.45 fm, and Co, Z = 27 $b_{coh}$ = 2.49 fm) can have a very different cross-section in neutrons even though they are similar in X-rays (Fig. 26). Neutrons can be a powerful tool to study compositional disorder in a material, because they provide a unique contrast between atoms that would look virtually equivalent from the point of view of X-rays. Additionally, the scattering length is constant as a function of the angle, so the intensity of the diffraction does not decay at high angles as it would with X-rays.

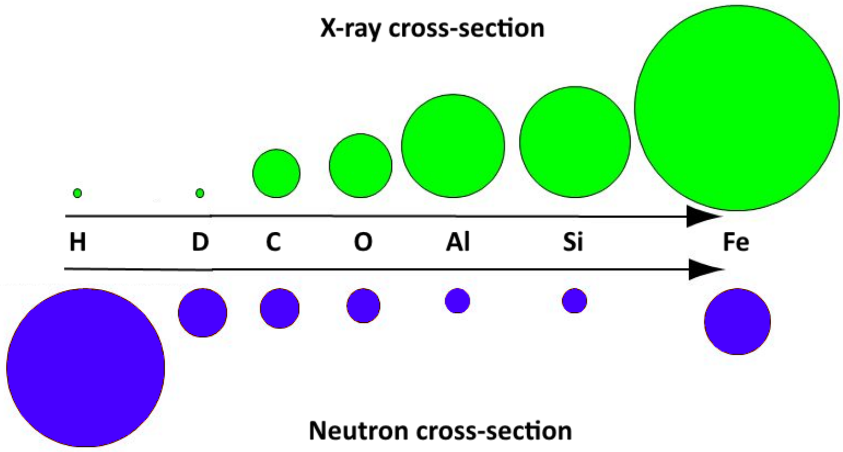


**Figure 26 – Graphic view of the total scattering cross-section for some elements, comparison of neutrons and X-rays. It is immediately evident that while the X-ray scattering power rises as a function of the Z number, neutrons do not have a simple dependency. The contrast provided for two elements might be remarkably different between neutrons and X-rays. It must also be noticed that the scattering of hydrogen is mostly incoherent, with a scattering length opposite to the one of deuterium, so neutrons can be a powerful tool to explore certain atomic disorders.**

A neutron is a zero-charge particle, but since its quark structure is composed of one up and two down quarks it has a net magnetic moment of $-1.042 \cdot 10^{-3}$ $\mu_B$ and ½ spin. As a result, neutrons are sensitive to long range magnetic ordering in the sample, because the presence of aligned spins interferes with the scattering process.

It has to be noted that a neutron is only sensitive to the component of the magnetization that is perpendicular to the scattering vector and that the intensity of the magnetic scattering signal is dependent on the intensity of this magnetisation (i.e. the amount of $\mu_B$ provided by the spins of the atom in the material). Moreover, this type of scattering is dependent on the density of the unpaired electrons in the valence shell, since they are the one susceptible to magnetic order. Consequently, the magnetic form factor has an angular dependency that decays even faster than the X-ray form factor. The net result is that the magnetic scattering signal cannot reflect the full nature of the magnetic order in a sample, it could be fairly faint for atoms with a weak effective magnetic moment, and it is only detectable at low diffraction angles.

The occurrence of magnetic scattering will be treated experimentally and the approach to data treatment and magnetic structure determination will be described in Section 2.2.5. More details on magnetism in the solid state will be provided in section 2.3. [84]

#### *2.2.4.2. Neutron sources*

Neutrons for scientific experiments are routinely produced through either spallation emission or fission. Spallation requires the creation of batches of protons, accelerated at high energy before hitting a tungsten target; neutrons are ejected following the pulses, with different velocities (i.e. wavelengths). Fission uses the splitting of heavy, unstable atoms to produce a steady flow of neutrons in isotropic directions that can be separated to select specific velocities. Similarly to synchrotron, spallation and fission sources are run as internationally founded facilities with access regulated on a proposal basis. Due to the safety issues related to having an active nuclear reactor in place, most of the neutron facilities use spallation methods and it is foreseen that in the future they will be the only sources for science.[85] All the neutron work in this thesis was performed at the scientific reactor of the Institute Laue-Langevin (ILL) in Grenoble, France.

The ILL has a reactor powered with enriched $^{235}U$ bars, which produce a high-flux of neutrons of various energies in every direction around the fuel element. In the core of the reactor temperatures are high (6000 K), so all the neutrons travel at high velocities (short-wavelength); the most efficient way to select different energy is using moderators to slow down the neutrons. For diffraction purposes, the most interesting type of neutrons are thermal neutrons, with temperatures between 6 and 1000 K and a corresponding wavelength between 1 and 0.08 nm, centred at $\lambda$ = 0.147 nm at T = 293 K. These neutrons can be produced by cooling down fission neutrons, first with a graphite moderator (1000 K) and then with a deuterated water moderator. The flux of neutrons that exits the cooling pool can be focused further into a specific wavelength with a germanium monochromator. Since it works with a constant wavelength, the ILL is the perfect neutron equivalent of the usual instruments in X-ray diffraction. [86]

The instruments employed in this thesis are D20 and D2B, part of the same beam guide for thermal neutrons at ILL. The beamline is famous for its high-flux and the possibility of high-resolution.

D2B is a high-resolution powder diffractometer optimized for medium sample volumes. The germanium monochromator that selects a single wavelength from the thermal neutron beam remains highly coherent up to 2θ = 135° and compensates the loss of flux intensities with a relatively high mosaicity. The diffracted beam is collected by 128 detector banks that can rotate around the sample in the 5-165° range; the total signal is computed as an average from the collection of different detector sections. This instrument has been used with a standard “orange” helium cryostat (1.5 < T < 320 K) and is outstanding for the detection of subtle phase transitions from powder diffraction. [87]

D20 feeds from the same thermal neutron guide but is optimized for high-flux experiments that allow for the collection of intense diffraction patterns even for very limited sample sizes (100 mg) in a fast and reproducible fashion. The incoming beam is monochromated by a germanium crystal but the take-off angle can be varied to maximize the intensity of the pattern in regions of interests (usually below 42° 2θ, or below 90° 2θ for structures with magnetic order). The diffracted beam is detected by a bank of position-sensitive detectors disposed in a half-circle of 1.5 m and covering a 154° range (Fig. 27). [88]

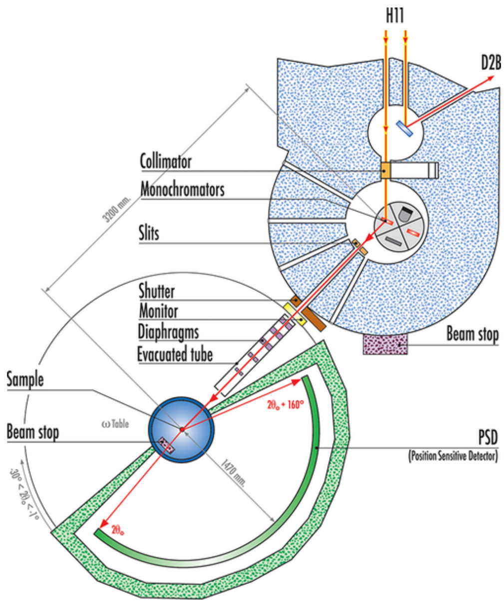


**Figure 27 – Schematic outline of the D20 beamline at ILL. The way the same neutron guide feeds both D20 and D2B is outlined, a detailed list of components is indicated for the D20 instrument only.[86]**

Technical details for the specific experiments performed on both instruments will be provided in the relevant sections.

## 2.2.5 Overview of data treatment

### *2.2.5.1. Single crystal data processing*

As discussed in Section 2.2.2, single crystal diffraction is the most powerful structural analysis technique available, due to the extent of information that can be extracted from the signal.

The prerequisite for a successful analysis is collection of data with adequate resolution and coverage of the diffraction sphere as wide as possible, in order to maximise the amount of reflections acquired as a function of angle. Provided that these standards are met, the analysis will need to convert a sequence of diffraction images into a list of indexed *hkl* reflections with associated intensities in order to gain a complete structural model for the crystal.

If the scattered vectors were to be detected with both their amplitude and phase, structure factor and electron density would be the perfect Fourier Transform equivalent of each other. However, the intensity of diffraction spots is only proportional to the square of the structure factor ($I_{hkl} \propto F_{hkl}^2$); in this form, the phase information is missing in the diffraction pattern and the two pictures lack of reversibility. This phase problem still poses a significant challenge for the solution of completely unknown structures: the intensity of specific reflections is more important than their position to identify the space group and unit cell composition.[89]

Structural solution and data analysis processes are remarkably simplified if, as it is the case in this thesis, a starting model for the crystal has already been provided through other techniques; the protocol to go from diffraction images to a refined structure can be divided in six steps:

1. Determination of lattice parameters. A computer program can easily identify diffraction spots and compute the corresponding *d*-spacing of the diffracting crystal. This process is called autoindexing.
2. Define the orientation matrix of the crystal. This matrix takes into account the specific orientation of the reciprocal lattice in respect to the incoming beam by considering positions of the h-indexed lattice vector, rotation in comparison to the

sample holder frame, instrumental parameters of spinning, and orthogonalization matrix. Most of these parameters are extracted with the aid of instrumental calibration data, but the orthogonalization matrix (B) depends on the calculated cell parameters.

$$B = \begin{pmatrix} a^* & b^* \cos \alpha^* & c^* \cos \beta^* \\ 0 & b^* \sin \alpha^* & -c^* \sin \beta^* \cos \alpha^* \\ 0 & 0 & c^* \sin \beta^* \sin \alpha^* \end{pmatrix}$$

3. Refine crystal parameters (cell metric, orientation, mosaicity), instrumental parameters (detector, positions, tilt) and beam parameters (orientation, divergence) with a least-square optimization.
4. Full integration of the images. Given the refined spatial and metric parameters, all detected diffraction spots can be integrated against an estimated background. With an appropriately fine ϕ-range of rotation, the process is performed in 3D as a function of *x*, *y* position and ϕ rocking. This results in a list of *h*, *k*, *l* indexes and associated intensity values.
5. Polarization and Lorentz factor corrections. Collected images are put on a common scale, accounting for variations in diffracting volume, source intensity, and absorption. A scale factor and a temperature factor can be applied to each image and minimized for the whole batch of frames. The success of this process relies on the symmetry interdependence between several frames of the same dataset.
6. Merging data. Once all the corrections have been applied to the final list of reflections, the corrected intensities are extracted through a weighted averaging process. With a large enough dataset, statistics can help identify outliers to discard and other effects in the sample.

In recent years software developments have significantly increased the speed of data processing.[90] This whole procedure can nowadays be performed within programs like CrysalisPro, but the sequential processing of most of single crystal data in this thesis relied on a Bruker software suite, composed of several programs to complete the protocol outlined above:

- SMART32: this program acquires the spatial setting file from the diffractometer. A relevant subset of frames is then provided in order to attempt a first peak search and cell indexing. An initial least-square refinement is performed to refine not only the cell parameters but also the instrument geometry. The main output of this program is a .p4p file that contains approximated cell parameters, corrections to the instrument settings and orientation matrix as defined above.[91]

- SAINT: this program performs the complete integration on the data, by reading all the frames of the dataset together with the .p4p file. Peak detection and integration are then performed by allowing a certain box size and calculating the intensity of peaks in the frame after a background estimation. The combination with the .p4p file creates a correspondence to a list of *hkl* intensities in a raw file. This program can also apply a filter to the edge of the detector, which is usually affected by poor reading and errors, to increase data quality. [63]
- SADABS: this program has the double feature of performing absorption correction to the intensities, within certain threshold parameters and refinement procedures, and to merge raw files from different datasets, all referring to the same crystal. Here, intensities are corrected and converted to derive the appropriate structure factors. The output is the first reflection file, with the list of structure factors associated to proper reflections.[92]
- XPREP: this program performs the final adjustment to the dataset and constructs the file with the refinable structural model. It assigns space group and unit cell content in order to set up an input file for the refinement. The reflection file is corrected further by applying the low and high-resolution cut-off; additionally, merging equivalent reflections increases the quality of the dataset. The input and the reflection files are to be paired and carried out for the structural refinement. [93]

The final step of the process is the incident angle correction, performed on the .hkl file with a purpose-written python script. The script accounts for the fact that the diffracted beam from the crystal could hit the detector at an angle different from 90°: two reflections that should have the same intensities will appear differently if one of them has a non-perpendicular incidence, because the intensity will be spread among a larger detector area. The correction ensures the best quality of data even for high-angle reflections.

The structural model can be refined using least squares programs that will optimize the crystal-data agreement by shifting parameters like atomic positions, thermal factors and unit cell dimension. In this thesis, all the structural models were refined with Shelxl, which requires two paired files as an input: the .ins file contains information about atomic positions, occupancies, thermal factors, cell parameters, composition and scattering constants of the atoms (as generated by XPREP), and can be modified with standard commands to perform during the run; the .hkl file is the list of all reflections according to their Miller's indexes (*hkl*), associated structure factors squared and relative errors ($F^2$, $\sigma(F^2)$). Reflections that should be absent according to the input symmetry of the .ins file are rejected automatically at the start of the program. A weighted least-square refinement is then performed using a full-matrix method; the number of cycles and weighting parameters can be set by the user:

$$wR_2 = \sqrt{\frac{\sum w(F_o^2 - F_c^2)^2}{\sum w(F_o^2)^2}}$$

The program calculates two R-factors, one for the intensity and one for the intensity deviation, using initial input values. However, since a R-index based on structure factors squared is more than double what would be obtained with the structure factors, after the refinement procedure the program outputs an $R_1$ value that estimates the quality of fit with calculated values of *F* within $4\sigma$ of uncertainty.

$$R_{int} = \sum \frac{|F_0^2 - \langle F_0^2 \rangle|}{\sum F_0^2} \qquad R_{sigma} = \sum \frac{|\sigma(F_0^2)|}{\sum F_0^2} \qquad R_1 = \frac{\sum ||F_o| - |F_c||}{\sum |F_o|}$$

In addition, the goodness-of-fit (GoF) is provided at every cycle, considering number of reflections (*n*) and of refined parameters (*p*):

$$GoF = \sqrt{\frac{\sum w(F_o^2 - F_c^2)^2}{(n-p)}}$$

A list file which reports all operations performed and possible errors that might occur during the run is generated. An updated .ins file with a .res extension is also produced and includes a suggested modified weight for further refinements and a standard crystallographic information file (.cif file).

The refinement procedure can be performed again with the updated file, until the weighting stabilises on a value.[94]

Shelxl is particularly powerful in its capability to recognize and treat twinned crystals.

A single crystal diffraction pattern collected on a twinned sample is affected by different issues depending on the twin domains present: a perfectly merohedral twin will overlap its reflections perfectly with the ones of the parent pattern, making it possible to perform the

indexing procedure and the orientation matrix generation; conversely, a non-merohedral twin will produce peaks that do not overlap and appear as additional peaks in the pattern, and if the relative position is extremely divergent the data processing can be seriously hindered.[95] All single crystals data treated in this thesis had either purely merohedral or pseudo-merohedral twins, so by choosing a big enough integration box two twinned reflections will have intensities registered within the same data point; with a good initial data processing, it is possible to refine the twin components afterwards. During the refinement process, the presence of intensities violating the systematic absences of the space group can be used to trace their presence of specific twin domains.
When a reasonable structural solution for the crystal is already present for a proper input, Shelxl provides suggestions about the presence of twins by examining systematic absences, rejected reflections and discrepancies between the apparent metric in comparison to the provided symmetry. The presence of specific twin components that contribute strongly to the pattern can be added to the refinement with the TWIN command, which provides the twin law in the form of a matrix to convert the *hkl* indexes of one domain to another and can be expressed for a number of twin domains, *n*. Shelxl will then provide a fractional value for the domain up to *n-1* (excluding the dominant one that will be assumed to be the main domain). This is possible because the program generally calculates the total structure factor squared in terms like the following:

$$F_c^2 = g^2 \sum_n [k_n F_{c,n}^2]$$

where $g$ is the overall F-relative scale factor, $k_n$ is the fractional contribution of twin domain $n$ and $F_{c,n}$ is the calculated structure factor squared of a twin domain $n$.

The twin refinement can be performed through different formats of Shelxl input files. HKLF4, that uses the general .hkl file with *h, k, l*, $F^2$ , $\sigma(F^2)$ as described above, works well for merohedral and pseudo-merohedral twinning, and it applies the matrix law in the TWIN command $n - 1$ times to create all the domains, two or more. HKLF5, which is a format that needs to be specifically generated to account for possible non-merohedral twins, has an additional column with a number for every group of reflections referring to a specific domain. As such, the .hkl file is directly accounting for the presence of twins and the .ins file only contains the line for the scaling factors.
If the twinning is truly pseudo-merohedral, the results with the HKLF5 procedure will end

up considering the same twins of HKLF4 and the structural refinement will give consistent results between the two formats. [67]

### *2.2.5.2. Rietveld method for powder diffraction analysis*

As previously discussed, a diffraction pattern collected from a powder sample loses the full 3D sphere with individual *hkl* reflections and instead presents cones of diffracted intensities from equivalently *d*-spaced crystal planes. This pattern can be collected either directly in a 2θ vs intensity format or as full rings of diffraction on a 2D detector; the latter will require an extensive calibration of the instrumental parameter and an appropriately spaced integration of intensities.

Diffraction data is always analysed as intensity as a function of diffraction angle, which is inherently limited in solving an unknown structure but can still be a source of important structural information for other crystallography issues. The widespread method of analysis is the Rietveld method of least square refinement, in which the full experimental profile gets compared with a calculated one for the same structure and the difference between the two is minimised:[96]

$$S_y = \sum_i w_i \left(y_{i,obs} - y_{i,calc}\right)^2$$

where $S_y$ is the residual to be minimised, $y_{i,\mathrm{obs}}$ and $y_{i,\mathrm{calc}}$ are the observed and calculated intensities and $w$ is the statistical weight. The procedure is performed for $y_i$ intensities recorded at positions $2\theta_i$.

The observed pattern is treated as a sum of background, modelled separately, and specific Bragg reflections on top of it. Provided that the structural model is known at least to a good degree of approximation in terms of space group and composition, the calculated pattern can be expressed as:

$$y_{i,calc} = s \cdot \sum_{hkl} L_{hkl} \, |F_{hkl}|^2 \, \phi(2\vartheta_i - 2\vartheta_{hkl}) \, P_{hkl} \, A + y_{i,bkg}$$

where $F_{hkl}$ is the structure factor, $\phi(2\vartheta_i - 2\vartheta_{hkl})$ describes the overall effect of instrumental and thermal widening that makes Bragg peaks broaden from an ideal Dirac-function peak, $L_{hkl}$ accounts for the Lorentz factor and various polarization and multiplicity effects, $A$ is the absorption for a given wavelength and atom type in the composition, $P_{hkl}$ is the preferred orientation that can influence intensity and shape of certain peaks in comparison to others because of microstructural effects in the crystallites and $y_{i,bkg}$ is the background for a given *i* step. The scale factor *s* scales the calculated pattern to match with the observed intensity.

The peak width is usually estimated with a mixed Gaussian-Lorentzian function that accounts for the most common peak shapes in diffraction, known as Pseudo-Voigt:

$$pV(x) = \eta L'(x) + (1-\eta)G'(x)$$

In which the overall function is a linear combination of Lorentzian (*L'*) and Gaussian (*G'*) with the same full width at half maximum (FWHM, known as $H^2$). $\eta$ accounts for the weight of the Lorentzian part (between 1 and 0). The peak shape is also angular dependent:

$$H^2 = U\tan^2\vartheta + V\tan\vartheta + W$$

All the parameters contributing to the FWHM (*U, V, W,* $\eta$) are refinable in the least square optimization. Since peak width is also influenced by thermal vibrations, shape parameters correlate strongly with the Debye-Waller factors; if an atom in a given position is considered, the thermal motion will displace its scattering factor *f* following:

$$f_T = f\exp\left(-\frac{B\sin^2\vartheta}{\lambda^2}\right)$$

where *B* is the isotropic thermal displacement ($B = 8\pi^2\langle u^2\rangle$, with $u^2$ as the mean square displacement of the atom from its average position).
Key parameters to modify the structural model are, of course, cell parameters, atomic position and occupancy of a given symmetry site.

Once the least-square routine is completed, it is possible to estimate how well the model is agreeing with experimental data through some standard factors (R-factors: profile, weighted profile, expected weighted profile):

$$R_p = \frac{\sum_{i=1,n}|y_i - y_{c,i}|}{\sum_{i=1,n} y_i} \qquad R_{wp} = \sqrt{\frac{\sum_{i=1,n} w_i|y_i - y_{c,i}|^2}{\sum_{i=1,n} w_i {y_i}^2}} \qquad R_{exp} = \sqrt{\frac{n-p}{\sum_{i=1,n} w_i {y_i}^2}}$$

where *n-p* is the number of degrees of freedom, with *n* being the total number of points in the pattern and *p* being the number of refined parameters. On the basis of the R-factors, an indication of the goodness of the fit (GoF) can be provided by the reduced $\chi^2$: [97]

$$\chi^2 = \left[\frac{R_{wp}}{R_{exp}}\right]^2$$

Rietveld refinements can be performed with programs like the FullProf Suite, which has been extensively used throughout this thesis. FullProf is capable of reading standardized crystal structure files (CIFs) and can handle the refinement of powder X-ray or neutron data, leaving control to the user for the parameters to be refined. [98]

The Rietveld method is routinely employed for crystal structures of powders. However, the same principles of least square refinement can be used to analyse patterns that have both a Bragg crystalline scattering and magnetic scattering.

The sensitivity of neutrons to magnetic order in a crystalline structure can modify a powder pattern significantly in comparison to its paramagnetic phase. With some adjustments, the Rietveld method can be applied to a magnetic diffraction pattern and provide invaluable insights into the so-called magnetic structure, which is a schematic model where magnitude and direction of magnetic moments are extracted alongside the crystal structure information.

Magnetic order is often accompanied by the appearance of additional diffraction peaks alongside the established Bragg peaks of the crystal. These satellites are confined to the low-angle region of the diffraction pattern and usually reflect a lowering of the symmetry in the structure; the modification of the translational symmetry of the lattice can be modelled with a reciprocal lattice vector, called propagation vector (***k***): if a magnetic cell is two times bigger than its paramagnetic equivalent in every direction, the metric can be described with $\boldsymbol{k} = \left(\frac{1}{2}, \frac{1}{2}, \frac{1}{2}\right)$ and resulting satellites for any given *hkl* of the original cell will be indexed as $h+\boldsymbol{k}$, $k+\boldsymbol{k}$, $l+\boldsymbol{k}$. A simplification of this behaviour is shown in Fig. 28.

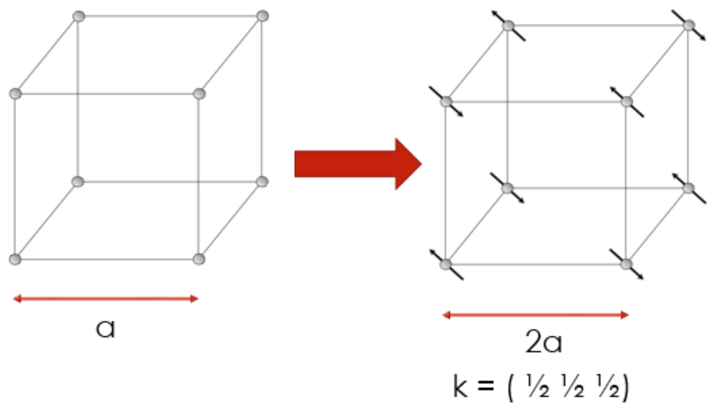


**Figure 28 – Cell metric for a non-magnetic or paramagnetic model unit cell compared with an antiferromagnetically ordered structure. Since neutrons are sensitive to spins, equal atoms with different spin ordering appear differently, and the translational symmetry of the cell can only be properly estimated with a 2a cell, hence the propagation vector indicated.**

The identification of the ***k*** vector operating within a certain structure can be aided, within the FullProf Suite, by the program K-Search: knowing the metric and the space-group of the paramagnetic cell, on the basis of the position and the intensities of the new reflections appearing in the pattern, the compatible ***k*** is outputted. The choice of the right solution is often straightforward, even though symmetry constraints might result in several *k*-vectors being perfectly equivalent (e.g. if the crystal has $a = b \neq c$, $k_x$ and $k_y$ might be interchangeable; if the crystal has an centrosymmetric space group with four-fold symmetry, $(k_x, k_y, k_z) = (-k_x, k_y, k_z) = (k_x, -k_y, k_z) =$ […] and all the permutation will form a "star" of symmetry equivalent vectors).

The magnetic moment of an atom *j* in the cell defined by the vector $\boldsymbol{R}_l$ can be represented by a generic Fourier series regardless of the specific magnetic structure configuration (ferromagnetic, ferrimagnetic, antiferromagnetic, etc):

$$m_{lj} = \sum_k S_{kj} \exp(-2\pi\, ikR_l)$$

The description of the way the magnetic structure changes under the relevant symmetry elements is provided by Irreducible Representations (Irreps). The Irreps for a given ***k*** as applied to a specific space group *G* can be calculated automatically within the FullProf Suite with the program called BasIreps. It has to be noted that the only atoms involved in the calculation will be the magnetic atoms in the cell, so the list of possible Irreps will be outputted for every given symmetry element applicable to every given magnetic atom.

The influence of the symmetry (and thus the basis vector $\Psi$) on the magnetic moment *m* in the *j*th cell as a function of ***k*** follows:

$$m_j = \psi_j \exp -2\pi\, ik \cdot r$$

One of the modelling options in FullProf considers the magnetic moment on a given site as the sum of the contribution of the various basis vectors and uses the Fourier coefficient *C* as refinable parameters:

$$m_i = \sum_{i=1,2,3} C_i \psi_i$$

The basis vectors $\psi$ can have components in multiple directions (e.g. 1 1 0) or a coefficient different from an integer if the ***k*** vector they are generated from is not an integer in itself (e.g. ½ 0 0, or with imaginary numbers like ½ + i√2).[99]

With the provided atomic positions, magnetic cell metric and appropriate Irreps as an input, the magnetic signal can be modelled in FullProf as an additional phase contributing to the pattern. In order to have physically meaningful results it is necessary to add some constraints, on the basis that metric of the cell, thermal parameters, occupancies and the like are determined by the crystal structure. Contrary to a structural diffraction phase, inputting a secondary phase as magnetic will mean that this phase will only add intensity to the pattern proportionally to the magnitude of the *C* coefficients. These coefficients can be related with the maximum amplitude of magnetic moment on a given site, and exact values of the moment for every symmetry related position are calculated with the FullProf Studio program, which can also visualise the magnetic structure.[100]

Magnetic Rietveld refinement has been extensively employed in this work and its application on magnetically complex systems will be the subject of Section 4.

#### *2.2.5.3. Pair distribution function (PDF) analysis*

The Rietveld method applied on powder diffraction patterns is able to extract important information about the average long-range structure based on Bragg peaks; every underlying signal is modelled with some sort of background function. However, the full diffraction signal from a sample could contain more information, encompassing amorphous behaviours and local structural phenomena, in the weaker diffuse signal that is ignored and generalised as background in the Rietveld approach.

The use of Pair Distribution Function (PDF) analysis has been increasingly popular in the last decade as a means to acquire information from the total scattering of materials.
This technique takes advantage of the Fourier relationship between reciprocal and real lattices and requires a conversion of a standard diffraction pattern (intensity of the scattering as a function of the diffraction angle/*d*-spacing) into a radial distribution. If we define the signal acquired from a powder diffraction experiment as the coherent intensity, $I_{coh}$, the total scattering structure function follows:

$$S(Q) = \frac{I_{coh}(Q) - \sum c_i |f_i(Q)|^2}{\sum c_i |f_i(Q)|^2} + 1$$

Where for every scattering atom *i*, *c* is the concentration and *f* is the atomic form factor (replaceable with the *b* scattering length if the experiment is performed with neutrons), all as a function of the momentum transfer $Q = \frac{4\pi \sin\vartheta}{\lambda}$. The PDF signal, *G(r)*, can be obtained as the result of Fourier-transforming the structure function over the desired Q-range:

$$G(r) = \frac{2}{\pi}\int_{Q=0}^{Q_{max}} Q(S(Q) - 1)\sin(Qr)\ dQ = \frac{2}{\pi}\int_{Q=0}^{Q_{max}} F(Q)\sin(Qr)\ dQ$$

This same integral can be expressed in a different, discrete form that only relies on the characteristics of atoms arranged in space:

$$G(r) = \left(\frac{1}{r}\sum_{\nu}\sum_{\mu}\frac{f(0)_\nu\, f(0)_\mu}{\langle f(0)\rangle^2}\ \delta\left(r - r_{\nu\mu}\right)\right) - 4\pi r\rho_0$$

where *f(0)* is the atomic form factor estimated at $Q = 0$ following the Z number of electrons, and $\rho_0$ is the average atomic number density. The parameter $r_{\nu\mu}$ is the distance separating $\nu$th and $\mu$th atom; out of the two summations, the first runs over all the atoms in the sample but the second is cut at $r_{max}$.[101]
A similar calculation can be remarkably less expensive in terms of computation and helps to highlight the nature of a pair distribution function *G(r)*: this quantity is not necessarily related to any experimental data and it represents the probability of finding another atom at a given distance *r* from the atom at the origin of the scattering event (Fig. 29).

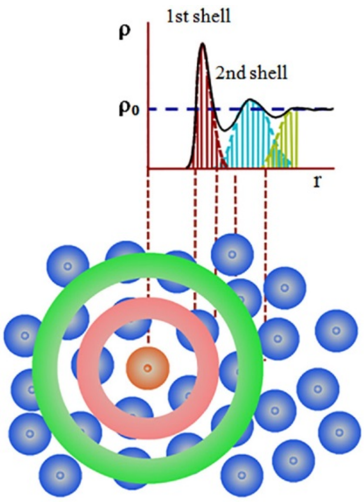


**Figure 29 – Visual depiction of the correspondence between the density of atoms in progressive shells around an "origin" point for the diffraction and the pair distribution function as a function of r.** [102]

The possibility of generating a pair distribution function does not depend on the presence of periodicity in the structure, and for this reason the technique is extensively used for disordered systems like glasses; however, a disordered system will experience destructive interferences quicker than an ordered lattice, so the PDF of a highly crystalline solid can show correlations up to very high *r* distances. From an operative point of view, in a structure like a spinel the first peak of probability of finding an atom will land on the M-O bond, identified as the first coordination shell, followed by M-M distances between two octahedra and M-M distances between tetrahedra, and so on.[71]

The structure function *S(Q)*, reduced structure function *F(Q)* and PDF signal *G(r)* are all readily available through the program Pdfgetx3 (for X-ray data). The program does not perform the two full integrals, which would be very computationally expensive, but instead relies on an algorithm to simplify the problem within the boundaries of experimental data. The starting point is a diffraction pattern in a *I* vs *2ϑ* form that the user will provide together with the wavelength at which the experiment was performed, to convert it into *I* vs *Q*; this intensity is considered as arising from coherent and incoherent phenomena:

$$I(Q) = a(Q)\, I_{coh}(Q) + b(Q)$$

where $I_{coh}(Q)$ is coherent scattering and a(*Q*) and b(*Q*) are additive incoherent contributions arising from inelastic phenomena and background scattering. The background is usually considered as most prominent, so to have data suitable for PDF the user will have to collect very accurate data for the empty sample holder in the same conditions as the final collection and input it alongside the diffraction pattern in the program. The $I_{coh}(Q)$ will be calculated after correcting for the background, appropriately scaled, and transformed in the structure function S($Q$) following the equation expressed above; to properly know atomic scattering factors $f(Q)$, the user needs to input the stoichiometric composition of the sample. To make the fast Fourier transform that follows computationally feasible, input data are resampled in an equidistant grid between the $Q_{min}$ and $Q_{max}$ that the user chooses as relevant for the data. In order to avoid affecting the behaviour of S($Q$), that should go between 0 and 1 for $Q \rightarrow \infty$, intensities are rescaled with a least-square optimisation. The algorithm then assumes that the reduced structure function F($Q$) deviates from the correct value through a slow change that can be estimated with an additive factor:

$$F_m(Q) = F(Q) + \beta_s(Q)$$

The Q-increasing background represented by $\beta_s(Q)$ is modelled with an *n*th-degree polynomial $P_n$ and then subtracted to $F_m(Q)$ to obtain the correct reduced structure function:

$$F_c(Q) = F_m(Q) - QP_n(Q)$$

In this form, Q$P_n$(Q) is an $(n+1)^{th}$-degree polynomial the value of which is calculated between 0 and a user defined value $Q_{maxinst}$ (usually coinciding with the $Q_{max}$ chosen for the data). The corrected function has the right asymptotic behaviour expected by the structure function but the approximation inserts systematic deviations from the ideal value of F($Q$). These deviations are arising from the polynomial and can be roughly estimated as equidistant ($n$+1) roots between 0 and $Q_{maxinst}$ with a half-period of $\frac{Q_{maxinst}}{n}$. The influence of this additional frequency is corrected within G($r$) with the introduction of an additional signal:

$$r_{poly} = \frac{\pi n}{Q_{maxinst}}$$

This estimation corrects the aberration on the PDF function up to the value of $r_{poly}$, inputted by the user, following the underlying assumption that the contribution will be high at low *r*. A default value of $r_{poly}$ is 0.9 Å but it can be increased, as long as it stays below the length of the shortest bond present in the structure.

An accurate tuning of $Q_{min}$, $Q_{max}$, $Q_{maxinst}$ and $r_{poly}$ is necessary to gain a PDF signal that is not artificially broadened by excessive cutting of the data and does not show too many "truncation wiggles" as a result of the Fourier transforming procedure. Pdfgetx3 has a particularly useful tool for the tuning of the parameters allowing the user to see the effect of the modification of these parameters directly on the plot of *F(Q)* and *G(r)*.[103]

Once the G(*r*) has been correctly generated, the actual modelling of PDF data follows a procedure not dissimilar to Rietveld refinement, by allowing the difference between calculated and experimental PDFs to be minimised with a least-square refinement. The program distributed for this procedure and used in this thesis is PDFgui.
A fit in PDFgui can be set by inserting a phase, which is the starting assumption of the average structure as obtained by other methods, and the dataset to associate with it as generated by Pdfgetx3; once the fit is set up, there are a number of refinable parameters to improve the fit:

- Technical parameters:
  - Scale factor, to scale the experimental data with the calculated PDF
  - Gaussian dampening, $Q_{damp}$, is a type of influence on the peak shape coming from the limited Q-resolution of the detector

$$B(r) = \exp\left(-\frac{(rQ_{damp})^2}{2}\right)$$

  - Experimental peak shape, with several contributions to account for the fact that at low *r* atomic motions are highly correlated. The overall broadening follows:

$$\sigma_{ij} = \sigma'_{ij}\sqrt{1 - \frac{\delta_1}{r_{ij}} - \frac{\delta_2}{r_{ij}^2} - Q_{broad}}$$

    where the uncorrelated width, $\sigma'_{ij}$, is corrected for *r*-depended anisotropy with several parameters. High-Q broadening, $Q_{broad}$, comes more from the diffractometer and is highly correlated with $Q_{damp}$. $\delta_1$ and $\delta_2$ are refinable parameters, but the choice of which of the two is most suitable for refinement is to be made by the user, accounting for the fact that the first is more prominent at high temperature and the second arises at low temperatures.
- Structural parameters:
  - Cell parameters, set as default by the input phase and can be constrained

to follow space group metrics

- Atomic positions, given as all positions in the unit cell, to which symmetry constraints can be added with an additional command and modified to follow specific requirements
- Thermal parameters, both isotropic and anisotropic, given as the root mean square displacement of the atom from its average position *u*.

A least square procedure will then compare observed G(*r*) ($G_{obs}$) and calculated G(*r*) ($G_{calc}$) and try to minimise the difference. The goodness of fit for every refined pattern *i* is then estimated as:

$$R_w = \frac{\sum_i \left[\frac{G_{obs,i} - G_{calc,i}}{dG_i}\right]^2}{\sum_i \left[\frac{G_{obs,i}}{dG_i}\right]^2}$$

It has to be noted that *dG* denotes the error on the G(*r*), but this error is remarkably challenging to calculate not only because of the Fourier transform procedure involved but also because inferring the error associated to the intensity in a pattern integrated from a 2D detector is a as of yet unsolved task: the presence of cross-correlation between pixels makes it so that the statistics cannot be simplified as a Poisson-type, and there is no set way of calculating it in the state-of-the-art processing of X-ray data analysis. As such, the routine approach in PDF modelling is giving equal weight to every *r*-point in the pattern by defaulting to *dG* = 1. [104]

The program is implemented in Python and allows a remarkable flexibility of the constraints that can be put on parameters. The features are particularly useful to analyse complex local distortions with precise geometric directionality, such as orbital molecules in transition metal oxides.
A detailed example of a PDF analysis will be provided in Section 3.4.

# 2.3 Magnetism

## 2.3.1. Fundamentals of magnetism

### *2.3.1.1. Magnetic moment of an atom*

The most fundamental way magnetism can be present in a molecule is connected to the motion of an electron in the confined region of an orbital: while the electron moves around with an orbital angular momentum ***L***, it also develops a magnetic moment ***μ***, directly proportional to ***L***. Since ***L*** is quantised, the magnitude of ***μ*** can also be quantised as

$$|\mu| = \sqrt{l(l+1)}\,\mu_B$$

where *l* is the orbital momentum quantum number (integer), and $\mu_B$ is the standard unit for the magnitude of the magnetic moment (Bohr magneton = 9.274 · $10^{-24}$ $Am^2$).

Additionally, an electron can have an intrinsic magnetic moment associated with its spin. This can be quantised as:

$$|S| = \sqrt{s(s+1)}\,\hbar$$

where *s* is the spin quantum number (= ½) and *ħ* is the Dirac constant (1.0546 · $10^{-34}$ Js/rad). When individual spin and orbital momenta are independent from each other, the moment can be expressed as:

$$\mu = \sqrt{4S(S+1) + L(L+1)}$$

where *S* is the total spin value and *L* is the total angular momentum of the orbitals, and are considered as not coupled.

Since an electron could have both orbital and spin contributions to the overall momentum, the effective magnetic moment for an atom can be expressed (and quantised) as:

$$\mu_{eff} = g_J\sqrt{J(J+1)}\,\mu_B$$

where $g_J$ is the Landè *g*-factor that accounts for the *S*, *L* and *J* degeneracy in energy and the way this degeneracy could be lifted in a magnetic field.

Following this quantum mechanical outline, a measurement of magnitude of a magnetic moment is expected to gain an amplitude that is integer and can be inferred from first principles of the quantum numbers.
While this approach is good for atoms and molecules, magnetism in solids adds additional complications that make results diverge from these expectations. [105]

### *2.3.1.2. Bulk magnetism*

Treating bulk magnetism requires consideration of deviations from the single atom behaviour. Interactions between multiple magnetic sites might be responsible, for instance, for the quenched, not-integer values of magnetic moment in transition metal oxides. Orbital contributions are usually to be considered for solids in which spin-orbit coupling is dominant; this usually occurs in systems with a marked degeneracy and localisation of orbitals, such as *f*-block rare earth metals. The orbital contribution is often quenched in *d*-blocks, because the degeneracy of the orbitals can be removed by the crystal field effect; in these cases, a "spin-only" approximation can be sufficient:

$$\mu_{eff} = \sqrt{n(n+2)}\,\mu_B$$

where *n* is the number of unpaired electrons (*n* = 2*S*, *L* = 0 from the previous formula).
The filling of the narrow *d*-orbital band and its interaction with *s*- and *p*-electrons from the valence band account for not-integer moments. The ideal value of magnetic moments derived from this formula can sometimes be exceeded if the compound shows some "orbital contribution" (implying $L \neq 0$).

The effective magnetic moment and ordering features of a magnetic material can be quantified through physical measurements.
The behaviour of magnetic materials is usually classified in terms of their experimental response to an applied magnetic field *H*. The susceptibility of a material can be described as the magnetization *M* as a function of the applied field:

$$\chi = \frac{M}{H}$$

When electrons in individual ions act independently from each other the compound has a paramagnetic behaviour: spins are randomly oriented and the net magnetization in absence of magnetic field is 0. Applying an external field encourages moments to align

parallel to the direction of *H* and yields a small susceptibility ($\chi_p \approx 10^{-3}$-$10^{-5}$).
The molar susceptibility of a compound at a given temperature can be related to the magnetic moment following the Curie equation:

$$\mu_{eff} = \sqrt{\left(\frac{3kT}{N_A}\right) \cdot \chi_M} = 2.83\sqrt{T \cdot \chi_M}$$

Where *k* is the Boltzmann constant ($k = 1.38065 \cdot 10^{-23}$ J·K$^{-1}$) and $N_A$ is the Avogadro number.
Removing thermal energy slows down the random motion of the spins, thus increasing the susceptibility of materials at lower temperature; this effect is systematised by the Curie-Weiss Law:

$$\chi = \frac{C}{(T - \vartheta)}$$

Where *C* is the material-dependent Curie constant, and $\vartheta$ is the Weiss constant and accounts for the presence of exchange interactions between electrons. Usually, $\vartheta$ can be approximated to the temperature at which the interactions are prominent enough to induce magnetic ordering in the structure. [103]

## 2.3.2. Magnetic ordering

### *2.3.2.1. Exchange interactions*

The exchange is a relevant parameter to consider in cases when the individual magnetic dipoles are not actually independent but influence each other. The energy exchanged in this interaction, simplified as involving only two neighbouring moments *i* and *k*, can be expressed as:

$$\Delta E = -2JS_iS_k$$

Where *J* is the exchange coupling constant. The sign of *J* pinpoints to possible cases of magnetic ordering: if positive, the most stable configuration has spins aligned in the same direction (ferromagnetism, $S_i \uparrow\uparrow S_j$); if negative, the base configuration has spins paired (antiferromagnetism, $S_i \uparrow\downarrow S_j$). Both of these ground states spontaneously arise in materials through a simple lowering of temperature, in response to fundamental physics interactions between atoms in the lattice.

Transition metal oxides require consideration of the fact that the first shell of coordination is composed by oxygen anions, in their nature non-magnetic. As such, magnetic cations can have an indirect second shell interaction that is mediated by the first shell.
The rules for magnetic exchanges in transition metal oxides are systematised through the Goodenough-Kanamori rules. Direct exchange is possible in systems where the magnetic metal centres are close with each other, like in the case of edge-sharing octahedral B sites in the spinel; alternatively, superexchange with mediated interactions will be favoured. A schematic of these two types of interactions is provided in Fig. 30. [106] [107]

The most stable ordering configuration type depends on both the electronic configuration of the metal cation (i.e. filling of the *d*-orbitals) and the M-O-M angle (e.g. the AFM superexchange is at 180°, the FM superexchange is at 90°, depending on the orbital occupation and the $e_g$ or $t_{2g}$ character of the interacting orbitals).

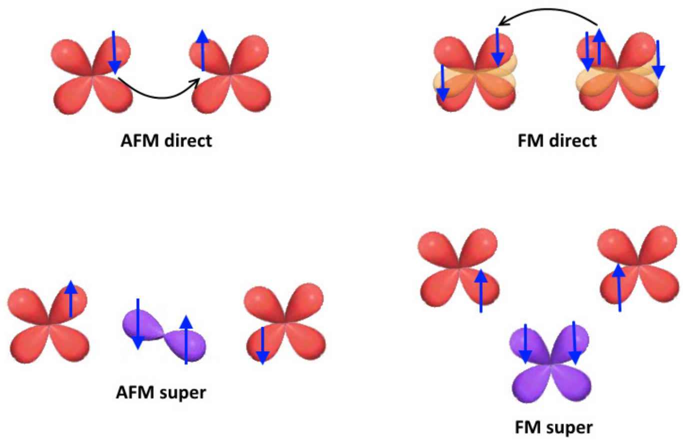


**Figure 30 – Direct and superexchange interactions schematics for antiferromagnetic and ferromagnetic coupling. The *d*-orbital metal cation are shown in pink (or faint yellow when perpendicular to the plane of the page), the oxygen *p* orbitals are in purple. Spins are indicated with blue arrows.**

The Goodenough-Kanamori rules provide an excellent check for systems that are structurally equivalent but present competing interactions. A valid example for spinel structures is provided by a comparison between $ZnCr_2O_4$ and $GeNi_2O_4$: the former has $Cr^{3+}$ in the octahedral position ($t_{2g}^3e_g^0$), the latter has $Ni^{2+}$ in the octahedral position ($t_{2g}^6e_g^2$). In the first case the possibility of AFM direct exchange between edge-sharing $Cr^{3+}O_6$ octahedra is dominant in comparison to 90° FM superexchange; the compound indeed is predominantly antiferromagnetic. [108] In the second case the $t_{2g}$ are filled, the direct exchange is thus not possible, but the 90° Ni-O-Ni interaction puts orthogonal $e_g$ orbitals in FM superexchange through the oxygen anions; as a result, the compound is predominantly ferromagnetic, but weak AFM next-nearest neighbour interactions are reported and influence the ordering. [109] Therefore, both of these compounds make good case studies on how the guidance of the exchange rule is necessary for a thorough analysis of the magnetic ordering, but the presence of conflicting interactions is often reflected in experimental challenges.

#### *2.3.2.2. Ordering types*

The ordering features arising in solids are often complex and varied, and a description of common ordered spin arrangements tends to go beyond the simple ferromagnet/antiferromagnet duality. A comprehensive profile of magnetic systems cannot be obtained through theoretical considerations only, so it is worth describing the various types of ordering and their signatures in magnetisation measurements.

A ferromagnetic material is characterised by a high susceptibility (up to $\chi \approx 10^4$) even in response to small magnetic fields. The alignment of spins can be enhanced by the application of an external field, up to a saturation magnetisation level in which all spins in the material are aligned. Once this stabilisation is obtained, the material can retain a magnetisation higher than the one it would normally have because thermal energy is not enough to disrupt the interactions; similarly, changing direction of the applied field tends to give rise to hysteresis phenomena, because spins offer a certain opposition (coercivity) to switching direction.

An antiferromagnetic material spontaneously leans towards a ground state with a zero net magnetisation, and thus with or without an applied magnetic field the susceptibility tends to approach zero, especially with the lowering of temperature. The hysteresis behaviour in these compounds is virtually not present: spins do not counteract the switching of direction of magnetic field so there is no coercivity broadening and the only possible contribution to a net magnetisation is the effect of canting (where the moments tilt away from a perfect alignment).

With a sufficiently high temperature, all materials reach a paramagnetic phase where magnetic interaction energies are overcome by the tendency towards a random arrangement. The turning point between ordered and disordered phase is called the Curie Temperature ($T_C$) in the case of ferromagnets and Néel temperature ($T_N$) in the case of antiferromagnets. The Curie-Weiss Law can be adapted as:

$$\chi = \frac{C}{(T - \vartheta)}$$

with $|\vartheta| = T_N$ or $T_C$ in ideal cases.

The temperature profiles of susceptibility at zero applied magnetic field are the first indication of what type of order the sample is assuming: ferromagnets get a sharp increase in their susceptibility below ordering (though the actual curve may show complex behaviours); antiferromagnets get a sharp decrease below $T_N$ and approach $\chi = 0$ when $T \rightarrow 0$ (Fig. 31). A Weiss constant can still be extrapolated from the fit of the paramagnetic region of any materials; it represents the value when the paramagnetic $1/\chi$ curve crosses $T = 0$, and it tends to have positive values for ferromagnets and negative values for antiferromagnets.

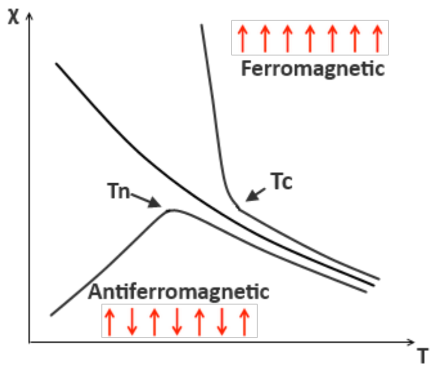


**Figure 31 – Schematic view of the susceptibility behaviour of a ferromagnetic and antiferromagnetic material as a function of temperature, in comparison to the central paramagnetic curve. The ordering transitions are indicated with arrows and a schematic view of the moment arrangement in the ordered phase is provided.**

Ferromagnetism and antiferromagnetism are just two examples of spontaneous magnetic order and sometimes they represent the extreme “ideal” behaviours. In addition to the aforementioned canting, crystals with transition metal or rare-earth cations in the right configuration can experience other orderings, such as:

- Ferrimagnetism, similar to an antiferromagnetic arrangement but, instead of pairing “up” and “down” spins of equal magnitude, there is a disproportion in either magnitude or quantity, leading to a net residual magnetisation. A famous example of this behaviour is $Fe_3O_4$;
- Helimagnetism, where the overall order is reached as a compromise between ferromagnetic and antiferromagnetic order. Spins propagate through the lattice in a spiral or helical order, turning at a certain angle at every translation. This is a very complex behaviour that tends to be present only at temperatures close to 0 K.

Additionally, other effects can be onset as a response to nanostructuring of the material or relate to the presence of even more complex interactions in samples (e.g. superparamagnetism, superdiamagnetism). Moreover, a material to undergo several ordering between the paramagnetic and the ordered ground state, especially if there are more magnetic ions interacting with each other or if the structure is open to complex exchange effects. [110]

The features of a magnetically ordered phase in a crystal are unavoidably tied to crystal symmetry, as directionality and possible interactions between atoms depend on their spatial arrangement. Magnetic order can often be a driving force for a change of symmetry in a crystal structure or it can influence the final low-temperature ground state in cases where several options are theoretically possible.
This consideration is particularly relevant for TMO spinels, because the triangular lattice outlined by B-sites presents four degenerate sites with the possibility of frustration: if this structural unit were to undergo an antiferromagnetic order, there would be no way to fulfil the requirement for all spins to be antiparallel to each other. As a consequence, the system does not have a straightforward unique ground state to land in and needs to remove conflicting interactions to reach a stable long-range order (Fig. 32).

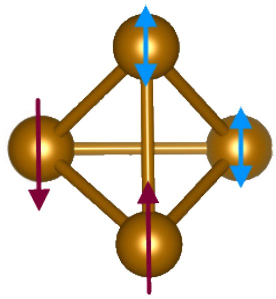

**Figure 32 – Antiferromagnetically ordered spins in a tetrahedron of equivalent cations. The antiparallel arrangement is achieved perfectly only for the spins outlined in red; the sites with the blue spins are shown as a double arrow to highlight how they would be unfulfilling in relation to one of the adjacent sites in whichever orientation they assume.**

Frustration usually leads to materials with a much lower ordering temperature, because it will always be more energetically favourable for spins to remain paramagnetic unless the lack of additional energy leaves exchange interactions as the only prominent ones in the system. At the same time, the Weiss constant derived from a fit of paramagnetic susceptibility of these materials is usually highly negative. It is useful to express the degree of frustration *f* as:

$$f = \frac{|\vartheta|}{T_N}$$

where the Weiss constant $\vartheta$ gives an energy scale for the magnetic interactions and $T_N$ is the Néel temperature of critical ordering of an antiferromagnet. An ideal, unfrustrated system should have $f \approx 1$, whereas an extremely magnetically frustrated system will not be able to reach ordering until $T_N \sim 0$ K, thus making $f \rightarrow \infty$. Intermediate cases with a significant frustration effect usually present $f \geq 10$. [111]

Transition metal oxides exemplify the effects of frustration on magnetic ordering: ferromagnetic or ferrimagnetic TMOs (e.g. $Fe_3O_4$ [112], $CrO_2$ [113], $Y_3Fe_5O_{12}$ [114]) have no issue with frustrated order and present Curie temperatures ($T_C$) well above room temperature. Conversely, transition metal oxides with spinel structure and reported antiferromagnetic ordering (e.g. $ZnV_2O_4$ [115], $LiMn_2O_4$ [116], $MgCr_2O_4$ [117], $Co_2GeO_4$ [118]) order at temperatures $T_N <$ 30 K.

In the majority of cases reported in literature, TMO spinels deal with the frustration associated with the antiferromagnetic ordering by breaking the symmetry of the lattice into a tetragonal crystal structure (most commonly going from *Fd-3m* to *I4₁/amd*, true for all the examples listed above). This symmetry reduction removes the degeneracy of the triangular B-sublattice: the cell elongates in two directions that correspond to one of the diagonal of the cubic faces; this brings the layers of $BO_6$ octahedra at higher interplanar distances and breaks the connectivity of B-B tetrahedra (Fig. 33). Frustration is immediately removed because every site can fulfil antiferromagnetic alignment rules without having to compromise exchange interactions.

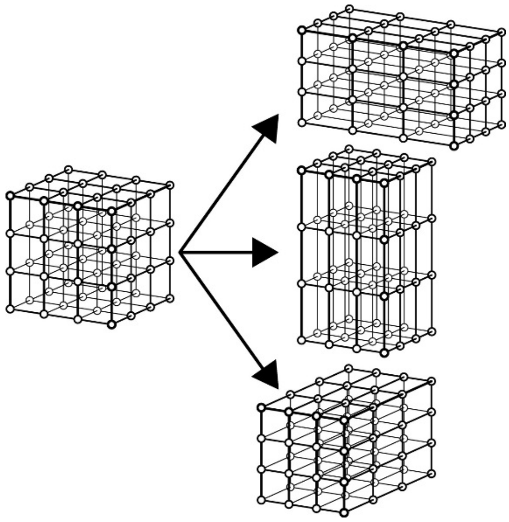

**Figure 33 – Possible tetragonal distortions of a cubic lattice, with elongation along a, b and c respectively shown on the left side.** [119]

When the orbital contribution to the connectivity is less prominent than the exchange interaction between adjacent spins, frustrated systems can experience more complicated and sometimes exotic ordering where the cubic symmetry is maintained and the antiparallel requirements of the spins are fulfilled differently.

A prominent example of frustrated ordering is the so-called “spin ice” arrangement, in which moments at the vertices of a tetrahedra align towards the centre of the unit. Since in a pyrochlore lattice the three crystallographic axes belong to a metrically equivalent unit cell, spins do not have any specific constraint of alignment and can as easily shift in the direction of a diagonal, such as [111]. With such an arrangement, the frustration situation is reversed, and the ferromagnetic state shows unfulfilled spin rules whereas the antiferromagnetic state is a perfectly fulfilled ground state (Fig. 34). The name of this type of arrangement is given in analogy with water ice, in which four water molecules in a tetrahedron will see two oxygens with shorts bonds and two with long bonds with hydrogen atoms.

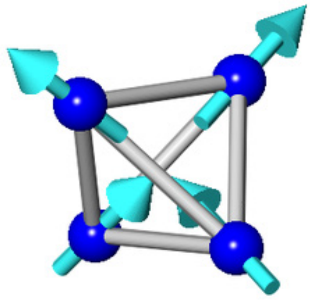

**Figure 34 – Spin-ice arrangement of a generic tetrahedra of equivalent cations. The spins are in the arrangement called "two-in two-out" that characterises this ordering.**

Spin-ice phases are of great interest in solid state magnetism, but they tend to occur in systems where exchange interactions are more prominent than orbital ones. Consequently, these magnetic ground states are commonly reported for rare-earth metal oxides ($Ho_2Ti_2O_7$[120], $Dy_2Ti_2O_7$ [121], etc.) but have not generally been detected in transition metal oxides. The difference is fundamentally related to the nature of *f* and *d* orbitals: *f* electrons are highly localized and their interaction with the second shell of coordination is negligible; *d* electrons can have significant interactions that tend to stabilize phases with cooperative long-range order and several concurrent contributions. [122]

Moreover, frustration can lead to states in which the consequences on the system are beyond long-range ordering: in quantum spin liquids (like resonating valence bond and valence bond crystals) magnetic ions with low spin can show fluctuations even at temperature approaching T = 0 K, because of quantum effects associated with spins [123]; by contrast, spin glasses never reach a proper long magnetic order and instead undergo a freezing at a certain temperature $T_f$, below which spins do not have enough thermal energy to maintain a dynamic paramagnetic state and just lock into a random spin arrangement.[124]

Magnetic ordering in the solid state is an evidently complex issue that is still open to discovery. Theoretical models of these systems are limited by the number of parameters to be considered and by the still-tentative understanding of their interaction. Experimental work is thus necessary in order to explore magnetic ground states.

Each of these phases has characteristic transitions and preferential detection methods and a comprehensive review is beyond the scope of this work. However, detailed identifying features will be provided for long-range ordered magnetism in frustrated systems.

## 2.3.3. Magnetic measurements

### *2.3.3.1. Instrumentation*

Most magnetic measurements performed in this thesis relied on the Quantum Design Magnetic Property Measuring System (MPMS), enabled with a Superconducting QUantum Interference Device (SQUID).

The SQUID is a particularly powerful magnetometry tool that relies on a superconducting ring bisected by two insulating junctions, called Josephson junctions; this ring is constantly swept with a bias current and the measured quantity is the voltage associated with phase change through the junctions every time the magnetic flux of the instrument changes. The changes in flux are quantized (one flux quantum $\Phi_0 = 2.0678 \cdot 10^{-15}$ $Tm^2$) and a proper calibration makes this instrument sensitive to incredibly small changes in magnetisation (threshold of $10^{-14}$ T of variation). The SQUID ring is connected to a sample chamber with superconducting detection coils and is equipped with electromagnets that can routinely operate with fields up in the -7 – 7 T range and temperatures between 2 and 400 K (Fig. 35). Magnetisation measurements on a sample can be performed with direct current (DC) or alternating current (AC). Sweeping the magnetisation as a function of temperature yields a susceptibility measurement, keeping the temperature set and sweeping through the applied magnetic field yields a hysteresis curve.[125]

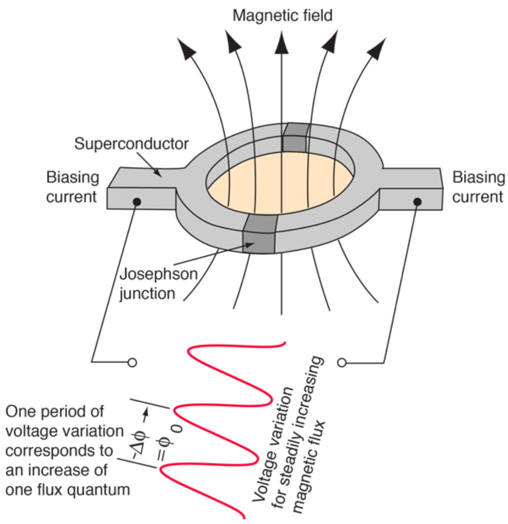


**Figure 35 – SQUID coil and its components. Every change in phase brought about by the magnetic flux will cause a change in measured voltage at the junctions. Schematics of the process are outlined in the image.** [126]

Additionally, the Physical Property Measuring System (PPMS) developed by Quantum Design was also employed. The PPMS is a remarkably flexible instrument that can be customised to perform a variety of physical measurements; magnetic fields can go up to 9 T and the temperature range is between 2 and 400 K with helium cooling, or down to 300 mK with $^3He$.
The PPMS is particularly useful for alternate current (AC) magnetisation measurements. Even though the MPMS SQUID has the capability for AC susceptibility, the best signal-to-noise ratio is actually obtained when measurements are performed with the ACMS feature of the PPMS.[127]

#### *2.3.3.2. Susceptibility measurements*

DC measurements require a sample moving through a set of superconducting coils with a fixed magnetic field applied to it. If the sample is non-magnetic the signal remains fixed to the one induced by the steady field; however, the presence of magnetic moments and ordering phenomena can induce an additional current that will travel to the SQUID ring and be detected with the change of current pattern. The resulting output voltage is proportional to the magnetisation of the sample (*M*) and in the DC setting it is directly proportional to applied field and susceptibility of the material:

$$M = \chi H$$

This type of measurement is usually performed as a function of temperature to detect the presence of ordering transitions in the sample. The most common setting is the so called Zero-Field Cooled (ZFC) in which the static field is kept low enough to not significantly influence the autonomous magnetisation of the sample (0.5 T), while the sample is cooled through the transition; conversely, a Field Cooled (FC) measurement makes the sample undergo the transition while cooling in a significantly higher field, which does not affect the detection capability of the SQUID but can highlight specific spin-ordering behaviours (e.g. an increase in the detected magnetisation for $T < T_C$ in ferromagnets).
Above the ordering temperature, the paramagnetic regime can be analysed with a linear regression of data in the form $\chi^{-1}$ vs T. Following the Curie-Weiss law, the slope of this fit will be the inverse of the Curie constant, the effective paramagnetic moment can be

calculated as $\mu_{eff} = \sqrt{8C}$ and the Weiss constant can be extracted from the intercept of the graph.

DC measurements can also be performed as a function of the applied magnetic field to detect hysteresis behaviours in the sample. When measuring the hysteresis, the temperature is kept constant and the field is swept between a maximum of 7 T and a minimum of – 7 T. Above the ordering temperature of a material, the response of a paramagnet is linear; below the ordering temperature, the behaviour of the loop is related to the type of magnetism occurring in the sample. In particular, a broad opening of the hysteresis is common for ferromagnets.

Another way to perform magnetisation measurements is using the differential susceptibility derived from the detection of alternating current (AC). When performing AC susceptibility measurements, sample position is kept fixed and magnetic field is applied with oscillations in a frequency range between 0.001 and 1000 Hz. The resulting susceptibility is a complex quantity, decoupled from the assumption of linearity, and follows:

$$\chi_{AC} = \left(\frac{\partial M}{\partial H}\right) = \chi' + i\chi''$$

Here the response of the sample is not only related to ordered spins, but may have contributions from dynamic magnetic systems and energy exchange processes. In particular, AC susceptibility measurements are interesting to understand if a sample still presents disordered spins (spin-glass components), which will be highlighted by a change of signal as a function of frequency; by contrast, a sample with ordered spins will show a transition always at the same frequency, making AC and DC susceptibility measurements fundamentally equivalent.
An example of data treatment for frequency dependent AC susceptibility will be detailed in Chapter 4. [128]

# 2.4 Heat Capacity Measurements

The heat capacity of a substance at constant pressure ($C_P$) is defined as the response in terms of internal energy U after a given rise of temperature:

$$C_P = \left(\frac{\partial U}{\partial T}\right)_T$$

Measuring the heat capacity is challenging and time-consuming, because an accurate detection relies on adding and removing heat from the sample while monitoring the temperature change in response.

Experimentally, a platform with a heating circuit and a thermometer is prepared with grease to ensure the thermal contact with the sample (Fig. 36).

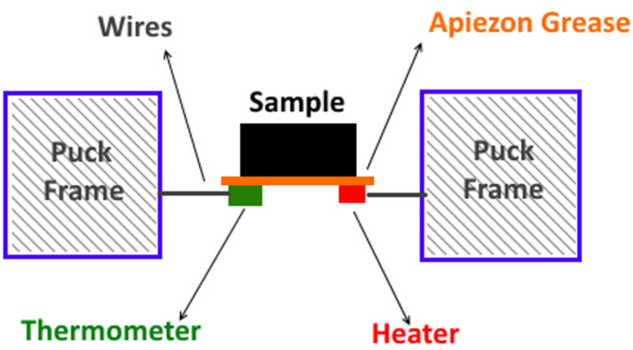


**Figure 36 – Schematic of heat capacity puck for measurements in the PPMS.**

Before measuring the sample, a full data collection is performed on the sample holder, which will act as calibrant and background for the PPMS; the system will execute a routine in which a known amount of power is provided to the puck to increase the heat, for a given time $\tau_1$, and the temperature response is measured for another set time $\tau_2$. Once the calibration measurement is completed, adding the sample onto the platform will change the response time and the software of the PPMS will deconvolute the signal in order to extract the response of the material. Heat capacity can be measured between 2 and 400 K with helium cooling, in applied magnetic fields between 0 and 9 T.

Heat capacity relates temperature as a function of time and is treated by the instrument as follows:

$$C_{tot}\frac{dT}{dt} = -K_w(T - T_b) + P(t)$$

where $C_{tot}$ is the heat capacity, with contributions from sample and platform, $K_w$ is the thermal conductance of the wiring, $T_b$ is the temperature of the sample holder and P(t) is the power applied. The software will isolate the contribution of the sample to the heat capacity as a function of temperature and save it as an output. Knowing the exact mass of the sample is necessary in order to obtain the molar heat capacity for further calculations. In order for heat dissipation to be related only to the sample, the measurement is performed in high vacuum, at constant pressure. A complete experiment usually requires at least two days.[126]

The magnitude of the heat capacity is related to the lattice, electronic, nuclear and magnetic components. Lattice contributions arise from phonons vibrations in the crystal and they are particularly prominent at high temperatures; when the temperature approaches 0 K, phonons tend to freeze and reduce the lattice contribution significantly, increasing the relevance of electronic, nuclear and magnetic components. This is especially interesting when the sample has a transition that can change the weight of one of these components significantly. In this thesis, the heat capacity probe was used to track magnetic contributions upon antiferromagnetic ordering: the onset of an ordering transition is accompanied by a sharp rise of $C_p$ at low-temperature, called λ-point transition.
Isolating the magnetic heat capacity contribution from the signal of the whole sample requires modelling of all other components. Modelling is performed with the assumption that at high temperature, away from the magnetic transition, only the lattice will be contributing; the expected profile of heat capacity is fitted with a Somerfield-Debye model, using base temperature values of $C_P$ and values at $T >> T_N$:

$$C_{model} = \gamma T + \beta T^3 + \delta T^5$$

Magnetic heat capacity can be extracted by subtracting the computed profile to the experimental one. The interesting feature of magnetic heat capacity is that it can help extract the variation of entropy ΔS associated with ordering, as:

$$\Delta S = \int_{T_{min}}^{T_{max}} \frac{C_{magnetic}}{T}$$

The theoretical value of this entropy change should be close to $R\ln(2S+1)$. Strong deviations from this value can be interpreted in terms of additional interactions in the sample significantly lowering the experimental change in entropy.[129]

# 3. THE VERWEY PHASE OF MAGNETITE

## 3.1 Overview of the Verwey transition

### 3.1.1. Structure of the Verwey phase

As introduced in Section 1.2.2, the applicability of magnetite to a variety of scientific fields is fundamentally associated with its electronic and magnetic properties that make it renowned as the original magnetic material. Since 1939, however, it has been known that upon lowering of temperature the behaviour of magnetite dramatically changes: cooling below T ~ 125 K causes a metal to semiconductor transition marked by electrical, magnetic, and heat capacity discontinuities.[24]

E. J. W. Verwey himself, whom the transition is named after, proposed a structural behaviour as a driving force of these physical changes. The conductivity in magnetite is driven by the hopping of the minority spin electron of $Fe^{2+}$ among all the possible octahedral B sites, and at high temperature the oxidation states are indistinguishable from each other, leading to an average $Fe^{3+}{}_T(Fe^{2.5+}{}_2)_OO_4$ inverse spinel structure; however, if the charges were to localise, the differentiation of $Fe^{2+}$ and $Fe^{3+}$ sites would hinder the electron mobility and cause a drop in conductivity compatible with the measured discontinuity. The proposed arrangement would lower the symmetry of the cubic structure to a tetragonal arrangement with alternate layers of $Fe^{2+}$ and $Fe^{3+}$, with each $B_4$ tetrahedron having two $Fe^{2+}$ and two $Fe^{3+}$.[130] However, in following works, P. W. Anderson reported how such arrangement in an undistorted tetrahedron would be highly degenerate and thus unlikely to be a stable low-temperature ground state; an order-disorder mechanism in tetrahedra with two extra electrons (2 $Fe^{2+}$ + 2 $Fe^{3+}$) was proposed as the driving force of the Verwey transition and it was kept as a general electrostatic condition to be fulfilled for all the following models.[131]

In keeping with concurring evidence of the effects of charge ordering in other oxides, models in the following decades discussed the possibility of polaron formation, either with a so called “molecular polaron” – created by expansion of distances between the two $Fe^{2+}$ sites in an Anderson tetrahedron – or as a weak $Fe_2^{5+}$ bond sharing the minority spin electron.[132, 133] However, the Verwey phase showed ferromagnetism in the structure even after the discontinuity point at $T_V$, and these pictures would require a spin singlet ground state; as such, the most recent speculative model accounted for a dimerization in which the charge ordering is only partial ($Fe^{(3-\delta)+}$-$Fe^{(2+\delta)+}$).[134, 135]

Each of these options would be associated with a structural modification and distortion of the spinel high-temperature structure to a lower symmetry ground state. This was corroborated by several experiments over decades of studies dedicated to this transition, but the exact symmetry of the Verwey phase remained a long-running controversy in crystallography.

#### *3.1.1.1. Preliminary structures*

Several structural models of increasingly lower symmetry have been proposed during the years, resulting from the effort of research groups from all over the world.[136] Each attempt at getting an unambiguous answer on the structure below $T_V$ required the use of state-of-the-art synchrotron and neutron instrumentation and the continuous development of these facilities provided the right experimental environment for these studies. The ground-state symmetry was finally pinpointed to be an acentric *Cc* monoclinic supercell, with a metric related to the cubic parent as $\sqrt{2}a_c\ \sqrt{2}a_c\ 2a_c$.
However, these studies were performed with X-ray and neutron powder diffraction, which were reliable for the general cell metric but did not provide accurate atomic positions.[137, 138]
In order to prove charge ordering and define its features in a definite manner, single crystal studies were needed. The extreme loss in symmetry from the high-temperature to low-temperature phase, though, caused severe twinning issues even with high purity single crystals; mechanical detwinning proved unsuccessful and an unconstrained model was not achievable, even with a known metric of the cell derived from the previous powder diffraction studies. As such, powder diffraction remained the preferential method of analysis.

Making use of insights gained from unsuccessful single crystal experiments[139] and of the new high-resolution instrumentation, two complementary studies using neutron and X-ray diffraction attempted to ascertain the presence of charge ordering. In the refinement the metric of the cell was reduced to a monoclinic *Pc* subcell, with an additional orthorhombic constraint on the iron sites; whereas the established *Cc* supercell has 16 distinct octahedral iron positions, a *Pc* subcell only has four. Though the use of Bond Valence Sum (BVS) calculations, the charge of these sites can be inferred from the relative lengths of the Fe-O bond connectivity. The resulting structure has arrays of irons that are on average ordered as $Fe^{3+}$ / $3Fe^{2+}$ or $Fe^{2+}$ / 3 $Fe^{3+}$.[140 141] However, these results are in contrast with the Anderson rule for the $B_4$ tetrahedra; moreover, they are not compatible with following diffraction studies that show previously unconsidered distortions in the monoclinic model.[142] As a result, even though these studies gave preliminary evidence of charge ordering features in the structure, they did not provide a definitive proof of its occurrence.

A better outcome on non-equivalence of the 16 sites in the monoclinic *Cc* supercell was obtained through resonant inelastic X-ray scattering, performed on the K-edge of iron. Using the monoclinic *Pc* subcell with orthorhombic constraints to approximate the displacement of iron sites, studies on single crystals[143 144] and powders[145] showed that shifts in the dispersions of the atomic scattering functions were compatible with charge ordering of at least 46% of the divalent and trivalent irons. Some approximate models of the ordered structure were provided and corroborated with *ab initio* calculations, but the main outcome was to have more precise constraints rather than a full model.

#### ***3.1.1.2. Unconstrained structural solution***

A full structural solution was achieved in 2012, more than 70 years after Verwey first reported the resistivity jump at 125 K.

The study was performed with high-energy synchrotron X-rays, with precise focusing of the beam and high-resolution of the detector in order to distinguish even faint reflection splittings. The twinning problem was overcome with the use of microcrystalline samples of dimensions between 100 and 40 μm: the small size limits the amount of twinning that can form, due to volumetric issues, and an additional detwinning was obtained with pre-alignment of the sample in the cubic phase with a 0.1 T magnet; the structure tends to align on the magnetic direction, retained as unique *c* axis in the monoclinic supercell, and the

number of twins will be reduced to merohedral and pseudo-merohedral only.
With an appropriate optimisation of the integration box size, the least twinned dataset was integrated with 91,433 symmetry-unique Bragg reflections. The derived structure confirms the symmetry of previous powder diffraction studies, [140 141] and does not show signs of further lowering of symmetry even after randomisation: the global minimum remains as reported even after refinement of 2000 starting models generated from the high-temperature structure with random atomic displacements.

The resulting structure can be related to the cubic *Fd-3m* parent through the application of 168 atomic displacements. Phase transitions driven by atomic displacements can often be analysed through the study of the displacement phonon waves allowed by the symmetry of the parent structure: a single phonon mode can displace multiple atoms, thus simplifying the overall description of the transition.[146] However, the analysis performed with the Isodistort program resulted in the same number of modes as the atomic coordinates, with equivalent amplitudes to the displacements, and thus the two descriptions are perfectly equivalent.

The main driving force of the displacement is the Jahn-Teller distortion of the octahedrally coordinated $Fe^{2+}$ sites, which freeze in their compressed octahedral form. $Fe^{3+}$ is not Jahn-Teller active, being a $3d^5$ ion, but has an ionic radius 0.1 Å smaller than the Jahn-Teller active $3d^6$ $Fe^{2+}$ cation; as such, with a careful analysis of the Fe-O bonds in octahedral B sites it is possible to distinguish 8 smaller, averaged $Fe^{3+}O_6$ sites and 8 larger, Jahn-Teller compressed $Fe^{2+}O_6$ octahedra.
Studying the distribution of the distances in the second coordination shell (B-B interactions) highlights the presence of interactions more complex than charge ordering alone: every $Fe^{2+}$ octahedron is in close proximity to two $Fe^{3+}$ octahedra perpendicular to the Jahn-Teller short axis. The orbital interactions that derive from these anomalously short distances (up to 0.16 Å shorter than the 2.967 Å average) allows for $t_{2g}$ orbital interactions and the delocalisation of the minority spin electron from the $Fe^{2+}$. The net result is the formation of seven $Fe^{3+}$-$Fe^{2+}$-$Fe^{3+}$ polarons and one $Fe^{2+}$-$Fe^{2+}$-$Fe^{3+}$ polaron, aligned in the direction of the $t_{2g}$ orbitals of the iron, which can be rationalised as a three-site orbital molecule ("*trimeron*", Fig. 37A). This distortion is cooperative and the ordering is not constrained to a single structural plane; rather, the crossing of trimerons at 120° and 60° of the connecting angle and multiple binding (up to three trimerons connected to the same site) helps reduce

the strain that would be associated with this structural transition (Fig. 37B). Each connection to a trimeron bond reduces the BVS of a given iron site by 0.1, and since the multi-connectivity is quite varied “trivalent” irons have a BVS between 3.0 and 2.6 (2.75 on average) and “divalent” irons have a BVS of 2.5 or smaller (2.47 on average). Following their fundamental description, trimerons should be symmetric around the central $Fe^{2+}$, but since the *Cc* monoclinic superstructure is inherently acentric there is a degree of asymmetry that varies from trimeron to trimeron.

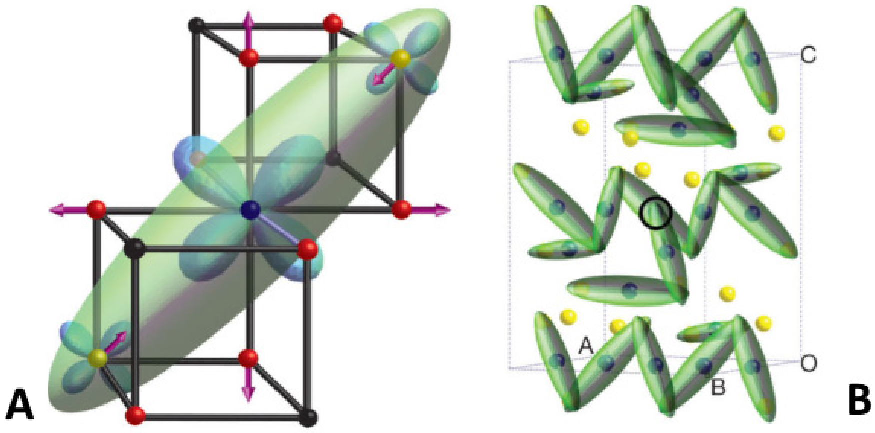


**Figure 37 – a) Single trimeron (green ellipsoid) linking three iron sites in a 3+/2+/3+ linear arrangement. Oxygen atoms are in red and the $t_{2g}$ orbitals sharing electron density are outlined. Divalent irons in blue and trivalent irons in yellow b) Trimeron distribution in a single *Cc* unit cell, with. Some $Fe^{3+}$ are not bonded and most trimerons are connected by a $Fe^{3+}$ at 120° or 60° with each other. Only one trimeron bonds two $Fe^{2+}$. [26]**

This structure is profoundly different from the original charge ordering proposed by Verwey, as there are no precise layers that are solely occupied by $Fe^{3+}$ and $Fe^{2+}$. Similarly, the Anderson condition for each tetrahedron of the pyrochlore lattice to contain two $Fe^{2+}$ is only satisfied for a quarter of the tetrahedra. However, the symmetry of this structure is more complex than the one anticipated in those preliminary considerations, and this model of the Verwey phase is compatible with electronic structure calculations both preceding[147] and following[148] this study.

Overall, the structure of $Fe_3O_4$ below the Verwey transition point was proved to be a remarkable distortion-driven phase transition and an interesting example of orbital molecule formation. The interaction of charge ($Fe^{2+}$/$Fe^{3+}$ states), spin (ferrimagnetism with a flip of the magnetic axis from [111] to [001]) and orbital (Jahn-Teller distortion) degrees of freedom creates a polaron with delocalised electron density that successfully “locks” the minority spin electron, thus explaining the abrupt change in resistivity and magnetisation.[26]

### *3.1.1.3. Base temperature behaviour*

The structural solution by Senn *et al.*[26] was implemented on the basis of single crystal diffraction data at 90 K from a 40 µm microcrystal with ~10% of twinning. Additional diffraction studies were performed on 22 highly stoichiometric microcrystals with low twinning percentages and dimensions in the 10-40 µm range. These studies tested the robustness of this model and whether or not this structure can be considered the real "ground state" of magnetite. Moreover, the transition was modelled through the Landau theory with a first order behaviour and critical temperature $T_V$ = 121.4 K.

Upon further lowering of the temperature, down to T = 20 K, the monoclinic *Cc* model with trimeron arrangement remains the refined minimum for the structure, without any sign of further lowering of symmetry. Analysis of the order parameters of this transition highlights the fundamentally "frozen" quality of the structure below $T_V$.

However, with a more in-depth study of bond distortions and site distributions, following the original work, it is possible to notice an increase to the segregation of $Fe^{2+}$ and $Fe^{3+}$. The second coordination shell, of B-B distances, was analysed to pinpoint the consistency of the trimeron formation: distances that are non-trimeron bonding increase upon further cooling, but the 16 trimeron B-B distances do not vary in arrangement and actually contract to create a tighter orbital molecule.

The electron localisation can thus definitely be defined as the driving force of the Verwey transition, and the monoclinic distorted model can be considered the definite ground state of magnetite below $T_V$, with little variation. [149]

## 3.1.2. Variability with chemical composition

A notorious feature of the Verwey transition since the early days of its study is its tendency to fall in a range of temperatures, instead of being a single, consistently reproducible value. The identification of $Fe_3O_4$ in minerals is usually considered successful if the sample shows a prominent transition at any point between 110 and 130 K; by contrast, any high-purity magnetite synthesised in controlled laboratory conditions has a transition centred around 125 K.

A systematic analysis of this behaviour was provided by J. M. Honig and his group on the basis of physical measurements, well before the full structural solution was achieved; in 1995, he reviewed his work and successfully correlated the variability in transition temperature with deviation of $Fe_3O_4$ from the theoretical stoichiometry. [150] A series of substituted magnetites were synthesised in single crystal form; the ratio of $Fe^{2+}$ and $Fe^{3+}$ in the octahedral sites was varied with off-stoichiometry in the oxygen ($Fe_{3(1-\delta)}O_4$) or with careful doping with cations ($Fe_{3-x}Zn_xO_4$ and $Fe_{3-x}Ti_xO_4$) and the occurrence of a Verwey transition was tested with heat capacity and resistivity measurements. A remarkable correlation was highlighted between the level of non-stoichiometry and the lowering of the transition temperature: extremely pure magnetites tend to have $T_V$ ~ 121 K, whereas a sample with impurity levels $x$ > 3% can go down to $T_V$ ~ 80 K; above 4% of doping, the Verwey transition is completely suppressed and the sample does not show discontinuity signatures even upon cooling below 80 K (Fig. 38).

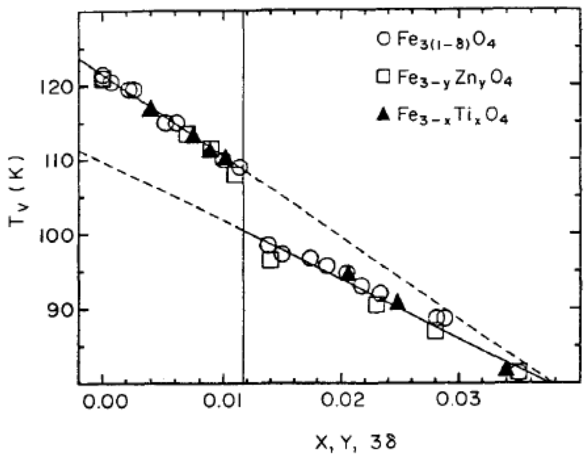


**Figure 38 – Summary plot from Ref[150], tracking the Verwey transition temperature $T_V$ as a function of doping for three different sets of substituted magnetite compounds. The two different interpolation lines, marked by a discontinuity around $x$ = 0.012, refer to the proposed change in order of the transition. Compounds with doping levels above $x$ = 0.035 do not show any discontinuity in the physical properties and are thus interpreted as systems with a suppressed Verwey transition.**

Honig also proposes an inherent change of order type in the transition with an increased level of doping: the profile of the λ-point in the heat capacity curves broadens and fades for doping > 1%, suggesting a change from a first order to second order phase transition. A substituted magnetite in the second order regime is discussed as having electrical and magnetic signatures of the Verwey transition but none of the structural discontinuity, the nature of which was still unknown at the time.

More recent works attempted to recreate the Honig results on Zn, Ti, Al substituted and oxygen deficient magnetites, and correlate the physical findings with a structural reasoning in light of the Senn *et al.* model for the low-temperature structure. However, the diffraction data were collected in powder form and the complexity of the monoclinic superstructure cannot be fully analysed without a single crystal pattern. As such, Kakol *et al.* performed only a preliminary analysis on data collected between 70 and 130 K for the different doping fractions. The symmetry of the structural model was increased to *R-3m* and the data were refined with a pattern matching procedure, where no real structural model is inserted and the least square routine optimises only the lattice parameters and the experimental peak shape.

By tracking the cell parameters is possible to confirm the presence of the structural transition, characterised by a decrease in volume at the temperature corresponding to the physically determined $T_V$. It has to be noted that this effect becomes less pronounced at doping levels > 1 %, as per Honig's deductions.

Some successful analysis on the dependency of the monoclinic β angle to the doping level has been shown. The angle was approximated from the rhombohedral γ angle as $\beta_M = \arccos\frac{-\sqrt{2}\cos\gamma_R}{\sqrt{(1+\cos\gamma_R)}}$ and seems to decrease and approach the ideal value of 90° that would characterise a cubic undistorted structure (Fig. 39).[151]

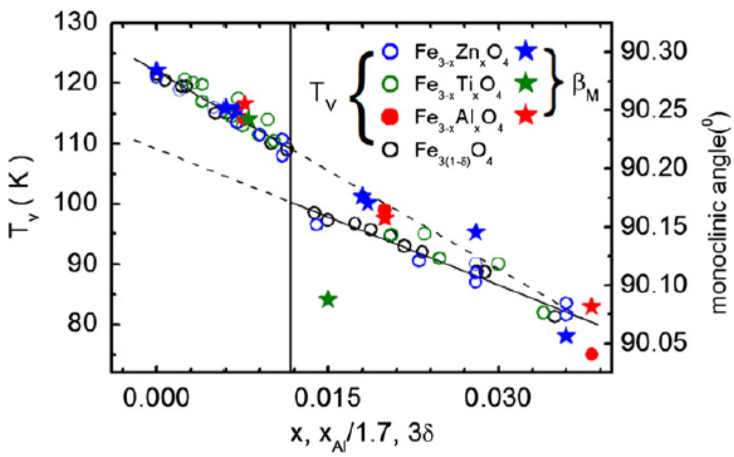


**Figure 39 – Summary plot from Ref[151], tracking the Verwey transition temperature $T_V$ (circles) and the approximated monoclinic angle β (stars) as a function of doping for three different sets of substituted magnetite compounds. Data for the oxygen deficient magnetite ($Fe_{3(1-\delta)}O_4$ were reproduced from Ref[150]). The physical measurements are in good agreement with the previous data, but the dependency is not as well reproduced for the monoclinic angle. A tendency of β to lower towards 90° can be noticed.**

In light of these recent findings, the present work aimed to dedicate more effort to tracking possible modifications of the original structural model, derived from a very high purity sample ($\delta$ < 0.0001), as an effect of doping.
Given the complexity of the self-organised orbital molecule ground state of $Fe_3O_4$, it is of interest to investigate whether the lowering of the transition temperature can be correlated with changes to the distortion features and the electronic exchanges and thus to modifications or disruption of the trimeron arrangement. The proposed complete lack of structural transition and the actual occurrence of a change in order of the transition require a more in-depth structural study.

In order to obtain definitive answers on the structural features of substituted magnetite and investigate the nature of the trimeron formation, an extensive crystallographic study were performed on randomly substituted (natural sample), oxygen deficient ($Fe_{3(1-\delta)}O_4$ with $3\delta$ ~ 0.01) and zinc-doped ($Fe_{3-x}Zn_xO_4$ with $x$ ~ 3%) magnetites single crystals. The results of these analyses will be the focus of the following sections.

# 3.2. *Structural studies on modified magnetite*

## 3.2.1. General methodology

This section will be dedicated to the presentation of the results collected on mineral magnetite (natural), off-stoichiometric magnetite ($Fe_{3(1-\delta)}O_4$ with $3\delta \approx 0.012$) and zinc-doped magnetite ($Fe_{3-x}Zn_xO_4$ with $x \approx 0.03$).
The synthesis and physical characterisation of samples was performed by Dr Elise Pachoud. Synchrotron data collection was supported by Dr Jon Wright, who also wrote some of the Python 2.7 programs for specialist data analysis that will be quoted. The analysis of the single crystal data was supported by Dr James Cumby, who was responsible for the integration of the zinc-doped magnetite dataset.
Methodologies that are shared by all the structural studies will be outlined in this subsection; sample-specific details will be in the following subchapters.

#### *3.2.1.1. Data collection*

Microcrystal X-ray diffraction on selected samples was collected at the ID11 beamline at ESRF, France. The set up consists of a rotating sample stage with variable *x, y, z* and ω and a single crystal sample holder in which the rotation can be controlled with the angle ϕ. The beam was generated on the platinum edge, leading to an energy X-rays of ~75 keV; the precise wavelength for each experiment was refined against precise structural data of the cubic phase from previous reports [140, 141, 26], or was provided by beamline calibrations prior to the experiment. The beam size was optimised at 100 µm, for microcrystals of dimension < 60 µm. The instrument setting was calibrated by Dr Wright before the start of the experiment, through standard silicon pattern measurements; an automatic centring macro for the microcrystal position is available in the purpose-built software of the beamline.
A nitrogen cryostream, optimised for temperatures between 80 and 400 K, was used for every experiment.

The experimental procedure followed the reported methods from Senn *et al.*[26]
In order to reduce the amount of twinning, magnetic pre-alignment was performed with the crystal suspended in unfrozen paratone oil, at room temperature; a small magnet with a field < 0.1 T was then slowly brought close to the sample, leaving the crystal free to rotate and align its magnetic axis with the field. Moving in the cryostream (T = 130 K) freezes the paratone oil and locks the sample into position, ready to proceed with centring and diffraction measurements.
Collections were performed with a high redundancy, in order to collect the highest number of reflections with high resolution and weak superstructure peak intensities at the same time.
Data integration and reduction was performed with the sequence of Bruker Softwares, in the routine summarised in Chapter 2, for both the natural and off-stoichiometric samples. The zinc-doped magnetite data were treated completely within the CrysalisPro suite.

#### *3.2.1.2. Data refinement and twin component analysis*

The refinement of the structural model was performed in Shelxl, with a full least-squares procedure on the cell parameters, atomic positions and anisotropic thermal factors, until convergence.

Every dataset had to account for twin component analysis, as every sample contained twins upon cooling below the Verwey transition.

The transition with symmetry reduction between from *Fd-3m* (space group order 48) to *Cc* (order 2) gives rise to a total of 24 possible twins, equivalent to 12 pairs related by inversion. Specific symmetry elements lost in the transition between cubic and monoclinic space groups can generate twin domains with a different spatial relationship with each other. In this structure, the only purely merohedral twin is the inversion twin; however, since other twins are pseudo-merohedral, it is feasible to integrate their intensity within the same box and obtain the correct metric of the cell.

Computations for twinning in monoclinic magnetite can be reduced by considering that of all the 23 twins (where the $24^{th}$ is the main crystallite, or "parent domain"), the ones generated by an operation that requires a non-unique *c* axis are removed with the magnetic alignment. The remaining ones relate to the parent domain through the following operations:

- Inversion twin:

$$\begin{bmatrix} -1 & 0 & 0 \\ 0 & -1 & 0 \\ 0 & 0 & -1 \end{bmatrix}$$

- Orthorhombic twin (*a/b* swap), arising from the loss of the 2-fold axis along *x*:

$$\begin{bmatrix} 0 & 1 & 0 \\ 1 & 0 & 0 \\ 0 & 0 & -1 \end{bmatrix}$$

- Monoclinic twin (*a/-a* swap), arising from the loss of the 2-fold axis along *z*:

$$\begin{bmatrix} -1 & 0 & 0 \\ 0 & -1 & 0 \\ 0 & 0 & 1 \end{bmatrix}$$

- Tetragonal twin, arising from the loss of the $3_2$ improper rotation axis along *x,y,z*:

$$\begin{bmatrix} 0.5 & 0.5 & -1 \\ -0.5 & -0.5 & 1 \\ 0.5 & -0.5 & 0 \end{bmatrix}$$

These twins relate monoclinic domain in *Cc* symmetry. For simplicity, they will be referred to as “orthorhombic twin”, “monoclinic twin” and “tetragonal twin” as per previous listing. The fractions of these twins can be estimated through the analysis of the reciprocal space slices (for the monoclinic twin component) and the intensity ratio of the reflections (for the orthorhombic twin component). The Python programs for this analysis were originally written by Dr Mark Senn.

In the HKLF4 format, covering all the possible twins requires the consideration of four possible domains, in the command form

$$TWIN \quad 0\,1\,0 \;\; -1\;0\;0 \quad 0\,0\,1 \quad\; 4$$

The input matrix is structured as a matric product that accounts for both the main domain plus the orthorhombic twin (*y,-x, z*) and the two possible monoclinic twins (equivalent in the β angle swap with [-*x,-y, z*] and [-*y,-x, z*]). The tetragonal twins are usually not present, and accounting for them only over-parameterises the refinement.
The HKLF5 format is the best choice to account for possible non-unique *c*-axis twins that might be present despite of the attempt of pre-alignment in the high temperature phase. Files are generated by a purpose-written Python program (developed by Dr Jon Wright) for all the 23 possible twins of magnetite; the quality of the refinement and its improvement with consideration of each twin is estimated through *R1* values. Multiple HKLF5 files with minimum *R1* values can be merged to create a reflection file in which only the relevant contributing domains are present.

#### *3.2.1.3. Bond distortion analysis*

Distortion modes associated with the local coordination of the structure were calculated with a Python program, purpose-written by Dr James Cumby; the program uses the output from the refinement to extract the atomic positions, applies symmetry restraints, and computes bond lengths and associated Q-modes. Q-modes relate to distortions within the octahedral B-sites. The deviation from a perfectly symmetrical octahedron are small enough that every single $FeO_6$ unit can be analysed in terms of the distribution of Fe-O bonds as if it were a regular site.

Considering a total of 7 atoms per octahedron, each one with 3 degrees of freedom, every unit has a raw number of 21 degrees of freedom (d.o.f.). These can be reduced by considering that the octahedron as a whole is not moving (-3 d.o.f.), is invariant by rigid symmetric rotation (-12 d.o.f.) and has one atom always constrained to be in the centre (-3 d.o.f); there are thus only 3 d.o.f. left, and those can be analysed by the Q-modes. Q-modes analyse the relative lengths of the six Fe-O bonds, which are perfectly equal and at 90° angles from each other in a perfect octahedron, but can show some interesting features in an octahedron with no prominent angular divergence.

One of the distortions is known as the $Q_{rad}$ "breathing mode" of the octahedron ($A_{1g}$) and it accounts for the overall distortion of the $FeO_6$ unit:

$$Q_{rad} = \sum_i \frac{d_i - \langle d \rangle}{\sqrt{6}}$$

where the sum is over the six Fe-O distances $d_i$ in each octahedron and <*d*> is the global average bond distance. The breathing mode $Q_{rad}$ is highly sensitive to the charge distribution in the structure, since the breathing of the octahedral bond distances is dependent on the radius of the central cation. This is the mode that helps distinguish larger $Fe^{2+}$ cations from smaller $Fe^{3+}$ cations.

The last two degrees of freedom of a $FeO_6$ unit are correlated by two or three-fold degeneracy. They can be calculated starting from the distortion in a specific *xyz* direction:

$$Q_x = \frac{2(d_{+x} + d_{-x}) - \left(d_{+y} + d_{-y} + d_{+z} + d_{-z}\right)}{2\sqrt{3}}$$

$$Q_y = \frac{2\left(d_{+y} + d_{-y}\right) - (d_{+x} + d_{-x} + d_{+z} + d_{-z})}{2\sqrt{3}}$$

$$Q_z = \frac{2(d_{+z} + d_{-z}) - \left(d_{+x} + d_{-x} + d_{+y} + d_{-y}\right)}{2\sqrt{3}}$$

From these modes we can account for the effect of the Jahn-Teller distortion on the octahedra, which in the monoclinic structure requires a balance between pure tetragonal ($Q_T$ or $Q_{JT}$) and purely orthorhombic ($Q_O$) contributions. Both have $E_g$ symmetry and were extrapolated from the direction-specific distortions following the procedure outlined by Senn *et al.*[26] These modes are related to orbital ordering in the structure; in particular, they are expected to show a relevant discontinuity for the $Fe^{2+}$ sites, as they are the only ones with Jahn-Teller active cations.[152]

A visual outline on the effects of $Q_{rad}$, $Q_O$ and $Q_{JT}$ modes on an octahedral site is provided in Fig. 40.

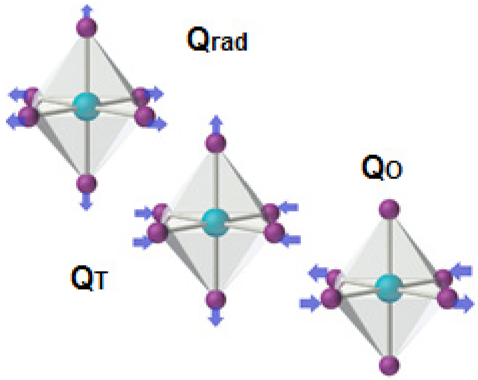


**Figure 40 – Graphical depiction of the radial breathing and distortion modes of an octahedron, as defined in the text. In the *Cc* monoclinic superstructure of magnetite the octahedra are symmetry distorted, with the six Fe-O bonds not all equal to each other and O-Fe-O bond angles diverging from 90°. However, the angular deviation is almost negligible and does not invalidate the analysis and the asymmetry in bond lengths is significant to the Q-mode analysis.**

In order to obtain an additional assignation of the charge distribution estimated from the Q-modes, the Bond Valence Sum (BVS) for every iron site was calculated following:

$$BVS_i = \sum_j \exp\left[\frac{(r_0 - r_{ij})}{0.37}\right]$$

where $r_{0,(Fe3+)} = 1.759$ and $r_{0,(Fe2+)} = 1.734$ and $r_{ij}$ is the interatomic distance for every pair of atoms *j* and *i*. The expression takes into account the whole chemical environment of a material, but only the interatomic interactions between two given atoms are left explicit; $r_0$ parameters summarise the atomic species involved in the bond, coordination number and their configuration. This calculation requires an interpolation procedure over all the atomic pairs in the structure, and was included in the Python program.[153]

The BVS values correlate strongly with $Q_{rad}$ and can be used as an additional identifier for the oxidation state of the iron atoms in the structure.

Errors on the Q-modes are in the order of 6 $10^{-3}$ Å for every structure and are included in the pointers dimensions in plots. Lists in tables show them with rounding at the third decimal accordingly.

## 3.2.2. Natural Magnetite

### *3.2.2.1. Elemental analysis*

The variability of a detected $T_V$ in geological samples highlights how the most readily available source for a chemically substituted magnetite are natural crystals. Rocks formed completely of magnetite are common, especially in South America where their abundance is the highest; moreover, the geological annealing these minerals experience over a long timescale tends to ensure a high crystallinity. [154]

The mineral magnetite used for the experiment was procured from the Brazilian mines of Ouro Perto and was kindly provided by Dr Jon Wright. The bulk mineral was first crushed and then finely ground with a mortar and pestle. From the resulting coarse powder, a 60 x 50 x 25 µm crystallite was selected with the aid of a microscope, to be comparable to the size of Senn *et al.* sample.

The actual composition was analysed through Electron MicroProbe Analysis (EMPA), in which the sample is irradiated with a focused electron beam in order to collect the resulting X-ray emission. Since every element has a very characteristic K-edge energy, emitted X-rays can be detected with an energy dispersive detector and the atomic composition of the sample can be determined from the resulting signals and their statistics. [155]
Results from both the crystallite and the bulk powder are summarized in Table 1. All the compositions have been normalised accounting for the ideal stoichiometric number of Fe as three, with every other detected signal a scaled fraction of this. The procedure was performed by Dr Elise Pachoud.

**Table 1 – Cation compositions from EMPA elemental analysis, normalised to the theoretical value of three cations per formula unit and with standard deviation derived from the signal statistics. Results are displayed for both the bulk mineral and for the microcrystal used for structural studies.**

| ***Element*** | **Bulk composition** | **Crystallite composition** |
|---:|---:|---:|
| *Fe* | 2.9866 | 2.9888 |
| *Al* | 0.0066(4) | 0.0054(4) |
| *Si* | 0.0030(3) | 0.0017(3) |
| *Mg* | 0.0020(2) | 0.0022(2) |
| *Mn* | 0.0018(6) | 0.0019(5) |

The overall level of doping is already fairly low (< 0.5%) and the spurious content is almost completely represented by cations that preferentially occupy a tetrahedral position in the lattice. The only exception is represented by Al, which can be located in both tetrahedral and octahedral sites. [156] As such, the octahedral sites will still be mostly occupied by iron cations, with a modified relative ratio of $Fe^{2+}$ and $Fe^{3+}$ to ensure charge balance. According to Honig's plot (Fig. 38) this crystallite should have a transition temperature around 117 K.

#### *3.2.2.2. Physical characterisation*

The occurrence of the Verwey transition in the natural magnetite sample was confirmed with DC zero-field cooled susceptibility in the MPMS SQUID, for both the bulk powder and single crystal, measured in a 500 Oe field between 140 and 100 K. The measurements were performed by Dr Elise Pachoud.
In both cases, there is a clear discontinuity in the susceptibility at $T_V$ = 119 K, with a broader profile in the case of the bulk powder that is compatible with the presence of multiple crystallites with some degree of variation of their composition (Fig. 41).

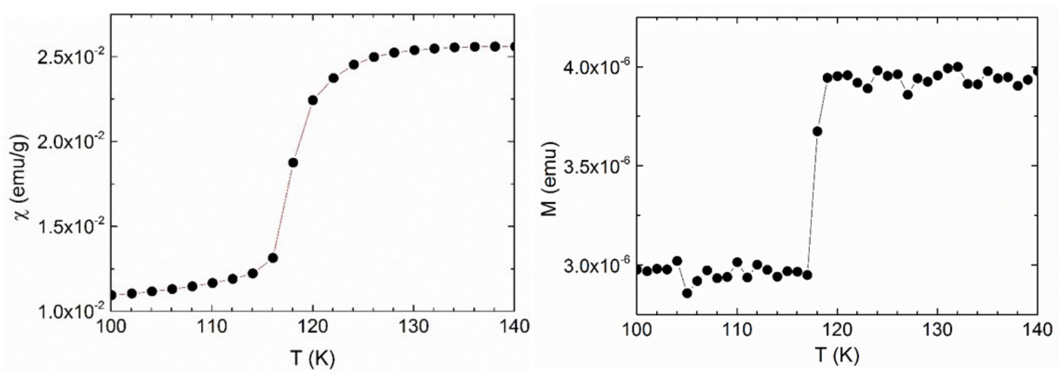


**Figure 41 – Thermal variation of the magnetisation of the bulk (left) and microcrystallite (right) natural magnetite sample, in a 500 Oe field.**

This transition temperature is ~ 6 K lower than the one reported by Senn *et al.* and is compatible with Honig's diagram, according to which the sample should follow a first order transition behaviour and undergo a structural transition upon cooling below $T_V$.

#### *3.2.2.3. Structural characterisation*

Diffraction data on the selected microcrystal were collected at the ID11 beamline at ESRF, France, following the instrumental setting and general procedure outlined in Section 3.2.1., with a 100 µm beam size and refined wavelength $\lambda = 0.15842(1)$ Å. Two full datasets were acquired at T = 90 K and T = 130 K; additionally, short exposure images were recorded while cooling to track the appearance of the Verwey phase through the modification of the diffraction pattern. A section of the diffraction images around $T_V$ is displayed in Fig. 42, with the superstructure reflections clearly appearing below 119 K.

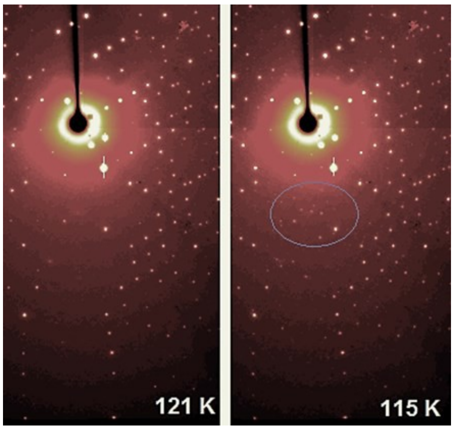


**Figure 42 – Two X-ray diffraction images from the natural magnetite crystal around $T_V$ = 119 K, collected while cooling at 0.5 K/min. The structural transition is marked by the appearance of superstructure reflections such as in the circled region.**

The appearance of superstructure peaks in regions where no Bragg peaks of the original cubic structure are present can be tracked as an additional indication of the Verwey transition. By computing the intensity of the superstructure peak on top of the background in frames collected upon cooling and upon warming, it becomes evident that the structural transition falls at $T_V$ = 120 K and it only shows a hysteresis of 1 K upon warming, in line with the susceptibility data (Fig 43).

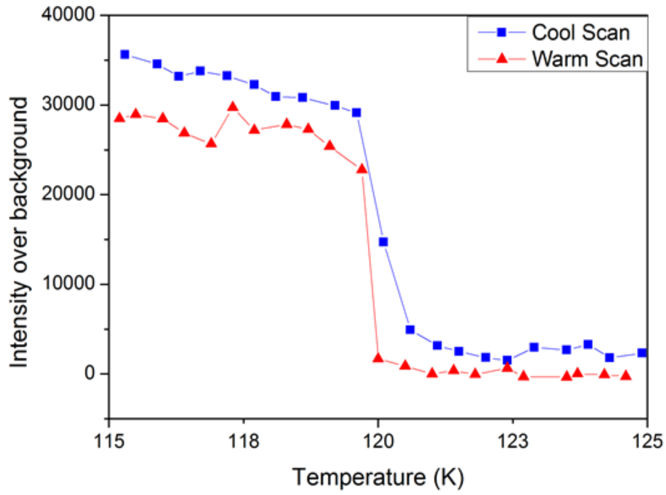


**Figure 43 – Thermal variations of intensity of a superstructure reflection, during cooling and warming scans. A purpose-written program was used to extract the intensity information after focusing of a suitable peak in the images.**

The full 90 K data set initially consisted of the same diffraction sphere with frames collected at different degrees of rotation and exposure time (1 deg/1 s, 0.2 deg/1s); each collection was performed with both high flux and low flux X-ray beams, to gain intensities from weak superstructure peak at high angle and Bragg peaks close to the saturated centre of the detector. These procedures were repeated three times, at different phi settings (ϕ = 45°, -45°, and 0°).

Each of these highly redundant datasets were provided with an orientation matrix and integrated with the SMART/SAINT software. An empirical absorption correction was applied with SADABS; equivalent reflections were merged within a single file before collapsing the three datasets into a single *hkl* reflections file in XPREP. The final dataset consisted of 45904 symmetry unique reflections with a resolution of 0.30 Å.

In an untwinned crystal with Cc symmetry only (0 2*k* 2*l*+1) reflections are expected to be present, but twinning gains intensities that can be indexed as (2*h* 0 2*l*+1). The plot of the intensities of reflections with *k* even and *l* odd is displayed in Fig. 44, and the slope of the interpolated line ${}^{\Delta x}/_{\Delta y}$ suggests the presence of less than 5% of orthorhombic twin domains. On the other hand, the monoclinic twin percentage is not immediately evident from the reciprocal space slices in this sample; if the amount of monoclinic twin domains is low, the splitting of the weak peaks at high-angle, which is the preferred identification method, is often indistinguishable from the background noise.

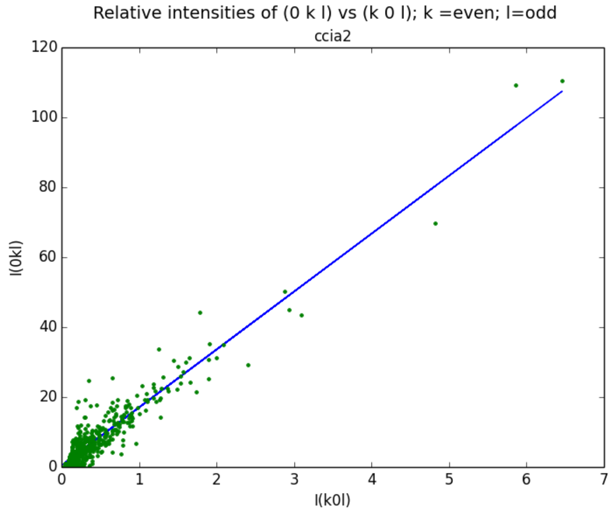


**Figure 44 – Relative intensities of reflections that can be affected by the orthorhombic *a/b* twins. The slope of the interpolated line is equivalent to < 5% of twin components being present.**

On the basis of these integrated intensities, structural refinements were performed in Shelxl taking the Senn *et al.* model as the initial starting coordinates. All atomic coordinates were refined freely in space group *Cc* and associated with anisotropic thermal parameters for all atoms. Both HKLF4 and HKLF5 file formats were used, but there was no difference in the results among the two; as such, the *c* axis can be considered successfully detwinned through magnetic alignment and the results reported are all associated with HKLF4 files. The structure was correctly refined using a *Cc* monoclinic supercell with $a$ = 11.860(2) Å, $b$ = 11.826(2) Å, $c$ = 16.749(3) Å, β = 90.267(9)°, $V_{cell}$=2348.97 Å$^3$. The least-squares procedure was completed with 507 refined parameters, including twin fractions (2.9% of *a/-a*, 2.8% of *a/b* and 2.3% of *a/-b* twins); the fit converged with $R_1$ = 3.69 % for the 82906 reflections with $F_0 > 4\sigma(F_0)$, and $R_1$ = 4.27 % for all 93108 reflections. A table with the refinement results is available in Appendix A1.

### *3.2.2.4. Distortion analysis*

The output of the structural refinement and the associated computed bond distances were used to calculate Q-modes and the related BVS values for the natural magnetite sample, following the procedure outlined in Section 3.2.1. Numerical values are summarised in Table 2, and a graphical depiction of $Q_{rad}$ vs $Q_{JT}/Q_O$ is provided in Figure 45.

Analysing these distributions provides insights on the site assignment in terms of $Fe^{3+}$ and $Fe^{2+}$ among the 16 non-equivalent B-sites in the monoclinic *Cc* structure. $Fe^{3+}$ containing sites are smaller than the average pseudo-octahedron ($Q_{rad} \leq 0$) and their Jahn-Teller active modes have a distribution centred on 0; this corresponds to the 8 sites that occupy the left side of the $Q_{rad}$ vs $Q_{JT}/Q_O$ plots and that can be also identified by a BVS ≥ 2.61. $Fe^{2+}$ containing sites are bigger than the average pseudo-octahedron ($Q_{rad} > 0$) and have a prominent Jahn-Teller distortion, which can be better identified by looking at the $Q_{JT}$ distribution, since it shows evidence of a better correlation in comparison to the $Q_O$; this corresponds to the 8 sites that occupy the right side of the $Q_{rad}$ vs $Q_{JT}/Q_O$ plots and that can be also identified by a BVS ≤ 2.57.

**Table 2 – Distortion modes and Bond Valence Sum values for each iron site in the monoclinic superstructure of the natural magnetite crystal. Rows are colour coded to follow the original trivalent (orange) or divalent (blue) assignation.**

| *Site* | $Q_{rad}$ (Å) | $Q_{JT}$ (Å) | $Q_O$ (Å) | BVS |
|---|---|---|---|---|
| *B1B1* | 0.036 | -0.036 | -0.001 | 2.48 |
| *B31* | -0.002 | -0.018 | -0.019 | 2.61 |
| *B32* | -0.006 | 0.001 | 0.003 | 2.64 |
| *B1A1* | 0.039 | -0.018 | -0.025 | 2.47 |
| *B1A2* | 0.047 | -0.049 | -0.003 | 2.44 |
| *B33* | 0.002 | -0.012 | -0.007 | 2.63 |
| *B41* | 0.054 | -0.050 | -0.006 | 2.43 |
| *B2A1* | -0.045 | -0.009 | -0.008 | 2.77 |
| *B34* | -0.054 | 0.013 | 0.004 | 2.80 |
| *B1B2* | 0.013 | -0.018 | -0.011 | 2.57 |
| *B43* | -0.092 | 0.003 | 0.002 | 2.94 |
| *B2B2* | -0.089 | 0.005 | 0.002 | 2.93 |
| *B44* | 0.058 | -0.043 | -0.011 | 2.41 |
| *B42* | 0.022 | -0.046 | -0.004 | 2.53 |
| *B2B1* | 0.032 | -0.047 | -0.006 | 2.50 |
| *B2A2* | -0.016 | 0.009 | 0.017 | 2.69 |

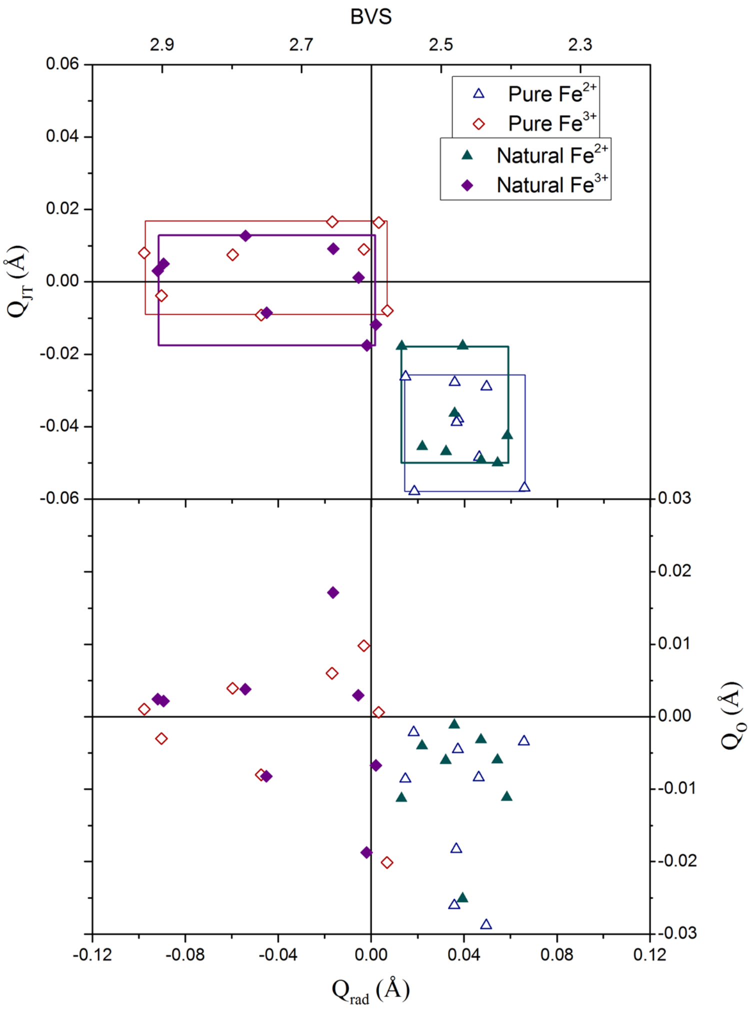


**Figure 45 – Distortion amplitudes of tetragonal Jahn–Teller ($Q_{JT}$) and orthorhombic ($Q_O$) modes plotted against the radial breathing mode for the 16 octahedral B sites in the *Cc* structure. Data for both the natural sample and the pure magnetite are displayed as per the legend. Domains of the 8 $Fe^{2+}$-like and 8 $Fe^{3+}$-like sites are shown as rectangles of matching colours. An approximate BVS scale is shown at the top of the plot.**

This distribution is remarkably consistent between the pure and natural samples, with both site assignments and overall profiles maintained. Overall, the structure seems to react to the chemical defects with a slight degree of overall oxidation; however, the effect of partial doping is noticeably not uniform and some sites appear to be more affected by it than others: the degree of divergence from the pure model is summarised in Table 3.

Table 3 – Deviation from the Senn *et al.* model, for each distortion mode Q and BVS values. The computed value follows Δ = (pure) – (natural). Rows are colour coded to follow the original trivalent (orange) or divalent (blue) assignation. It is evident how not every site is effected in the same way and to the same degree from the sample doping; the BVS of 9 sites out of 16 shows a tendency to oxidation that is compatible with the shift in $T_V$.

| *Site* | $\Delta Q_{rad}$ (Å) | $\Delta Q_{JT}$ (Å) | $\Delta Q_O$ (Å) | ΔBVS |
|---|---|---|---|---|
| *B1B1* | 0.002 | -0.002 | -0.003 | -0.01 |
| *B31* | 0.009 | 0.010 | -0.001 | -0.03 |
| *B32* | 0.009 | 0.015 | -0.002 | -0.03 |
| *B1A1* | -0.004 | -0.010 | -0.001 | 0.01 |
| *B1A2* | -0.001 | 0.001 | -0.005 | -0.00 |
| *B33* | -0.005 | 0.021 | 0.017 | 0.01 |
| *B41* | -0.005 | 0.021 | -0.023 | 0.01 |
| *B2A1* | -0.002 | -0.001 | 0.000 | 0.01 |
| *B34* | -0.006 | -0.005 | 0.000 | 0.01 |
| *B1B2* | 0.002 | -0.008 | 0.003 | -0.01 |
| *B43* | 0.002 | -0.007 | -0.005 | -0.01 |
| *B2B2* | -0.008 | 0.003 | -0.001 | 0.03 |
| *B44* | 0.007 | -0.014 | 0.008 | -0.03 |
| *B42* | -0.003 | -0.012 | 0.002 | 0.01 |
| *B2B1* | 0.005 | 0.008 | -0.012 | -0.02 |
| *B2A2* | 0.000 | 0.008 | -0.011 | -0.02 |

The natural magnetite structure can still be considered charge ordered (from the distribution of the radial breathing) and orbital ordered (from the distribution of the tetragonal distortion), and the two features show coupling. The orthorhombic distortion ($Q_o$) is instead decoupled from orbital or charge ordering and reflects secondary distortions due to the high connectivity of the network of $FeO_6$ octahedra. The values between pure and natural samples can be closely related to each other for every Q-mode (maximum variation Δ ~ 0.02 Å) and BVS values (maximum variation Δ ~ 0.03).

On the basis of site assignment and mode analysis, a last calculation can be performed by computing the nearest neighbours between B sites. The B-B distances are listed in terms of oxidation state of the binding sites ($Fe^{3+}$-$Fe^{3+}$, $Fe^{2+}$-$Fe^{3+}$,$Fe^{2+}$-$Fe^{2+}$), with a special consideration for B sites placed in a perpendicular direction to a Jahn-Teller short axis.
A histogram of the B-B bond lengths, binned in terms of their divergence from the average B-B distance in the structure, is displayed in Fig. 46. From this histogram it can be inferred that the sample presents anomalous clustering in addition to charge and orbital ordering: the distances from $Fe^{2+}$ states to their two B site neighbours (usually $Fe^{3+}$ ions) in the local

orbital ordering plane, identified by the Jahn-Teller axis, are anomalously shortened in comparison to the global average (2.9614(8) Å at 90 K). This is the identifying sign of the formation of the trimeric orbital molecules ("trimerons") of $Fe^{3+}$-$Fe^{2+}$-$Fe^{3+}$ in a linear arrangement.

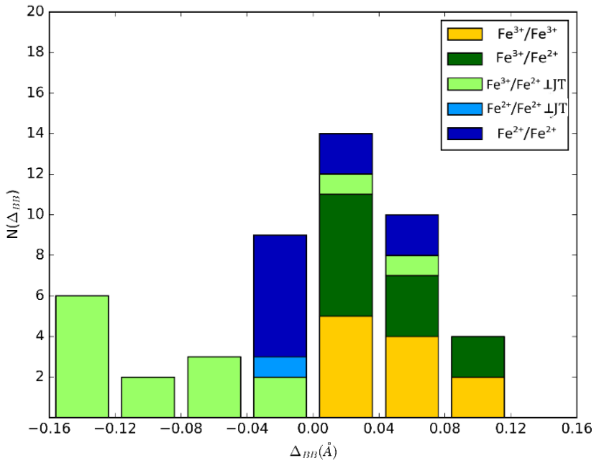


**Figure 46 – Histogram of B-B bond distances, binned in terms of their deviation from the global average. The legend describes the colouring in terms of charge of the bonded sites and directions in comparison to the orbital ordering: light shades are in perpendicular to the Jahn-Teller short axis. Of the $Fe^{2+}/Fe^{3+}$ perpendicular to the short Fe-O bond, 13 have distances anomalously short in comparison to the global average.**

In accord with the Senn *et al.* model, there are still 8 trimerons in the structure (7 $Fe^{3+}$-$Fe^{2+}$-$Fe^{3+}$, 1 $Fe^{2+}$-$Fe^{2+}$-$Fe^{3+}$) outlining an equivalent connectivity. 14 of the expected 16 trimeron Fe-Fe contacts are shorter than the average B-B distance in the structure. The number of trimeron bonds involving a trivalent-like site can be correlated to the decrease of its calculated BVS (Fig. 47); the trend is confirmed in the natural magnetite dataset and it is consistent with the pure sample accounting for the average systematic increase of the BVS values in the natural crystal.

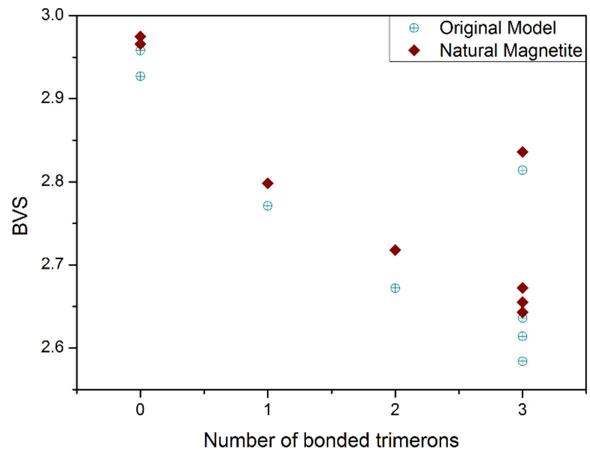


**Figure 47 – BVS as a function of the number of trimeron connecting to a site, for both the natural and pure samples. The natural magnetite, having slightly oxidised octahedral positions, has BVS values systematically higher, but the overall trend is comparable. A non-connected $Fe^{3+}$-like site has a BVS close to the theoretical value of 3; every connection decreases the BVS by ~0.1, but the effect is more prominent for sites between one and two connecting trimerons than it is for sites joining three trimerons. Among the three trimeron sites, the B34 site has a high BVS in both datasets, in an effect that might be related to the length of the trimeron bond.**

Systematic differences of the B-B distances can be visualized by plotting the divergence from the average value in both datasets. The plot in Fig. 48A is of $\Delta D_{BB}$(natural) versus $\Delta D_{BB}$(pure), which is an approximate way to compare the histograms from the two datasets: the trimeron bonding in the natural magnetite sample is very similar to that in the pure sample, with the same pattern of short and long Fe-Fe distances; however, whilst two perfectly equivalent datasets would have data lying on the bisecting line, a slight systematic increase of the anomalously short $\Delta D_{BB}$ (trimeron bonds) can be detected for the natural magnetite dataset.

Further detail of this divergence is provided by plotting the $\Delta\Delta D_{BB} = \Delta D_{BB}$(pure) - $\Delta D_{BB}$(natural) against $\Delta D_{BB}$ (pure), as per Fig. 48B: this plot demonstrates that the magnitude of differences between the two structures ($-0.015 < \Delta\Delta D_{BB} < 0.010$ Å) is only ~10% of the overall B-B shifts ($-0.20 < \Delta D_{BB}$(pure) $< 0.10$ Å). The relatively large values of $\Delta\Delta D_{BB}$ for trimeron distances show that the Fe-Fe bonds, which are very short in the pure sample, are slightly elongated in the natural material; conversely, changes to the non-trimeron B-B distances are smaller as a consequence of the changes to the trimerons.

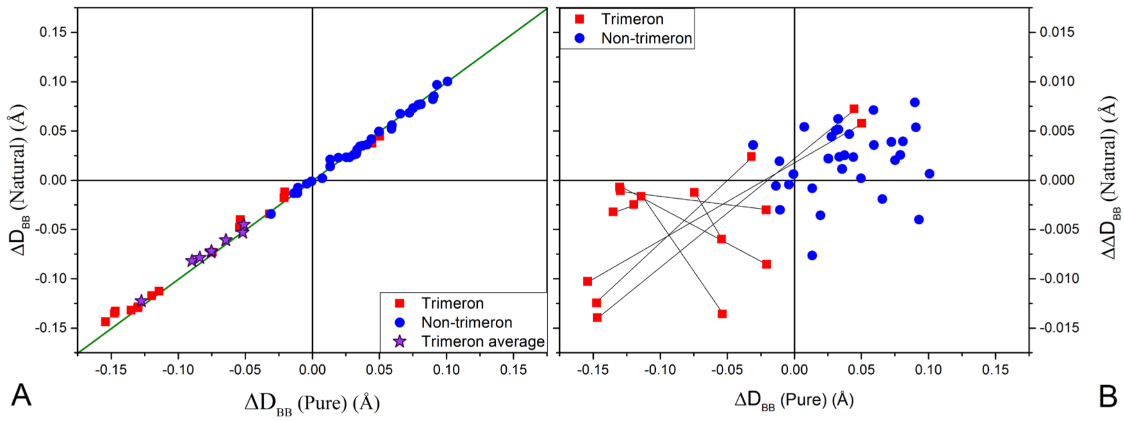


**Figure 48 – A) Left: Comparison of the variation of B-B distances from the global average for the natural and pure datasets. Deviations from the bisecting line show a slight elongation of the trimeron-bonding distances, resulting in an average elongation of the trimeron bond length. B) Right: Plot of $\Delta\Delta D_{BB} = \Delta D_{BB}(\text{pure}) - \Delta D_{BB}(\text{natural})$ against $\Delta D_{BB}(\text{pure})$, showing changes to the B–B distances in the natural sample relative to those in the pure sample. Different symbols are used for trimeron and non-trimeron distances, and pairs of distances in the same trimeron are connected.**

On average, the trimeron dimensions are consistent in the two models, even though a slight tendency to elongation can be seen. As in the pure model, trimerons are not perfectly symmetric around the $Fe^{2+}$ centre, as an effect of the acentricity of the *Cc* superstructure, and neither is their elongation in the natural sample. Considering the total trimeron lengths, there is only one trimeron (*B31-B1A1-B33*) that is more than 0.01 Å longer than the equivalent delocalization region in the original structure (Fig 49).

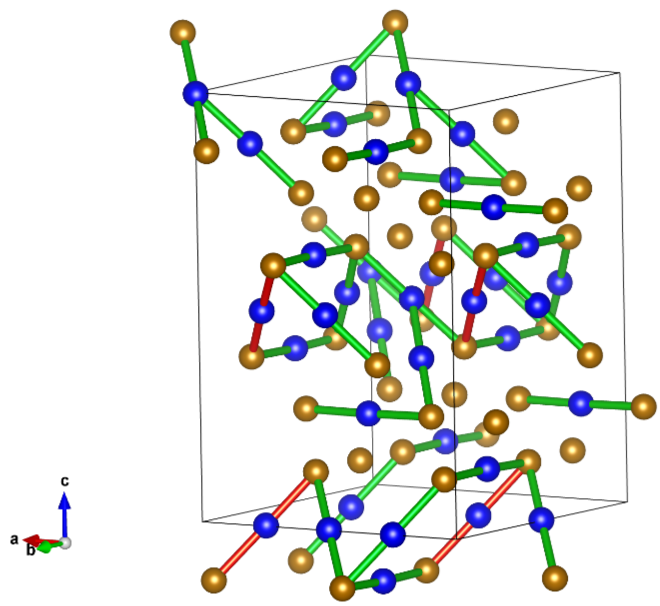


**Figure 49 – Tridimensional spatial arrangement of the trimerons in the low temperature *Cc* monoclinic structure of natural magnetite. $Fe^{2+}$ positions are in blue, $Fe^{3+}$ positions are in yellow. The connectivity is equivalent to the Senn *et al*. model, but trimerons with elongation > 0.01 Å are highlighted as red bonds.**

In light of these structural results, it is possible to state that the complex electronic ordering of charges, orbital states, and $Fe^{3+}$-$Fe^{2+}$-$Fe^{3+}$ trimerons discovered in pure synthetic magnetite below the Verwey transition is also present in a microcrystal fragment obtained from a natural crystal.
Small differences are observed between the two crystal structures, notably a slight loss of $Fe^{2+}$ orbital distortions and elongated Fe-Fe trimeron distances in the natural sample due to the dopants. However, the overall long range electronic order is still preserved over a domain scale of a few tens of microns, as observed in microcrystals of the pure sample.

## 3.2.3. Off-stoichiometric magnetite

### *3.2.3.1. Sample preparation*

In the original work by Honig [150], the synthesis of $Fe_{3(1-\delta)}O_4$ with variable 3δ compositions was performed with a skull melting technique, which gives sizeable crystals of high purity but requires very specific induction furnaces that was part of the available equipment. Therefore, in this work several adjustments had to be made to the original procedure in order to obtain the desired samples.
The starting point of the synthesis is the production of pure stoichiometric magnetite, synthesised at high temperature from hematite in an inert atmosphere:

$$^3/_2\ Fe_2O_3 \xrightarrow{1580\ ℃\ in\ Ar\ flux} Fe_3O_4 + {}^1/_4\, O_2$$

The synthesis yielded a powder composed of small microcrystals. Tuning the oxidation state of the product requires a reannealing at high-temperature, with a well-controlled oxygen environment; this was obtained in a closed tube furnace under a $CO/CO_2$ flow, where the oxygen content is calibrated with a probe sensitive to the $pO_2$ to reproduce the original conditions.
The reannealing was performed a 1200°C, with a reaction time tuned to obtain equilibration of the sample. The sample was then quenched rapidly to stabilise the oxidation ratio obtained at high temperature in a metastable phase.
The correspondence between targeted and actual 3δ values was confirmed with

susceptibility measurements.

Both the synthesis and the physical characterisation work was carried out by Dr Elise Pachoud.

### *3.2.3.2. Physical characterisation*

The occurrence of the Verwey transition and its lowering with increasing 3δ was confirmed through susceptibility measurements as a function of temperature; the results are displayed in Fig. 50. In comparison with a pure sample with $T_V$ ~ 125 K, the three samples obtained with the oxygen controlled synthesis show a lowering of transition temperature down to $T_V$ = 123, 120 and 103 K which is directly proportional to the degree of partial oxidation δ. From the correlation plot from Honig (Fig. 38) we can derive the stoichiometry deviation of these three crystallites to be 3δ = 0.001, 0.009 and 0.012 respectively.

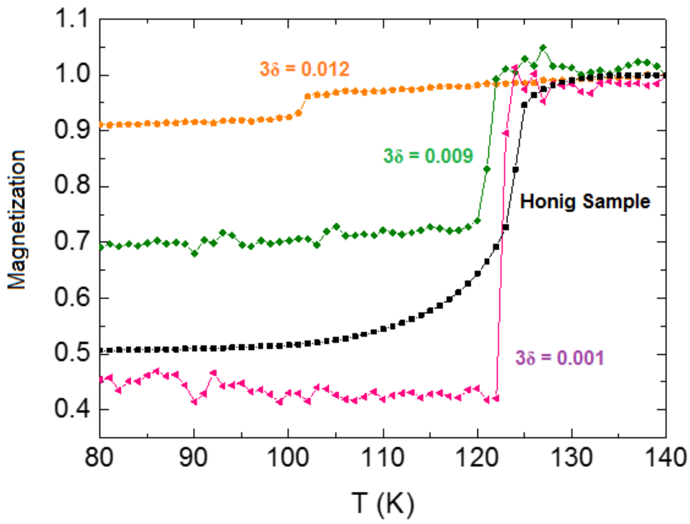


**Figure 50 – Thermal variation of the magnetisation in a 500 Oe field for each of the off-stoichiometric samples in comparison with the sample of magnetite provided by Honig for the original study by Senn *et al.*[26]**

Unfortunately, with the modified synthetic method employed, trying to tune the conditions to obtain 3δ > 0.012 resulted in an uncontrolled oxidation to maghemite, which is the completely oxidised equivalent of $Fe_3O_4$ with only $Fe^{3+}$ and vacancies to occupy the octahedral sites and which does not show any Verwey transition. Consequently, only these three compositions were available for structural analysis.

### *3.2.3.3. Structural characterisation*

Even though all the three $Fe_{3(1-\delta)}O_4$ samples were analysed with single crystal X-ray diffraction at ESRF, the only one regarded as relevant is the one with highest oxidation ($3\delta = 0.012$, $T_V = 103$ K), the results of which will be reported in this section. The features of $3\delta = 0.001$ and $3\delta = 0.009$ do not add significant information in comparison to the original model and the natural sample. According to Honig's study, the $3\delta = 0.012$ sample falls at in the borderline region between first and second order transition behaviour.

Diffraction data on the selected microcrystal were collected at the ID11 beamline at ESRF, France, with the same instrument model and collection procedure outlined in the previous sections.

The presence of the Verwey structural transition in the $3\delta = 0.012$ microcrystal was confirmed by the appearance of the superstructure peaks in the single frame acquisition performed while cooling at a rate of ~ 0.5 K/s. The structural transition can be placed consistently around 103 K in both the dataset collected upon cooling and the one collected upon warming (Fig. 51).

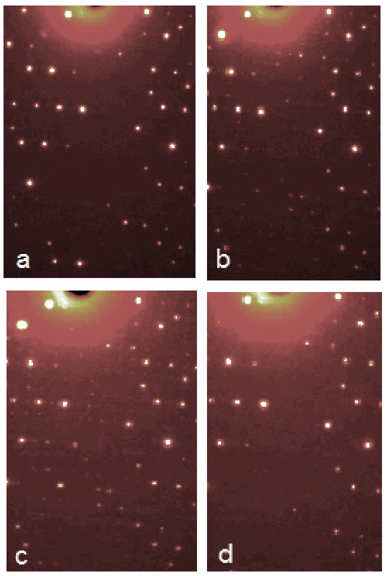


**Figure 51 – Four sequential images that show the appearance and disappearance of weak superstructure spots in the same region of the pattern. The frames show the transition upon cooling (a and b) and warming (c and d). In both cases, $T_V$ is around 103 K.**

The peak intensity on top of the background was computed in order to follow the appearance and disappearance of a given reflection as a function of temperature. A superstructure peak was tracked for this procedure; the onset of the structural transition can be confidently placed at T = 100 – 103 K (Fig. 52). The evident structural change and its sharp profile suggest that the transition is still first-order like, which could be compatible with the borderline composition.

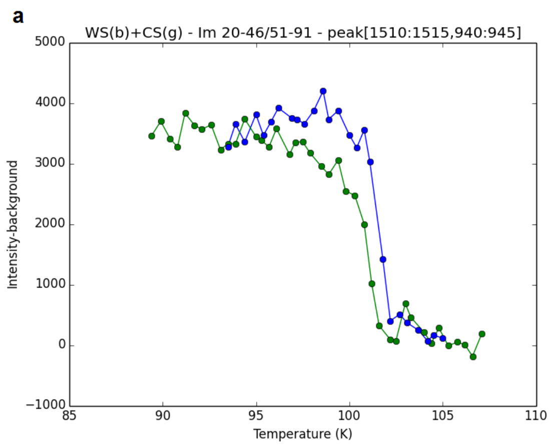


**Figure 52 – Superstructure peak disappearance at $T_V$ = 103 K, upon cooling (blue) and warming (green), with a very modest hysteresis of ~1 K detected.**

Data integration and reduction was performed with the same procedure outlined for the natural magnetite sample. The resulting reflection file is a merge of three different datasets collected with high redundancy to maximise the information contained.

Twin fractions in this sample were estimated after integration through the analysis of the reciprocal space slices (for the monoclinic component) and the intensity ratio of the reflections (for the orthorhombic component).
The plot of the intensity of reflections with *k* even and *l* odd is displayed in Fig. 53; the slope of the interpolated line ${}^{\Delta x}/_{\Delta y}$ suggests the presence of less than 10% of orthorhombic domains.

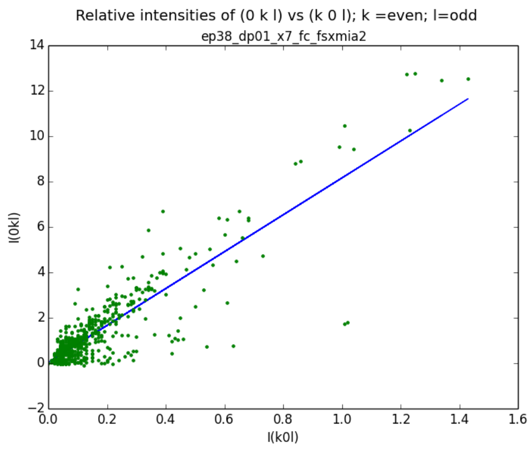


**Figure 53 – Relative intensities of reflections that can be affected by the orthorhombic a/b twins. The slope of the interpolated line is equivalent to < 10% of twin components present.**

Monoclinic twinning is only visible at high *k* order and it is accompanied by a slight splitting of peaks along the *c** direction. The peak splitting is reduced at low diffraction angle, so with a short wavelength like the one in use in this experiment, detecting the splitting in the reciprocal space slices is complicated. A reciprocal space slice calculated for a 16x16x16 Å supercell is displayed in Fig. 54, and in the expanded section of interest we can notice the smearing of the peaks that suggests the presence of two comparable intensities merging into one ellipsoidal-shaped reflection.

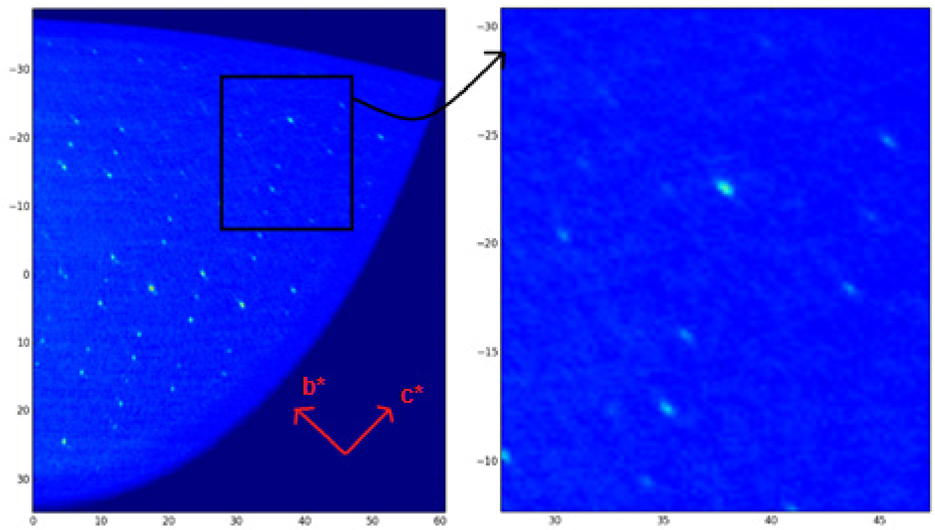


**Figure 54 – Reciprocal space slice over a high-angle plane roughly perpendicular to *l* (noticeable for the presence of the superstructure peaks). Approximate b* and c* axis directions are shown as red arrows. It can be noticed that the smearing of the intensity is reduced at lower angles.**

The structure was refined in a *Cc* monoclinic supercell with $a$ = 11.867(1) Å, $b$ = 11.845(2) Å, $c$ = 16.760(3) Å, β = 90.16(1)°, $V_{cell}$ = 2355.97 Å$^3$. The Shelxl refinement was completed with 508 refined parameters, including twin domains, with refinable atomic positions and anisotropic thermal factors for all atoms. The fit is concluded with $R_1$ = 3.73% for the 95,338 reflections with $F_0 > 4\sigma(F_0)$, and $R_1$ = 5.33% for all 113,655 reflections.
Twin components were refined with the command TWIN 0 -1 0 1 0 0 0 0 -1 4, which led to an overall orthorhombic twin component ~8.0% (4.36% *a/b* twin and 4.04% *a/-b* twin) and 46.51% monoclinic *a/-a* twin. Refinements were performed with the HKLF4 file format, since there is no evidence of the presence of a non-aligned *c*-axis either in the reciprocal space slices or in the R values gained after cross-analysis of all 23 possible twins in HKLF5 format. Refined twin percentages are in accordance with the reciprocal space analysis. Full refinement outcomes are available in Appendix A2.

The twinning is evidently more prominent in the synthetic non-stoichiometric sample than with the natural one. This can be rationalised by considering that the 3δ = 0.012 sample was synthesised directly in microcrystal form after just some days of annealing; conversely, the natural magnetite crystallite was part of a bigger bulk crystal that, as every mineral has, experienced annealing on geological timescales. In this light, it is possible that the synthetic sample had higher residual levels of strain in the lattice that favoured the formation of twins.
Given the results, the structural solution by Senn *et al.* is consistent and applicable with good refinement results even on these more complex crystals.

### 3.2.3.4. Distortion analysis

In consistency with the natural sample, distortion modes associated with the local coordination of the structure were calculated with a purpose-written Python program. The program uses the output from the refinement file to extract the atomic positions, applies the due symmetry restraints and computes bond lengths, associated Q-modes and BVS values. The values are listed in Table 4.
The results are displayed visually in Fig. 55, with tetragonal and orthorhombic Jahn-Teller contributions, respectively, as a function of the breathing mode ($Q_{JT}/Q_O$ vs $Q_{rad}$). Both the correlations are plotted in comparison to the original model by Senn *et al.* Additionally, the

formal oxidation state of iron for every site was estimated with Bond Valence Sum (BVS), strongly correlated with $Q_{rad}$ and used as an additional identifier.

The sample still shows evidence of charge and orbital ordering from the distribution of radial tetragonal Jahn-Teller breathing modes, but it is evident by comparison with the pure $Fe_3O_4$ sample that both features are less pronounced. A combined analysis of the distribution of modes and of the BVS allows the same charge distribution as the original Senn *et al*. model to be assigned. Two particular sites represent a more tentative assignation: B31 is theoretically $Fe^{3+}$-like, but verges on positive $Q_{rad}$, with a prominent $Q_O$ and has a BVS close to but not higher than 2.6; B1B2 is theoretically $Fe^{2+}$-like but has no $Q_{rad}$, and a modest $Q_{JT}$, even though $Q_O$ is still significant, and its BVS = 2.61. Apart from the B1B2 site, a BVS ≥ 2.58 consistently identifies $Fe^{3+}$-like sites, and BVS ≤ 2.52 identifies $Fe^{2+}$-like sites.

**Table 4 – Distortion modes and Bond Valence Sum values for each iron site in the monoclinic superstructure of the off-stoichiometric magnetite crystal. Rows are colour coded to follow the original trivalent (orange) or divalent (blue) assignation.**

| *Site* | $Q_{rad}$ (Å) | $Q_{JT}$ (Å) | $Q_O$ (Å) | BVS |
|---|---|---|---|---|
| *B1B1* | 0.032 | -0.004 | -0.020 | 2.48 |
| *B31* | 0.002 | -0.001 | -0.018 | 2.58 |
| *B32* | 0.002 | 0.002 | 0.010 | 2.59 |
| *B1A1* | 0.044 | -0.008 | -0.052 | 2.45 |
| *B1A2* | 0.031 | 0.005 | 0.028 | 2.49 |
| *B33* | -0.002 | 0.010 | 0.005 | 2.63 |
| *B41* | 0.028 | -0.011 | -0.019 | 2.49 |
| *B2A1* | -0.034 | 0.010 | 0.012 | 2.72 |
| *B34* | -0.049 | -0.014 | -0.005 | 2.77 |
| *B1B2* | -0.000 | -0.008 | -0.021 | 2.61 |
| *B43* | -0.070 | -0.004 | -0.004 | 2.85 |
| *B2B2* | -0.079 | -0.001 | -0.008 | 2.88 |
| *B44* | 0.056 | -0.030 | -0.028 | 2.41 |
| *B42* | 0.022 | -0.032 | -0.004 | 2.52 |
| *B2B1* | 0.030 | -0.047 | -0.000 | 2.49 |
| *B2A2* | -0.014 | -0.000 | -0.010 | 2.64 |

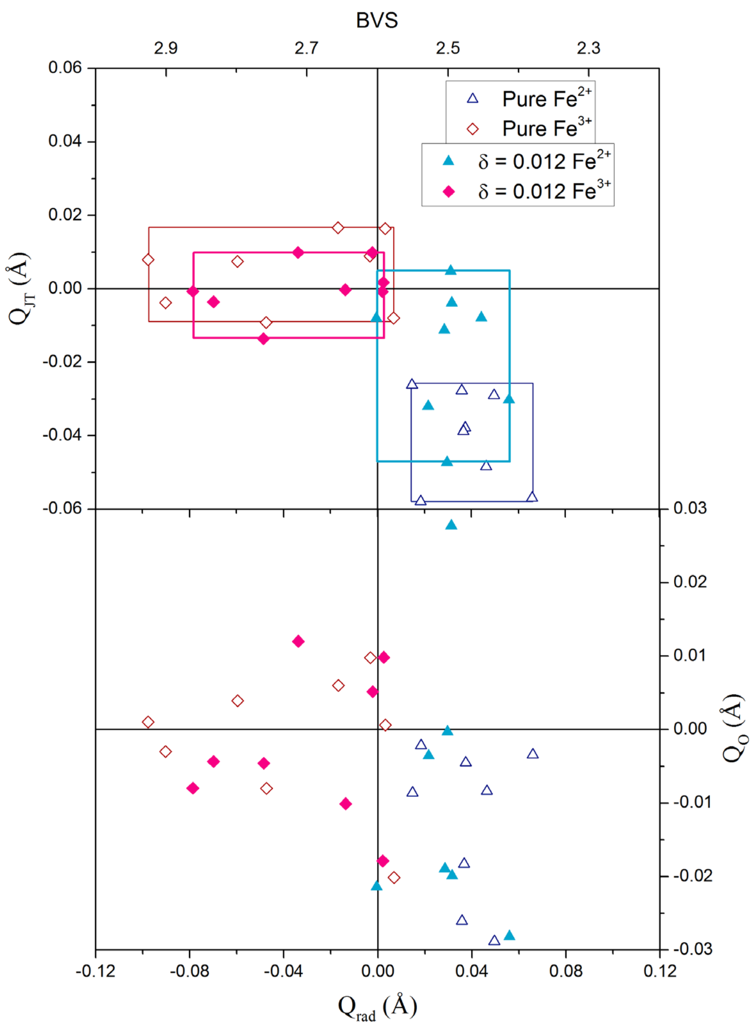


**Figure 55 – Distortion amplitudes of tetragonal Jahn–Teller ($Q_{JT}$, A) and orthorhombic ($Q_O$, B) modes plotted against the radial breathing mode for the 16 octahedral B sites in the *Cc* structure. Data for both the off-stoichiometric sample and pure magnetite are displayed as per the legend. Domains of the 8 $Fe^{2+}$-like and 8 $Fe^{3+}$-like sites are shown as rectangles of matching colours. An approximate BVS scale is shown at the top of the plot.**

The extent of the deviations from the pure sample are listed in Table 5. Deviations of the Q-modes above 0.02 Å, with maximum values up to 0.05 Å, are common in this structure. There is a net tendency to oxidation of the octahedral irons, with $Fe^{2+}$-like sites undergoing an average increase of BVS of 0.02, but $Fe^{3+}$-like sites counterbalance with their average decrease in BVS of ~ 0.04.

**Table 5 – Deviation from the Senn *et al.* model, for each distortion mode Q and BVS values. The computed value follows Δ = (pure) – (off-stoichiometric). Rows are colour coded to follow the original trivalent (orange) or divalent (blue) assignation. As in the natural model, not every site is affected in the same way and to the same degree from the sample doping. The BVS of 6 sites out of 16 shows an increase in comparison to the pure sample.**

| *Site* | $\Delta Q_{rad}$ (Å) | $\Delta Q_{JT}$ (Å) | $\Delta Q_O$ (Å) | ΔBVS |
|---|---|---|---|---|
| *B1B1* | 0.006 | -0.034 | 0.015 | -0.01 |
| *B31* | 0.005 | -0.007 | -0.002 | 0.00 |
| *B32* | 0.001 | 0.015 | -0.009 | 0.02 |
| *B1A1* | -0.008 | -0.020 | 0.026 | 0.03 |
| *B1A2* | 0.015 | -0.053 | -0.036 | -0.04 |
| *B33* | -0.001 | -0.001 | 0.005 | 0.01 |
| *B41* | 0.021 | -0.018 | -0.010 | -0.06 |
| *B2A1* | -0.014 | -0.019 | -0.020 | 0.05 |
| *B34* | -0.011 | 0.021 | 0.009 | 0.05 |
| *B1B2* | 0.015 | -0.018 | 0.013 | -0.05 |
| *B43* | -0.020 | 0.000 | 0.001 | 0.08 |
| *B2B2* | -0.019 | 0.009 | 0.009 | 0.08 |
| *B44* | 0.010 | -0.027 | 0.025 | -0.03 |
| *B42* | -0.003 | -0.026 | 0.001 | 0.02 |
| *B2B1* | 0.007 | 0.009 | -0.018 | -0.02 |
| *B2A2* | -0.003 | 0.017 | 0.016 | 0.03 |

Keeping the same site assignation allows the second coordination shell distances to be computed in a way that is comparable with the pure and natural sample datasets. A histogram of the B-B bond lengths, listed according to the oxidation state of the binding site and the directionality with the orbital ordering axis, is provided in Fig. 56. Fifteen $Fe^{3+}$-$Fe^{2+}$ and one $Fe^{2+}$-$Fe^{2+}$ distances in perpendicular to the Jahn-Teller short axis are anomalously short in comparison to the global average (2.9691(8) Å at 90 K). Therefore, the off-stoichiometric magnetite still shows evidence of trimeron formation.

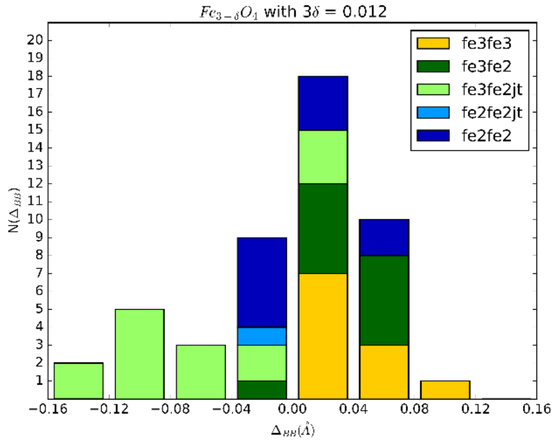


**Figure 56 – Histogram B-B bond distances, binned in terms of deviation from the average. The legend describes the colouring in terms of the charge of the bonded sites and the directions in comparison to the orbital ordering: light shades are perpendicular to the Jahn-Teller short axis. Of the $Fe^{2+}/Fe^{3+}$ perpendicular to the short Fe-O bond, 13 have distances anomalously short in comparison to the average.**

The connectivity of the 8 trimerons (7 $Fe^{3+}$-$Fe^{2+}$-$Fe^{3+}$, 1 $Fe^{2+}$-$Fe^{2+}$-$Fe^{3+}$) is still equivalent to the one outlined by the Senn *et al*. model. It is worth noticing that B31 and B1B2 are bonded in a trimeron and as such the shift in distortion modes and BVS that they experience might be a correlated feature.

The decrease in calculated BVS as a function of the number of bonds involving a trivalent-like site does not show the same approximately linear trend that characterises the natural and pure samples (Fig. 57). This can be interpreted as the net result of the charge disorder imposed by the non-stoichiometry in the octahedral sites.

Systematic differences in B-B distances can be visualized in Figure 58, comparing the off-stoichiometric and pure model on the same graph. Fig. 58A is a $\Delta D_{BB}$(off-stoichiometric) *versus* $\Delta D_{BB}$(pure), an equivalent to histograms of both datasets, and shows a marked tendency to elongation of the trimeron-bonding B-B distances. This is compatible with a higher B-B average distance, and it is reflected in the net elongation of the total trimeron bond lengths.

The plot of $\Delta\Delta D_{BB} = \Delta D_{BB}$(pure) - $\Delta D_{BB}$(off-stoichiometric) *vesus* $\Delta D_{BB}$ (pure), as per Fig. 58B, is a graphical depiction of the magnitude of differences between the two structures: the shift values ($-0.045 < \Delta\Delta D_{BB} < 0.030$ Å) are more than double than those of the natural magnetite sample and account for ~25% of the overall B-B shifts ($-0.20 < \Delta D_{BB}$(pure) $< 0.10$ Å). Moreover, this plot confirms how the trimeron B-B distances are the most affected by the shift, with a net elongation in comparison to the pure model, whereas the non-trimeron distances are compressed with a less prominent shift.

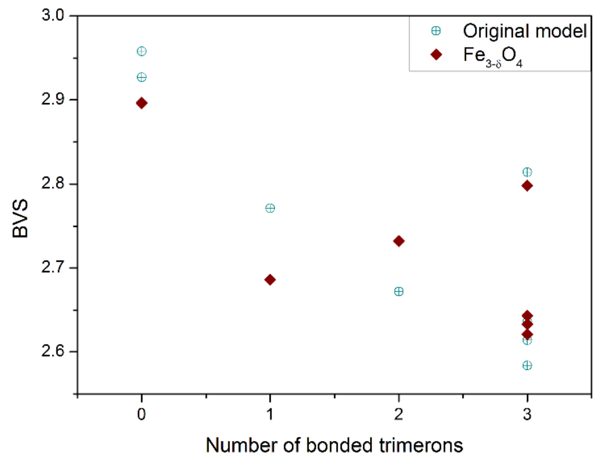


**Figure 57 – BVS as a function of the number of trimerons connecting to a site, for both the off-stoichiometric and pure structures. The 3δ = 0.012 magnetite lacks the approximately linear trend of the pure sample, with a notable outlier in the single bonded site (corresponding to B2A1). In contrast with the natural magnetite, where the trend of BVS increase was shared equally among all octahedral sites, the off-stoichiometric magnetite has $Fe^{2+}$-like sites with increased BVS and a majority of slightly $Fe^{3+}$-like sites with lower BVS; accordingly, the BVS values in this plot are often lower than the original ones, but are affected by a high disorder.**

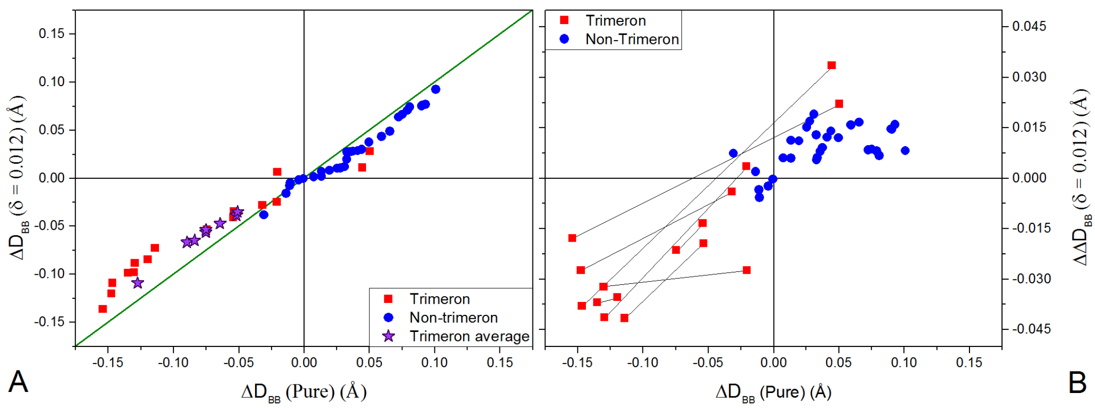


**Figure 58 – A) Left: Comparison of the variation of B-B distances from the global average between the off-stoichiometric and pure datasets. Deviations from the bisecting line show a net elongation of the trimeron-bonding distances, and therefore of average trimeron bond lengths. B) Right: Plot of $\Delta\Delta D_{BB} = \Delta D_{BB}(pure) - \Delta D_{BB}(3\delta = 0.012)$ against $\Delta D_{BB}(pure)$, showing changes to the B–B distances relative to those in the pure sample. Different symbols are used for trimeron and non-trimeron distances, and pairs of distances in the same trimeron are connected.**

The outline of the trimeron connectivity is the same in the off-stoichiometric structure as it was in the pure structure (Fig. 59). However, all orbital molecules are elongated by a minimum of 0.02 Å, reaching peaks up to 0.05 Å elongation in comparison to the Senn *et al*.

model. This elongations is given as net value of the total trimeron bond length, since the distortions are asymmetric around the central $Fe^{2+}$; however, it is worth noting that amongst the 16 bond lengths, only four are compressed, and all the others instead show various degrees of elongation. Considering all the total lengths, two trimerons are elongated of 0.05 Å or more: B31-B1A1-B33 and B34-B1A2-B32.

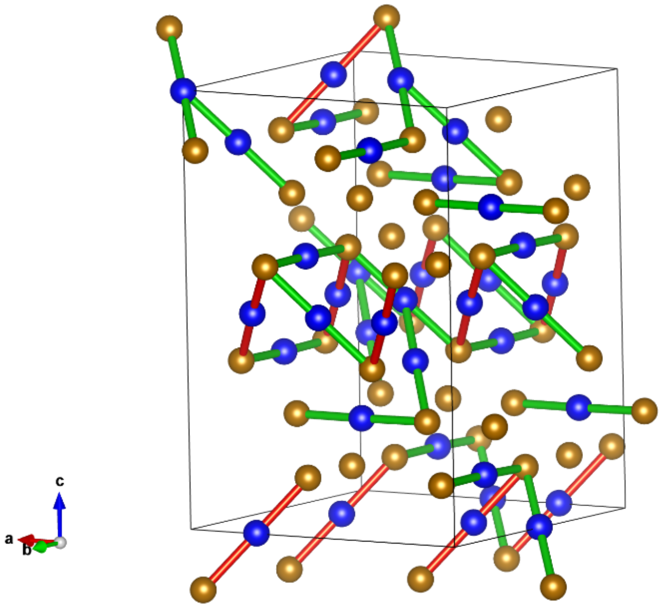


**Figure 59 – Tridimensional spatial arrangement of the trimerons in the low temperature *Cc* monoclinic structure of 3δ = 0.012 magnetite. $Fe^{2+}$ positions are in blue, $Fe^{3+}$ positions are in yellow. The connectivity is equivalent to the Senn *et al*. model, but trimerons with elongation > 0.05 Å are highlighted as red bonds.**

These structural results offer proof that the Verwey structure of doped magnetite maintains cooperative ordering features that are comparable to the one discovered for pure magnetite. This level of systematic doping sits on the edge of what Honig labelled as the first to second order transition, but the behaviour at the crossing of $T_V$ is consistent with a first order transition, corroborated by the presence of the same structural transition that characterises pure and natural magnetite. In contrast with the natural sample, however, the charge disorder effect is more systematically focused on sites that can be labelled as $Fe^{2+}$-like. There is a general trend towards the loss of distortion features in both the first and second coordination shells of the $FeO_6$ octahedra, which reflects a general elongation of the trimeron bond lengths.

## 3.2.4. Zn-doped magnetite

### *3.2.4.1. Sample preparation*

The sample was synthesised at high temperature from hematite and zinc oxide in inert atmosphere:

$$\frac{2.97}{2} Fe_2O_3 + 0.03\ ZnO \xrightarrow{1580\ ^{\circ}C\ in\ Ar\ flux} (Fe^{3+}_{0.97}Zn^{2+}_{0.03})_T(Fe^{3+}_{0.97}Fe^{2+}_{1.03})_O O_4 + \frac{0.97}{4} O_2$$

This was then quenched rapidly to stabilise the oxidation state. The resulting material has $Zn^{2+}$ replacing the iron $Fe^{3+}$ in the tetrahedral A sites.

The synthesis yielded a powder composed of small microcrystals. A reannealing process at high temperature did not improve the physical properties of the sample, so the material was carried forward for structural and physical characterisation as synthesised.

Both synthesis and physical characterisation work were carried out by Dr Elise Pachoud.

### *3.2.4.2. Physical characterisation*

The occurrence of the Verwey transition and its lowering with increased doping value was confirmed through susceptibility measurements as a function of temperature; the results are displayed in Fig. 60. The data is provided with a comparison to the pure sample with $T_V$ ~ 125 K used in the Senn *et al.* study, and there is a clear lowering of transition temperature by ~ 35 K. In accord with both the synthetic conditions and the correlation plot from Honig (Fig. 38), the sample is compatible with $Fe_{3-x}Zn_xO_4$ with x = 0.03. With $T_V$ = 90 K, this sample belongs to the second order regime, according to Honig; in this regime the presence of a physical transition is supposedly not associated with a structural distortion.[150]

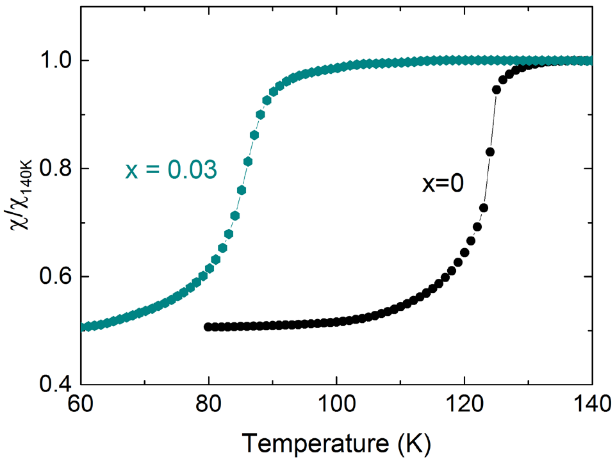


**Figure 60 – Susceptibility as a function of temperature measured in a 500 Oe field for pure magnetite (x = 0) and 3% Zn-doped magnetite. For a better comparison, data are normalised to the susceptibility at 140 K, well above $T_V$ for both samples.**

### *3.2.4.3. Structural characterisation*

A first confirmation of the occurrence of structural transition was provided by high-resolution powder diffraction performed in a helium cryostat at the ID22 beamline at ESRF, France. The powder sample was ground and loaded in a 0.5 mm borosilicate capillary; the high-resolution multistage analyser was used to collect powder patterns between T = 35 K and T = 325 K in 5 K steps, with λ = 0.354224(1) Å.

Between 85 and 90 K, the pattern shows clear signs of cubic to monoclinic phase transition, exemplified in Figure 61 with the splitting of the cubic 440 reflection.

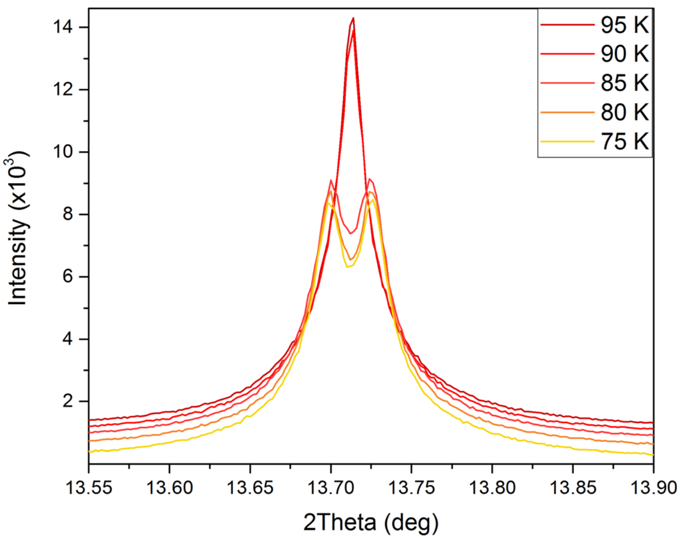


**Figure 61 – Raw powder diffraction data from ID22, showing the splitting of the 440 cubic reflection upon transition from cubic *Fd-3m* to monoclinic *Cc*.**

The monoclinic model at T = 80 K was refined against the data by Dr Elise Pachoud to extract an accurate cell dimension: *a* = 11.87949(16) Å, *b* = 11.85663(21) Å, *c* = 16.78993(22) Å and β = 90.1721(12)°. These values are kept as the most precise cell determination available for the Zn-doped magnetite and are used in the single crystal refinements.

A ~50 µm microcrystal was selected from the bulk product and diffraction data were collected at the ID11 beamline at ESRF, France. The same instrument model and collection procedure as outlined in previous sections were applied, but the cryostream was set at its lower temperature limit in order to collect data from T = 80 K to T = 130 K.
The presence of the Verwey structural transition in the Zn-doped sample was confirmed by the appearance of the superstructure peaks in the single frame acquisition performed while warming at a rate of ~ 0.5 K/s. The structural transition can be placed consistently around 90 K (Fig. 62), in accordance with both the physical property measurements and powder diffraction data.

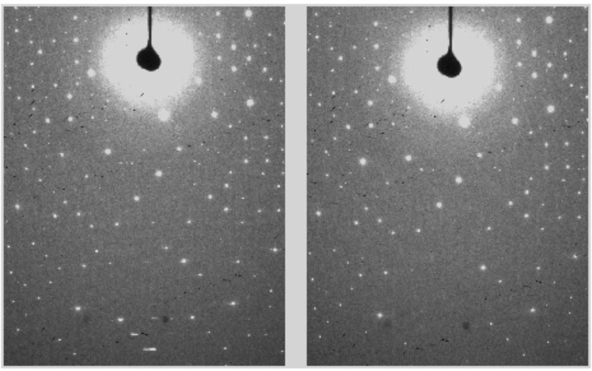


**Figure 62 – Sections of single crystal patterns collected upon warming. The superstructure peaks are evident in the base temperature frame and disappear upon warming above T = 90 K.**

Integration and structural refinement were performed by Dr James Cumby, using the Crysalis Pro software and Shelxl.
Upon analysis of the full reflection sphere, obtained by merging redundant collections into a single file, the microcrystal was found to have two diffracting domains. This was not observed in any of the previous samples and it may be related to the stabilisation of grain boundaries induced by the Zn-doping. Integration with *Cc* monoclinic superstructure symmetry was still possible, and the non-merohedricity of the two domains distinguished

them upon analysis: the domains, in a 60/40 ratio, are approximately related by the law $\left\{\left[\frac{1}{2}, -\frac{1}{2}, -\frac{1}{2}\right] \left[\frac{1}{2}, -\frac{1}{2}, \frac{1}{2}\right] [-1, -1, 0]\right\}$. The final reflection file was generated from the integration of the dominant domain only, and was refined using the atomic positions from original Senn *et al*. model with the lattice parameters fixed at the values obtained by powder diffraction. In comparison to the pure, natural and off-stoichiometric samples, a proper refinement of the twin fractions required a refinement of 8 twins related by inversion, in order to account for additional strain effects related to the multi-domain diffraction; only four domains are prominent.

A full list of the refinement results is available in Appendix A3.

#### *3.2.4.4. Distortion analysis*

The distortion modes associated with the local coordination of the structure and the associated BVS values are listed in Table 6.

**Table 6 – Distortion modes and Bond Valence Sum values for each iron site in the monoclinic superstructure of the Zn-doped magnetite crystal. Rows are colour coded to follow the original trivalent (orange) or divalent (blue) assignation.**

| *Site* | $Q_{rad}$ (Å) | $Q_{JT}$ (Å) | $Q_O$ (Å) | BVS |
|---|---|---|---|---|
| *B1B1* | 0.031 | -0.016 | -0.012 | 2.50 |
| *B31* | -0.021 | -0.003 | -0.005 | 2.68 |
| *B32* | -0.007 | -0.005 | -0.013 | 2.64 |
| *B1A1* | 0.064 | -0.025 | -0.015 | 2.40 |
| *B1A2* | 0.009 | -0.027 | -0.007 | 2.58 |
| *B33* | 0.011 | 0.009 | 0.006 | 2.60 |
| *B41* | 0.019 | 0.019 | 0.013 | 2.54 |
| *B2A1* | -0.023 | 0.010 | 0.005 | 2.69 |
| *B34* | -0.025 | 0.006 | 0.006 | 2.69 |
| *B1B2* | -0.002 | -0.010 | -0.008 | 2.61 |
| *B43* | -0.017 | 0.022 | 0.003 | 2.67 |
| *B2B2* | -0.058 | 0.007 | 0.002 | 2.82 |
| *B44* | 0.065 | -0.010 | -0.030 | 2.40 |
| *B42* | -0.046 | 0.000 | 0.016 | 2.77 |
| *B2B1* | 0.016 | -0.028 | -0.006 | 2.55 |
| *B2A2* | -0.015 | 0.011 | 0.002 | 2.66 |

The results are displayed in Fig. 63, with tetragonal and orthorhombic Jahn-Teller contributions, respectively, as a function of the breathing mode ($Q_{JT}/Q_O$ vs $Q_{rad}$). Both of the correlations are plotted in comparison to the original model by Senn *et al.* Additionally, the formal oxidation state of iron for every site was estimated from the Bond Valence Sum (BVS), strongly correlated with $Q_{rad}$ and used as an additional identifier. $Fe^{2+}$-like states are considered to have a BVS ≤ 2.58, with B1B2 being a slight outlier with BVS = 2.61 and B42 being out of trend with BVS = 2.77; $Fe^{3+}$-like states can be considered as having BVS ≥ 2.64, with B33 being a slight outlier with BVS = 2.60.

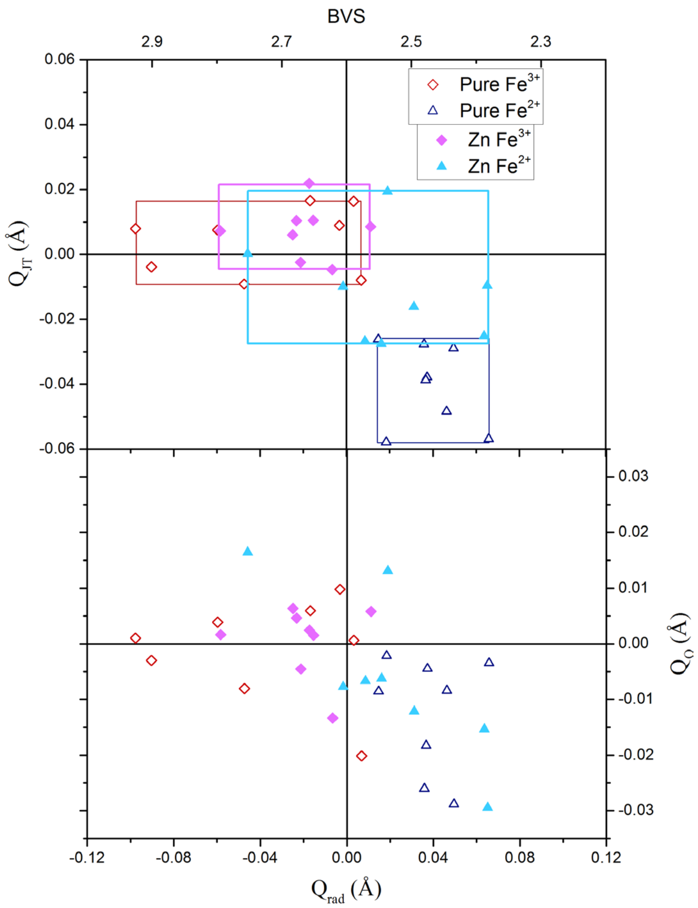


**Figure 63 – Distortion amplitudes of tetragonal Jahn–Teller ($Q_{JT}$, A) and orthorhombic ($Q_O$, B) modes plotted against the radial breathing mode for the 16 octahedral B sites in the *Cc* structure. Data for both the Zn-doped sample and the pure magnetite are displayed as per the legend. Domains of the 8 $Fe^{2+}$-like and 8 $Fe^{3+}$-like sites are shown as rectangles of matching colours. An approximate BVS scale is shown at the top of the plot.**

Q-modes in this structure deviate from the stoichiometric magnetite model in a highly uncorrelated manner, but there are several examples of values increasing between 0.02 Å and 0.08 Å in comparison to the original model. The $Fe^{2+}$-like sites have a more extreme increase in BVS changes, increasing of up to 0.14 (not considering B42) with an average of 0.07 rise. This is counterbalanced by the $Fe^{3+}$-like sites, whose BVS decreases by 0.065 on average from equivalent sites in pure stoichiometric magnetite. On a site by site basis, however, it has to be considered that this effect is non-linear, as detailed in Table 7.

**Table 7 – Deviation from the Senn *et al.* model, of each distortion mode Q and the BVS values. The computed values follows Δ = (pure) – (Zn). Rows are colour coded to follow the original trivalent (orange) or divalent (blue) assignation. As in the natural model, not every site is affected in the same way and to the same degree by the sample doping. The BVS of 9 sites out of 16 have a higher BVS than the original model, but the concurrent lowering of the remaining sites almost completely counterbalances on average. Three-quarters of the 2+-like sites show an increase in BVS, in contrast to one-quarter of the 3+-like sites.**

| *Site* | $\Delta Q_{rad}$ (Å) | $\Delta Q_{JT}$ (Å) | $\Delta Q_{O}$ (Å) | ΔBVS |
|---|---|---|---|---|
| *B1B1* | 0.006 | -0.022 | 0.008 | -0.03 |
| *B31* | 0.028 | -0.006 | -0.016 | -0.10 |
| *B32* | 0.010 | 0.021 | 0.014 | -0.02 |
| *B1A1* | -0.028 | -0.003 | -0.011 | 0.09 |
| *B1A2* | 0.038 | -0.022 | -0.002 | -0.13 |
| *B33* | -0.014 | 0.000 | 0.004 | 0.03 |
| *B41* | 0.031 | -0.048 | -0.042 | -0.10 |
| *B2A1* | -0.024 | -0.020 | -0.013 | 0.08 |
| *B34* | -0.035 | 0.001 | -0.002 | 0.12 |
| *B1B2* | 0.016 | -0.016 | -0.001 | -0.05 |
| *B43* | -0.073 | -0.026 | -0.006 | 0.26 |
| *B2B2* | -0.039 | 0.001 | -0.001 | 0.14 |
| *B44* | 0.001 | -0.047 | 0.026 | -0.01 |
| *B42* | 0.064 | -0.058 | -0.019 | -0.23 |
| *B2B1* | 0.021 | -0.011 | -0.012 | -0.07 |
| *B2A2* | -0.001 | 0.006 | 0.005 | 0.01 |

The fact that, among all previously divalent-like irons, B42 appears to have lost all its features can be correlated with the nature of Zn doping. As discussed, the doping affects the tetrahedral sites only, but charge balance requires a modification of the octahedral site from ($Fe^{2+}_1$ $Fe^{3+}_1$) to ($Fe^{2+}_{0.97}$ $Fe^{3+}_{1.03}$), averaging though all the sites. Since there are 16 B sites in the monoclinic *Cc* structure, an average 3% increase is equivalent to oxidising half of a divalent site (1/16 = 6.25%). In light of the findings, the site might be identified as B42, which shifts from a completely divalent-like behaviour in pure magnetite (BVS = 2.54) to a completely trivalent-like behaviour in Zn-doped magnetite (BVS = 2.77).

For the sake of performing comparable computations, the site assignation in terms of charges was kept consistent with that used for the pure, natural and off-stoichiometric datasets. In this modelling, B42 is thus still computed as a 2+-like site.

A histogram of the B-B bond lengths, listed according to the oxidation state of the binding site and the directionality with respect to the orbital ordering axis, is provided in Fig. 64. Fifteen $Fe^{3+}$-$Fe^{2+}$ and one $Fe^{2+}$-$Fe^{2+}$ distances perpendicular to the Jahn-Teller short axis are anomalously short in comparison to the global average (2.9676(8) Å at 80 K). Therefore, even Zn-doped magnetite can be considered as having trimeron ordering.

The connectivity of the 8 trimerons (7 $Fe^{3+}$-$Fe^{2+}$-$Fe^{3+}$, 1 $Fe^{2+}$-$Fe^{2+}$-$Fe^{3+}$) is still equivalent to the one outlined in the Senn *et al*. model.

The decrease in calculated BVS as a function of the number of bonds involving a trivalent-like site disrupts the approximately linear trend that characterised the natural and pure samples, with a deviation more marked than the one found in the off-stoichiometric magnetite (Fig. 65). As in the previous sample, the prominence of this effect might be related to the extreme charge disorder effects in Zn-doped magnetite.

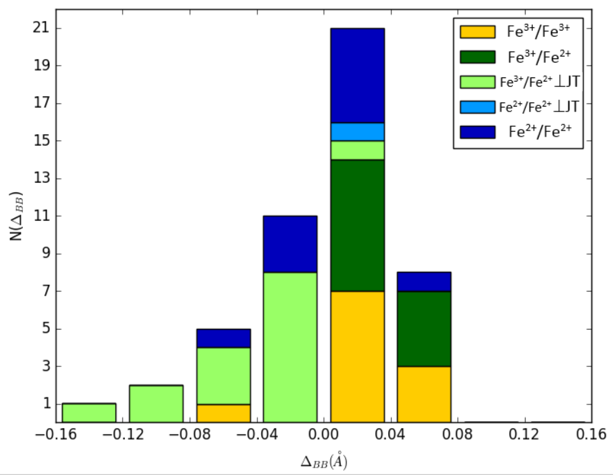


**Figure 64 – Histogram of B-B bond distances, binned in terms of their deviation from the average. The legend describes the colouring in terms of the charge of the bonded sites and their directions in comparison to the orbital ordering: light shades are perpendicular to the Jahn-Teller short axis. Of the $Fe^{2+}/Fe^{3+}$ perpendicular to the short Fe-O bond, 13 have distances anomalously short in comparison to the average.**

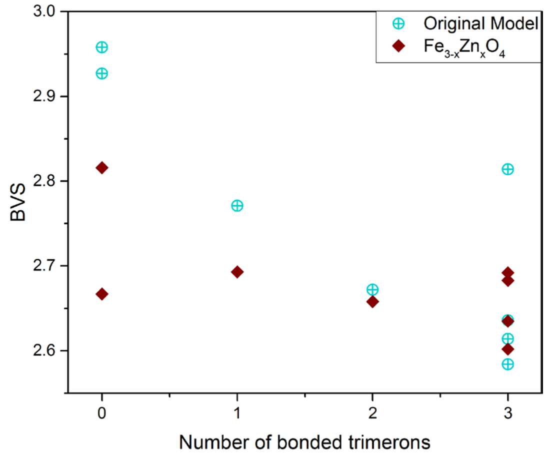


**Figure 65 – BVS as a function of the number of trimerons connecting to a site, for both the Zn-doped and pure structures. The 3% Zn magnetite completely loses the approximately linear trend seen for the pure sample, and the BVS of a site like B43, bonded to no trimerons, is comparable to sites bonded to one, two and even three trimerons. The trend of non-linear reduction of the $Fe^{3+}$ sites, already observed in the off-stoichiometric magnetite, reaches an extreme in this sample.**

Systematic differences of the B-B distances are displayed in Figure 66, comparing the off-stoichiometric and pure model on the same graph. Fig. 66A shows a $\Delta D_{BB}$(off-stoichiometric) versus $\Delta D_{BB}$(pure), an equivalent to the histograms of both datasets, and shows an extreme tendency to elongation of the trimeron-bonding B-B distances. Accordingly, the total trimeron bond lengths increase, but the overall B-B distance considering every iron site is not higher, signalling that the contraction of the non-trimeron bonding distances is counterbalancing the lengthening of the trimeron bonding ones.

The plot of $\Delta\Delta D_{BB} = \Delta D_{BB}$(pure) - $\Delta D_{BB}$(Zn) *versus* $\Delta D_{BB}$ (pure), as per Fig. 66B, is a graphical depiction of the magnitude of the differences between the two structures: the shift values ($-0.09 < \Delta\Delta D_{BB} < 0.030$ Å) are double those of off-stoichiometric magnetite and roughly four times those of natural magnetite. These shifts account for ~50% of the overall B-B shifts ($-0.20 < \Delta D_{BB}$(pure) $< 0.10$ Å). Moreover, this plot shows how trimeron distances are the most affected by the shift, with a net elongation in comparison to all the previous models, whereas the non-trimeron distances are compressed with a less prominent shift that is almost comparable to the one already computed for the off-stoichiometric magnetite.

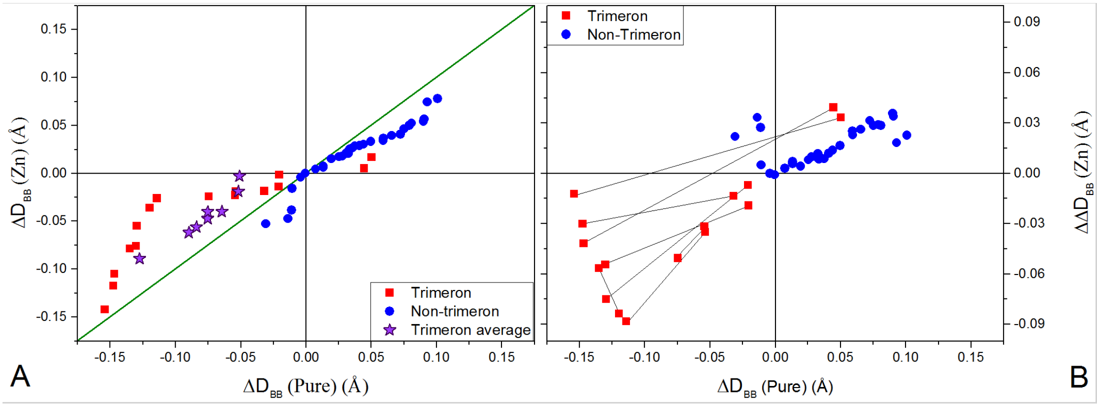


**Figure 66 – A) Left: Comparison of the variation of B-B distances from the global average between the Zn-doped and pure datasets. Deviations from the bisecting line show a significant elongation of the trimeron-bonding distances, and therefore of average trimeron bond lengths. B) Right: Plot of $\Delta\Delta D_{BB} = \Delta D_{BB}$(pure) - $\Delta D_{BB}$(Zn) against $\Delta D_{BB}$(pure), showing changes to the B–B distances relative to those in the pure sample. Different symbols are used for trimeron and non-trimeron distances, and pairs of distances in the same trimeron are connected.**

The full trimeron connectivity, as originally computed for the pure model and already reproduced for natural and off-stoichiometric structures, is depicted in Fig. 67. However, in comparison with stoichiometric magnetite, the orbital molecules have an average elongation of 0.06 Å, computed from the net value of the total trimeron bond length to compensate for the acentricity around the central 2+-like atom. Looking at the trimeron specific behaviour, only 3 out of 8 have an elongation between 0.024 Å and 0.049 Å, with all the remaining trimerons elongated between 0.056 Å and almost 0.077 Å and the notable exception of one trimeron elongated by almost 0.15 Å. In this structure there are no compressed trimerons, in contrast with the previous magnetite samples discussed.
Of the trimerons elongated by more than 0.05 Å, none corresponded to the one that also experienced elongation in the natural and off-stoichiometric samples. However, as discussed, the average elongation is already higher than the maximum elongation observed in other samples. The most elongated trimeron is the one bonding B1B2 – B42 – B2A2, which is also the only trimeron of the Verwey structure to bond two $Fe^{2+}$-like and one $Fe^{3+}$-like sites. Considering that, as discussed, B42 is a site that does not have the proper features for a $Fe^{3+}$ charge assignation, this trimeron should be considered as disrupted in the Zn-doped magnetite. By contrast, B43 (ΔBVS = 0.26) is originally trimeron non-bonding and does not influence this picture.

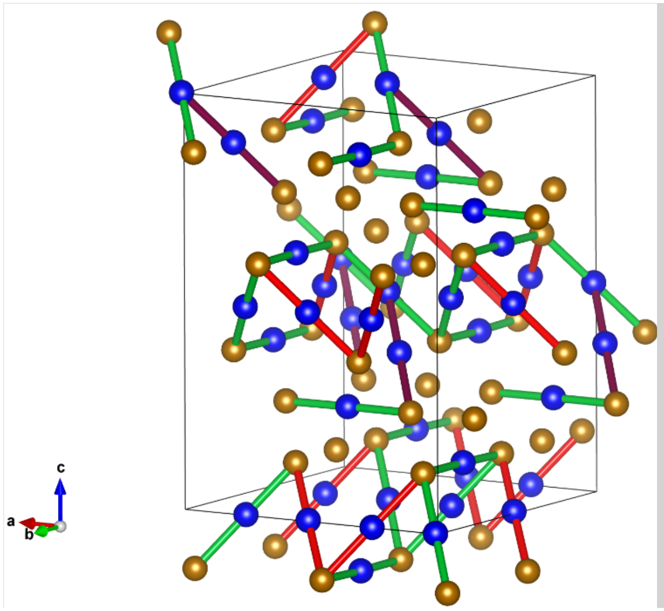


**Figure 67 – Tridimensional spatial arrangement of the trimerons in the low temperature *Cc* monoclinic structure of Zn-doped magnetite. $Fe^{2+}$ positions are in blue, $Fe^{3+}$ positions are in yellow. The connectivity is equivalent to the Senn *et al.* model, but trimerons with elongation > 0.05 Å are highlighted as red bonds and the single trimeron elongated of almost 0.15 Å is displayed in purple.**

The structural results for Zn-doped magnetite show a remarkable consistency with the occurrence of the Verwey structure and its features even upon extreme oxidation. The sample should belong to the second-order transition regime according to Honig, but the structural transition is definitely present and consistent with the one of pure or less doped magnetite. It can thus be argued that the Verwey phase remains first order in the whole doping regime. However, the general trend towards loss of distortion already detected in the previous samples might provide a new systematic explanation for the change in transition temperature.

This will be discussed in the following subsection, providing a cross-comparison of all the relevant features of natural, off-stoichiometric and Zn-doped magnetite.

### 3.2.5. Cross-comparison

All the three samples analysed in this study and the pure magnetite of the Senn *et al*. study[26] show physical discontinuities upon cooling, and can be confidently placed on the correlation plot outlined by Honig [150] (Fig. 68).

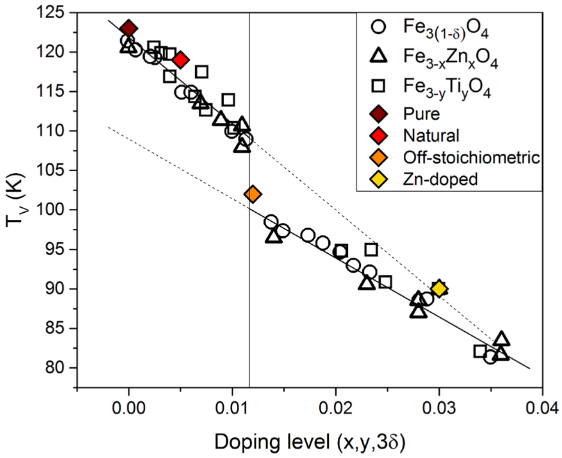


**Figure 68 –Honig's plot, with the four samples investigated in the course of this study added with coloured points. The black and white points, trend lines and discontinuity point are from Ref. 150.**

The structural transition is found in all the three doped samples. The microcrystal diffraction data can be consistently indexed with the monoclinic *Cc* supercell; no further symmetry reduction is observed. A plot of the cell parameters and β angle of the monoclinic cell as a function of doping is provided in Fig. 69. The monoclinic *b* parameter and β angle show a discontinuity around 1.1% doping; as detected in previous studies,[149 150] the monoclinic angle lowers and approaches an undistorted 90° value with the increasing level of doping; by contrast, *a* and *c* are mostly constant throughout the doping range. Overall, there is no systematic change of the cell volume (Table 8), which stays within a maximum of 4 Å$^3$ variation from that of the pure magnetite sample.

**Table 8 – Unit cell volumes for all the sample analysed, ordered by increasing level of doping.**

| | Pure | Natural | Off-stoichiometric | Zn-doped |
|---|---|---|---|---|
| *Volume (Å$^3$)* | 2363.18(2) | 2361.01(7) | 2368.06(7) | 2364.86(6) |

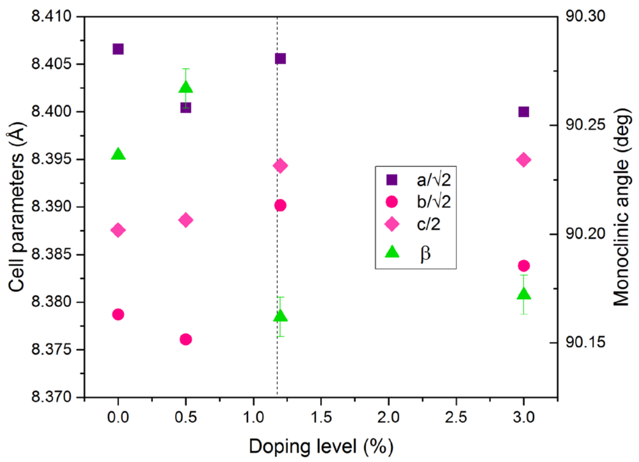


**Figure 69 – Monoclinic cell parameters (as *a*/√2, *b*/√2, *c*/2) and angle (β) as a function of doping percentage. The cell parameters scale with the left y-axis, whilst the angle scales with the y-right axis. The discontinuity line determined by Honig [150] is also plotted. Data for x = 0 are from Ref[141]. Errors are included in the pointers if not displayed.**

The main differences between these four structures is found in their distortion features. Computing the Q-modes for the first coordination shell of the 16 octahedral sites outlines a disorder rising incrementally with the level of doping. In the pure structure, with a 1:1 ratio of $Fe^{2+}$ and $Fe^{3+}$ in the octahedral position, the divalent sites are clearly characterised by both an expansion of the octahedra around the bigger cation and a marked Jahn-Teller distortion; the latter is increasingly lost and by 3% of doping one of the 2+-like sites (B42) assumes all the behaviours of a 3+ like iron atom. The plot of $Q_{JT}$ distortions is provided in Figure 70.

It can be noticed that this disorder effect does not influence all the sites equally, and some of the 2+-like sites maintain a consistent behaviour throughout the doping series. The 3+-like sites, conversely, show a tendency towards expansion, with $Q_{rad}$ increasing in the series.

Overall, the doping seems to reduce the distortion features and cluster all the 16 sites closer to a median point.

A full cross-over is only ever achieved by the B42 site in the zinc-doped magnetite, so for most sites it is still possible to assign a divalent or trivalent charge on the basis of a positive or negative $Q_{rad}$, often corroborated by the $Q_{JT}$ mode.

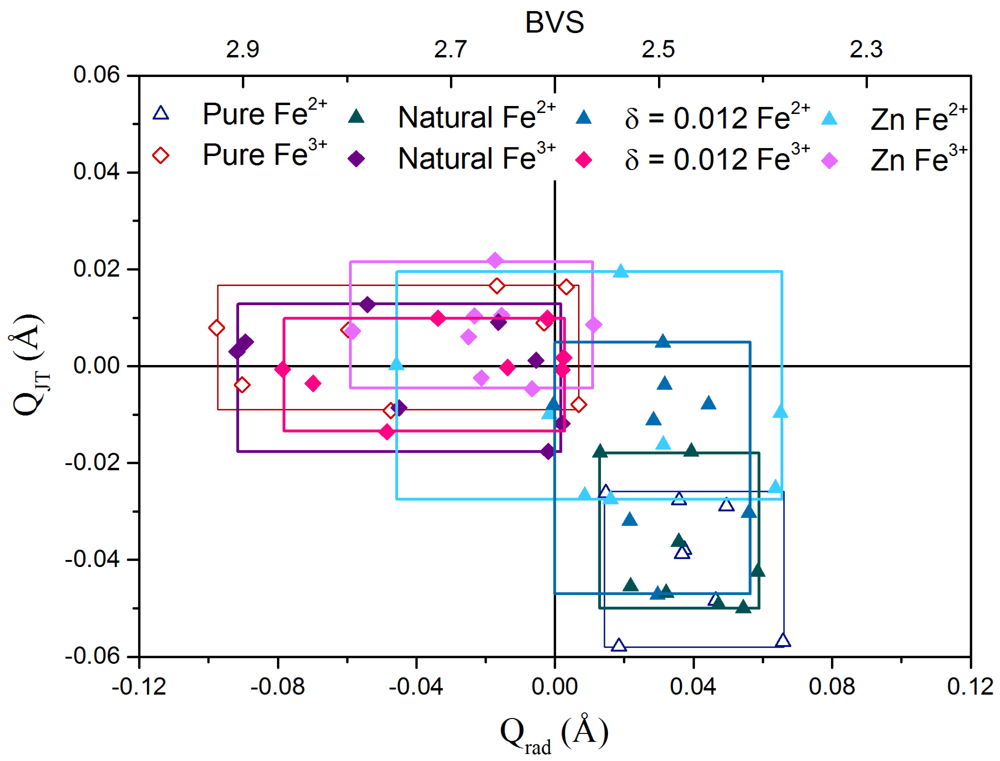


**Figure 70 – Distortion amplitudes of tetragonal Jahn–Teller ($Q_{JT}$) modes plotted against the radial breathing mode ($Q_{rad}$) for the 16 octahedral B sites. Data for all structures are displayed as per the legend. Regions where the 8 $Fe^{2+}$-like and 8 $Fe^{3+}$-like sites are located are shown as rectangles of matching colours, following the original assignation of sites. An approximate BVS scale is shown at the top of the plot.**

The BVS correlates strongly with $Q_{rad}$ and offers an additional criterion for site assignation. A list of the average BVS values for divalent- and trivalent-like sites in all the samples is listed in Table 9, keeping the site assignation of pure magnetite throughout the series. It has to be noted that in the Zn-doped magnetite sample $\langle BVS \rangle_{di}$ decreases to 2.51 when B42 is considered among trivalent-like sites; the latter, conversely, have an increased $\langle BVS \rangle_{tri}$ = 2.69. The magnitude of the changes do not hinder the general trend, so a consistent site assignation was preferred.

**Table 9 – Average BVS for $Fe^{2+}$-like and $Fe^{3+}$-like sites in the different structures, listed at increasing level of doping.**

| | PURE | NATURAL | OFF-STOICHIOMETRIC | Zn-DOPED |
|---|---|---|---|---|
| **$\langle BVS \rangle_{DI}$** | 2.47 | 2.48 | 2.49 | 2.54 |
| **$\langle BVS \rangle_{TRI}$** | 2.75 | 2.75 | 2.71 | 2.68 |

With rising oxidation, it can thus be concluded that the differentiation between charges in the 16 octahedral sites becomes less prominent, in what can be interpreted as a charge disorder effect.

Understanding how doping affects the charges can be aided by an analysis of the shift in BVS values in comparison with the pure model (Table 10). It is evident how not all the charges are influenced equally and there is no clear trend to correlate them throughout the doping series. Therefore, the average picture remains the most reliable, in keeping with the long-range average nature of a diffraction signal.

**Table 10 – Deviation of BVS from the Senn *et al.* model, computed as Δ = (pure) – (doped). Rows are colour coded to follow the original trivalent (orange) or divalent (blue) assignation. A negative value corresponds to oxidation, and a positive value corresponds to reduction.**

| Site | Natural | Off-stoichiometric | Zn-doped |
|---|---|---|---|
| **B1B1** | -0.01 | -0.01 | -0.03 |
| **B31** | -0.03 | 0.00 | -0.10 |
| **B32** | -0.03 | 0.02 | -0.02 |
| **B1A1** | 0.01 | 0.03 | 0.08 |
| **B1A2** | -0.00 | -0.04 | -0.13 |
| **B33** | 0.01 | 0.01 | 0.03 |
| **B41** | 0.01 | -0.05 | -0.10 |
| **B2A1** | 0.00 | 0.05 | 0.08 |
| **B34** | 0.01 | 0.04 | 0.12 |
| **B1B2** | -0.01 | -0.05 | -0.05 |
| **B43** | -0.01 | 0.08 | 0.26 |
| **B2B2** | 0.03 | 0.08 | 0.14 |
| **B44** | -0.03 | -0.03 | -0.01 |
| **B42** | 0.01 | 0.02 | -0.23 |
| **B2B1** | -0.02 | -0.02 | -0.07 |
| **B2A2** | -0.01 | 0.03 | 0.01 |

Apart from the B42 site in the Zn-doped magnetite, all the sites can be consistently assigned to either divalent or trivalent behaviour in consistency with the original Senn *et al.* model for pure magnetite. As such, for consistency and a more direct comparison, the site assignation was left invariant when analysing the second coordination shell of the $BO_6$ octahedra.

It can be noticed from the histograms of B-B distances (Fig. 46, 56, 64) that their distribution is becoming increasingly centred around zero, losing the characteristic tail of anomalously short distances. A normal distribution around zero without deviations would be expected for a randomly distributed structure with no orbital molecule formation. The average B-B distance remains mostly constant throughout the series, with no discernible trend (Table 11). This effect may be rationalised by considering that trimeron bonding and trimeron non-bonding distances have a negative correlation, with the former elongating while the latter shorten (Fig. 48, 58, 66).

**Table 11 – Average B-B distance in the different structures, listed at increasing level of doping.**

| | Pure | Natural | Off-stoichiometric | Zn-doped |
|---|---|---|---|---|
| *Average B-B distance (Å)* | 2.9674(8) | 2.9664(8) | 2.9691(8) | 2.9676(8) |

Trimerons are inherently asymmetric, reflecting the acentricity of the *Cc* monoclinic superstructure. As such, the elongation tends not to affect the two bond lengths in each orbital molecule evenly. When the total length of the delocalisation region is considered, however, all trimerons are elongated. With the exception of the trimeron bonding around B41, there is a consistent trend of elongation for every trimeron, with a stretching of the orbital molecule delocalisation region as a function of increased level of doping (Table 12).

**Table 12 – Variation of the trimeron distances around a given divalent sites. The original values from the Senn *et al.* model are provided (rounded up from uncertainty). The discrepancy is computed as Δ = (pure) – (doped). The ordering of the columns follows an increasing doping level and is colour-coded from red to yellow for the current study.**

| | Pure | | Natural | | Off-stoichiometric | | Zn-doped | |
|---|---|---|---|---|---|---|---|---|
| *Binding site* | *T1 (Å)* | *T2 (Å)* | *ΔT1 (Å)* | *ΔT2 (Å)* | *ΔT1 (Å)* | *ΔT2 (Å)* | *ΔT1 (Å)* | *ΔT2 (Å)* |
| ***B1B1*** | 2.848 | 2.832 | -0.006 | -0.001 | -0.023 | -0.017 | -0.084 | 0.007 |
| ***B1A1*** | 2.935 | 2.820 | 0.003 | -0.017 | -0.009 | -0.040 | -0.014 | -0.043 |
| ***B1A2*** | 2.914 | 2.853 | -0.013 | 0.004 | -0.027 | -0.032 | -0.035 | -0.039 |
| ***B41*** | 3.018 | 2.813 | 0.014 | -0.009 | 0.037 | -0.068 | 0.051 | -0.076 |
| ***B1B2*** | 3.012 | 2.821 | 0.001 | -0.011 | 0.015 | -0.050 | 0.058 | -0.123 |
| ***B44*** | 2.946 | 2.838 | -0.008 | 0.003 | -0.029 | 0.005 | -0.026 | -0.013 |
| ***B42*** | 2.947 | 2.837 | -0.002 | -0.001 | 0.012 | -0.059 | -0.038 | -0.108 |
| ***B2B1*** | 2.893 | 2.913 | 0.000 | -0.005 | -0.035 | -0.003 | -0.020 | -0.029 |

| | Pure | Natural | Off-stoichiometric | Zn-doped |
|---|---|---|---|---|
| *Binding site* | *$T_{tot}$ (Å)* | *$\Delta T_{tot}$ (Å)* | *$\Delta T_{tot}$ (Å)* | *$\Delta T_{tot}$ (Å)* |
| *B1B1* | 5.680(1) | -0.007 | -0.040 | -0.077 |
| *B1A1* | 5.755(1) | -0.014 | -0.049 | -0.056 |
| *B1A2* | 5.767(2) | -0.009 | -0.059 | -0.074 |
| *B41* | 5.831(2) | 0.005 | -0.030 | -0.024 |
| *B1B2* | 5.833(1) | -0.010 | -0.036 | -0.065 |
| *B44* | 5.784(2) | -0.005 | -0.024 | -0.039 |
| *B42* | 5.784(2) | -0.002 | -0.047 | -0.145 |
| *B2B1* | 5.806(2) | -0.005 | -0.038 | -0.049 |

## 3.2.6 Overall conclusions

In this section, the structural analysis of single crystal X-ray diffraction data for natural (0.05% doping), off-stoichiometric (1.2% doping) and Zn-doped (3% doping) magnetite samples was presented.

All these materials have a discontinuity in susceptibility upon cooling, with the Verwey transition shifting to lower temperatures with an increased level of doping ($T_{V,0.05}$ = 119 K, $T_{V,0.012}$ = 102 K, $T_{V,0.03}$ = 90 K). In contrast with the change of transition order proposed by Honig,[150] all the structures undergo a structural transition from cubic to monoclinic, and the ground state diffraction pattern can be consistently indexed and fitted with the established trimeron model. Consequently, it can be concluded that the Verwey transition remains first order throughout the range of doping investigated, with no evidence for further structural transitions. The variation of cell metrics reveals a discontinuity in *b* and β at doping ≥ 1%, but the overall cell volume remains almost constant.

An extensive analysis in comparison to the established model for pure stoichiometric magnetite, as reported by Senn *et al*.,[26] outlined an incremental loss of Jahn-Teller distortion features. This effect can be correlated to charge disorder, confirmed by the trends in BVS values. Overall, it is still possible to assign 8 trivalent and 8 divalent sites, with the exception of a single iron site (B42) in the 3% Zn-doped magnetite. This can be interpreted as a targeted oxidation arising from the charge compensation of Zn insertion in the tetrahedral sites.

Orbital molecules are still present in all the samples, with the same highly interconnected features as found in pure $Fe_3O_4$. The loss of a divalent site in the Zn-doped magnetite corresponds to the loss of the only “odd” trimeron, disrupting a $Fe^{2+}$-$Fe^{2+}$-$Fe^{3+}$ arrangement.

Therefore, the ground state of magnetite can be considered fundamentally unvaried, and remarkably robust to chemical defects of various nature.

The lowering of the transition temperature can be cross-correlated with the average elongation of the total trimeron delocalisation region throughout the series.

Trimerons lock into position and become a delocalisation region for the minority spin electron of $Fe^{2+}$ when the distortions freeze enough to allow orbital interaction between

the B sites. Since the increased level of doping causes the distortion features to decrease, particularly the Jahn-Teller compression of the divalent iron atoms, the phonon energy loss needs to be more substantial in order for the atoms to interact.
The general charge disorder, lowering the net difference between divalent-like and trivalent-like sites, lowers the electron density shared among the three sites. Trimerons in doped magnetite can thus be considered less strongly bound, but their formation remains the driving force of the Verwey transition.

Consequently, the suppression of the Verwey transition a > 4% level of doping, reported by Honig[150] and not investigated in the current work, might be interpreted as the level of doping at which the distortion features of the structure and related distinction between divalent and trivalent sites corresponds to a lack of orbital molecule bonding. The structure may thus remain undistorted, and no discontinuity in physical features arising from the confinement of the minority spin electron is to be expected.
Even in lack of a change from first to second order behaviour of the transition, the 1% doping point might correlate to changes in transition behaviour from the point of view of the loss of distortion features and increase in charge disorder. The lack of samples in the 1-4% doping region, however, prevents the formulation of a definite answer for this slight discontinuity.

# 3.3 Pair Distribution Function Analysis

## 3.3.1. Introduction

Magnetite, as the original magnetic material, has been extensively characterised using a variety of techniques in its high temperature phase. Even before an unconstrained model for the ground state of $Fe_3O_4$ was disclosed, some of these results had been interpreted as a possible persistence of ordering above $T_V$. Optical conductivity spectra show a clear opening of a charge gap below $T_V$ that evolves into a pseudo-gap between 125 and 300 K.[157] Additionally, critical diffuse neutron scattering was reported over a broad region in reciprocal space, decreasing as a function of temperature below 200 K and disappearing abruptly at $T_V$. [158]

Following the report on the Verwey structure of magnetite, lattice dynamics studies reported a strong electron-phonon coupling and an anomalous phonon broadening between $125 < T < 293$ K, interpreted as charge-orbital fluctuations above $T_V$; [159] hard X-ray photoelectron spectroscopy (PES) shows finite density of states at the Fermi energy for the polaronic half-metal, with remnant order at $T < 300$ K and a clear gap formation below $T_V$.[160] The only study to date that explores the region above room temperature is resonant inelastic X-ray scattering on the magnetic excitations of iron: these excitations, driven by polaronic distortions, persist in the cubic structure up to T = 550 K, albeit decreasing gradually above T = 350 K.[161]

Most of the structural studies performed over a wide range of temperatures have a geological focus, and as such were performed on natural samples. Two reports from neutron[162] and X-ray diffraction,[163] performed on mineral magnetite, offer an excellent track of the thermal evolution of the spinel structure to temperatures above $T_C$ = 858 K, but do not report evidence of any structural distortions.

A recent work by Bosak *et al.* on the diffuse scattering shows that the Bragg intensities and superstructure peaks of the *Cc* superstructure model blur into diffuse scattering features, texturing around specific reflections at T = 126.5 K; the intensity of diffuse scattering decreases upon raising temperature, but it is still present at T = 300 K. The study was performed with synchrotron X-ray diffraction on highly stoichiometric sample of $Fe_3O_4$, carefully synthesised and treated to obtain a 50 µm single crystal with purified surface in order to be comparable to the Senn *et al.* study.[26] From a qualitative point of view, evidence of diffuse squares around the spinel reflections and diffuse arcs to replace the superstructure spot chains are a signal of retention of ordering on the short range (Fig. 71). This is interpreted as a persistence of the low-T structure above $T_V$, even though the transition point is marked by a loss in commensurability of the diffraction. The characteristic length of correlation is estimated to be around 2 unit cells at $T_V$ + 2.5 K and just a little larger than 1 unit cell at room temperature; presence of trimerons on a local scale in an overall metrically cubic phase is proposed, with a correlation length of ~ 1.5 nm above $T_V$. Although Bosak *et al.* also attempted some *ab initio* calculations to verify this qualitative analysis, a full solution of the local ordering was not achievable with single crystal diffuse scattering, especially because the dataset has a roughly 8 twin components that would heavily hinder any detailed and quantitative analysis.[164]

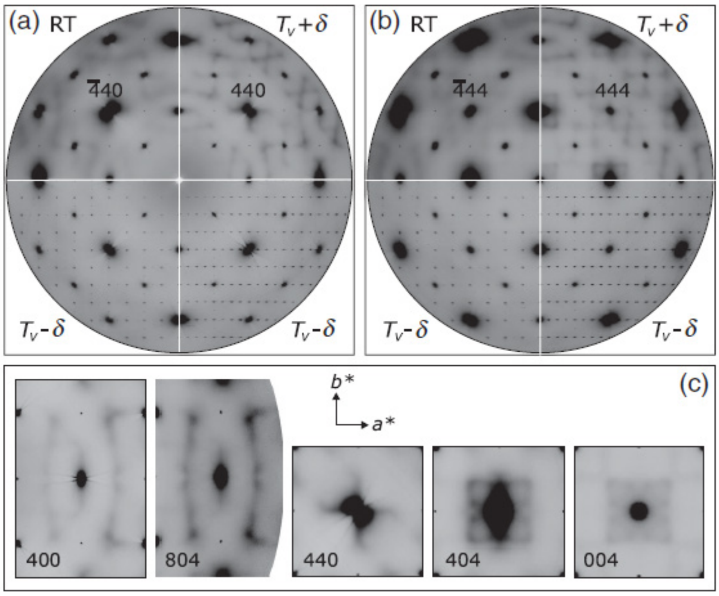


**Figure 71 – Evolution of the scattering from below to above the Verwey transition temperature, from Ref[162]. Figure a) shows a cut through the hk0 plane, b) shows a cut through the hk4 plane. Additionally, some cuts on specific reflections of interest, showing the texturing of diffuse scattering above $T_V$, are displayed.**

Conventionally, orbital molecule states are treated as the consequence of a structural distortion that arises in the crystal, driven by phonon freezing. Above the transition temperature, thermal vibrations usually disrupt the interaction and cause the disappearance of metal-metal clusters. [165] [166] However, recent findings in $LiRh_2O_4$ [167], $Li_2RuO_3$, [168] $AlV_2O_4$ [52] and $GaV_2O_4$ [53] reported persistence of orbital molecules up to temperatures that can be more than double the ordering onset temperature. In these cases, interactions transition from long-range to short-range ordering regimes; whilst the average structure by conventional diffraction analysis might look undistorted and appear to lack ordering, Pair Distribution Function (PDF) analysis has proven effective to detect the persistence of local distortions. Moreover, this technique uses powder scattering data, it is inherently unaffected to the twinning effects that can hinder single crystal studies.

From the concurring evidence above, it is possible to suggest that the local arrangement of B-B irons persists well above the Verwey temperature, up to at least 550 K. Given the complexity of the trimeron ordering, a study on the evolution of the structure up to the paramagnetic regime, above $T_C$ = 858 K, is of interest. No comprehensive PDF study has been reported for magnetite, but preliminary unpublished studies by Dr Simon Kimber, currently instrument scientist at Oak Ridge National Laboratory, showed no clear splitting of the octahedral iron-iron distances upon ordering, as in the case of $AlV_2O_4$ [52] and $GaV_2O_4$,[53] but rather a broadening.

To account for these complexities, a full experiment was performed over a large temperature span (90 to 923 K) to cover regions below the Verwey transition, in the nominally cubic phase, and above the Curie paramagnetic transition of magnetite.

### 3.3.2. Data collection and processing

The data were collected at the ID11 beamline at ESRF, Grenoble, with a wavelength of ~ 0.15815 Å. The 2D FReLoN camera detector was aligned prior to the experiment in order to access the largest region of Q-space available and collect very high angle diffraction. The instrument was set in spinning capillary mode to minimise powder orientation effects.
The large temperature range for the experiment could only be covered with the use of two sample environments: a nitrogen cryostream (90 K < T < 400 K) and a hot air blower (498 K < T < 930 K).
The sample used was the same $Fe_3O_4$ analysed in the Senn *et al.* paper.[26] A very highly stoichiometric (δ < 0.0001) single crystal provided by Honig was ground and sieved to

obtain a fine powder with granularity lower than 20 µm. In air and oxidising environments, magnetite is sensitive to oxidation towards maghemite; to avoid sample reaction during the high-temperature segment of the experiment, a 0.5 mm quartz capillary was loaded in a glovebag under Ar atmosphere and sealed with high temperature cement.

The data were collected in accumulation mode, in which every temperature was collected for 10 minutes in 10 s exposures and merged in a single file.
In the low-temperature segment, data were collected between 90 and 400 K with 10 K spacing. In the high-temperature segment, data were collected between 498 and 848 K with 50 K spacing, plus one last dataset at 923 K. In both cases, the temperature was stabilised for 10 minutes before starting the data collection.

Due to the requirements of a PDF experiment, diffraction from an empty quartz capillary, silicon and ceria were collected before the dataset of interest.
The empty 0.5 mm quartz capillary will contribute to the diffuse scattering throughout the whole experiment, so it needs to be carefully accounted for in the data processing. The empty background was collected at 90, 200, 473, 573, 673, 773 and 873 K.
The diffraction pattern of a silicon standard is collected to generate the instrument configuration and provide a guide for the masking of dead pixels, determining detector aberrations, calibration of the sample-detector distance, and computation of the experimental wavelength; these parameters will be part of the instrument configuration (.poni file) necessary to integrate the diffraction rings. Ceria is used as a standard with very precise cell parameters and well-known crystal structure: its diffraction can not only provide an additional calibration for the wavelength but its PDF can also be used to refine the instrumental PDF fitting parameters $Q_{broad}$ and $Q_{damp}$ (Q-dependent, detector-related parameters, as discussed in Section 2).

The azimuthal integration of diffraction rings was performed with the pyFAI software.[169]
The instrumental setting for the cryostream dataset was first generated at 90 K, but movements of the detector throughout the data collection required the generation of a separate instrument model for every frame. The procedure of recalibration was aided by Dr Jon Wright. The high temperature dataset did not suffer from these aberrations, but in order to allow for the change in sample environment the detector position had to be moved; this dataset thus has a different instrument model again.

The 130 K pattern was used as an internal standard for the wavelength. Keeping the cell parameters and structural model fixed to the highly accurate values of previous studies,[11,12] the wavelength was refined to $\lambda = 0.156720(1)$ Å for the low temperature dataset. This value is considered as the real value of the wavelength and will be used in all the data processing of the low-temperature dataset. The high temperature dataset was refined to scale with the low-temperature one, and the derived wavelength used for the processing is $\lambda = 0.156582(1)$ Å.

The integrated datasets, in 2theta vs intensity format, were Fourier-transformed to PDFs with the PDFgetX3 program.[170] For each pattern, the background used was the one measured at the temperature close to the experimental one, and scaled appropriately. The Fourier transform was computed between $Q_{min} = 1.85$ Å$^{-1}$ and $Q_{max} = 21$ Å$^{-1}$, with an *r*-grid between 0 and 30 Å in 0.1 Å spacing. The computing parameters were set as $Q_{maxinst} = 21$ Å$^{-1}$ and $r_{poly} = 1.6$ Å. These parameters were optimised to minimise the influence of the truncation ripples without affecting the shape or quality of the PDF profile.

The ceria dataset was Fourier transformed with $Q_{min} = 1.52$ Å$^{-1}$ and $Q_{max} = 20$ Å$^{-1}$, with an *r*-grid between 0 and 30 Å in 0.1 Å spacing. The computing parameters were set as $Q_{maxinst} = 20$ Å and $r_{poly} = 0.7$ Å.
The PDF obtained from this standard sample was refined to determine the instrumental broadening, resulting in $Q_{damp} = 0.0475(4)$ Å$^{-1}$ and $Q_{broad} = 0.0186(3)$ Å$^{-1}$. These parameters were used for the magnetite PDF fit and kept fixed without refinement for all measured temperatures, as they are assumed to be instrument-dependent and not sample-dependent.

### 3.3.3. Data analysis

In accordance with the preliminary dataset collected by Dr Simon Kimber, the low-temperature structural transition in magnetite is not accompanied by a prominent change in the *r*-distribution. The cooperative distortions that drive the Verwey transition from cubic to monoclinic involve subtle changes of both Fe-O and Fe-Fe bonds throughout the structure. As seen in the previous section, the distortions have a maximum magnitude of ~0.2 Å, and only on certain atomic sites; therefore, there is no substantial variation of the

PDF pattern going from the cubic to the monoclinic structures. The difference is more subtly outlined by a change in shape of the first and second G(*r*) peaks below $T_V$, but the rest of the temperature range does not show significant changes (Fig. 72).

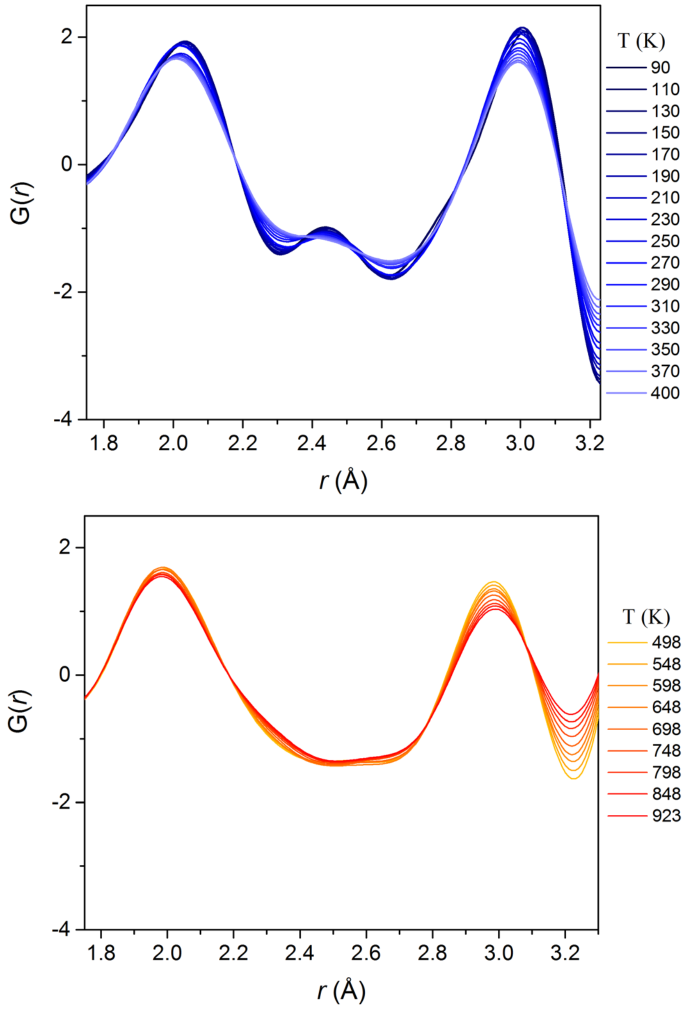


**Figure 72 –PDFs at multiple temperatures, displayed in the region of the first and second coordination shells (Fe-O, ~2 Å, and octahedral Fe-Fe, ~3 Å). The peak at ~2.4 Å is a termination ripple. Temperatures are colour coded as per the legend (cryostat dataset: top, hot-air blower dataset: bottom). Most patterns outline the region of temperatures with short-range ordered orbital molecules, and as such they predictably do not show any sharp variation in features, apart from thermal smoothing of the functions. The slight jump in intensities in the cryostat dataset is centred around 270 K, and can thus be ascribed to ice crystallites from the sample environment melting.**

Fits of both the cubic and the monoclinic structures to the 90 K data are qualitatively similar, but the computed goodness of the fit is improved by using a distorted monoclinic structure (Fig. 73). With this model, which has 96 atomic positions with limited symmetry constraints, it is impossible to perform a free refinement of the *xyz* coordinates of all atoms, since a PDF does not have the same amount of information as a single crystal diffraction pattern.

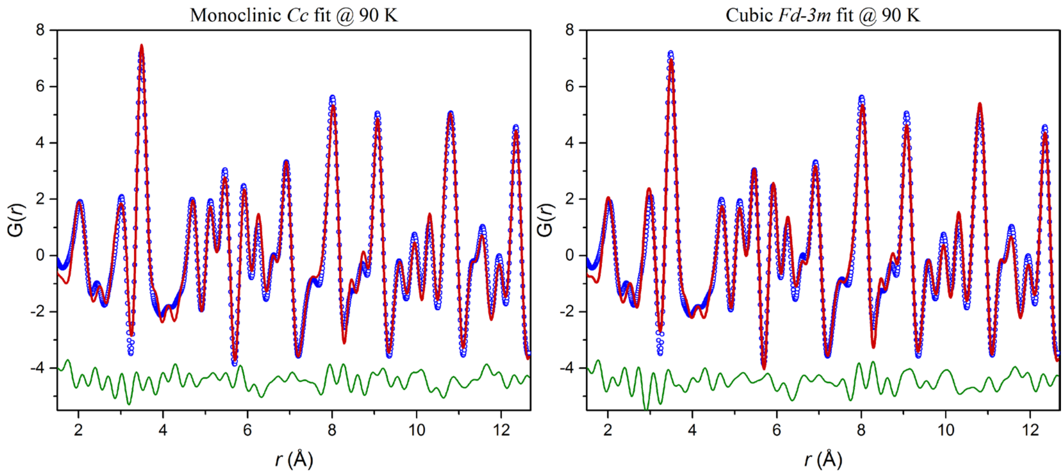


**Figure 73 – Comparison of fits to the 90K PDF of magnetite using fully distorted monoclinic (left) and undistorted cubic (right) models; experimental data are in open blue circles, fits are in red and difference curves are in green. Fits are visually similar and of comparable quality overall, but the goodness of fit ($Rw_{monoclinic}$ = 13.67% vs $Rw_{cubic}$ = 14.73%) highlights the distorted structure as better description.**

To estimate the evolution of distortion features as a function of temperature, a series of structural models were generated.
The high-resolution cubic model at 130 K from Wright *et al.*[139,140] was used as a reference cubic spinel; the refined structure has *a* = 8.38758(1) Å and $O_{xyz}$ = 0.25490(5). The VESTA software[171] was used to generate a supercell of the cubic structure, with cell metric *a* = *b* = 11.86182(3) Å, *c* = 16.77515(1) Å and all angles 90°, with the same atomic positions that a monoclinic *Cc* supercell would have, if not distorted.

The high-resolution monoclinic *Cc* superstructure, as reported by Senn *et al.*,[26] was first shifted to a metrically cubic unit cell (*a* = 11.8888(3) Å, *b* = 11.84940(3) Å, *c* = 16.77515(1) Å, *β* = 90.2363(2) ° → *a* = *b* = 11.86182(3) Å, *c* = 16.77515(1) Å, β = 90°). In order to have perfectly equivalent positions from one model to another, the two structures were run through the IsoDistort software[172], using the cubic structure as a parent and the monoclinic structure as the distorted ground state; it was then possible to obtain a structure with equivalent listing of symmetry positions, but with coordinates modified as an effect of the distortion. The final cell metric used was the cubic equivalent of the Senn *et al*. model.
The magnitude of the shift in position from one model to another can be calculated as $p_c$ −

$p_m$ for every coordinate $p$. A series of intermediate structural models were generated following:

$$p_i = p_c + x_V \cdot (p_c - p_m)$$

In this approach, $x_V = 0$ is the cubic spinel and $x_V = 1$ is the established monoclinic model. Models with $x_V = 0.2, 0.4, 0.6, 0.8, 1.2$ were also generated, to test intermediate distortions, and are fully listed in Appendix A4.

Each of the $x_V$ models were refined in PDFgui [173] over a distance range between 1.5 and 12.66 Å, including simulation of termination ripples. Refined parameters in the fits were: the cell parameters (following the $\sqrt{2}a_c\ \sqrt{2}a_c\ 2a_c$ constraint of the monoclinic supercell in comparison to the cubic cell), isotropic thermal parameters (refined separately for O sites, Fe B-sites, and Fe A-sites), and the $\delta_1$ shape parameter. Refinements were performed sequentially as a function of temperature, using the converged fitting model of the $T_{n-1}$ PDF as a starting configuration to fit the PDF at $T_n$. The refinement outputs for every $x_V$ model as a function of temperature are reported in the Appendix section.

For every temperature, the plot of $R_w$ as a function of $x_V$ shift was fitted with a mixed polynomial and exponential curve (Fig. 74), with A, B, C and D as refined parameters computed in OriginLab[174]:

$$(A \cdot {x_V}^2 + B \cdot x_V + C) \cdot \exp(D \cdot x_V)$$

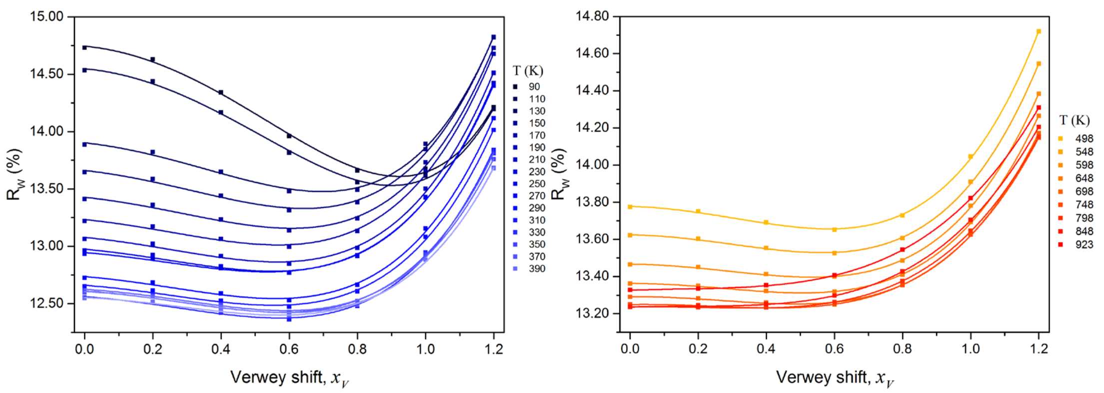


**Figure 74 – Goodness of fits for the different PDFs, expressed as $R_w$, as a function of Verwey shift $x_V$, for multiple temperature refinements (cryostat dataset: left, hot-air blower dataset: right). The temperatures are colour coded and indicated by the legends. Data points are the experimental outcome of PDFgui, the fitting line is obtained as indicated in the text**

This fitting procedure allows the $x_V$ at which the minimum $R_w$ is found to be extracted for each temperature step. In order to determine accurate values of the cell parameters, thermal parameters, and atomic displacement, a weighted average procedure was performed with a purpose-written Python program, so that as, for example, the parameters for the structure with $x_{V,\,min}$ = 0.9 are a weighted average of the fit outcomes from $x_V$ = 1 and $x_V$ = 0.8. The table of weighted average results as a function of temperature, and related minimum-$R_w$ $x_V$ are available in Appendix A4.

### 3.3.4. Results and discussion

The minimisation procedure and subsequent weighted averaging of the results outline a consistent trend for the cell parameters and thermal parameters of magnetite as a function of temperature (Fig. 75). There is no prominent discontinuity in the data: the cell parameters vary around $T_V$, as expected from the phase transition, and then have a small increase above 300 K, which can be ascribed to the change from cooling to heating in the cryostream sample environment. Thermal parameters linearly increase with temperature, and the small discontinuity in the oxygen $U_{ISO}$ is likely due to the change of sample environment as there are no other discontinuities.

The thermal variation of the $x_V$ at which the minimum $R_w$ is found highlights an interesting feature of local ordering in the sample: even though the fully monoclinic structure ($x_V$ = 1, long-range distorted) is the best model only under $T_V$ = 123 K, the cubic model ($x_V$ = 0, long-range disordered) represents the minimum only at temperatures around the Curie temperature (T ≥ 858 K); PDFs at temperatures between 150 and 700 K are better fit by partially distorted models with $x_V$ ~ 0.6 and as $T_C$ is approached critical behaviour of the minimum-$R_w$ $x_V$ is observed (Fig. 76).

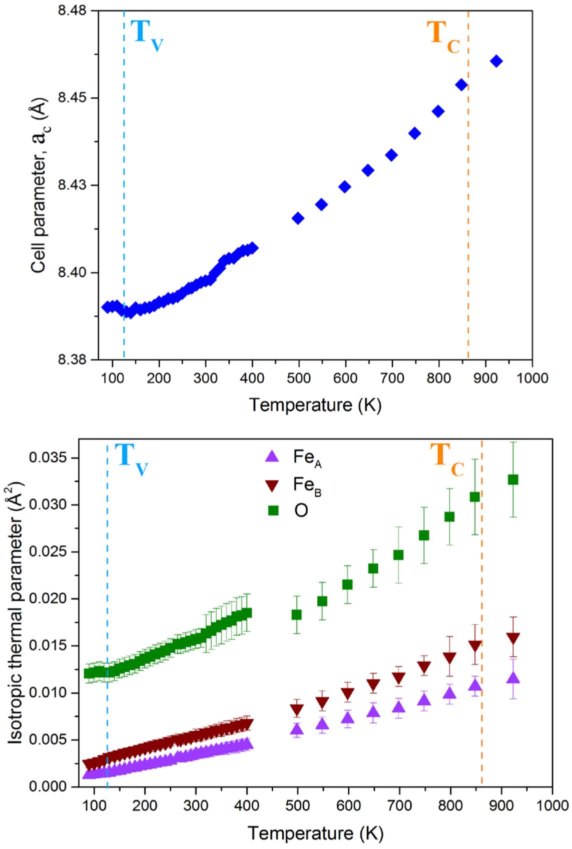


**Figure 75 – Cell parameters expressed as the cubic metric (top) and isotropic thermal parameters (bottom), as a function of temperature. The data are extracted from the $x_V$ fit as the weighted average for the minimum-$R_w$ $x_V$ shift at a given temperature. The Verwey transition temperature ($T_V$ ~ 125 K) and the Curie temperature ($T_C$ ~ 860 K) are marked with dashed lines. Errors bars are included when not within the data point.**

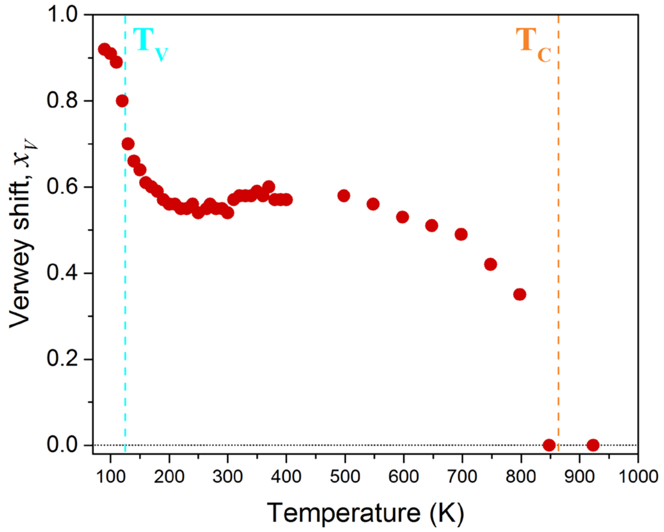


**Figure 76 – Temperature evolution of the derived Verwey shift that gives the best fit to the PDF data. It is evident that the fully monoclinic structure is only the minimum point below $T_V$ = 125 K. From T = 150 K to T = 700 K the shift is approximately $x_V$ ~ 0.6. The fits that give an undistorted cubic structure ($x_V$ = 0) are around the Curie point at which ferrimagnetic order onsets. All values have an approximate error of ~ 0.05.**

As seen above for the 90 K data, fits are comparable from a qualitative point of view; the only slight difference that is evident to the eye is the effect of the shift on the model to the fitting of the second peak, corresponding to octahedral B-B distances. However, the $R_w$ values are still different enough to allow a computation of the minimum point, as outlined in the previous section, and make one model better than the others (Fig. 77).

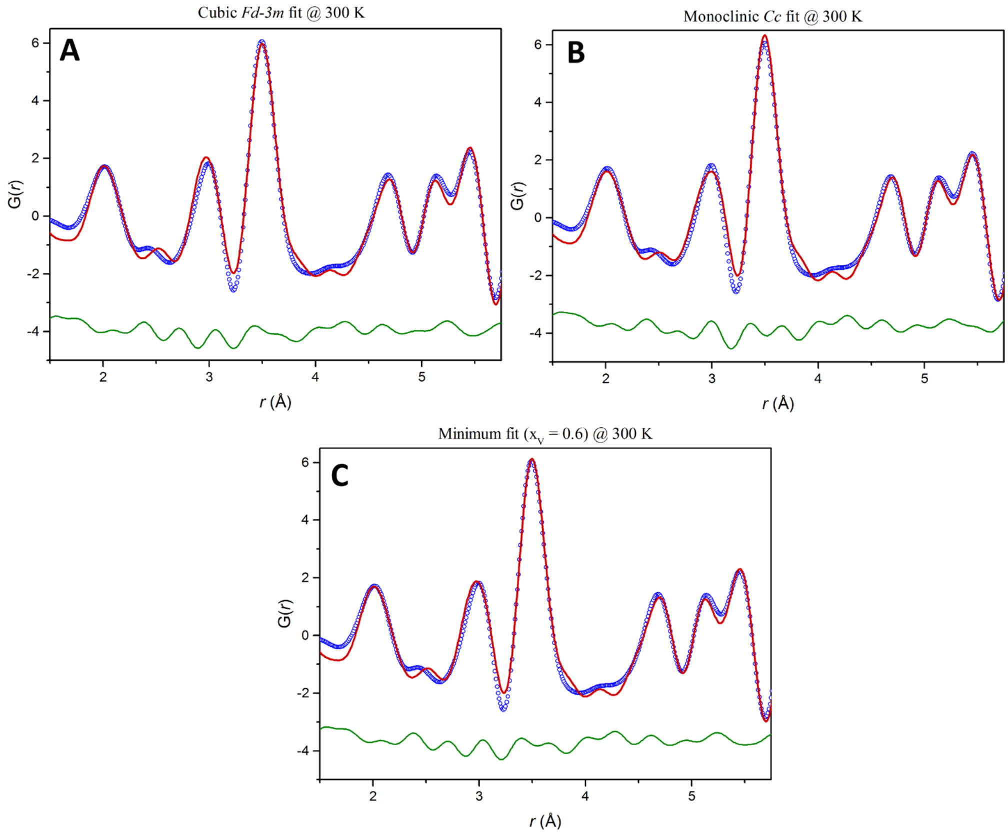


**Figure 77 – Comparison of fits to the 300 K PDF using undistorted cubic ($x_V$ = 0, A), fully distorted monoclinic ($x_V$ = 1, B), and partially distorted cubic ($x_V$ = 0.6, C). Experimental data are in open blue circles, fits are in red and difference curves are in green. The calculated minimum for this temperature is $x_{V,\,min}$ = 0.54. Fits are of comparable quality overall, but the peak at r ~ 3 Å, representing B-B distances, is overfitted, underfitted, and reasonably fitted in sequence. A comparison of the goodness of the fit sees $Rw_{monoclinic}$ = 13.90%, $Rw_{06}$ = 12.36%, $Rw_{cubic}$ = 12.54%, so the $x_V$ = 0.6 is a better model for the structure at 300 K.**

This structural evidence points towards a $Fe_3O_4$ system where, even above the Verwey temperature, $Fe^{3+}$-$Fe^{2+}$-$Fe^{3+}$ clusters persist through local interactions. The effect of the temperature is to increase the length of correlations up to their complete decoupling. This effect can be demonstrated by comparing the atomic displacements induced by thermal vibrations and the structural displacements associated with the minimum-$R_W$ $x_V$ model at any given temperature: at the Verwey transition, the atomic displacement overcomes the thermal vibration for both the tetrahedral and octahedral Fe sites, and the structure becomes long-range distorted as an effect of phonon freezing (Fig. 78).

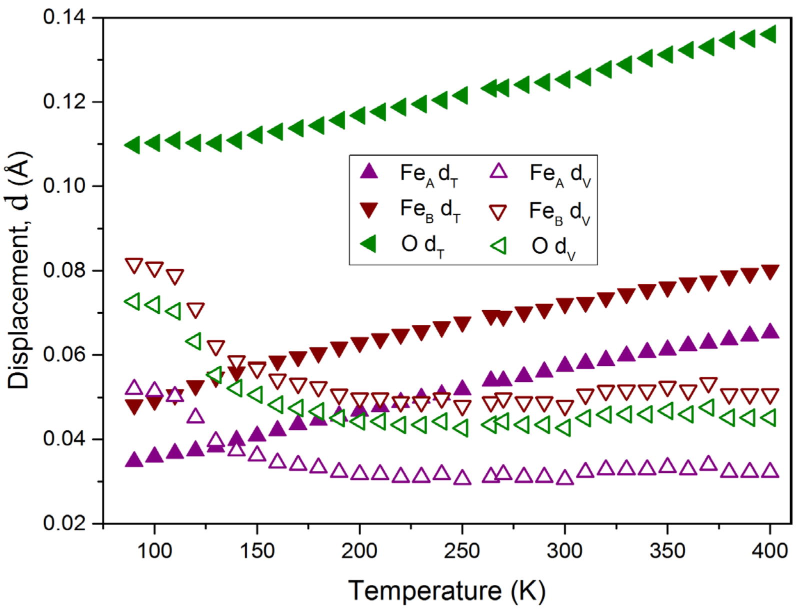


**Figure 78 – Atomic displacement from the structure ($d_V = x_{V,min} \cdot (p_c - p_m)$) and from thermal vibrations ($d_T = \sqrt{U_{ISO}}$) as a function of temperature, using the weight-averaged value corresponding to the minimum shift obtained from the fitting. Thermal vibrations dominate the displacement of the atoms down to $T_V$ = 125 K, when the structural displacements become more significant; this temperature corresponds to the appearance of long-range ordered features and above it the clustering of B sites in orbital molecules is to be considered only on a local scale.**

## 3.3.5. Conclusions

The PDF analysis of perfectly stoichiometric magnetite over a large temperature region offered proofs on the persistence and evolution of orbital molecule distortions above their long-range ordering transition.

Approximating the monoclinic structure model as a metrically cubic cell and computing models with shifted atomic positions successfully overcame the limitation of normal refinement procedures given by the resolution of the technique. For most of the temperature range ($200 < T < 700$ K) the best fit is obtained for a model that has atomic positions shifted by ~55% from the undistorted spinel structure; a full distortion is only found in the ground state, below the Verwey temperature, and complete loss of order is only achieved above the Curie Temperature.

Therefore, it can be concluded that trimerons are still present on the local scale in magnetite above $T_V$, albeit with reduced distortion than the one associated with full electronic delocalisation and ordered polaron formation. As such, the material can be electrically conductive, because the time scale and strength of these correlations is smaller than vibrations imposed by thermal energy. The Verwey temperature can thus be defined as the temperature where the thermal displacement of the atoms is taken over by the charge, orbital and spin interactions, making the distortion displacement more prominent. On a local scale, the trimeron interactions persist up to the complete decoupling of spin ordering above the ferrimagnetic to paramagnetic transition point at $T_C$. The results are in good agreement with the previous results detailed in the literature and provide a structural explanation for several of the anomalies detected in magnetite.

The persistence of orbital molecules on the short-range scale is consistent with the behaviour of orbital molecules in other spinels, such as $AlV_2O_4$ [52] and $GaV_2O_4$.[53] Being able to associate the paramagnetic Curie temperature with the onset of complete loss of structural order in magnetite successfully shows these orbital molecules to be the result of coupling charge, orbital and spin degrees of freedom, as the local disorder does not disappear completely until the spins decouple.

The experimental data were acquired with the help of Dr Simon Kimber and processed with the help of Dr Jon Wright. The analysis and interpretation of data was supported by Prof J. Paul Attfield.

# 4. UNCONVENTIONAL MAGNETISM IN Fe(II) SPINELS

## *4.1 Introduction*

Among iron-containing minerals, $Fe_3O_4$ is the only naturally occurring spinel of mixed valence; however, provided that the right charge and relative cation ratio requirements are met, other compositions can crystallise in the spinel structure in a variety of conditions.[12] A particularly interesting case is the situation in which divalent iron with marked preference for octahedral coordination is paired with a tetravalent cation, commonly from the *p*-block of the periodic table, in the tetrahedral site. In contrast with magnetite, these materials lack charge degree of freedom, but retain spin and orbital degrees of freedom associated with the presence of $Fe^{2+}$ as the only *d*-block element. In particular, the B-sites of a spinel structure outline a uniformly frustrated lattice where all the nearest neighbour interactions are equivalent; therefore, these systems can be magnetically frustrated and are susceptible to peculiar magnetic ordering and correlations (e.g. quantum spin liquid states, monopole excitations in spin ices, as introduced in Chapter 2). [175]

The two systems investigated in this Section are $Fe_2GeO_4$ and the high-pressure polymorph $\gamma$-$Fe_2SiO_4$. Both are naturally occurring and their physical properties have been studied, primarily with a focus on geologically relevant features; however, since geology deals with properties and mechanisms at either ambient or high-pressure/high-temperature conditions, literature reports show little details on their low-temperature behaviours.

$Fe_2GeO_4$ occurs in spinel form at ambient condition and it also has the mineral name of Brunogeierite. In nanoparticle form, it has been investigated for its possible storage capability when embedded on graphene; [176] [177] no other prominent application has been proposed for it, since at ambient conditions the compound is paramagnetic and has a low conductivity. [178]

Prior to this investigation, there was no consistent report of its low-temperature structural and magnetic behaviour. While susceptibility measurements have shown that this compound has an ordering at $T < 10$ K, possibly antiferromagnetic in nature, a complete model of the magnetic structure has not been reported.[179] [180] Two preliminary reports on the subject have widely diverging results. According to single crystal and powder investigations of Chaix *et al.*, the structure has two sequential transitions with one incommensurate and one commensurate propagation vector at $T < 9$ K, but a full magnetic structure solution was never published.[181] Zou *et al*., conversely, claim that the structure is a spin-glass with some possible field-induced magnetic ordering, shifting the onset to $T < 21$ K.[182]

Neither of these studies refers to structural distortion, which is the preferred method for the release of frustration in transition metal pyrochlores. It is interesting to note that, by contrast, a structural transition upon antiferromagnetic ordering is evident for $Co_2GeO_4$ and there is evidence of reduction of symmetry from peak broadening in the diffraction pattern of $Ni_2GeO_4$. However, there are no conclusive data on $Fe_2GeO_4$ and no further studies are available.[183]

In the case of $Fe_2SiO_4$, the geological prominence represents the key role of this material: the high-pressure spinel form (γ), in solid solution with $Mg_2SiO_4$, has the generic mineral name of Ringwoodite and is the main constituent of Earth's mantle; the low-pressure polymorph (α) is known as Fayalite and is a widely abundant silicate even on the Earth's crust. [184]

There are extensive studies on the high-pressure and high-temperature behaviour of this material, using a variety of techniques and mostly focusing on assessing structural tensile properties, wave propagation and the existence of even higher-pressure polymorphs. While these studies are of high relevance in order to reach scientifically sound conclusions on the composition of the inner layers of the Earth, they give little account of the ground state of the material. [185] [186] [187] [188]

Early reports mark the presence of an antiferromagnetic transitions at $T = 11$ K, which was more recently confirmed through heat capacity measurements by Yong *et al.*[179] [189] The assumption of antiferromagnetic order is based on the behaviour of the susceptibility curve, and in light of this suggestion some DFT calculations on the system concluded that the ground-state is most likely to be a distorted tetragonal structure in which the frustration of the pyrochlore lattice of $Fe^{2+}$ in antiferromagnetic arrangement is released through distortion. However, there are no reported neutron studies on this structure. [190]

The ground states of $Fe_2GeO_4$ and γ-$Fe_2SiO_4$ were characterised through neutron powder diffraction, magnetisation (AC and DC), and heat capacity measurements. Both materials have been synthesised from precursor powders in the laboratory.
The complete report of the results will be the subject of the next two subsections and an attempt to systematise the findings will be provided in the conclusions of the chapter.

# *4.2 $Fe_2GeO_4$*

## 4.2.1. Synthesis and preliminary characterisation

$Fe_2GeO_4$ was synthesised as a polycrystalline powder by grinding stoichiometric quantities of Fe (-22 mesh, 99.998%, Alfa Aesar), $GeO_2$ (99.999% Alfa Aesar), and $Fe_2O_3$ (99.999% Sigma Aldrich) powders and pressing them into a pellet.
In order to ensure the correct oxidation state of iron, the reaction was carried out in evacuated silica tubes, heating in a box furnace at 900°C for 60 hr, then slow-cooling for 12 hrs. A single iteration of this process is sufficient to successfully transform the raw mixture, vaguely pink in colour due to the effect of the red $Fe_2O_3$ and the white $GeO_2$, into the black spinel form. However, it is necessary to note that the same stoichiometric ratio and conditions can also synthesise $FeGeO_3$, with equivalent oxidation states of the elements involved, as an impurity.

$FeGeO_3$ is well known in the literature for its high-pressure post-perovskite polymorph, but it is also reported that the ambient pressure monoclinic *C2/c* structure has two magnetic ordering transitions ($T_1 \approx 50$ K, $T_2 \approx 14$ K) and a bulk magnetisation signal dominated by ferromagnetic coupling. [191] [192] Although literature reports claim the same starting materials and formation environment for both compounds, no note has been made on the necessity to tune the conditions to obtain a single product. Experimental evidence acquired in the course of this work, however, suggests that within a pelleted sample any loose powder in the sealed tube and the surface of the pellet will be converted into $FeGeO_3$, whereas the inner part of the pellet will be consistently composed of pure $Fe_2GeO_4$. With some careful manipulation of the product it is possible to separate the former from the latter: the bright orange colour of $FeGeO_3$ makes it clearly distinguishable from the black $Fe_2GeO_4$. Detecting a monoclinic by-product in a mainly cubic powder sample can be challenging with laboratory X-ray diffraction, but the sensitivity of the SQUID allows the presence of $FeGeO_3$ to be ascertained through the divergence of the ZFC-FC curve. An example of $Fe_2GeO_4$ and $FeGeO_3$ susceptibility is provided in Fig. 79.

These criteria allowed to optimise the synthesis procedure and obtain 3.5 g of pure $Fe_2GeO_4$ to be carried forward for a complete physical characterisation and structural studies.

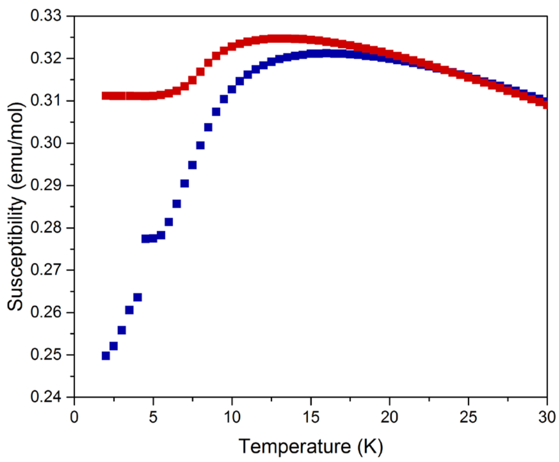


**Figure 79 – Molar susceptibility as a function of temperature for a sample of $Fe_2GeO_4$ with $FeGeO_3$ impurities. The diffraction pattern of this sample can be fitted to a cubic spinel with no discernible impurity but the magnetic behaviour has a clear signature compatible with the one reported by Redhammer *et al*. for $FeGeO_3$. Samples with this magnetic behaviour were discarded, the proper profile of $Fe_2GeO_4$ with its purely antiferromagnetic transition is displayed in Figure 81.**

Long collections with a Bruker D2 diffractometer confirmed the marked preference of $Fe^{2+}$ for the octahedral position and the confinement of $Ge^{4+}$ to the tetrahedral A-sites of the spinel in the final sample (Fig. 80). Avoiding disorder is particularly vital in magnetic structure studies because a site mixing involving magnetic elements can highly influence and possibly even prevent a proper solution of the signal from neutron diffraction.

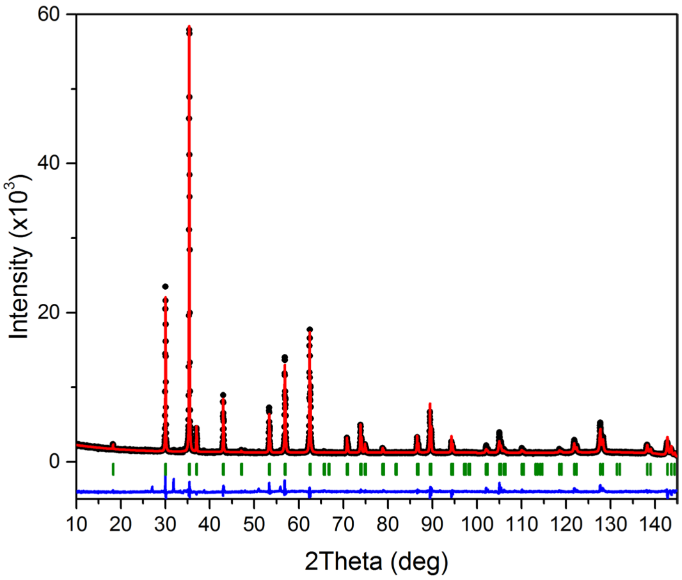


**Figure 80 – Rietveld refinement on laboratory X-ray diffraction of $Fe_2GeO_4$. Experimental data are in black, fit is in red, the difference curve is in blue and the Bragg reflections predicted for the structure are in green. The fit has $R_{wp}$ = 4.03% and $\chi^2$ (g.o.f.) = 5.17 and shows no reflections in addition to the ones indexed as a cubic spinel. The computed cell has a = 8.40718(9) Å, x_O = 0.24670(6) and $B_{O,Fe,Ge}$ = 0.22(2) Å$^2$. The refined occupancies yield 97.4(1)% of Ge in the tetrahedral site and 99.4(7)% of Fe in the octahedral. Within the accuracy of a laboratory machine, the material can be deemed as perfectly site-ordered.**

## 4.2.2. Physical characterisation

The Quantum Design MPMS XL7 SQUID magnetometer was used to measure the DC susceptibility of the sample. As discussed above, there is a stark contrast between the curve for a sample with $FeGeO_3$ impurities (Fig. 79) and the one for a pure $Fe_2GeO_4$ (Fig. 81A). The overall profile as a function of temperature seems to confirm the assumption within the literature of antiferromagnetic ordering, with an onset at $T \approx 9$ K. The Curie-Weiss law was fitted to the inverse susceptibility to points between 150 K and 400 K gives an effective paramagnetic moment of 4.25 $\mu_B$, consistent with high-spin $3d^6$ $Fe^{2+}$ spins, and a Weiss temperature of $\vartheta$ = - 19.6 K, which is compatible with an antiferromagnet. The degree of frustration, expressed as $f = \frac{|\vartheta|}{T_N} \approx 2.2$, does not point towards a highly frustrated phase, that is commonly identified by $f \geq 10$. [109]

A closer look at the low-temperature behaviour of the ZFC-FC profile (Fig. 81B) highlights the presence of some interesting additional features. The T < 9 K cusp overlaps the ZFC and FC curves, in a standard antiferromagnetic profile, but the second kink in the susceptibility at T < 7 K is also accompanied by a splitting of the FC curve. This type of behaviour is usually associated with a ferromagnet, and the presence of a small component of ferromagnetically aligned spins is also detected in the hysteresis loop at 2 K (Fig. 81C, 81D). The profile of the hysteresis at base temperature is largely flat, but the presence of a small coercivity opening and saturation magnetisation, albeit with a very modest residual moment of ~0.05 $\mu_B$, represent additional evidence of ferromagnetic components in the ordered phase of the sample.

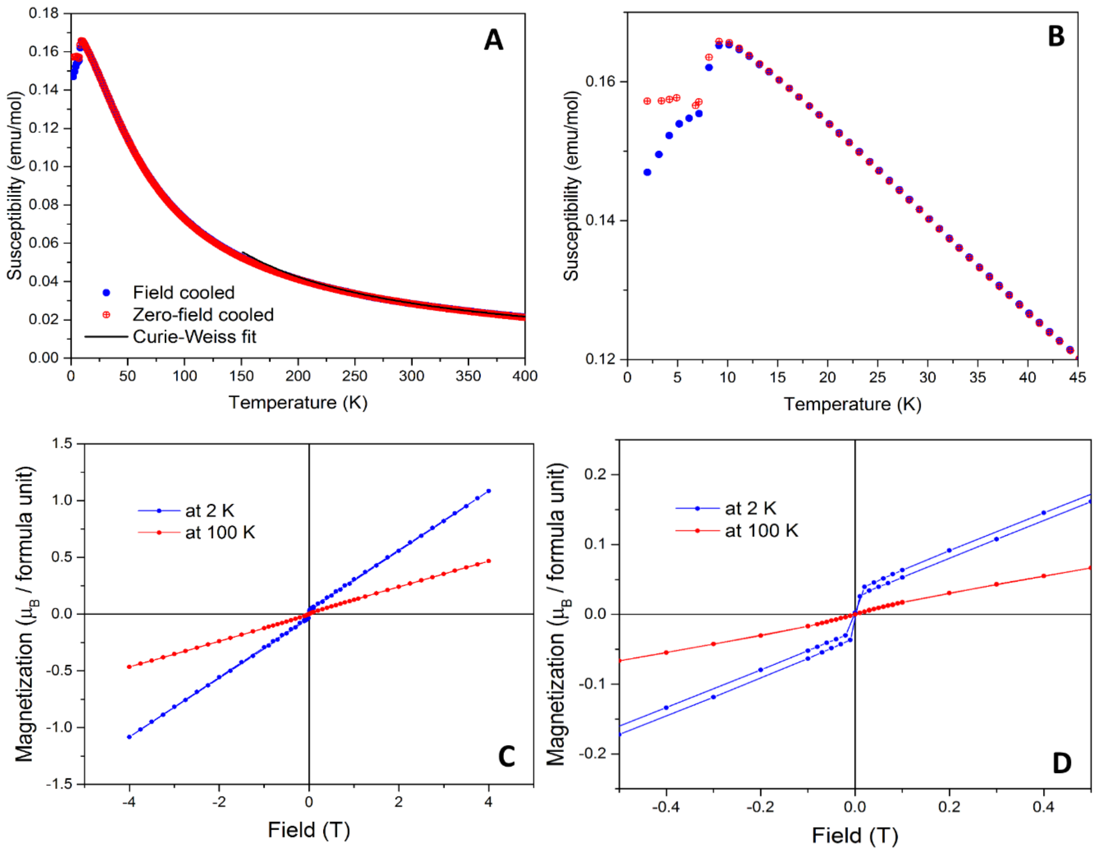


**Figure 81 – A) Magnetic susceptibility in an applied field of 0.5 T as a function of temperature, the Curie-Weiss fit is performed between 150 K and 400 K; B) Shows a magnified view focused on the low temperature region where magnetic transitions occur at $T_{m1}$ ≈ 9 K and $T_{m2}$ ≈ 7 K. C) Hysteresis loop of magnetization for $Fe_2GeO_4$ as a function of temperature, up to 4 T at 100 and 2 K; D) shows a blow-up of the low field region, with the slight opening of the hysteresis loop compatible with the presence of a ferromagnetic component.**

The Quantum Design PPMS was used for AC susceptibility and heat capacity measurements. AC susceptibility results are largely consistent with their DC equivalent: measuring magnetisation as a function of temperature reveals a jump in the response at T ~ 8.6 K; varying frequency of applied magnetic field does not shift the profile, clearly signifying that there should be no residual disordered components in the system below ordering (i.e. no spin-glass behaviour or the like). Unfortunately, signal strength is not sufficient to detect the second weak transition as an additional peak. However, it is possible to detect a change in slope at T < 6 K that can be assigned to the second ordering (Fig. 82).

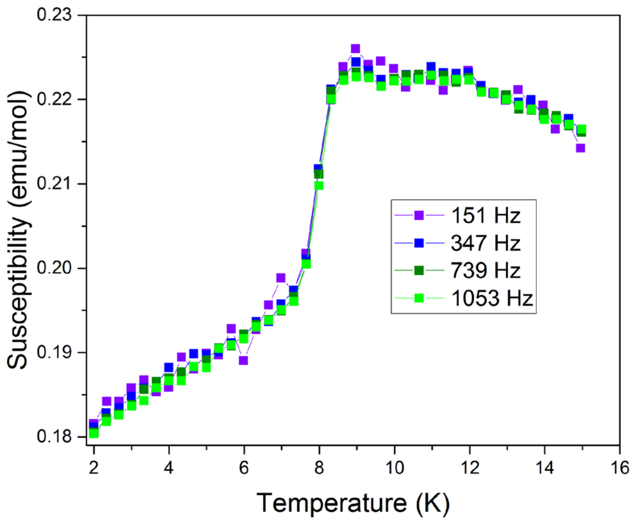


**Figure 82 – Real part of the AC susceptibility in an oscillating magnetic field with amplitude 9 Oe and frequencies as shown. No frequency-dependence of the features that would evidence spin-glass behaviour is observed.**

Heat capacity measured on 1 mg of sample shows a broad feature at T ~ 10 K that corroborates the presence of an ordering transition in the material; additionally, a small kink below 7 K is compatible with a second ordering. The heat capacity signal collected between 150 and 2 K is sufficient to model the lattice component to $C_p$ as outlined in Section 2.4 and extract the magnetic contribution as a difference. The integration of the difference curve provides an estimation of the change in entropy associated with magnetic ordering (Fig. 83). The $C_{P,mag}/T$ curve has significant values well above the magnetic ordering temperature, with relevant contributions up to 50 K, but the integration between 2 and 55 K gains $\Delta S = 5.77$ J mol$^{-1}$K$^{-1}$ , which is only 43% of the theoretical value for ordering of a 3d$^6$ cation like $Fe^{2+}$ ($R\ln(2S+1) = 13.38$ J mol$^{-1}$ for $S = 2$). This result suggests the presence of additional processes of interaction within the material, either in ordering type or interactions between the magnetic cations, sufficient to make the drop in entropy less prominent than it should be.

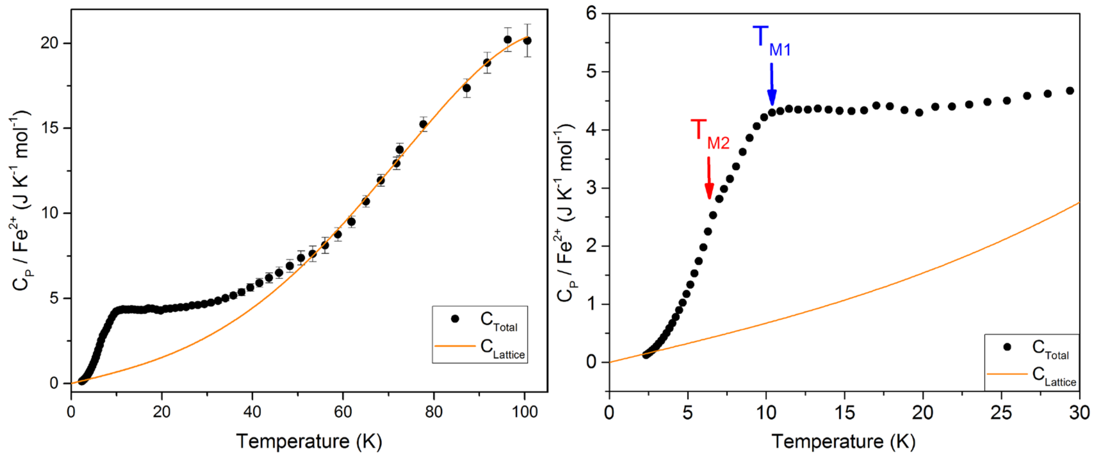


**Figure 83 – Heat capacity variation with the lattice contribution fitted by the polynomial $C_p = \gamma T + \beta T^3 + \delta T^5$. The low temperature region (right image) shows two discontinuities, marked as $T_{m1}$ and $T_{m2}$. The magnetic contribution is evident up to 55 K.**

The overall physical characterisation profiles a system that is more complex than what could be assumed from other magnetic spinels. The sample appears to be magnetically ordered on a long-range scale, but a thorough investigation of the mechanism requires direct probing of the structure.

### 4.2.3. Structural characterisation

The most reliable data on the crystal structure of $Fe_2GeO_4$ in its magnetically ordered phase were acquired at ESRF, Grenoble, using the facilities of the ID22 beamline.
The sample was loaded in a 0.5 mm borosilicate capillary and measured with hard X-rays ($\lambda$ = 0.1917 Å) at 5 K, using a closed-circle helium cryostat with vacuumised sample environment.
The diffraction rings were collected on a flat panel Perkin Elmer XRD 1611CP3 and integrated according to the instrument configuration through the PyFAI suite.[169] ID22 allows the detection of high-resolution peaks up to $2\vartheta = 50^{\circ}$ (equivalent to 25 $Å^{-1}$ in Q-space) and is suited for spotting distortions in a structure.
The resulting diffraction pattern was analysed through Rietveld refinement (Fig. 6) and correctly modelled with an undistorted cubic *Fd-3m* spinel structure, with iron fully ordered in octahedral coordination. The tetragonal distortion in *$I4_1/amd$* reported for the nickel and cobalt germanate equivalents is marked by a splitting of the *400* and *440* cubic reflections,

but there was no sign of such occurrence in the experimental profile at 5 K.

The refined spinel structure has cell parameter $a$ = 8.40626(4) Å, oxygen position $x$ = 0.2470(2) and thermal factors $B_{Fe}$ = 0.132(6) Å$^2$, $B_{Ge}$ = 0.081(6) Å$^2$, $B_O$ = 0.13(2) Å$^2$ at 5 K. Trying to refine site disorder does not improve the fit and yields values Fe in tetrahedral positions and Ge in octahedral position < 1%; the results are reported for a fully site-ordered structure.

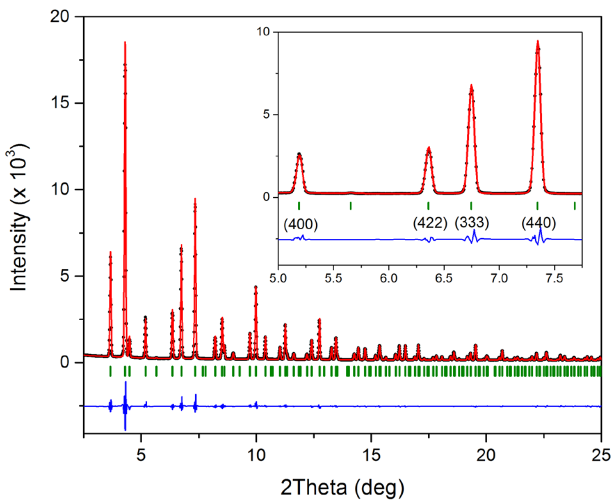


**Figure 84 – Fit of the cubic spinel model to the synchrotron x-ray diffraction profile (λ = 0.1917 Å) at 5 K, with low-angle peaks in the inset. No peak splitting or broadenings that would evidence a lattice distortion are observed. The fit has $R_{wp}$ = 4.92% and $\chi^2$ (g.o.f.) = 1.06 and shows no reflections in addition to the ones indexed as a cubic spinel.**

The lack of distortion in concurrence with evidence of antiferromagnetic ordering in physical measurements is peculiar, since transition metal oxides tend to break the frustration of antiparallel spins in a pyrochlore-like lattice by lowering the symmetry that makes the magnetic sites equivalent.

## 4.2.4. Magnetic structure solution through neutron data

### *4.2.4.1. Data collection*

Neutron diffraction data were collected from 3.5 g of sample at the ILL facility in Grenoble, making use of the D2B and D20 instruments, the specifications of which are outlined in Chapter 2. The acquisition procedure and initial data processing was aided by Dr Clemens Ritter, instrument scientist at the ILL facility.

D2B was used to acquire high-resolution profiles at wavelength λ = 1.59475 Å, using a wide take-off angle of monochromation ($2\vartheta_M$ = 135°) in order to have a powder pattern with resolution of $\Delta d/d \sim 10^{-4}$ for diffraction data up to 2ϑ = 145°. At base temperature (2 K) a further increase of resolution as obtained with a 10' collimation in addition to full flux acquisition. Further collections were performed at 6, 10, 50, 100, 200, 300 K with full flux mode only, in order to track the full temperature evolution of the structure alongside the neutron scattering in the low-temperature ordered regions.
The data from D2B need to be integrated from the 2D angular resolved streaks of its wide-angle detector. While the data from the full width have more intensity only the high-resolution data from the central region were carried forward for refinements.

Additional NPD data were collected from D20 with λ = 2.41 Å, making use of the high-flux of the instrument to acquire a very intense signal in the low-angle region, characteristic for magnetic neutron scattering.
Long acquisitions were performed at 1.8, 2.5, 12, 15 and 25 K. In addition, a ramp collection with lower collection statistics in the 2.5 and 9.5 K range in ~ 0.3 K steps was used to follow the evolution of the magnetic structure. The multiple temperature collections were repeated in both the take-off settings of D20: the high take-off angle (90°) gives peaks with good resolution up to 2ϑ = 100°; it was used to gain structural and magnetic data in order to adjust the model from synchrotron and D2B data in the current instrument through the structural reflections. The low take-off angle (42°) has a good resolution with peaks up to 2ϑ = 50°, which do not properly cover the structural reflections due to the long wavelength used in this experiment. Nonetheless, this offers the best intensity for the magnetic reflections region.

#### *4.2.4.2. Data analysis*

The D2B wide-angle collection corroborates the lack of a structural distortion already highlighted by synchrotron data. The structure remains a cubic spinel down to 2 K (Fig. 85).

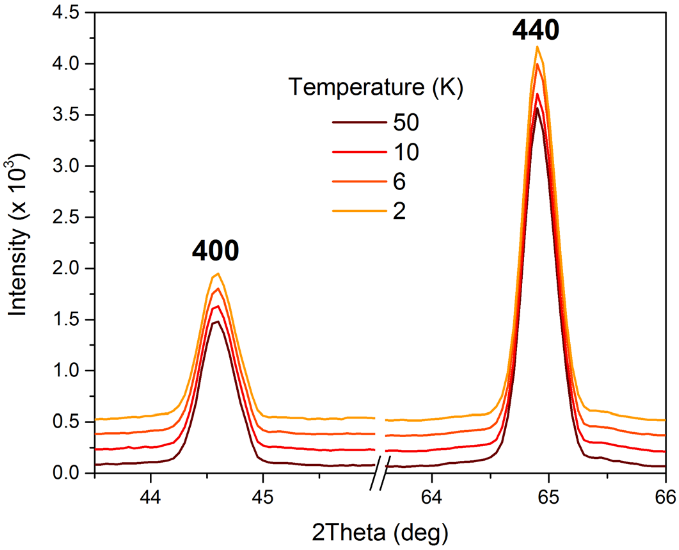


**Figure 85 – Raw diffraction data at multiple temperatures from the D2B high-resolution instrument, focused on the 400 and 440 reflections. In a system affected by tetragonal distortions these reflections split or broaden across the transition; in $Fe_2GeO_4$ the shape and positions of these fundamental peaks remain unvaried as a function of temperature. An artificial offset is applied to display the data as a waterfall, temperatures are colour-coded and associated with a legend.**

A refinement of crystal structure before the onset of the magnetic transition was performed with data at 50 K (Fig. 86), resulting in cell parameter $a$ = 8.41013(5) Å, oxygen position $x$ = 0.24672(9) and thermal factors $B_{Fe}$ = 0.037(2) Å$^2$, $B_{Ge}$ = 0.181(3) Å$^2$, $B_O$ = 0.373(2) Å$^2$. In keeping with synchrotron data, the refined site disorder yields less than 2% mixing between Fe and Ge and does not improve the goodness of the fit; consequently, the structure was assumed to be site-ordered with full occupancy of Fe in octahedral and Ge in tetrahedral coordination for all the following refinements.

Refinements at intermediate temperatures give consistent results and are reported in Appendix B1.

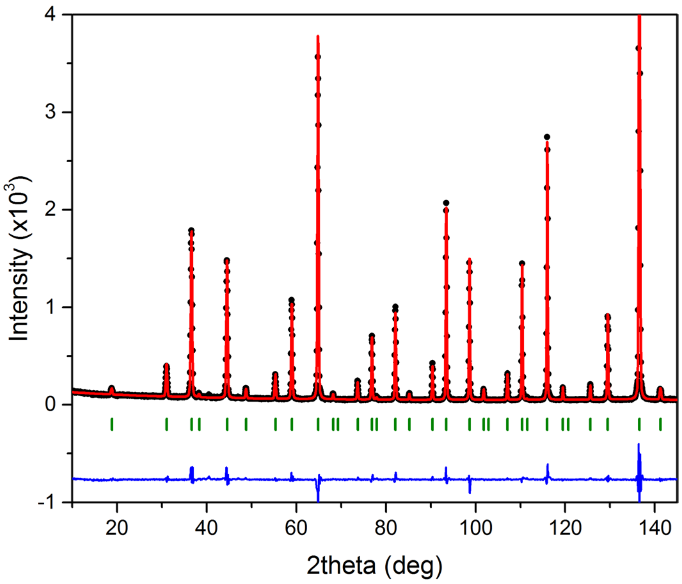


**Figure 86 – Fit of the cubic spinel model to D2B diffraction data (λ = 1.59475 Å at 50 K). The fit has $R_{wp}$ = 7.2% and shows no reflections in addition to the ones indexed as a cubic spinel.**

Data from both D2B and D20 have a clear sign of long-range magnetic ordering with an onset at T < 10 K: the passing of transition temperature is marked by the appearance of additional diffraction peaks at low-angle that rapidly saturate to high intensity upon further cooling. Visual evidence of this process is provided in Fig. 87, in which the consistency of the structural model allows for the subtraction of the Bragg peaks, constant at all temperatures, and to highlight the appearance of new reflections.

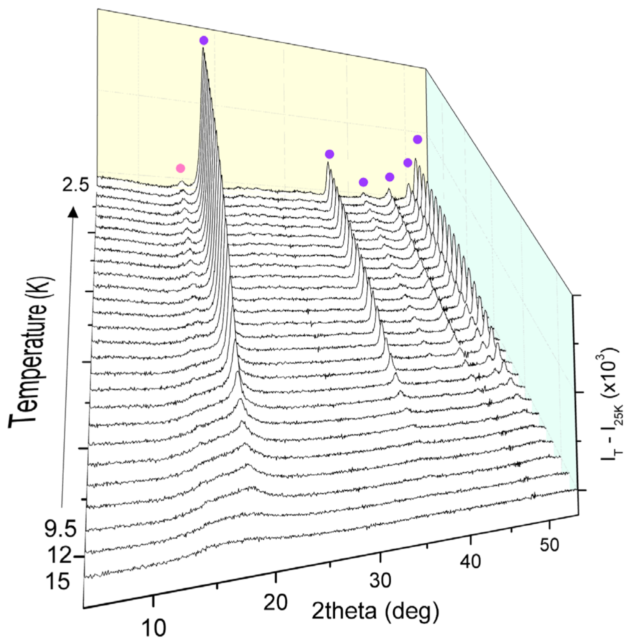


**Figure 87 – Magnetic scattering profiles obtained by subtracting the 25 K D20 data from profiles between 2.5 and 9.5 K, recorded in ~0.3 K steps, and at 12 and 15 K. The six magnetic peaks with purple labels appear below 9 K have propagation (vector $k_1$), while the weak peak indicated in pink appears below 7 K (vector $k_2$).**

Magnetic reflections are indexed using the positions in the difference curve 2 – 25 K for the 42° take-off dataset. The lack of evidence of distortions allows the consideration of these additional reflections as superstructure peaks of a cubic cell with refined cell parameters *a* = 8.38805(2) Å at base temperature and the association with a propagation vector **k** ≈ (⅔ ⅔ 0) through the use of the program k-search within the FullProf Suite. Applying this **k** to a *Fd-3m* structure in BasIrreps highlights the presence of two magnetically distinct sites arising from a single crystallographic position: iron in the crystal structure is in (½ ½ ½), but magnetic symmetry distinguishes them in Fe1 = (½ ½ ½) and Fe2 = (¾ 0 ¼).
The correct choice of irreducible representations for the structure is achieved through trial and error. A magnetic refinement procedure immediately highlights the incommensurate nature of the vector, which is more correctly written as $\mathbf{k_1}$ = (⅔+$\delta_1$ ⅔+$\delta_1$ 0) with degree of incommensurability $\delta_1$ ~ 0.025 at 2 K.

At a first approximation, all the intensities can be correctly matched and modelled by considering magnetic intensity arising only from Fe1 iron atoms, leaving half the sites in the cubic unit cell not ordered; however, the refined value of Fe1 moment in the [110] cubic direction has a maximum value of 5.6 $\mu_B$, unphysically high in comparison to the theoretical maximum of 4 $\mu_B$ for $Fe^{2+}$.

This issue can be resolved by considering that in a metrically cubic system a magnetic signal arising from the *ab* plan will have equivalent reflections in a powder pattern can be related with 4-fold and 3-fold symmetry planes through the crystal. As a result, ordering both iron sites in the exact same way would give rise to additional reflections, but the signal is too intense to have only half of the iron sites ordered. However, components on the *ab* plane that would give magnetic scattering of neutrons would be equivalent for two mutually perpendicular lattices of spins.

This model can be achieved by considering two mutually perpendicular propagation vectors, $\mathbf{k}_{1\_1} = (\frac{2}{3}+\delta_1\ -\frac{2}{3}-\delta_1\ 0)$ and $\mathbf{k}_{1\_2} = (\frac{2}{3}+\delta_1\ \frac{2}{3}+\delta_1\ 0)$ with $\delta_1 = 0.025$. These vectors are symmetry equivalent and part of the so-called "star" of propagation vectors in a cubic system; the second numbering refers to the specific site they are applied to. The full irreducible representations associated with the application of both to an *Fd-3m* lattice of iron atoms gives the same site splitting as a single approximate **k**, and only varies the signs on the basic vectors (Table 13 and Table 14).

**Table 13 – Irreducible representations and basis vectors (BV) for $Fe_2GeO_4$ with propagation vectors $k_1 = (\frac{2}{3}+\delta_1\ -\frac{2}{3}-\delta_1\ 0)$. The two magnetically independent atoms are Fe1 at (½,½,½) and Fe2 at (¾,0,¼). Symmetry-related positions are generated by the operators 1: (x,y,z), 2: (x+ ¼ ,y+ ¾ ,-z+ ½ ) for Fe1 and 1: (x,y,z), 2: (-y+1,-x+1,-z) for Fe2. The sublattice of Fe2 is not refined with this propagation vector so for clarity the irreducible representation for it are not displayed in this table (available in Appendix B1). This propagation vector is thus referred to as $k_{1\_1}$.**

| Propagation vector $\mathbf{k}_{1\_1}$ | | | | | |
|---|---|---|---|---|---|
| Irreps | $\Gamma_1$ | | $\Gamma_3$ | | |
| BV | $\psi_1$ | | $\psi_1$ | | $\psi_2$ |
| Atom | $m_x$ | $m_x$ | $m_x$ | $m_y$ | $m_z$ |
| Fe1_1 | 1 | -1 | 1 | 1 | 1 |
| Fe1_2 | $-½+\frac{i\sqrt{3}}{2}$ | $½-\frac{i\sqrt{3}}{2}$ | $-½+\frac{i\sqrt{3}}{2}$ | $-½+\frac{i\sqrt{3}}{2}$ | $½-\frac{i\sqrt{3}}{2}$ |
| Irreps | $\Gamma_2$ | | $\Gamma_4$ | | |
| BV | $\psi_1$ | | $\psi_1$ | | $\psi_2$ |
| Atom | $m_x$ | $m_x$ | $m_x$ | $m_y$ | $m_z$ |
| Fe1_1 | 1 | -1 | 1 | 1 | 1 |
| Fe1_2 | $½-\frac{i\sqrt{3}}{2}$ | $-½+\frac{i\sqrt{3}}{2}$ | $½-\frac{i\sqrt{3}}{2}$ | $½-\frac{i\sqrt{3}}{2}$ | $-½+\frac{i\sqrt{3}}{2}$ |

**Table 14 – Irreducible representations and basis vectors (BV) for $Fe_2GeO_4$ with propagation vectors $k_1$ = (⅔+$\delta_1$ ⅔+$\delta_1$ 0). The two magnetically independent atoms are Fe1 at (½,½,½) and Fe2 at (¾,0,¼). Symmetry-related positions are generated by the operators 1: (x,y,z), 2: (y+ ¾ ,x+ ¼ ,-z+ ½ ) for Fe1 and 1: (x,y,z), 2: (x+ ¼ ,y+ ¾ ,-z+ ½ ) for Fe2. The sublattice of Fe1 is not refined with this propagation vector so for clarity the irreducible representation for it are not displayed in this table (available in Appendix B1). This propagation vector is thus referred to as $k_{1\_2}$.**

Propagation vector $\mathbf{k_{1\_2}}$

| Irreps | $\Gamma_1$ | | | | | $\Gamma_3$ | | | |
|---|---|---|---|---|---|---|---|---|---|
| BV | $\psi_1$ | | $\psi_2$ | | $\psi_3$ | $\psi_1$ | | $\psi_2$ | |
| Atom | $m_x$ | $m_y$ | $m_x$ | $m_y$ | $m_z$ | $m_x$ | $m_y$ | $m_x$ | $m_y$ |
| Fe2_1 | 1 | -1 | -1 | 1 | 1 | 1 | 1 | 1 | 1 |
| Fe2_2 | $½ - \frac{i\sqrt{3}}{2}$ | $-½ + \frac{i\sqrt{3}}{2}$ | $-½ + \frac{i\sqrt{3}}{2}$ | $½ - \frac{i\sqrt{3}}{2}$ | $-½ + \frac{i\sqrt{3}}{2}$ | $½ - \frac{i\sqrt{3}}{2}$ | $½ - \frac{i\sqrt{3}}{2}$ | $½ - \frac{i\sqrt{3}}{2}$ | $½ - \frac{i\sqrt{3}}{2}$ |
| Irreps | $\Gamma_2$ | | | | | $\Gamma_4$ | | | |
| BV | $\psi_1$ | | $\psi_2$ | | $\psi_3$ | $\psi_1$ | | $\psi_2$ | |
| Atom | $m_x$ | $m_y$ | $m_x$ | $m_y$ | $m_z$ | $m_x$ | $m_y$ | $m_x$ | $m_y$ |
| Fe2_1 | 1 | -1 | -1 | 1 | 1 | 1 | 1 | 1 | 1 |
| Fe2_2 | $-½ + \frac{i\sqrt{3}}{2}$ | $½ - \frac{i\sqrt{3}}{2}$ | $½ - \frac{i\sqrt{3}}{2}$ | $-½ + \frac{i\sqrt{3}}{2}$ | $½ - \frac{i\sqrt{3}}{2}$ | $-½ + \frac{i\sqrt{3}}{2}$ | $-½ + \frac{i\sqrt{3}}{2}$ | $-½ + \frac{i\sqrt{3}}{2}$ | $-½ + \frac{i\sqrt{3}}{2}$ |

Fe1 and Fe2 respectively outline two equivalent spin sublattices perpendicular to each other on the [110] direction of the cubic cell (Fig. 88). The net refined moment for this model is $\mu_1$ = 3.94(3) $\mu_B$, perfectly compatible with high-spin $Fe^{2+}$ values. The value of $\mu_1$ represents the maximum achievable through the structure. Given the constraints imposed by the irreducible representations, the ratio between the experimental magnetic intensities can only be fitted with modulated magnitude: over a periodicity of 33 unit cells (~ $1/\delta_1$), the moment modulates from the maximum of 3.94(3) $\mu_B$ to a minimum of 0.

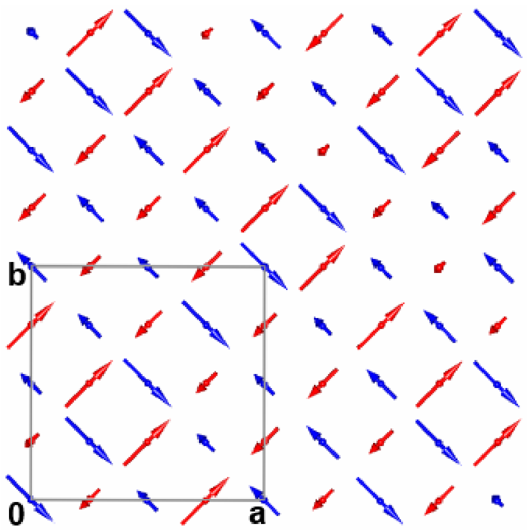


**Figure 88 – The $k_1$ order below $T_{m1}$ with sinusoidal modulation of the Fe1 (blue) and Fe2 (red) moment amplitudes in the [$\bar{1}\bar{1}$0] and [110] directions respectively. Moments vary between 0 (fully frustrated) and 4 $\mu_B$ (fully ordered) values. Zero-moment positions are not visible because the projection only encompasses four cells.**

The outlined model accounts for most of the signal at 2 K, but leaves one peak completely unfitted. A closer analysis of the temperature evolution of the magnetic signal highlights the appearance of this peak at a temperature lower than the first magnetic ordering ($T < 9$ K). This very weak peak gains intensity at $T < 7$ K and cannot be ascribed to an impurity, as any spurious signal from the sample environment is successfully spotted by comparison with a higher temperature profiles (Fig. 89).

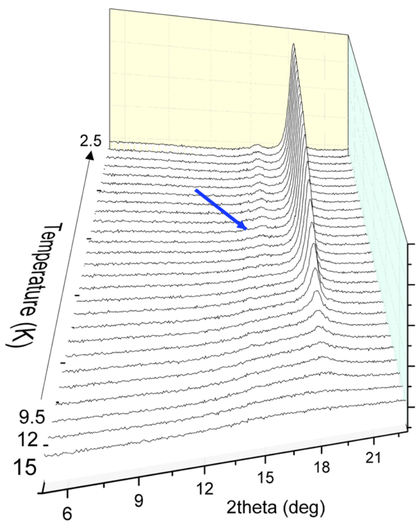


**Figure 89 – Multi-temperature raw diffraction from a $T_{2K}$ – $T_{25K}$ ramp. The blue arrow highlights the appearance of an additional magnetic reflection at $T < 7$ K.**

This reflection does not fit the original $\mathbf{k_1}$ vectors, but it is correctly indexed by considering a commensurate equivalent, $\mathbf{k_2}$ = (⅔+$\delta_2$ ⅔+$\delta_2$ 0) with $\delta_2$ ~ 0. Both vectors are considered as arising from two mutually perpendicular sublattices, so even the commensurate canting is modelled as $\mathbf{k_{2\_1}}/\mathbf{k_{2\_2}}$ in analogy with the double propagation of $\mathbf{k_{1\_1}}/\mathbf{k_{1\_2}}$; the vector is approximately invariant, so the same Irreducible representations listed in Table 1 are used. A successful fit can be achieved by considering a canting of spins on both sublattices; this canting can either be in plane, shifting the spins away from the [110] diagonal, or out of plane, shifting the spins in the [001] direction. It is not possible to ascertain from the goodness of the fit which one of these two options is correct and they must be considered as equivalent possibilities.

A complete fit with two propagation vectors and crystal structure to both D2B and D20 42° take-off data is shown in Fig. 90. The refined coefficient for the irreducible representations corresponding to the magnetic refinement and the associated R-values are listed in Table 15, for the D20 data, as they have the highest intensity for the magnetic signal.

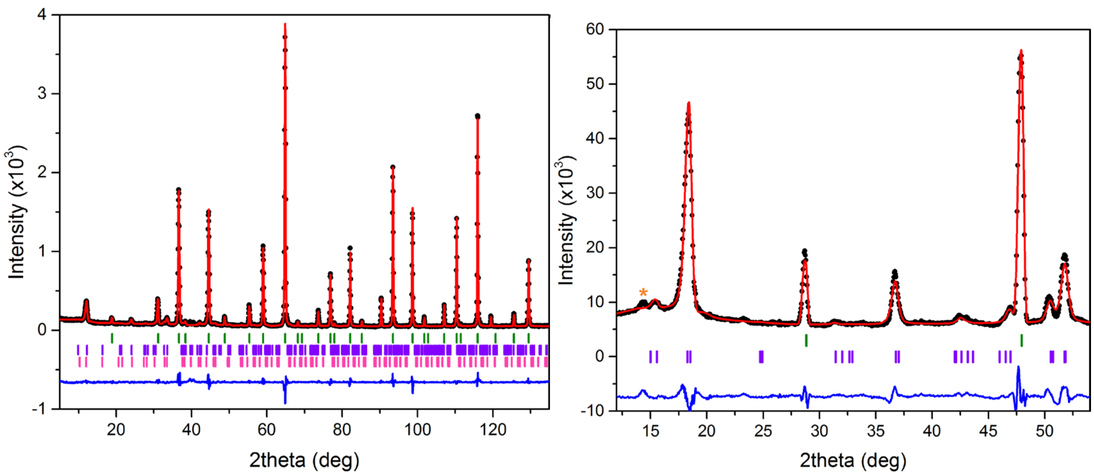


**Figure 90 – Rietveld refinement of D2B (left, λ = 1.54 Å) and D20 42-take-off (right, λ = 2.41 Å) data at 2 K. Experimental data are in black, fits are in red, difference curves are in blue, Bragg reflections of the *Fd-3m* spinel are in green; in the D2B data the k1 and k2 reflections are separated for clarity in violet and pink, but since they are refined in the same phase as multiple k-vectors in the D20 data they are shown in a single violet series. A small non-magnetic impurity peak is labelled in orange.**

**Table 15 – Refined components and resultant moments for $Fe_2GeO_4$ at 1.8 K following the symmetry analysis in Table 1. Results for two refinement models with canting of moments described (*ab* plane canting, *c* canting) by different $k_2$ BVs are shown.**

| Atom | P.V. | IrRep:BV | $\mu_x$ ($\mu_B$) | $\mu_y$ ($\mu_B$) | $\mu_z$ ($\mu_B$) | $\mu$ ($\mu_B$) |
|---|---|---|---|---|---|---|
| Fe1_1 | $\boldsymbol{k}_{1\_1}$ | $\Gamma_1$: $\psi_1$ | 2.79(2) | 2.79(2) | 0 | 3.94(3) |
| Fe2_1 | $\boldsymbol{k}_{1\_2}$ | $\Gamma_4$: $\psi_1$ | 2.79(2) | 2.79(2) | 0 | 3.94(3) |
| Fe1_1 | $\boldsymbol{k}_{2\_1}$ | $\Gamma_3$: $\psi_1$ | 0.65(5) | 0.65(5) | 0 | 0.92(7) |
| Fe2_1 | $\boldsymbol{k}_{2\_2}$ | $\Gamma_2$: $\psi_1$ | 0.65(5) | 0.65(5) | 0 | 0.92(7) |

Residual $R_{wp}$ = 14.2%, Bragg-R factor = 1.54%, Magnetic R-Factor = 5.22%

| Atom | P.V. | IrRep:BV | $\mu_x$ ($\mu_B$) | $\mu_y$ ($\mu_B$) | $\mu_z$ ($\mu_B$) | $\mu$ ($\mu_B$) |
|---|---|---|---|---|---|---|
| Fe1_1 | $\boldsymbol{k}_{1\_1}$ | $\Gamma_1$: $\psi_1$ | 2.81(4) | 2.81(4) | 0 | 3.97(5) |
| Fe2_1 | $\boldsymbol{k}_{1\_2}$ | $\Gamma_4$: $\psi_1$ | 2.81(4) | 2.81(4) | 0 | 3.97(5) |
| Fe1_1 | $\boldsymbol{k}_{2\_1}$ | $\Gamma_4$: $\psi_2$ | 0 | 0 | 0.84(8) | 0.84(8) |
| Fe2_1 | $\boldsymbol{k}_{2\_2}$ | $\Gamma_1$: $\psi_3$ | 0 | 0 | 0.84(8) | 0.84(8) |

Residual $R_{wp}$ = 14.2%, Bragg-R factor = 1.52%, Magnetic R-Factor = 4.41%

The canting component has a magnitude of $\mu_2$ = 0.92(7)/0.84(8) $\mu_B$ at 2 K. Since this second phase is commensurate, canting components do not have the same modulation of the main phase and are instead characterised by an alternate sequence of full-half-half-full values. This does not hinder the amplitude-modulated antiferromagnetic behaviour of the main phase, but gives an overall ferromagnetic shift to the spins, since the tilt affects every spin in the same way (i.e. all to the left from the diagonal or all up from the plane).
When considering the total amplitude arising from both the main $\mathbf{k}_{i1}$ phase ordering and the $\mathbf{k}_{i2}$ canting, the moment of the $Fe^{2+}$ at 2 K, $\mu_{tot}$ = 4.05(8) $\mu_B$, is in perfect agreement with the theory.
The overall magnetic structure considering both the main propagations and the two canting options is shown in Figure 91.

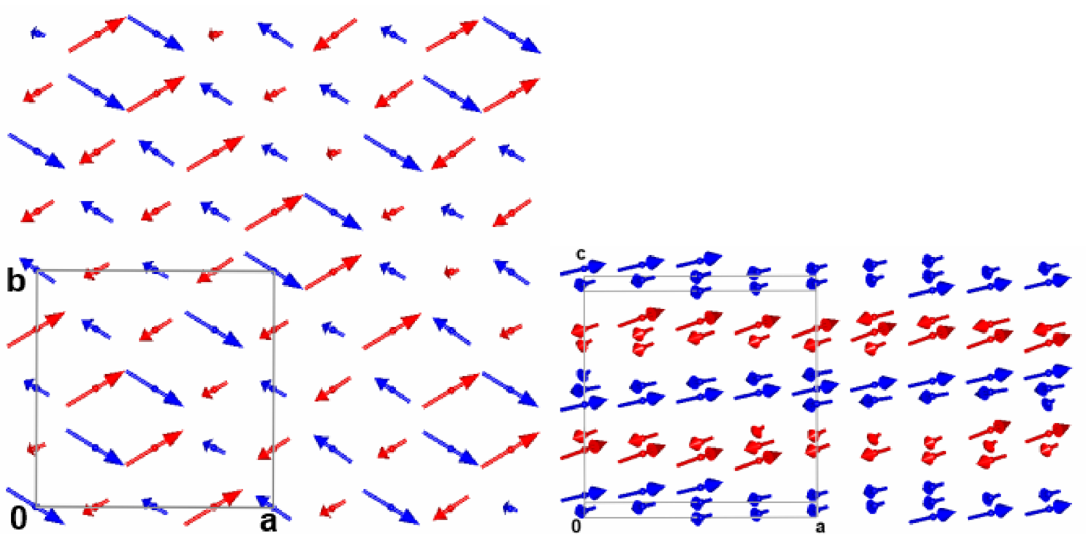


**Figure 91 – $k_1$ order with additional modulated tilting, following the propagation vector $k_2$ below $T_{m2}$. On the left, the tilting is in plane and away from the diagonal; on the right, the tilting is out of plane along the *c* axis.**

The evolution of both phases can be followed through sequential refinements of the diffraction patterns collected as a function of temperature. The outcome is summarised in Fig. 92, where the maximum magnetic components and the propagation vector are displayed as a function of temperature. It can be noted that the incommensurability of $\mathbf{k_2}$ is centred on zero, with significant error bars; as such, the propagation vector cannot be considered fundamentally different from a commensurate $\mathbf{k_2}$ = (⅔ ⅔ 0). Moreover, the evolution of the magnetic amplitude, proportional to the appearance of magnetic scattering, can be correlated with an experimental transition temperature through a critical fit:

$$\mu = \mu_0 \left(1 - \frac{T}{T_m}\right)^{\beta}$$

This law only has physical meaning close to the transition, when the values are far from saturation. For the first magnetic transition data were fitted at T > 6.5 K with $\beta_1$ = 0.35(6) and $T_{M1}$ = 8.6(2) K, for the second magnetic transition data were fitted at T > 5.5 K with $\beta_2$ = 0.3(1) and $T_{M2}$ = 7.2(2) K. The accord with the physical data is satisfactory and allows pairing between evidence from susceptibility and neutron diffraction refinement.

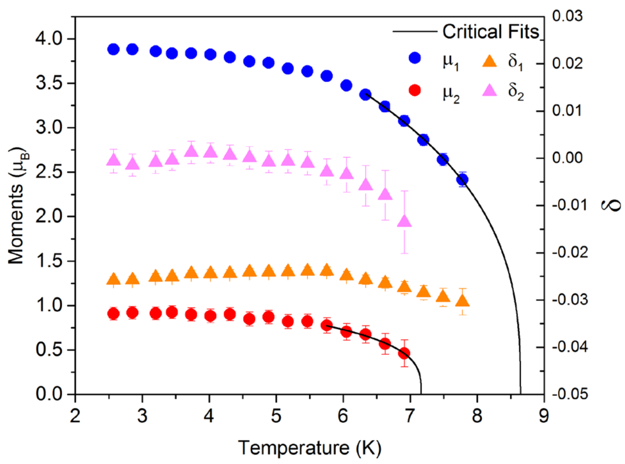


**Figure 92 – Temperature variations of the magnetic moments μ and propagation vector contributions δ for Fe1 and Fe2 with canting in the *ab*-plane. Error bars are included in the data point dimensions when not displayed.**

The representation analysis and magnetic refinement procedure was performed in collaboration with Dr Angel Arevalo Lopez. The overall results outline a successful application of physical characterisation and magnetic neutron diffraction towards the aim of unveiling the ordering feature of a crystalline material.

#### *4.2.4.4. Summary and interpretation of results*

The magnetic ordering in $Fe_2GeO_4$ presents several points of unconventionality in the picture derived from physical measurements and magnetic neutron diffraction.

DC and AC susceptibility data are in accord with the presence of a long-range ordering at T < 9 K, with antiferromagnetic features and a small degree of frustration ($\vartheta$ = - 19.6 K, $f$ ~ 2.2). However, at T < 7 K the magnetisation curve shows evidence of ferromagnetic contribution, as pinpointed by both ZFC-FC splitting and hysteresis loop bending.

Neutron diffraction highlights the presence of long-range magnetic order but the onset of the magnetic transition is not accompanied by structural distortion from cubic to tetragonal, as it is the case in most geometrically frustrated transition metal oxides with antiferromagnetic ordering. In accordance with one preliminary report [7], magnetic intensities outline two transitions: $T_{m1}$ = 8.6(2) K and $T_{m2}$ = 7.2(2) K with propagation vectors $\mathbf{k_1}$ = (⅔+$\delta_1$ ⅔+$\delta_1$ 0) with $\delta_1$ = 0.025(1) and $\mathbf{k_2}$ = (⅔ ⅔ 0) respectively; these values of the ***k*** components are not usually reported for transition metal oxide systems (e.g. $ZnV_2O_4$

[$\boldsymbol{k}$ = (0 0 1)] [193], $LiMn_2O_4$ [$\boldsymbol{k}$ = (½ ½ ¼)] [194], $MgCr_2O_4$ [$\boldsymbol{k}$ = (½ ½ ½)] [195] and $Co_2GeO_4$ [$\boldsymbol{k}$ = (½, ½, ½)] [9, 196], all tetragonal with *$I4_1/amd$* symmetry below orbital or antiferromagnetic ordering transitions).

The magnetic model associated with this ordering applies each propagation vector to two distinct Fe sites, equivalent from the symmetry point of view. The main vector, $\mathbf{k_1}$, imposes an incommensurate model with modulated amplitudes of the ordered spins onto two mutually perpendicular sublattices. Fe1 and Fe2 are both ordered in collinear antiferromagnetic chains of spins pointing parallel to their propagation direction. Below the second ordering temperature, this arrangement experiences a slight canting, the commensurate nature of which could be tentatively explained by an attempt of the structure to stabilise the two interacting incommensurate sublattices.
The modulation at 2 K, considering all magnetic contributions, spans between a completely unfrustrated $\mu$ = 4.05(8) $\mu_B$ and a fully frustrated 0 µB over 33 unit cells.
On average, the magnitude of the ordered moments is 64% of the ideal value: approximately one-third of the spins remain dynamic below the magnetic ordering transitions. This is qualitatively consistent with the reduction of magnetic entropy highlighted by heat capacity measurements.

In addition to the lack of distortion and the uncommon propagation vector, the amplitude-modulation of moments in the $Fe_2GeO_4$ is highly unusual in insulating transition metal oxide.
Frustrated systems often show complex spin textures (e.g. helimagnets or skyrmions), but they are always characterised by uniform moment amplitudes while spin directions change. Conversely, frustrated elliptical spiral structures tend to modulate only over a partial range, e.g. in $FeTe_2O_5Br$,[197] and 'idle spin' orders provide a special case where some spins remain disordered due to frustration of their interactions with surrounding uniformly ordered spins (e.g. pyrochlore $Gd_2Ti_2O_7$ below 0.7 K [198]).
The only close spin density wave analogue that has been found in literature is $Ca_3Co_2O_6$, the ordered phase of which shows chains of collinear spins modulated between 0 and 5.0 $\mu_B$ for S = 2 $Co^{3+}$ moments with a strong orbital contribution. [199] What these two systems have in common is the fact that they are based on high spin $3d^6$ ions. This suggests that an additional factor operates in these materials.

Both $FeTe_2O_5Br$ ($S$ = 5/2 $Fe^{3+}$) and $Gd_2Ti_2O_7$ ($S$ = 7/2 $Gd^{3+}$) have a strong geometric frustration but no orbital degeneracy in the magnetic cations; as such, the exchange energies can be stabilised with spin arrangements of various amplitudes to compensate for unfavourable orientations. By contrast, both $Fe_2GeO_4$ and $Ca_3Co_2O_6$ have a rare collinear arrangement with a full amplitude modulation in their ground state, and they are both based on cations with unquenched orbital contributions.

Accounting for dynamism in these orbital interactions can lead to a model in which the degree of frustration can be a modulated quantity in itself. If the modulation in the lattice occurs with the same periodicity of the spin density wave, the system can present a "frustration wave".

### *4.2.4.5. Frustration wave order*

$Fe_2GeO_4$ is a system with high-spin $Fe^{2+}$ cations and a degenerate $t_{2g}^4e_g^2$ ground state. In this configuration, one $t_{2g}$ orbital is doubly-occupied and two are half-occupied; the latter can present $t_{2g}$-$t_{2g}$ magnetic exchange interactions, but the intrinsic directionality of these orbitals forces the exchange to occur mainly across the shared edges of $FeO_6$ octahedra and only more weakly through the 90° Fe-O-Fe pathway. The Goodenough-Kanamori exchange rules, introduced in Chapter 2, provide a guidance for the nature of these interactions. Direct $t_{2g}^1$-$t_{2g}^1$ interactions are antiferromagnetic ($J_{AF}$) but the $t_{2g}^2$-$t_{2g}^1$ interactions are ferromagnetic ($J_F$) (Fig. 93); there are also $t_{2g}^2$-$t_{2g}^2$ configurations that are theoretically possible, but they are extremely unfavourable from the Coulomb interaction point of view and, as already proven for the ground state of magnetite, they tend to be avoided at low temperatures, and this also seems to be the case for the ground state of $Fe_2GeO_4$.

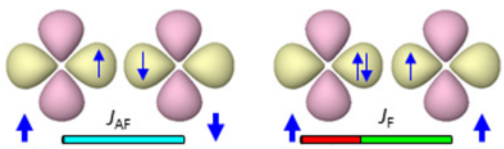


**Figure 93 – Nearest-neighbour $Fe^{2+}$-$Fe^{2+}$ $t_{2g}$ orbitals and associated magnetic exchange interactions. The $t_{2g}^1$-$t_{2g}^1$ interaction (left) leads to antiferromagnetic coupling $J_{AF}$ between the cation spins (schematically represented as the light blue bar). The $t_{2g}^2$-$t_{2g}^1$ interaction (right) shows $t_{2g}^2$ orbital order and associated ferromagnetic coupling $J_F$ (schematically represented as the red and green bar).**

Each tetrahedron of four $Fe^{2+}$ spins thus has two antiferromagnetic $t_{2g}^1$-$t_{2g}^1$ and four ferromagnetic $t_{2g}^2$-$t_{2g}^1$ interactions along its edges, and these have two distinct arrangements as shown in Fig. 16. For the sake of modelling, and considering the type of configuration involved, it is possible to approximate the strengths of interaction as comparable between antiferromagnetic and ferromagnetic interactions ($J_{AF} \approx -J_F$).

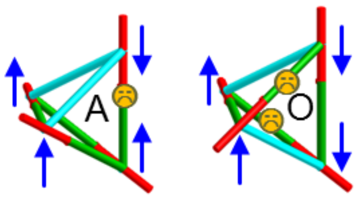


**Figure 94 – The two configurations for orbital order and magnetic interactions within tetrahedra of four $Fe^{2+}$ cations. Four edges have orbital order and ferromagnetic couplings and two are antiferromagnetic. Tetrahedra where antiferromagnetic couplings are on Adjacent edges (A, left) have a 3 up/1 down spin collinear ground state, i.e. two spins adjacent to the frustrated interaction are partially frustrated but the others are unfrustrated. Tetrahedra where antiferromagnetic couplings are on Opposite edges (O, right) are instead uniformly frustrated, with ferromagnetic and antiferromagnetic ground states of comparable energy.**

The configuration where antiferromagnetic couplings are on adjacent (A) edges of the tetrahedron is the simplest collinear ground state: with a 3 up/1 down configuration, two spins are unfrustrated while the other two are partially frustrated. By contrast, if the ferromagnetic coupling occurs on opposite edges of the tetrahedron (O configuration), the overall coupling has all equally frustrated spins.
The configurations shown in Fig. 94 are just two of the 24 equivalent A-type and 6 O-type that are possible when considering the arrangement of spin direction and edge. Hence, statistically speaking, in the absence of longer-range orbital correlations 80% of $Fe_4$ tetrahedra are A-type at any instant in the orbitally fluctuating state and 16% of $Fe^{2+}$ spins are in a locally unfrustrated environment at the apices between two A-type tetrahedra. It is thus reasonable to assume that the degree of frustration can have large fluctuations in an environment that is orbitally dynamic. At low temperatures the loss of thermal energy contribution to the dynamism can lead to clustering of unfrustrated spins; the resulting ordering may be considered not only from the magnetic point of view, but also from the "frustration wave" point of view.

In the specific case of $Fe_2GeO_4$, frustration wave order arises from exchange interactions between ordered spin components in one sublattice mediated by the dynamic components of their neighbours in the other. Fig. 95 provides an illustration of this effect with a simplified model where the ordered Fe1 spins are represented by a commensurate approximant (⅔ -⅔ 0).

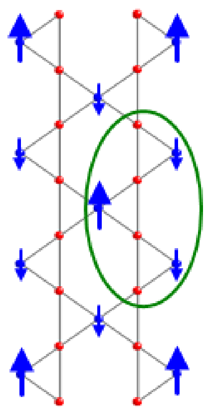

**Figure 95 – Approximant model for the Fe1 spin order in $Fe_2GeO_4$. Fe1 moments form ferromagnetic chains perpendicular to the image plane; one third have fully ordered up spins (+*S*) and two thirds are partially-fluctuating down spins (-*S*/2). Perpendicular ordered spins at Fe2 sites (red) are not shown.**

In the simplified model, Fe1 is composed of fully ordered up spins (+S), aligned ferromagnetically with each other, and of partially fluctuating down spins (-S/2). The link between +S and –S/2 passes through Fe2 spins, but since the ordering of the Fe2 sublattice is in perpendicular direction with Fe1 there is no direct exchange occurring. It is however possible that Fe1 spins will couple with fluctuating components of Fe2 spins, as shown in Fig. 96.

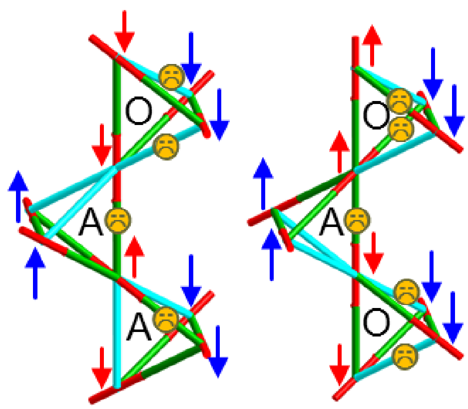


**Figure 96 – Two of the fluctuating local configurations for orbital and spin orders within the representative unit of three tetrahedra circled in Fig. 11. Static Fe1 spin components (blue) are coupled through the dynamic components of the Fe2 spins (red). The central tetrahedron is always A-type with two fully ordered blue +S spins (no frustrated interaction with the nearest-neighbours). The top and bottom tetrahedra fluctuate between A and O configurations and have -*S*/2 spins with some frustrated interactions. The Fe2 spin components fluctuate between up and down states.**

Once again, the coupling can have either A or O arrangement: A-type tetrahedra lead to unfrustrated interactions around the Fe1 (+S) chain, but the two adjacent tetrahedra can fluctuate between A and O configurations leading to some frustrated interactions at the other Fe1 (-S/2) chains. The Fe2 spins have no static order parallel to Fe1 spins but have components fluctuating between up and down states in the various possible configurations. By nature of this description, the orbital states fluctuate in a highly-correlated manner but there is no finite localisation and orbital ordering.
On the basis of this simplified picture, it is possible to draw a similar orbital arrangement picture for any sampled region in the full incommensurate structure shown in Fig. 88. It can also be argued that the small incommensurability of the actual magnetic structure is likely a result from next-nearest neighbour magnetic couplings that are neglected in the model above.

The unconventional features of the magnetic structure of $Fe_2GeO_4$ can thus be rationalised in terms of an orbitally degenerate state that deals with the inherent frustration of the antiferromagnetic ordering by using the "degree of frustration" as a spatial quantity to be distributed throughout the structure, leading to an amplitude modulated ground state. This explanation was detailed by Prof J. Paul Attfield, who also kindly provided the graphic depictions of the concurring interactions.

In order to ascertain whether this occurrence is a unique case or may be systematised as a new type of frustrated ground state, it would be beneficial to explore other systems that promise the same configuration.

# 4.5 γ-$Fe_2SiO_4$

## 4.5.1. Synthesis and preliminary characterisation

With the aim to find a system closely related to $Fe_2GeO_4$, replacing $Ge^{4+}$ with $Si^{4+}$ is an obvious choice, since the two cations are close enough in dimension to apply only modest chemical pressure by substitution. However, at normal conditions the ratio between $Fe^{2+}$ and $Si^{4+}$ sets the field of stability of $Fe_2SiO_4$ in the olivine family, with orthorhombic crystal structure.

It has been known since the early days of high pressure science that spinels are the high-pressure polymorph of olivines with the right stoichiometric ratio. This is indeed the case for $Fe_2SiO_4$, the conversion of which from low-pressure α phase to high pressure cubic γ phase was reported in 1958 by Ringwood, who also successfully identified the role of γ-$Fe_2SiO_4$ in the composition of the Earth's mantle in the form of γ-(Mg,Fe)$SiO_4$ (Ringwoodite). [200] [201]

From this early report, the conditions of high-pressure/high-temperature synthesis are calculated to be 4.5 GPa and 700°C. Experimentally, the application of 6 GPa and 400°C allowed the full conversion of the precursor to green, cubic crystals.[200] More recent studies performed *in situ* with synchrotron powder diffraction confirm the occurrence of a full polymorphic transformation at 410°C and 6.9 GPa. [202]

With the Multi-Anvil high pressure apparatus it is possible to obtain enough γ polymorph for a neutron powder diffraction study. The sample is thermodynamically metastable at normal conditions but the kinetics of conversion are slow enough to be considered stable at room temperature or lower. It is difficult to stabilise temperatures lower than 600°C in large volume high-pressure equipment, so most syntheses described in the literature are performed at much higher temperatures and pressures than the original study by Ringwood ($P > 7$ GPa, $T > 1200$°C). Although such a procedure surely yields a phase-pure high-pressure polymorph, there are multiple reports of significant cation disorder in the product: given the similar dimension of $Fe^{2+}$ and $Si^{4+}$ and the possibility of the two cations to assume both octahedral or tetrahedral coordination, an overshoot in temperature and pressure favours site mixing, with $Fe^{2+}$ in tetrahedral sites and $Si^{4+}$ in octahedral sites. [203] [204] [205]

For the purpose of a magnetic structure solution, it is of paramount importance to eliminate or at least reduce site disorder, as it would hinder the magnetic ordering of the sample and its resulting magnetic diffraction signal. The synthetic conditions in this work have been optimised to avoid this issue.

The low-pressure polymorph α-$Fe_2SiO_4$ was synthesised as a polycrystalline powder by grinding stoichiometric quantities of Fe (-22 mesh, 99.998%, Alfa Aesar), $SiO_2$ (99.999% Alfa Aesar), and $Fe_2O_3$ (99.999% Sigma Aldrich) powders and pressing them into a pellet. The reaction was carried out in evacuated silica tubes, heating in a box furnace at 900°C for 60 hr, then slow-cooling for 12 hrs. The resulting green powder was usually reground and made into a pellet again to carry out another cycle of reaction in a silica tube, in order to assure the full reactivity of the Fe powder. The purity of the sample was confirmed by laboratory X-ray diffraction before proceeding with the synthesis.
α-$Fe_2SiO_4$ was transformed to spinel-type γ-$Fe_2SiO_4$ in a Walker-type multi-anvil press in BN capsule with graphite heater, pressurizing at 6 GPa at 700°C for 20 minutes before quenching. These conditions were set as the optimal conditions after performing several syntheses at 6 GPa and temperatures in the range 900 – 600 °C; the reported synthesis is the one that consistently yielded a pure cubic *Fd-3m* sample with no orthorhombic impurities and a refined occupancy of Fe in the octahedral site > 99% by lab X-ray diffraction (Fig. 97).

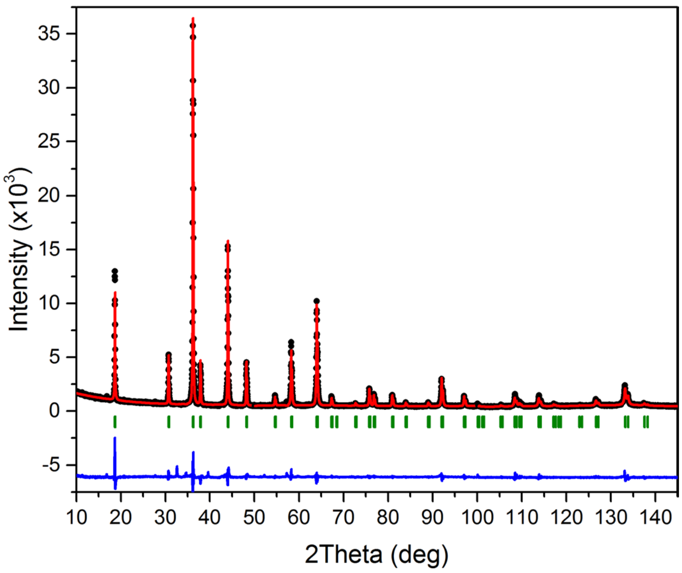


**Figure 97 – Rietveld refinement on laboratory X-ray diffraction of γ-$Fe_2SiO_4$. Experimental data are in black, fit is in red, the difference curve is in blue and the Bragg reflections are in green. The fit has $R_{wp}$ = 6.22% and $\chi^2$ (g.o.f.) = 5.4 and shows no reflections in addition to the ones indexed as a cubic spinel. The computed cell has a = 8.2229(1) Å, x_O = 0.2411(4) and $B_{Fe}$ = 0.89(9) Å², $B_{Si}$ = 0.9(1) Å², $B_O$ = 0.91(8) Å². The refined occupancies yield to the presence of 96.5(8)% of Si in the tetrahedral site and 99.1(4)% of Fe in the octahedral. Within the accuracy of a laboratory machine, the material can be deemed as perfectly site-ordered.**

As each synthesis yields ~7 mg of sample, product from multiple runs was combined in order to obtain a total of 128 mg of sample and have a sufficient volume for high-flux neutron experiments. Before combining the runs in a single powder sample, each batch was checked with laboratory X-ray diffraction and magnetometry measurements.

### 4.2.2. Physical characterisation

The Quantum Design MPMS XL7 SQUID magnetometer was used to measure the DC susceptibility of the sample. The overall profile as a function of temperature is in accord with early literature report of antiferromagnetic behaviour of this material, with onset of the ordering at T ≈ 11 K. [5] The Curie-Weiss fit to the inverse susceptibility between 150 K and 300 K gives an effective paramagnetic moment of 5.10(3) $\mu_B$ and a Weiss temperature of $\vartheta$ = 0.23(1) K; this moment is slightly high for $Fe^{2+}$ but the tendency towards divergence of the fit from the ideal Curie-Weiss curve at temperatures below 150 K might point towards the presence of unaccounted orbital contributions. The Weiss temperature is small but not negative, which is compatible with an antiferromagnet but not with the presence of a prominent frustration in the system.
In keeping with $Fe_2GeO_4$, the low-temperature behaviour of the ZFC-FC profiles suggests the presence of two transitions: one susceptibility maximum at $T_1 \approx 10$ K and divergence of field and zero-field cooled susceptibilities at $T_2 \approx 6$ K; this splitting is a sign of ferromagnetic components influencing the susceptibility of the sample and was previously unreported (Fig. 98).

Given the similarity in the susceptibility behaviour of γ-$Fe_2SiO_4$ and $Fe_2GeO_4$, hysteresis loops were collected above the first magnetic transition (100 K, paramagnetic), in the antiferromagnetic region (8 K) and at base temperature, where the material shows evidence of ferromagnetic components (2K). The hysteresis behaviour corroborates the susceptibility results: the 8 K is compatible with an antiferromagnet, with no coercivity opening of the loop; at 2 K, the loop has a clear coercivity effect that opens up the loop and results in a modest residual saturation magnetisation of ≈ 0.01 $\mu_B$ per Fe (Fig. 99). Even though the residual magnetisation is smaller than the one detected in $Fe_2GeO_4$ at 2 K, the coercivity of the ground state of γ-$Fe_2SiO_4$ appears to be more pronounced.

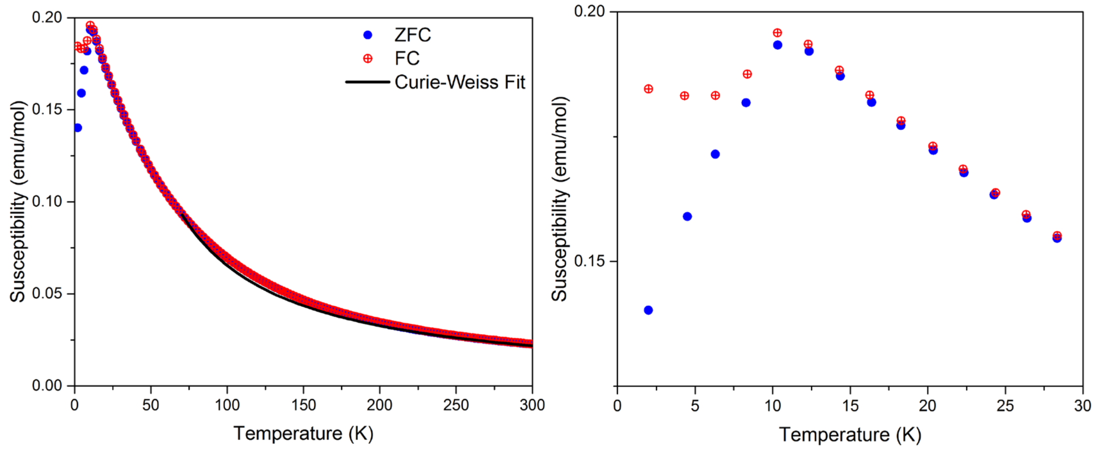


**Figure 98 – Susceptibility as a function of temperature in ZFC (blue) and FC (red), with 0.5 T of applied field, for γ-$Fe_2SiO_4$. The Curie-Weiss fit is displayed in black. A better focus on the low temperature behaviour is provided in the right image.**

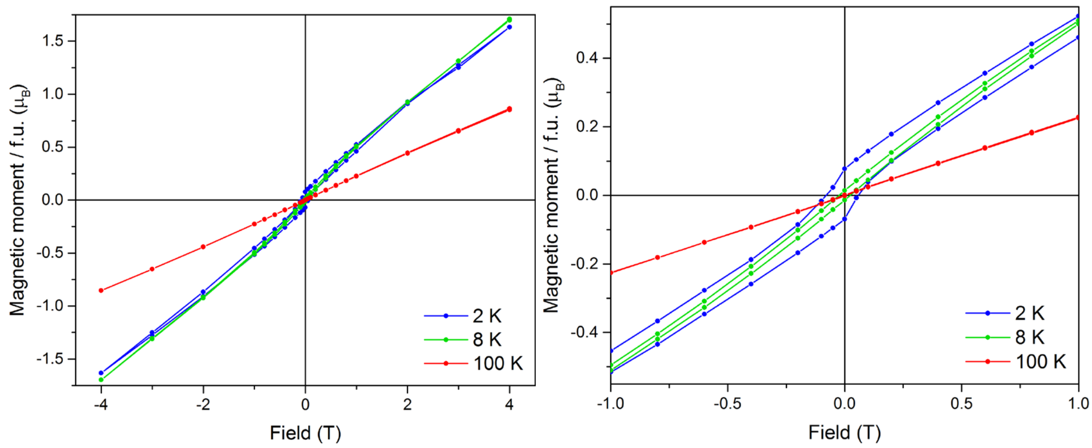


**Figure 99 – Hysteresis loops at 2, 8 and 200 K. The blow-up of the low field region (right) provides a better visual on the slight opening of the hysteresis loop as an effect of the second transition in the material.**

The Quantum Design PPMS was used for AC susceptibility and heat capacity measurements. The AC susceptibility provides additional evidence for the presence of two transitions, with one prominent drop at ~ 12 K and a smaller peak at ~ 6.5 K (Fig. 100A). In contrast with the $Fe_2GeO_4$, however, there is a slight frequency dependency of the first transition peak. This is a common sign of a “spin-glass” behaviour, when spins not ordered on the long-range undergo a freezing, the temperature of which is frequency dependent. In order to model the glassy behaviour, the maximum of each peak was extracted by modelling the AC susceptibility peak shape between 10 and 18 K with an asymmetric double sigmoidal function. The fitting does not have a direct physical meaning but allows for an accurate extraction of the maximum position of the peak. Maxima of each peak are treated as the freezing temperature $T_f$ of glassy spins in the sample, and represent the frequency-dependent parameter that can be modelled with a modified Arrhenius equation called the Vogel-Fulcher law,[205] a typical analysis for spin-dynamic samples:

$$ln\omega = ln\omega_0 - \frac{E_A}{k_B(T_f - T_0)}$$

where ω is the frequency in $s^{-1}$, $\omega_0$ is a characteristic frequency, $E_A$ is the activation energy and $T_0$ is the ideal glass temperature or temperature of freezing at ω = 0. The successful fit to this equation is shown in the inset of Fig. 100B.

The AC susceptibility signal highlighting the second transition does not have such spin-glassy behaviour, and the concurring physical evidence points towards a magnetic long-range ordered ground state.

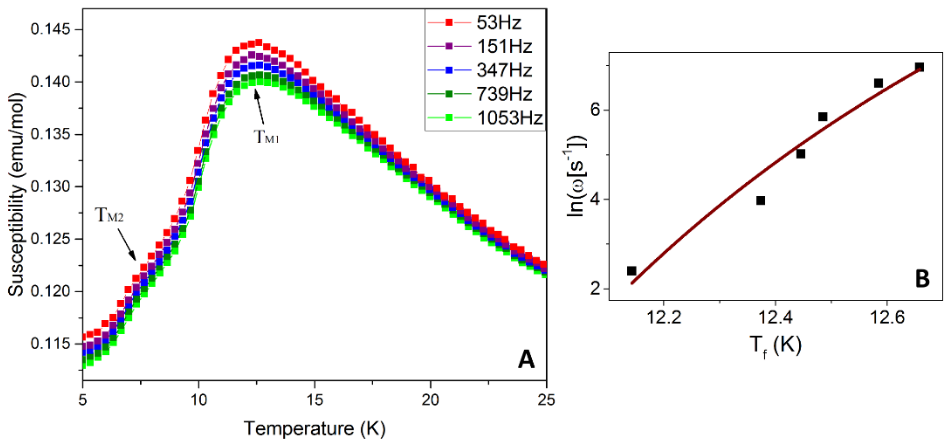


**Figure 100 – A) AC susceptibility of γ-$Fe_2SiO_4$ in an oscillating magnetic field with amplitude 9 Oe and frequencies as shown. The two magnetic transitions clearly appear in these measurements at $T_{M1}$ = 12.6 K and $T_{M2}$ = 7.7 K. A slight frequency-dependence of the features is observed in the peak of $T_{M1}$. B) The spin freezing temperatures $T_f$ are extracted by single peak fitting; the red line shows a fit of the Vogel-Fulcher law[206], with $T_0$ = 10.44(1) K, ln($\omega_0$/s) = 22(2) and $E_a/k_B$ = 35(4) K.**

A study of heat capacity is already available in literature and is the most recent detailed investigation of physical properties for γ-$Fe_2SiO_4$ below room temperature. However, the main focus within that study was to extract thermodynamic properties of the paramagnetic phase and there is no proper analysis of the magnetic ordering transition; a prominent discontinuity is reported at 11 K and a small shoulder at 7 K is interpreted as a Schottky-anomaly arising from the 3*d* orbitals of $Fe^{2+}$. [207] [208]

In this work, the focus is instead on the low-temperature region of the heat capacity. The profile measured on 1 mg of sample is in accord with literature data, with a discontinuity at T ~ 11 K that can be associated with antiferromagnetic ordering in the sample; the second transition highlighted by magnetometry is not clearly detected, but the broadness of $C_p$ around the transition might mask this feature. The lattice component of heat capacity can be modelled through the data collected between 2 and 100 K, as outlined in Section 2.4. The magnetic contribution can be obtained as a difference curve, the integration of which provides an estimation of the change in entropy associated with magnetic ordering (Fig. 101). The $C_{P,mag}/T$ curve has significant values well above the magnetic ordering temperature, with relevant contributions up to 50 K (Fig. 101 inset), but the integration between 2 and 50 K gains $\Delta S = 6.73$ J mol$^{-1}$K$^{-1}$ , which is ~50% of the theoretical value for the ordering of a 3$d^6$ cation like $Fe^{2+}$ ($R\ln(2S+1) = 13.38$ J mol$^{-1}$ for $S = 2$). The low integrated value seems to suggest the presence of additional processes of interaction within the material and complex interactions between magnetic cations, leading to a drop in entropy.

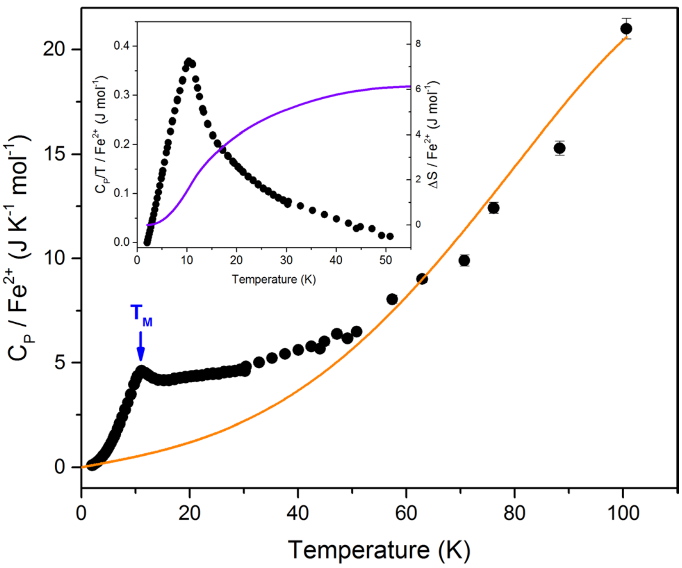


**Figure 101 – Heat capacity variation with the lattice contribution fitted by the polynomial $Cp = \gamma T + \beta T^3 + \delta T^5$ for γ-$Fe_2SiO_4$ and $T_{m1}$ marked. The inset plot shows Cp/T after subtraction of the lattice contribution and the curve shows the integration of the magnetic entropy per $Fe^{2+}$ ion. Error bars are within the data point dimensions when not displayed.**

Overall, physical data are promising in terms of using γ-$Fe_2SiO_4$ as a structural and magnetic analogue of $Fe_2GeO_4$. A thorough neutron magnetic diffraction study is necessary to clarify the level of similarity between the two ground states.

## 4.3.3. Magnetic structure solution through neutron data

### *4.3.3.1. Data collection and structural characterisation*

The small quantity of product available from a high-pressure/high-temperature synthetic route limited the application of structural studies: the high-resolution of D2B could not be exploited, since it requires at least 1 g of powder, and the difficulty of recovering a sample from a capillary ruled out the use of synchrotron X-ray diffraction. The high-flux of D20, by contrast, is the best choice to acquire an intense structural and magnetic signal simultaneously from ~120 mg of sample.

Data collection and processing were performed with the aid of Dr Clemens Ritter, instrument scientist at the ILL facility.

The data from D20 were acquired at 90° take-off with λ = 1.54 Å at T = 1.8, 25 and 50 K; the wide angle of collection and shorter wavelength assure the acquisition of enough crystalline Bragg reflections to accurately refine the structure. The refinement of this data confirms the purity of the sample, apart from two easily discerned spurious peaks that are constant with temperature and can be ascribed to the cryostat. Moreover, there is no evidence of peak splitting or peak broadening in the dataset above and below the transition: the structure can be consistently refined as an *Fd-3m* spinel with no tetragonal distortion. The cubic structural refinement ($R_{wp}$ = 9.8%) gives cell parameter $a$ = 8.2195(3) Å, $x$ = 0.2416(1) and $B_{Fe}$ = 0.01(3) Å$^2$, $B_{Si}$ = 0.01(3) Å$^2$, $B_O$ = 0.10(4) Å$^2$. The results for the refinement of γ-$Fe_2SiO_4$ at 25 K are displayed in Fig. 102.

Data at 90° take-off angle, λ = 1.54 Å and T = 1.8 K have a clear sign of long range magnetic ordering in the low angle region. In order to obtain a better intensity and resolution on the magnetic signal, additional data were collected with 42° take-off angle at λ = 2.41 Å; long collections with improved statistic were performed at T = 1.8, 7 and 25 K, and a ramp collection spanned temperatures between 2.5 and 14 K in ~0.5 K steps. Ramp and base temperature data analysis will be provided in the next subsection, other temperature datasets are available in Appendix B2.

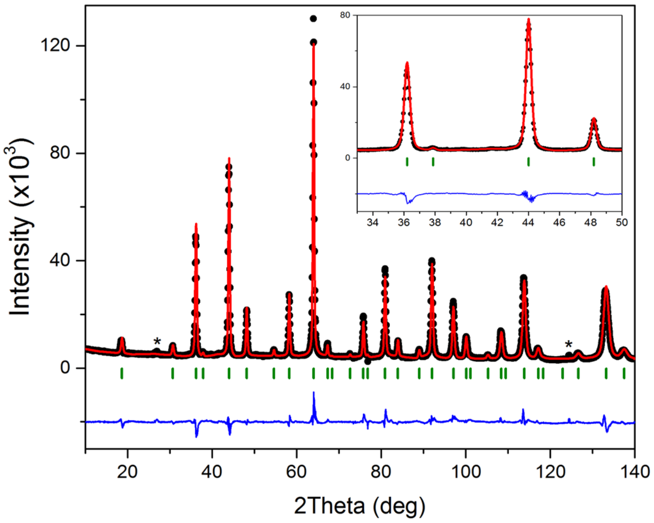


**Figure 102 – Fit of the cubic spinel model to neutron powder diffraction for γ-$Fe_2SiO_4$ with 90° take-off angle (λ = 1.54 Å) at 25 K. As shown in more detail in the inset centred on the 400 cubic reflection, no peak splitting or broadenings that would evidence a lattice distortion are observed; the features of this profile do not change with temperature reduction. Data are in black, fit is in red, difference curve is in blue and Bragg reflections are in green; a small non-magnetic impurity peak is labelled with an asterisk.**

#### *4.3.3.2. Data analysis*

Data at both take-off angles have clear signs of long-range magnetic ordering with onset at T < 12 K, corroborating DC susceptibility and heat capacity data and ruling out a full spin-glass behaviour. Below the transition temperature, a first group of peaks arises in the low-angle region. By T ~ 8 K the intensities of these peaks saturate but there is a stark appearance of a second, separate set of magnetic reflections that mark a second ordering in the sample, as already suggested by DC and AC susceptibility. Visual evidence of this process is provided in Fig. 103, in which the consistency of the structural model allows the subtraction of the Bragg peak intensities, constant at all temperatures, and highlights the appearance of the new reflections.

The first set of magnetic reflections is indexed using the positions in a difference curve 8 – 25 K for the 42° take-off dataset, after scaling the 25 K dataset in order to account for different statistics; this procedure aims to recognise reflections from the first ordering only. Symmetry analysis and magnetic structure solutions were performed in collaboration with Dr Angel Arevalo Lopez.

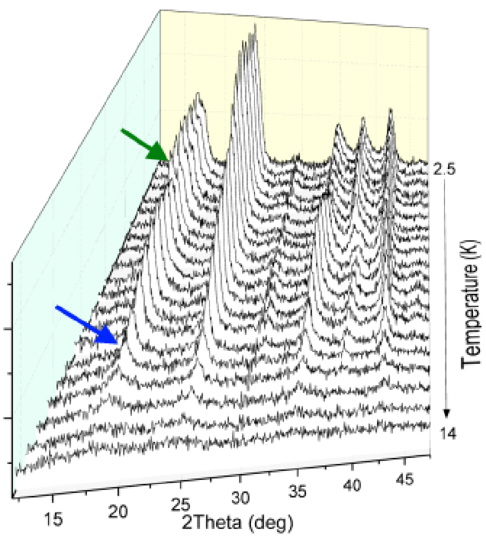


**Figure 103 – Magnetic scattering profiles between 2.5 and 14 K, recorded in ~0.5 K steps. The data are displayed as a difference curve ($T – T_{25K}$). The first set of magnetic reflection is highlighted with a blue arrow; the appearance of the second set of reflections is marked by a green arrow.**

Given the lack of structural distortion, these reflections may be considered as superstructure peaks of a cubic cell with refined cell parameters $a$ = 8.2204(1) Å at 25 K and they can be approximately associated with a propagation vector **k** = (¾ ¾ 0) through the use of the program k-search within the FullProf Suite. Whilst the magnetic peaks of the first phase are roughly commensurate close to the onset temperature, there is a marked shift in their position upon cooling, leading to a propagation vector more appropriately defined as $\mathbf{k_1}$ = (¾+δ ¾+δ 0). Applying this **k** to a *Fd-3m* structure in BasIrreps highlights the presence of two magnetically distinct sites arising from a single crystallographic position: the iron in the crystal structure is in (½ ½ ½), but the magnetic symmetry distinguishes them into Fe1 = (½ ½ ½) and Fe2 = (¾ 0 ¼).

Once the first set of peaks is correctly indexed, peaks arising from the second ordering of the sample can be indexed in the difference curve of 2 – 25 K data for the 42° takeoff dataset. Using the same approximate cell parameters and the cubic *Fd-3m* cell, the additional reflections index on a commensurate $\mathbf{k_2}$ = (1 0 0) propagation vector.

Although the second phase has different ordering features from the ones observed in $Fe_2GeO_4$, the first phase shows a marked similarity. As such, the magnetic intensities from each transition are fitted by a double-*k* model in which different propagation vectors $\boldsymbol{k}_{1\_j}$ apply to sites Fe*j* (*j* = 1 or 2): $\boldsymbol{k}_{1\_1}$ = (¾+$\delta_1$ -¾-$\delta_1$ 0) and $\boldsymbol{k}_{1\_2}$ = (¾+$\delta_1$ ¾+$\delta_1$ 0) with δ ~ 0.03 at 2 K. The irreducible representations generated for these vectors are listed in Table 16.

**Table 16 – Irreducible representations and basis vectors (BV) for the $T_{m1}$ = 13 K magnetic ordering of γ-$Fe_2SiO_4$ with propagation vectors $k_{1\_1}$ = (¾+$\delta_1$ -¾-$\delta_1$ 0) and $k_{1\_2}$ = (¾+$\delta_1$ ¾-$\delta_1$ 0). The two magnetically independent atoms are Fe1 at (½,½,½) and Fe2 at (¾,0,¼). Symmetry-related positions are generated by the operators 1: (x,y,z), 2: (x+ ¼ ,y+ ¾ ,-z+ ½ ). Only the active representations are displayed for clarity; the full list of irreducible representation for both sites with both orientation of the vector are available in Appendix B2.**

Propagation vector $\mathbf{k}_{11}$

| Irreps | $\Gamma_3$ | | |
|---|---|---|---|
| BV | $\psi_1$ | | $\psi_2$ |
| Atom | $m_x$ | $m_y$ | $m_z$ |
| Fe1_1 | 1 | 1 | 1 |
| Fe1_2 | $-\frac{\sqrt{2}}{2}+\frac{i\sqrt{2}}{2}$ | $-\frac{\sqrt{2}}{2}+\frac{i\sqrt{2}}{2}$ | $\frac{\sqrt{2}}{2}-\frac{i\sqrt{2}}{2}$ |

Propagation vector $\mathbf{k}_{12}$

| Irreps | $\Gamma_2$ | | |
|---|---|---|---|
| BV | $\psi_1$ | | $\psi_2$ |
| Atom | $m_x$ | $m_y$ | $m_z$ |
| Fe2_1 | 1 | -1 | 1 |
| Fe2_2 | $i$ | $-i$ | $-i$ |

The correct choice of irreducible representations is achieved through trial and error. Two magnetic components for each sublattice were required to fit the intensities: the dominant component is in the *c*-direction and the second is in the *ab*-plane. However, since this magnetic structure has irreducible representations with non-zero imaginary components, there are two mathematically equivalent solutions that would fit the same coefficients, indistinguishable from powder diffraction data. As such, there are two possible magnetic structures for $\mathbf{k_1}$: a canted magnetic structure, where both coefficients are treated with their corresponding real component of the irreducible representations, or an elliptical helix, where one coefficient has an imaginary component (whether it is the *c* coefficient or the *ab* coefficient makes no difference to the results) (Fig. 104). The basis vectors and refined coefficients associated with both solutions are listed in Table 17.

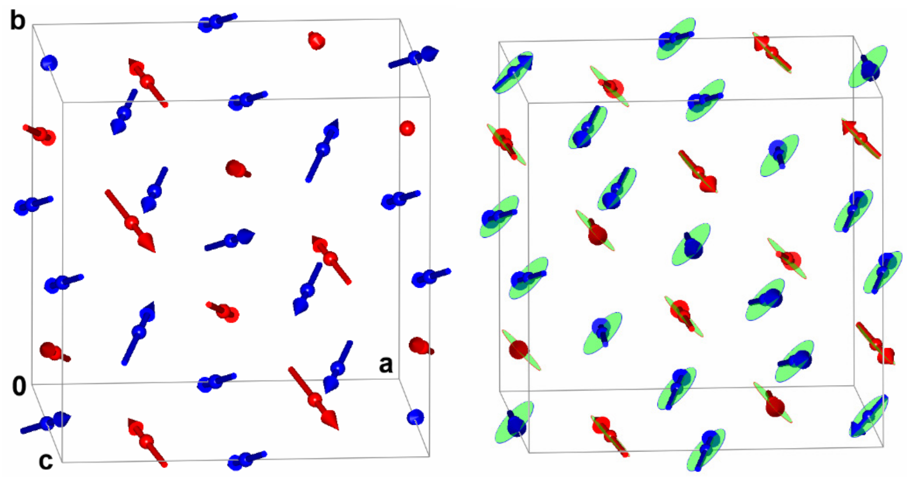


**Figure 104 – (Left) Canted model for the $k_1$ = (¾+$\delta_1$ ¾+$\delta_1$ 0) order observed below $T_{m1}$, showing Fe1 (blue) and Fe2 (red) moments. (Right) Elliptical helix model for the k1 order, showing the planes of rotation for the moments.**

**Table 17 – Refined components and resultant moments for the $T_{m1}$ = 13 K k1 magnetic ordering of γ-$Fe_2SiO_4$ at 1.8 K following the symmetry analysis in Table 3. Two combinations of the BVs give equivalent fits to the data. Model 1, the canted magnetic structure shown in Fig. 26 left, uses the combination $\psi_1 + \psi_2$ for both irreducible representations and has moments varying between 0 and 2.77(9) $\mu_B$. Model 2 describes an elliptical helical magnetic structure as shown in Fig. 26 right, using the combination $i\psi_1 + \psi_2$ for both irreducible representations and has moments varying between 1.22(6) and 2.49(7) $\mu_B$.**

| Atom | P.V. | IrRep:BV | $\mu_x$ ($\mu_B$) | $\mu_y$ ($\mu_B$) | $\mu_z$ ($\mu_B$) |
|---|---|---|---|---|---|
| Fe1_1 | $k_{1\_1}$ | $\Gamma_3$: $\psi_1$, $\psi_2$ | 0.86(4) | 0.86(4) | 2.49(7) |
| Fe2_1 | $k_{1\_2}$ | $\Gamma_2$: $\psi_1$, $\psi_2$ | 0.86(4) | 0.86(4) | 2.49(7) |

The $\mathbf{k}_2$ phase is fitted as an additional magnetic phase, and the representation that leads to the best fit has moments having a '2-in 2-out' spin ice order: for each $B_4$ tetrahedron in the structure, two spins point towards and two away from the centre (Fig. 20). The irreducible representations generated by the application of a $\mathbf{k}_2$ vector to a *Fd-3m* lattice of $Fe^{2+}$ cations are listed in Table 18.

The coefficients necessary to obtain this model have components along *x* and along *yz*, refined simultaneously and initially left unconstrained. However, given their very small divergence from the perfect direction and the fact that the magnetic diffraction from this phase overlaps with the $k_1$ reflections in multiple points of the pattern, it was deemed more appropriate to constrain them along the body diagonals of the tetrahedra; this constraint relates the magnitude of the coefficient to its angular dependence, so that the coefficient along *x* locks with the one along *yz* with a factor of √2 ($m_x = m_{yz}/\sqrt{2}$). The final refinement uses Γ2:$\psi_4$ and Γ2:$\psi_5$, with refined components $m_x(\psi_4) = m_{yz}(\psi_5)/\sqrt{2} = 0.92(3)\ \mu_B$ at 1.8 K. The total resulting moment is 1.29(4) $\mu_B$. The model of the $k_2$ phase is depicted in Figure 105.

**Table 18 – Symmetry analysis for the magnetic ordering of γ-$Fe_2SiO_4$ in cubic *Fd-3m* setting with propagation vector $k_2$ = (1 0 0). The magnetic atom is Fe1 at (0.5, 0.5, 0.5). Symmetry-related positions are generated by the operators 1: (x,y,z), 2: (-x+ ½ ,-y,z+ ½ ), 3: (y+ ¼ ,x+ ¾ ,-z+ ¼ ), 4: (-y+ ¼ ,-x+ ¼ ,-z+ ¾ ).**

| IrRep | $\Gamma_2$ | | | | | | | | | |
|---|---|---|---|---|---|---|---|---|---|---|
| BV | $\psi_1$ | $\psi_2$ | | $\psi_3$ | | $\psi_4$ | $\psi_5$ | | $\psi_6$ | |
| Atom | $m_x$ | $m_y$ | $m_z$ | $m_y$ | $m_z$ | $m_x$ | $m_y$ | $m_z$ | $m_y$ | $m_z$ |
| Fe1_1 | 1 | 1 | 1 | 1 | 1 | 1 | 1 | 1 | 1 | 1 |
| Fe1_2 | -1 | -1 | 1 | -1 | 1 | 1 | 1 | -1 | 1 | -1 |
| Fe1_3 | -1 | 1 | -1 | 1 | -1 | 1 | -1 | 1 | -1 | 1 |
| Fe1_4 | 1 | -1 | -1 | -1 | -1 | 1 | -1 | -1 | -1 | -1 |

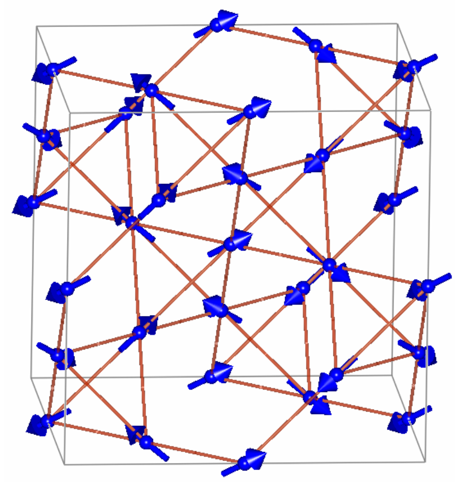

**Figure 105 – The additional $k_2$ = (1 0 0) ordered spin ice phase observed below $T_{m2}$. The pyrochlore lattice is outlined in brown, the two-in two-out moments, with constant magnitude, are in blue.**

The combined Rietveld refinement including crystal phase and the two magnetic phases is shown in Figure 106. Given the better resolution in the Bragg diffraction region, the 90° take-off dataset with λ = 1.54 Å was taken as the reference point for structural parameters ($a$ = 8.2080(3) Å, $x$ = 0.2402(3) and $B_{Fe}$ = 0.01(3) Å$^2$, $B_{Si}$ = 0.01(3) Å$^2$, $B_O$ = 0.10(4) Å$^2$, $R_{wp}$ = 9.3%); the 42° take-off dataset with λ = 2.41 Å was taken as the reference point for the previously reported magnetic refinement parameters, and has a $R_{mag1}$ = 4.23% for the $\mathbf{k}_{i1}$ phase and $R_{mag1}$ = 6.69% for the $\mathbf{k_2}$ phase.

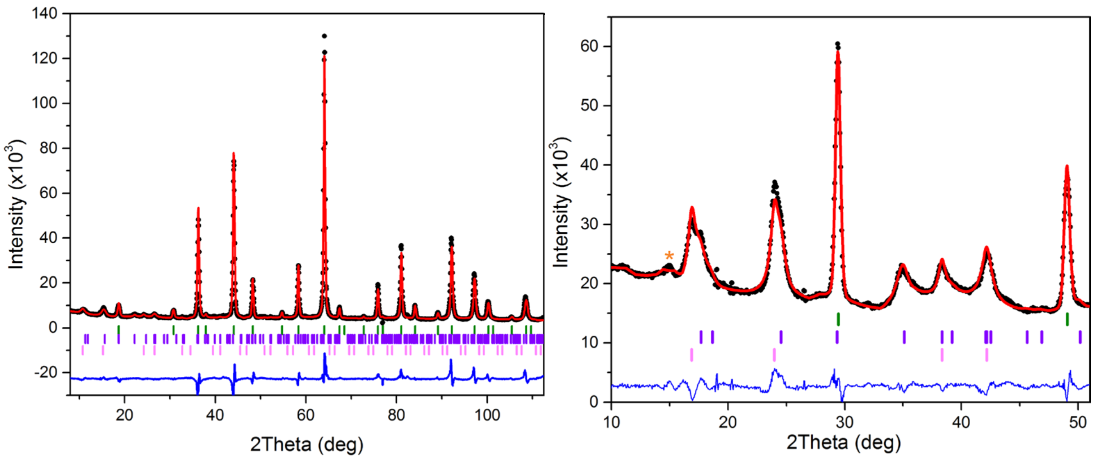


**Figure 106 – Fit of the crystal and magnetic structures at 2 K, to D20 data at 2K with 90° takeoff angle (left) and 42° takeoff angle (right). Experimental data are in black, fits are in red, difference curve is in blue. Magnetic reflection markers are in violet (ki1) and pink (k2), and structural reflections are in green. A weak impurity peak in the 42° takeoff dataset is labelled with an asterisk.**

Given the nature of magnetic refinement from powder diffraction with multiple phases, the phase fractions cannot be independently determined; however, it can be derived by normalising the moment magnitudes to the total number of Fe in pure γ-$Fe_2SiO_4$. At 1.8 K, the maximum amplitudes in the canted description (vector $\mathbf{k_1}$, 2.77(9) $\mu_B$) and the spin-ice phase (vector $\mathbf{k_2}$**,** 1.29(4) $\mu_B$) sum up to 4.1(1) $\mu_B$; as a consequence, the sample comprises of 68% of the $\mathbf{k_1}$ and 32% $\mathbf{k_2}$ phase, both with ideal (maximum) moment values of 4.0 $\mu_B$. Moment magnitudes vary between 0 and 4.0 $\mu_B$ in the canted model and between 1.8 and 3.6 $\mu_B$ for the elliptical helical model for the $\mathbf{k_1}$ phase, and are instead constant at 4.0 $\mu_B$ in the $\mathbf{k_2}$ phase.

The evolution of both phases can be followed through sequential refinements of diffraction patterns collected as a function of temperature. The parameters followed were the total magnitude of the moment (arising from both magnetic coefficients in each phase) and the incommensurate shift of $\mathbf{k}_1$. The outcome is summarised in Fig. 107.

It can be noted that the incommensurability of $\mathbf{k_1}$ is small at a temperature close to the transition, so the vector starts as commensurate ($\mathbf{k}$ = (¾ ¾  0)) and assumes an increasingly incommensurate behaviour upon cooling, stabilising at δ ~ 0.03 below the onset of the second transition.

The evolution of the magnetic amplitude, proportional to the appearance of magnetic scattering, can be correlated with an experimental transition temperature through a critical fit:

$$\mu = \mu_0 \left(1 - \frac{T}{T_m}\right)^{\beta}$$

The first magnetic transition data were fitted at T > 8 K with $\beta_1$ = 0.18(5) and $T_{M1}$ = 11.2(4) K. The second magnetic transition data were fitted at T > 5.5 K with $\beta_2$ = 0.18(1) and $T_{M2}$ = 7.48(2) K.

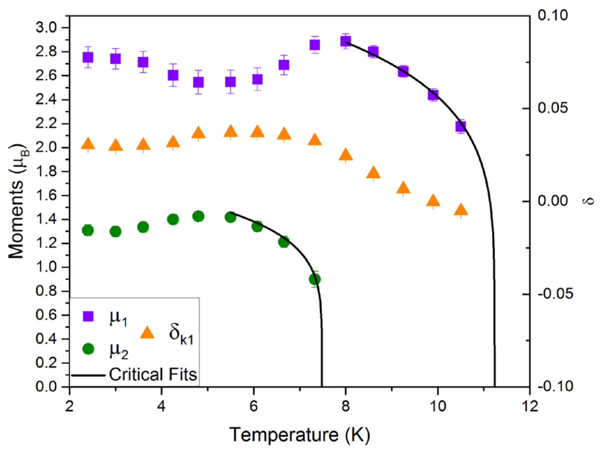


**Figure 107 – Temperature variations of the magnetic moments μ and propagation vector contributions δ for the two magnetic phases of γ-$Fe_2SiO_4$, with associated critical fit profile. Error bars are within the data point dimensions when not displayed.**

The overall results outline another complex magnetic ordering, comprising of multiple magnetic phases, in accordance with physical characterisation. The ordering features of this material are, however, surprisingly complex and not perfectly overlapping with $Fe_2GeO_4$. The main outcomes and their relevance are summarised in the following section.

#### *4.2.4.4 Summary of results*

The magnetic ordering in γ-$Fe_2SiO_4$ presents several points of similarity with its germanium spinel analogue, in both physical behaviour and features extracted from the magnetic neutron diffraction. However, it has additional complexities that challenge a direct interpretation as a frustration wave ordering example.

DC and AC susceptibility data show clear signs of two long-range ordering transitions: the first one at $T < 12$ K has an antiferromagnetic behaviour, confirmed by the hysteresis loop at 8 K, but a very modest Weiss temperature that does not suggest the presence of a prominent frustration. The second one at $T < 7$ K is accompanied by ZFC-FC splitting which, paired with the opening of the hysteresis at 2 K, is compatible with ferromagnetic contributions to the magnetism.
Whilst these features are compatible with $Fe_2GeO_4$, the AC susceptibility around 12 K has a slight frequency dependence of the profile, usually a sign of spin glass behaviour. This dynamism could either arise from the residual disordered spins of the first ordering, or from the part of the spins that acquire long range order at $T < 7$ K.
Although the second transition is not clearly detected by heat capacity measurements in this case, the integrated entropy is again markedly reduced (~50%) from its theoretical value.

The presence of two transitions is corroborated by the appearance of two sets of magnetic reflections, one at $T_{M1} = 11.2(4)$ K and the other at $T_{M2} = 7.48(2)$ K, neither of which is accompanied by a structural distortion from cubic to tetragonal.
The onset of the first transition is in keeping with what has been reported from physical measurements in the literature. The peaks index with propagation vector $\mathbf{k_1} = (¾+\delta\ ¾+\delta\ 0)$ with $\delta_1 \sim 0.03$, similar to the $(⅔+\delta_1\ ⅔+\delta_1\ 0)$ with $\delta_1 \sim -0.025$ of $Fe_2GeO_4$; whereas in the germanium sample the incommensurability is basically constant, in the silicate the vector starts with $\delta \sim 0$ and becomes more incommensurate while approaching the second transition, stabilising after its appearance. The second transition has never been reported previously, and its magnetic diffraction peaks index with propagation vector $\mathbf{k_2} = (1\ 0\ 0)$.
These two transitions have two different magnetic structures and have been refined with two different magnetic phases.

Applying the first propagation vector to the structure generates irreducible representations for two distinct Fe sites (equivalent in the crystalline structure); in keeping with $Fe_2GeO_4$ the incommensurate modulation is imposed on two mutually perpendicular sublattices. However, the resulting magnetic structure is not collinear and can be represented by two models. The first one is a canted structure where the incommensurability induces a modulation of amplitudes between 0 and 4 $\mu_B$ over ~ 40 unit cells, similar to the one in $Fe_2GeO_4$. The second one is an incommensurate elliptical helix order where the modulation is reduced to the range 1.8 – 3.6 $\mu_B$, with no zero moments present. The two representations are mathematically equivalent and cannot be distinguished.

The second propagation vector does not split the iron sites in two different sublattices and the ordering of the iron moment on every B site can be fitted into a 2-in-2-out arrangement towards the centre of each $B_4$ tetrahedra and a constant moment magnitude of 4 $\mu_B$. This arrangement is generally known as "spin ice" configuration and is inherently ferromagnetic, thus explaining the signal splitting in DC ZFC-FC. However, it is also remarkably uncommon in transition metal oxides: it tends to be one of the preferred ordering types of rare-earth pyrochlores, like $Sm_2Mo_2O_7$ [209] and $Nd_2Mo_2O_7$, [210] where the exchange coupling interactions are weak and large dipolar interactions couple with local anisotropy. The only other example of spin ice ordering in transition metal oxides in the literature is the $V^{3+}$ sublattice of $FeV_2O_4$, although this phase is tetragonally distorted with both $Fe^{2+}$-$V^{3+}$ and $V^{3+}$-$V^{3+}$ magnetic interactions operating.[211]
The spins that acquire long-range ordering with the $\mathbf{k_2}$ vector may be interpreted as the disordered components that give a frequency-dependent behaviour at T = 12 K. Upon further cooling, the onset of the spin-glass phase orders all the remaining spins in the structure, and the second bent in AC susceptibility is not frequency-dependent.

Overall, the ground state of γ-$Fe_2SiO_4$ is evidently more complex than what was expected on the basis of the results for $Fe_2GeO_4$. The concurrent ordering of modulated wave state and spin ice phase requires a fine energy balance in a transition metal oxide system, and while the first ordering might be another example of frustration-wave driven state, there are additional and more subtle interactions at play.

# 4.4 Overall conclusions

In this chapter, $Fe_2GeO_4$ and γ-$Fe_2SiO_4$ have been proven to undergo long-range magnetic ordering and the magnetic structures of both compounds have been presented.

$Fe_2GeO_4$ has a prominent ordering below $T_{m1}$ = 8.6(2) K ($\mathbf{k_1}$ = (⅔+$\delta_1$ ⅔+$\delta_1$ 0) with $\delta_1$ = -0.025(1)) and an additional ordering at $T_{m2}$ = 7.2(2) K ($\mathbf{k_2}$ = (⅔ ⅔ 0)), and it remains structurally cubic down to base temperature. The resulting ground state is a collinear antiferromagnet with moments ordered in the [110] plane. The incommensurability of $\mathbf{k_1}$ is reflected in an amplitude modulated magnetic structure, with magnitude of the moments spanning from μ = 4.05(8) $\mu_B$ to 0 $\mu_B$ over 33 unit cells; this arrangement is slightly canted either away from the *ab* plane diagonal or along the *c* direction under $T_{m2}$.
γ-$Fe_2SiO_4$ has a first ordering at $T_{M1}$ = 11.2(4) K ($\mathbf{k_1}$ = (¾+δ ¾+δ 0) with $\delta_1$ ~ 0.03) and the other at $T_{M2}$ = 7.48(2) K ($\mathbf{k_2}$ = (1 0 0)). The ground state has 62% of $\mathbf{k_1}$ phase, which is either a canted modulated structure on two perpendicular sublattices with moments between 4 $\mu_B$ and 0 over 40 unit cells or a helical structure with moments between 1.8 – 3.6 $\mu_B$, and 38% of $\mathbf{k_2}$ phase, which is a 2-in-2-out spin ice phase with constant saturated moments.

The ordering of both materials is highly unconventional for transition metal oxides, which tend to remove frustrated interactions by distorting the lattice from cubic to tetragonal, and the associated propagation vectors are equally unique. Focusing on just the $\mathbf{k_1}$ orders, the peculiar magnetic behaviour could be systematised in terms of exchange interactions between ordered spin components in one sublattice mediated by dynamic components of their neighbours in the other: orbital states fluctuate in a highly-correlated manner (without localisation or orbital order) in *n* layers $B_4$ tetrahedra; the alternation of configurations, where one layer is A type with unfrustrated spins and the other fluctuates between A and O, leads to a generic $\boldsymbol{k} = (\frac{n}{n+1}\ \frac{n}{n+1}\ \ 0)$ modulation. The magnetic structure of $Fe_2GeO_4$ has *n* = 2, γ-$Fe_2SiO_4$ has *n* = 3, and in both materials the propagation vector modulates the degree of frustration and the amplitude of moments as long-range ordered quantities.

A “frustration wave” type of ordering has been detailed for $Fe_2GeO_4$ in Section 4.2.4.5, and the fundamentals could be applied to the $T_{m1}$ ordering of γ-$Fe_2SiO_4$ in its modulated canted structure. However, the mathematically equivalent possibilities of a helical order and the

observation of a spin ice phase competing with the frustration wave state reveals a finer energy balance between two competing and different ground states. As such, using γ-$Fe_2SiO_4$ as a direct equivalent to $Fe_2GeO_4$ would not be feasible.
A more direct comparison could be derived from the reported magnetic structure of $Ca_3Co_2O_6$, which is still a $3d^6$ frustrated lattice but in a rhombohedral *R-3m* arrangement instead of an *Fd-3m* spinel.

Overall, the magnetic characterisation work for both materials is a very successful application of physical and structural methods to unveil the nature of spin ordering in iron containing spinel. The resulting magnetic structures are unconventional and previously unpredicted.

# 5. CONCLUSIONS AND FUTURE DIRECTIONS

This thesis reported the ordering phenomena that occur in iron-containing transition metal oxides with spinel structure in light of their charge, orbital and spin degrees of freedom. The two main line of work involved the exploration of the Verwey phase of magnetite, $Fe_3O_4$, and the magnetic structure solution of two normal spinel oxides, $Fe_2GeO_4$ and γ-$Fe_2SiO_4$.

Chapter 3 was dedicated to $Fe_3O_4$ and the study of the evolution of its distorted monoclinic phase as a function of doping.
Doping of magnetite was achieved by using a natural sample, inherently impure around 0.05% ($T_V$ = 119 K), and two synthetic samples, off-stoichiometric with deviation 3δ ~ 1.2% ($T_V$ = 102 K) and Zn-doped with 3% Zn content ($T_V$ = 90 K). Microcrystal diffraction acquired at T = 90 K and T = 80 K proves that all samples distort below the transition temperature. There is no evidence for further lowering of symmetry from the monoclinic *Cc* superstructure recently disclosed for pure magnetite[26] and no change in the order of the phase transition, first order throughout the range, is detected. The three-site orbital molecules ("trimerons") are present in every sample, but the doping induces charge disorder that reflects in an incremental loss of distortion features. In comparison to the perfectly stoichiometric magnetite (average trimeron length $\langle T \rangle$ = 5.780(2) Å), trimerons in the doped structures elongate up to 0.07 Å in the series ($\langle T \rangle_{nat}$ = 5.786(2) Å, $\langle T \rangle_{3\delta}$ = 5.821(2) Å, $\langle T \rangle_{Zn}$ = 5.846(2) Å). Moreover, the Zn-doped sample has evidence of a localised oxidation effect on a previously divalent-like B site, which reflects in the loss of one polaron. This study represents the first unconstrained structural analysis of doped magnetite microcrystals with high-resolution X-ray diffraction. Previous assumptions in the literature, for which samples with 1.2% doping and more have a second order structural behaviour and lack of structural transition[149], were therefore disproven. A new physical reasoning for the lowering of transition temperature is proposed with the elongation of

trimerons as an effect of charge disorder, but the Verwey phase of magnetite proved to be remarkably stable to doping.

Following literature reports on anomalies related to the Verwey transition up to room temperature and above, the evolution of the trimeron-ordered ground state as a function of temperature was followed with Pair Distribution Function analysis on pure magnetite from T = 90 K to T = 923 K. The analysis successfully proved that, whilst the long-range ordered distorted structure is only obtained below $T_V$ = 125 K, the trimerons that characterise it remain locally interacting to almost seven times the long-range ordering temperature; the fully disordered cubic spinel only represents the true minimum both at short- and long-range above the Curie temperature of paramagnetic onset ($T_C \approx 860$ K). Persistence of orbital molecule on the local scale was already reported for other transition metal oxide spinels with similar metal-metal clustering, but this is the first case in which a complete decoupling of the interactions is observed and correlated at the loss of the spin degrees of freedom. Future analysis on the presented data will attempt to explore the length scale evolution of this feature when considering the PDF fit over the first, second, and third unit cell distance; this will provide a direct comparison with literature diffuse scattering data that estimate the length of correlation to be around 1 unit cell at 298 K.[164] Overall, these results provide new important insights on the behaviour of orbital molecules, not only in terms of formation and disruption but also in relationship to the effect of doping. This knowledge may prove important with the aim of applying these new cooperative ordering ground states to information technology and “orbitronics” applications.

Future directions in this line of research might involve studying new phases with edge-sharing or face-sharing octahedral networks that have the possibility for orbital molecule formation. In particular, chains of Ti or V octahedra are featured in the triclinic $Ti_4O_7$[212] and $V_4O_7$,[213] also known as Magneli phases, and the effect of doping in these structures could also be explored.[214]

Chapter 4 was dedicated to the magnetic structure solutions of $Fe_2GeO_4$ and its high-pressure silicon analogue, γ-$Fe_2SiO_4$. Both samples have two sequential transitions: a prominent antiferromagnetic one (T = 8.6 K for $Fe_2GeO_4$ and T = 11.2 K for γ-$Fe_2SiO_4$) and an additional ferromagnetic one (T = 7.2 K for $Fe_2GeO_4$ and T = 7.5 K for γ-$Fe_2SiO_4$). Magnetic neutron diffraction at multiple temperatures proved that both materials undergo long-range magnetic ordering, with appearance of additional magnetic peaks, without any structural distortion from the cubic *Fd-3m* structure.

In $Fe_2GeO_4$, the first ordering follows the incommensurate propagation vector $\mathbf{k_1}$ = (⅔+$\delta_1$ ⅔+$\delta_1$ 0) with $\delta_1$ = 0.025(1) on two mutually perpendicularly iron sublattices; the second ordering represents a canting of the incommensurate structure with commensurate $\mathbf{k_2}$ = (⅔ ⅔ 0). This structure is particularly interesting because it presents a modulation of the moment magnitude, which goes from saturation (4 $\mu_B$) to 0 over 33 unit cells. In order to explain this effect, a "frustration wave" model is proposed. In this model, the degree of frustration is an ordered quantity in itself and can be distributed throughout the structure by the interaction of spin and orbital degree of freedom.

In γ-$Fe_2SiO_4$ the first ordering follows the incommensurate propagation vector $\mathbf{k_1}$ = (¾+δ ¾+δ 0) with $\delta_1$ ~ 0.03 on two mutually perpendicular sublattices; data can be fitted with either a spin modulated structure (as in $Fe_2GeO_4$) or a helical structure (with less modulation). The second ordering follows a commensurate $\mathbf{k_2}$ = (1 0 0) propagation, corresponding to a spin-ice ferromagnetic phase; this phase is characteristic of rare-earth pyrochlore lattices and it has never been observed in a structure with only one transition metal oxide.

These results significantly expand the literature, which had no complete report on the magnetic structures of both materials and usually sees them as purely antiferromagnetic below the ordering temperature. The frustration wave order model might provide new insights on the effect of frustration on materials that do not contain *f*-block cations and have a significant orbital contribution to the magnetism.

Future directions involve exploring new phases that might show similar ordering, in particular "spinelloid" phases in which doping and high-pressure result in a partial distortion of the spinel structure, with modified *ccp* stacking sequence. In particular, the $Fe_3O_4$-$Fe_2SiO_4$ composition diagram at high pressure has several spinelloid phases that have never been explored in their low temperature magnetic and structural behaviour.[215] Moreover, $Fe_2GeO_4$ and $Fe_2SiO_4$ have solubility in the spinel stability region at high-pressure,[216] and this could also be explored in terms of modification of the two magnetic structures disclosed in this work.

# REFERENCES

[1] Müller, K. A., and Burkard, H. "$SrTiO_3$: An intrinsic quantum paraelectric below 4 K". *Phys. Rev. B* **19**, 3593 (1979)
[2] Sreedhar, K., *et al.* "Electronic properties of the metallic perovskite $LaNiO_3$: correlated behavior of 3d electrons". *Phys. Rev. B* **46**, 6382 (1992)
[3] Vijatović, M. M., Bobić, J. D., and Stojanović, B. D. "History and challenges of barium titanate: Part II"
*Sci. Sint.* **40**, 235-244 (2008)
[4] Kobayashi, K. I., Kimura, T., Sawada, H., Terakura, K., and Tokura, Y. "Room-temperature magnetoresistance in an oxide material with an ordered double-perovskite structure". *Nature* **395**, 677 (1998)
[5] Shirk, B. T., and Buessem, W. R. "Temperature dependence of $M_s$ and $K_1$ of $BaFe_{12}O_{19}$ and $SrFe_{12}O_{19}$ single crystals". *J. Appl. Phys*. **40**, 1294-1296 (1969)
[6] Anderson, P. W. "The theory of superconductivity in the high-$T_c$ cuprate superconductors" (Vol. 446). Princeton, NJ: Princeton University Press (1997)
[7] Rao, C. N. R. "Transition metal oxides". *Annu. Rev. Phys. Chem.* **40**, 291-326 (1989)
[8] Valchev, V. C., and Van den Bossche, A. "Inductors and transformers for power electronics". *CRC press*. (2005)
[9] Goldman, A. "Ferrites for Magnetic Recording" in "Modern Ferrite Technology", 353-373. *Springer* (2006)
[10] Dionne, G. F. "A review of ferrites for microwave applications". *Proceedings of the IEEE* **63**, 777-789. (1975)
[11] Buschow, K. H. J. "Magnetism and processing of permanent magnet materials" in *Handbook of Magnetic Materials* **10**, 463-593. (1997)
[12] Hill, R. J., Craig, J. R., and Gibbs, G. V. "Systematics of the spinel structure type". *Phys. Chem. Miner.* **4**, 317-339 (1979)
[13] Bragg, W. H. "The structure of magnetite and the spinels". Nature **95**, 561. (1915)
[14] Roth, W. L. "The magnetic structure of $Co_3O_4$". *J. Phys, Chem, Solids* **25**, 1-10. (1964)
[15] Jarosch, D. "Crystal structure refinement and reflectance measurements of hausmannite, $Mn_3O_4$". Miner. Petrol. **37**, 15-23.
[16] Néel, L. "Magnetic properties of ferrites: ferrimagnetism and antiferromagnetism". *Ann. Phys*, 3, 137-198. (1948)
[17] Shull, C.G., Wollan, E.O. and Koehler, W.C. "Neutron scattering and polarization by ferromagnetic materials". *Phys Rev B* **4**, 912–921. (1951)
[18] Zaliznyak, I. A. "Spin Structures and Spin Wave Excitations" in Handbook of Magnetism and Advanced Magnetic Materials, *Wiley Online Library* (2007)
[19] Drabble, J. R., Whyte, T. D., and Hooper, R. M. "Electrical conductivity of magnetite at low temperatures". *Solid State Commun*. **9**, 275-278. (1971)
[20] Yanase, A., and Siratori, K. "Band structure in the high temperature phase of $Fe_3O_4$". *J. Phys. Soc. Jpn* **53**, 312-317. (1984)
[21] Wasilewski, P. and Kletetschka, G. "Lodestone: Nature's only permanent magnet-What it is and how it gets charged". *Geophys. Res. Lett*. **26**, 2275-2278. (1999)
[22] Blackman, M. "The Lodestone: a Survey of the History and the Physics". *Contemp. Phys.* **24**, 319-331. (1983)
[23] Kirschvink, J. L., Jones, D. S., and MacFadden, B. J. "Magnetite biomineralization and magnetoreception in organisms: a new biomagnetism" (Vol. 5). *Springer Science & Business Media*. (2013)

[24] Verwey, E. J. W. "Electronic conduction of magnetite ($Fe_3O_4$) and its transition point at low temperatures" *Nature* **144**, 327-328. (1939)
[25] Moskowitz, B. M., Frankel, R. B., and Bazylinski, D. A. "Rock magnetic criteria for the detection of biogenic magnetite". *Earth Planet. Sci. Lett*. **120**, 283-300. (1993)
[26] Senn, M. S., Wright, J. P., and Attfield, J. P. "Charge order and three-site distortions in the Verwey structure of magnetite". *Nature* **481**, 173-176. (2012)
[27] Smit, J. and Wijn, H. P. J. "Les Ferrites". *Bibliotheque Technique Philips*, Dunod, Paris. (1961)
[28] Cullity, B. D. "Introduction to Magnetic Materials". *Addison-Wesley*, Massachusetts. (1972)
[29] Zhang, J., et al. "Catalytic Activity of Titanomagnetite in Heterogeneous Fenton Reaction: Contribution from Structural $Fe^{2+}$ and $Fe^{3+}$". *J. Nanosci. Nanotecho*. **17**, 7015-7020. (2017)
[30] Jin, S., and Wang, C. "Synthesis and first investigation of excellent lithium storage performances of $Fe_2GeO_4$/reduced graphene oxide nanocomposite". *Nano Energy* **7**, 63-71. (2014)
[31] Yamada, I., *et al*. "A Perovskite Containing Quadrivalent Iron as a Charge-Disproportionated Ferrimagnet". *Angew Chem Int Edit* **47**, 7032-7035. (2008)
[32] Rao, C. N. R., and Raychaudhuri, A. K. "Colossal magnetoresistance, charge ordering and other novel properties of manganates and related materials". In Advances In Chemistry: A Selection of CNR Rao's Publications (1994–2003) (pp. 133-174). (2003)
[33] Ikeda, N., et al. "Ferroelectricity from iron valence ordering in the charge-frustrated system $LuFe_2O_4$". *Nature* **436**, 1136-1138. (2005)
[34] Pinheiro, C. B., and Abakumov, A. M. "Superspace crystallography: a key to the chemistry and properties" IUCrJ 2, 137-154. (2015)
[35] Goodenough, J. B. "Magnetism and crystal structure in non-metals" (No. 62 863SR2). Massachusetts Inst Of Tech Lexington Lincoln Lab. (1962)
[36] Image modified from: https://chem.libretexts.org/Core/Inorganic_Chemistry/Crystal_Field_Theory/Crystal_Field_Theory
[37] Jahn, H. A., and Teller, E. "Stability of polyatomic molecules in degenerate electronic states. I. Orbital degeneracy." In Proceedings of the Royal Society of London A: Mathematical, Physical and Engineering Sciences (Vol. 161, No. 905, pp. 220-235). The Royal Society. (1937)
[38] Sturge, M. D. "The Jahn-Teller effect in solids". *Solid state Phys.* **20**, 91-211. (1968)
[39] Rao, C. N. R., Arulraj, A., Cheetham, A. K., and Raveau, B. "Charge ordering in the rare earth manganates: the experimental situation". *J. Phys-Condens Mat* **12**, R83.(2000)
[40] Chatterji, T., Fauth, F., Ouladdiaf, B., Mandal, P., & Ghosh, B., "Volume collapse in $LaMnO_3$ caused by an orbital order-disorder transition." *Phys Rev B* **68**, 052406. (2003)
[41] Radaelli, P. G., Cox, D. E., Marezio, M., and Cheong, S. W., "Charge, orbital, and magnetic ordering in $La_{0.5}Ca_{0.5}MnO_3$." *Phys Rev B* **55**, 3015. (1997)
[42] Schmidt, M., *et al.* "Spin Singlet Formation in $MgTi_2O_4$: Evidence of a Helical Dimerization Pattern". *Phys. Rev.* L **92**, 056402. (2004)
[43] Kimber, S. A., et al. "Valence bond liquid phase in the honeycomb lattice material $Li_2RuO_3$". *Phys. Rev. B* **89**, 081408. (2014)
[44] Senn, M. S., Arevalo-Lopez, A. M., Saito, T., Shimakawa, Y. and Attfield, J. P. "Nonmagnetic spin-singlet dimer formation and coupling to the lattice in the 6H perovskite $Ba_3CaRu_2O_9$". *J. Phys-Condens. Mat.* **25**, 496008. (2013)
[45] Kimber, S. A., *et al.* "Charge Order at the Frontier between the Molecular and Solid States in $Ba_3NaRu_2O_9$", *Phys. Rev.* L **108**, 217205. (2012).
[46] Knox, K. R., *et al.* "Local structural evidence for strong electronic correlations in spinel $LiRh_2O_4$", *Phys. Rev. B* **88**, 174114. (2013).
[47] Jin-no, T., Shimizu, Y., Itoh, M., Niitaka, S. and Takagi, H. "Orbital reformation with vanadium trimerization in $d^2$ triangular lattice $LiVO_2$ revealed by $^{51}V$ NMR". *Phys. Rev. B* **87**, 075135. (2013)
[48] Guignard, M., *et al.* "Vanadium Clustering/Declustering in P2–$Na_{1/2}VO_2$ Layered Oxide". *Chem. Mater.* **26**, 1538-1548. (2014)
[49] Takubo, K., *et al.*, "Orbital states of V trimers in $BaV_{10}O_{15}$ detected by resonant x-ray scattering". *Phys. Rev. B* **86**, 085141. (2012)
[50] Klein, Y., *et al.*, "Antiferromagnetic order and consequences on the transport properties of $Ba_4Ru_3O_{10}$". *Phys. Rev. B* **84**, 054439. (2011)

[51] Horibe, Y., *et al.*, "Spontaneous formation of vanadium "molecules" in a geometrically frustrated crystal: $AlV_2O_4$". *Phys. Rev.* L **96**, 086406. (2006)
[52] Browne, A. J., Kimber, S. A., and Attfield, J. P. "Persistent three-and four-atom orbital molecules in the spinel $AlV_2O_4$". *Phys. Rev.* M **1**, 052003. (2017)
[53] Browne, A. J., Lithgow, C., Kimber, S. A., and Attfield, J. P. "Orbital Molecules in the New Spinel $GaV_2O_4$." *Inorg. chem*. **57**, 2815-2822. (2018)
[54] Bernevig, B. A., Hughes, T. L., and Zhang, S. C. "Orbitronics: The intrinsic orbital current in p-doped Silicon". *Phys. Rev.* L **95**, 066601. (2005).
[55] Wold, A. and Dwight, K. "Solid state chemistry: synthesis, structure, and properties of selected oxides and sulphides". *Springer Science & Business Media*. (2012)
[56] Demazeau, G. "High pressures and chemical reactivity: an approach to the synthesis of novel materials". High Pressure Res. **28**, 483-489. (2008)
[57] Bridgman, P. W., "The resistance of 72 elements, alloys and compounds to 100,000 Kg/Cm$^2$" *Proc. Am. Acad. Arts Sci.* **81**, 165 (1952).
[58] https://www.voggenreiter-gmbh.de/en/services/laboratory-equipment/walker-type-modul/
[59] Walker, D., Carpenter, M. A. and Hitch, C. M., "Some simplification to multianvil devices for high-pressure experiments". *Am. Miner.* **75**, 1020. (1990)
[60] Walker, D. "Lubrication, gasketing, and precision in multianvil experiments". *Am. Miner.* **76**, 1092-1100. (1991)
[61] Image from http://www.seas.upenn.edu/~chem101/sschem/solidstatechem.html
[62] Giacovazzo, C. "Fundamentals of crystallography" (Vol. 7). *Oxford University Press*, USA. (2002)
[63] "International Tables for Crystallography". Volume A, Space-Group Symmetry. edited by Theo Hahn. Dordrecht, London. Published for the International Union of Crystallography by Kluwer Academic Publishers. (2002)
[64] Aroyo, M. I., Kirov, A., Capillas, C., Perez-Mato, J. M., and Wondratschek, H. "Bilbao Crystallographic Server. II. Representations of crystallographic point groups and space groups". *Acta Crys. A* **62**, 115-128. (2006)
[65] Landau, L. D. "On the theory of phase transitions". *Zh. eksp. teor. Fiz*, 7, 19-32. (1937)
[66] Haas, C. "Phase transitions in crystals with the spinel structure". *J. Phys. Chem. Solids* **26**, 1225-1232. (1965)
[67] Pitteri, M. and Zanzotto, G. "Continuum models for phase transitions and twinning in crystals". *CRC Press*. (2002)
[68] Kovalev, O.V, "Representation of the Crystallographic Space Groups. Irreducible Representations, Induced Representations and Corepresentations". 2nd Edition, Ed. by Harold T. Stokes and Dorian M. Hatch, *Gordon and Breach Science Publishers*, ISBN 2-88124-934-5 (1993)
[69] Image modified from http://cronodon.com/Atomic/Photon.html
[70] Krane, K. S., "Modern physics", 2nd Edition ISBN 0-471-82872-6. Wiley-VCH. (1995)
[71] Bragg, W.H., Bragg, W.L. "The reflexion of X-rays by crystals". *Proc. R. Soc. Lond. A* **88**, 428–38. (1913)
[72] Warren, B. E. "X-ray Diffraction". *Courier Corporation*. (1969)
[73] Egami, T., and Billinge, S. J. "Underneath the Bragg peaks: structural analysis of complex materials". Elsevier. (2003)
[74] Image modified from http://xray0.princeton.edu/~phil/Facility/Guides/MAD_example1.html
[75] Taylor G. "The phase problem". Acta Crys. D **59**, 1881. (2003)
[76] http://www.polycrystallography.com/XRDanalysis.html
[77] Dinnebier, R. E., and Billinge, S. J. (Eds.). "Powder diffraction: theory and practice". *Royal Society of Chemistry* (2008)
[78] https://www.bruker.com/products/x-ray-diffraction-and-elemental-analysis/x-ray-diffraction/d2-phaser/overview.html
[79] http://www.esrf.eu/about/synchrotron-science/synchrotron
[80] http://www.esrf.eu/UsersAndScience/Experiments/StructMaterials/ID11
[81] http://www.esrf.eu/id22
[82] Squires, G. L., "Introduction to the theory of thermal neutron scattering". *Cambridge University Press* (UK), 3rd ed., (2012)

[83] Sivia, D. S., "Elementary scattering theory for X-ray and neutron users". *Oxford University Press* (UK). (2011)
[84] Lovesey, S. W., "Theory of neutron scattering from condensed matter", vol. I., *Oxford University Press* (UK). (1986)
[85] Fernandez-Alonso, F. and Price D. L., "Experimental Methods in the Physical Sciences", "Neutron Scattering – Fundamentals" Volume 44, Pages 2-545, (2013)
[86] https://www.ill.eu/science-technology/about-neutrons/
[87] https://www.ill.eu/instruments-support/instruments-groups/instruments/d2b/description/instrument-layout/
[88] https://www.ill.eu/instruments-support/instruments-groups/instruments/d20/description/instrument-layout/
[89] Luger, P. "Modern X-ray Analysis on Single Crystals: A Practical Guide". *Walter de Gruyter*. (2014)
[90] Balke, A. J. et al., "*Crystal Structure Analysis Principles and Practice*". *Oxford Science Publications* (UK) (2009)
[91] http://www.ndsu.edu/chemistry/files/mcl/smart5_UserManual.pdf
[92] http://xray.tamu.edu/pdf/manuals/sadabs.pdf
[93] http://www.px.nsls.bnl.gov/crys/xprep/doc/xprep.pdf
[94] http://shelx.uni-ac.gwdg.de/SHELX/shelxl_user_guide.pdf
[95] Britton, D. "Estimation of twinning parameter for twins with exactly superimposed reciprocal lattices". *Acta Crystallogr.* **28**, 296-297. (1972)
[96] Rietveld, H., "A profile refinement method for nuclear and magnetic structures". J. Appl. Crystallogr. **2**, 65-71. (1969)
[97] Young, R. A., "The Rietveld Method". *Oxford University Press* (UK). (1995)
[98] Rodriguez-Carvajal J., "FULLPROF 2000: A Rietveld Refinement and Pattern Matching Analysis Program". Laboratoire Léon Brillouin (CEA-CNRS), France (2008). https://www.ill.eu/sites/fullprof/php/reference.html
[99] P. G. Radaelli, "Magnetic Structure Determination from Neutron Powder Diffraction Data" (Notes from course given at Consener's House, Abingdon, 2002). http://www.pcg-scmp.org/imagesFhj/8/8a/Magnetic_Rietveld_handouts.pdf
[100] Rodríguez-Carvajal, J., "Recent advances in magnetic structure determination by neutron powder diffraction". *Physica B* **192**, 55-69. (1993)
[101] Thorpe, M. F. (Ed.). "Local Structure from Diffraction". *Springer Science & Business Media*. (1998)
[102] Yue, X., Inoue, A., Liu, C. T., & Fan, C. "The development of structure model in metallic glasses". *Materials Research*, (AHEAD), 0-0. (2017)
[103] Juhás, P., Davis, T., Farrow, C. L., and Billinge, S. J. "PDFgetX3: a rapid and highly automatable program for processing powder diffraction data into total scattering pair distribution functions". *J. Appl. Crystallogr.* **46**, 560-566. (2013)
[104] Farrow, C. L., et al. "PDFfit2 and PDFgui: computer programs for studying nanostructure in crystals". *J Phys-Condens Mat* **19**, 335219. (2007)
[105] Mohn, P. "Magnetism in the solid state: an introduction", Vol. 134. *Springer Science & Business Media*. (2006)
[106] Goodenough, J. B. "An interpretation of the magnetic properties of the perovskite-type mixed crystals $La1-_{x}Sr_{x}CoO_{3-\lambda}$". *J. Phys. Chem. Solids* **6**, 287-297. (1958)
[107] Kanamori, J. "Superexchange interaction and symmetry properties of electron orbitals". *J. Phys. Chem. Solids* **10**, 87-98. (1959)
[108] Ji, S., *et al*. "Spin-lattice order in frustrated $ZnCr_2O_4$." Phys. Rev. L **103**, 037201. (2009)
[109] Tomiyasu, K., and Kagomiya, I. "Magnetic structure of $NiCr_2O_4$ studied by neutron scattering and magnetization measurements". *J Phys Soc Jpn* **73**, 2539-2542. (2004)
[110] Crangle, J. "Solid State Magnetism". *Springer Science & Business Media*. (2012)
[111] Ramirez, A. P. "Strongly geometrically frustrated magnets." *Annu. Rev. Mater. Sci*. **24**, 453-480. (1994)
[112] Neel L. "Magnetic properties of ferrites: ferrimagnetism and antiferromagnetism". *Ann. Phys. Paris* **3**, 137-98. (1948)
[113] Coey, J. M. D. and Venkatesan, M. "Half-metallic ferromagnetism: Example of $CrO_2$". *J. App. Phys.* **91**, 8345-8350. (2002)

[114] Rodic, D., Mitric, M., Tellgren, R., Rundlof, H. and Kremenovic, A. “True magnetic structure of the ferrimagnetic garnet $Y_3Fe_5O_{12}$ and magnetic moments of iron ions”. *J. Magn. Magn. Mater.* **191**, 137-145. (1999)
[115] Reehuis, M., Krimmel, A., Büttgen, N., Loidl, A. and Prokofiev, A. “Crystallographic and magnetic structure of $ZnV_2O_4$”. *Eur Phys J B* **35**, 311-316 (2003).
[116] Wills, A. S., Raju, N. P. and Greedan, J. E. “Low-Temperature Structure and Magnetic Properties of the Spinel $LiMn_2O_4$: A Frustrated Antiferromagnet and Cathode Material”. *Chem mater* **11**, 1510-1518 (1999).
[117] Ortega-San-Martin, L., Williams, A. J., Gordon, C.D., Klemme, S. and Attfield, J.P., “Low temperature neutron diffraction study of $MgCr_2O_4$ spinel”. *J Phys-Condens Mat* **20**, 104238 (2008)
[118] Diaz, S. et al., “Magnetic frustration in the spinel compounds $GeCo_2O_4$ and $GeNi_2O_4$”, *Phys. Rev. B* **74**, 092404 (2006)
[119] Zimmer, J. “Jog my shape memory: dynamics as a challenge in mathematical materials science”, *Phil. Trans. R. Soc. A* **364**, 3285-3300 (2006)
[120] Harris, M. J., Bramwell, S. T., McMorrow, D. F., Zeiske, T., and Godfrey, K. W. “Geometrical frustration in the ferromagnetic pyrochlore $Ho_2Ti_2O_7$”. *Phys. Rev. L* **79**, 2554. (1997)
[121] Ramirez, A. P., Hayashi, A., Cava, R. J., Siddharthan, R. and Shastry, B. S. “Zero-point entropy in ‘spin ice’”. *Nature* **399**, 333-335. (1999)
[122] Gingras, M. J. and McClarty, P. A., “Quantum spin ice: a search for gapless quantum spin liquids in pyrochlore magnets”. *Rep Prog Phys* **77**, 056501. (2014)
[123] P. A. Lee, “An end to the drought of quantum spin liquids”. *Science* **321**, 1306 (2008)
[124] Sherrington, D. “Spin glasses”. In *Physics Of Novel Materials* (pp. 146-204). (1999)
[125] MPMS Squid Manual: https://www.mrl.ucsb.edu/sites/default/files/mrl_docs/instruments/fundmanual.pdf
[126] http://hyperphysics.phy-astr.gsu.edu/hbase/Solids/Squid.html
[127] PPMS Manual: https://www.qdusa.com/sitedocs/productBrochures/1070-002.pdf
[128] S. Elliot, “The Physics and Chemistry of Solids”. *Wiley* (1998)
[129] C. Kittel and H. Kroemer, “Thermal Physics”. *W. H. Freeman* & Co. (1980)
[130] Verwey, E. J. W., Haayman, P. W. and Romeijn, C. W. “Physical Properties and Cation Arrangement of Oxides with Spinel Structures II. Electronic Conductivity”. *J. Chem. Phys.* **15**, 181 (1947)
[131] Anderson, P. W., “Ordering and antiferromagnetism in ferrites”. *Phys. Rev.* **102**, 1008. (1956)
[132] Chakraverty, B. K., “Charge ordering in $Fe_3O_4$, $Ti_4O_7$ and bipolarons”. *Phil. Mag. B* **42**, 473-478. (1980)
[133] Yamada, Y., “Charge ordering and lattice instability in magnetite”. In AIP Conference Proceedings (Vol. 24, No. 1, pp. 79-85). AIP. (1975)
[134] Seo, H., Ogata, M., and Fukuyama, H., “Aspects of the Verwey transition in magnetite”. *Phys. Rev. B* **65**, 085107. (2002)
[135] Van Den Brink, J., and Khomskii, D. I., “Multiferroicity due to charge ordering.” *J. Phys.: Condens. Matter* **20**, 434217. (2008)
[136] Walz, F., “The Verwey transition-a topical review”. *J. Phys. Condens. Matter* **14**, R285. (2002)
[137] Iizumi, M., and Shirane, G., “Crystal symmetry of the low temperature phase of magnetite”. *Solid State Commun*. **17**, 433-436.
[138] Yoshida, J., and Iida, S. “X-ray study of the phase transition in magnetite”. *J. Phys. Soc. Jpn.* **42**, 1627-1633. (1979)
[139] Iizumi, M., *et al*. “Structure of magnetite ($Fe_3O_4$) below the Verwey transition temperature.” *Acta Crys. B* **38**, 2121-2133. (1982)
[140] Wright, J. P., Attfield, J. P., & Radaelli, P. G. “Long range charge ordering in magnetite below the Verwey transition”. *Phys. Rev. L* **87**, 266401. (2001)
[141] Wright, J. P., Attfield, J. P., and Radaelli, P. G. “Charge ordered structure of magnetite $Fe_3O_4$ below the Verwey transition”. *Phys. Rev. B* **66**, 214422. (2002)
[142] Blasco, J., García, J., and Subías, G. “Structural transformation in magnetite below the Verwey transition.” *Phys. Rev. B* **83**, 104105.
[143] Nazarenko, E., *et al.* “Resonant X-ray diffraction studies on the charge ordering in magnetite”. *Phys. Rev. L* **97**, 056403. (2006)

[144] Joly, Y., et al. "Low-temperature structure of magnetite studied using resonant x-ray scattering." *Phys. Rev. B* **78**, 134110. (2008)
[145] Goff, R. J., Wright, J. P., Attfield, J. P., and Radaelli, P. G. "Resonant x-ray diffraction study of the charge ordering in magnetite". *J. Phys.: Condens. Matter* **17**, 7633. (2005)
[146] Wang, D., and Angel, R. J., "Octahedral tilts, symmetry-adapted displacive modes and polyhedral volume ratios in perovskite structures". *Acta Crys. B* **67**, 302-314. (2011)
[147] Yamauchi, K., Fukushima, T., and Picozzi, S.. Ferroelectricity in multiferroic magnetite $Fe_3O_4$ driven by noncentrosymmetric $Fe^{2+}/Fe^{3+}$ charge-ordering: First-principles study." *Phys. Rev. B* **79**, 212404. (2009)
[148] Senn, M. S., Loa, I., Wright, J. P., and Attfield, J. P. "Electronic orders in the Verwey structure of magnetite." *Phys. Rev. B* **85**, 125119. (2012)
[149] Senn, M. S., Wright, J. P., Cumby, J., and Attfield, J. P. "Charge localization in the Verwey structure of magnetite." *Phys. Rev. B* **92**, 024104. (2015)
[150] Honig, J. M. "Analysis of the Verwey transition in magnetite". *J. Alloy Compd*. **229**, 24-39. (1995)
[151] Kąkol, Z., *et al*. "The effect of doping on global lattice properties of magnetite $Fe_{3-x}Me_xO_4$ (Me= Zn, Ti and Al)". *J. Solid State Chem*. **192**, 120-126. (2012)
[152] M. D. Sturge, "Solid State Physics", edited by F. Seitz, D. Turnbull, and H. Ehrenreich (Academic Press, New York, 1967), Vol. 20.
[153] Palenik, G. J. "Bond valence sums in coordination chemistry using oxidation state independent $R_0$ values." *Inorg. Chem.* **36**, 122-122. (1997).
[154] Dearing, J. A., Bird, P. M., Dann, R. J. L., & Benjamin, S. F., "Secondary ferrimagnetic minerals in Welsh soils: a comparison of mineral magnetic detection methods and implications for mineral formation." *Geophys J Int* **130**, 727-736. (1997)
[155] Reed, S. J. B. "Electron microprobe analysis. Electron Microprobe Analysis", *Cambridge University Press* (1997)
[156] Kozłowski, A., Metcalf, P., Kąkol, Z., and Honig, J. M., "Electrical and magnetic properties of $Fe_{3-z}Al_zO_4$ (z< 0.06). *Phys. Rev. B* **53**, 15113. (1996)
[157] Park, S. K., Ishikawa, T., and Tokura, Y., "Charge-gap formation upon the Verwey transition in $Fe_3O_4$." *Phys. Rev. B* **58**, 3717. (1998)
[158] Shapiro, S. M., Iizumi, M. and Shirane, G., "Neutron scattering study of the diffuse critical scattering associated with the Verwey transition in magnetite ($Fe_3O_4$)." *Phys. Rev.* **B** 14, 200-207 (1976)
[159] Hoesch, M., *et al*., "Anharmonicity due to electron-phonon coupling in magnetite." *Phys. Rev. L* **110**, 207204. (2013)
[160] Taguchi, M., *et al.*, "Temperature dependence of magnetically active charge excitations in magnetite across the Verwey transition." *Phys. Rev. L* **115**, 256405. (2015)
[161] Huang, H. Y., *et al.*, "Jahn-Teller distortion driven magnetic polarons in magnetite." *Nature Comm*. **8**, 15929 (2017)
[162] Levy, D., Giustetto, R., and Hoser, A. (2012). "Structure of magnetite (Fe 3 O 4) above the Curie temperature: a cation ordering study." *Phys. Chem. Miner.* **39**, 169-176.
[163] Okudera, H., Kihara, K., and Matsumoto, T., "Temperature dependence of structure parameters in natural magnetite: single crystal X-ray studies from 126 to 773 K." *Acta Crys. B* **52**, 450-457. (1996)
[164] Bosak, A., *et al*. "Short-range correlations in magnetite above the Verwey temperature." *Phys. Rev. X* **4**, 011040. (2014)
[165] Goodenough, J. B., "Direct cation--cation interactions in several oxides." *Phys. Rev.* **117**, 1442. (1960)
[166] Attfield, J. P., Orbital molecules in electronic materials. *APL Mater.* **3**, 041510. (2015)
[167] Knox, K. R., *et al.,* "Local structural evidence for strong electronic correlations in spinel $LiRh_2O_4$." *Phys. Rev. B* **88**, 174114. (2013)
[168] Kimber, S. A., et al., "Valence bond liquid phase in the honeycomb lattice material $Li_2RuO_3$." *Phys. Rev. B* **89**, 081408. (2014)
[169] Kieffer, J., and Wright, J. P., "PyFAI: a Python library for high performance azimuthal integration on GPU". *Powder Diffr*. **28**, S339-S350. (2013)

[170] Juhás, P., Davis, T., Farrow, C. L., and Billinge, S. J., "PDFgetX3: a rapid and highly automatable program for processing powder diffraction data into total scattering pair distribution functions." *J. Appl. Crystallogr.* **46**, 560-566. (2013)
[171] Momma, K., & Izumi, F., VESTA: a three-dimensional visualization system for electronic and structural analysis. *J Appl Crystallogr* **41**, 653-658. (2008)
[172] Campbell, B. J. , Stokes, H. T. Tanner, D. E. & Hatch, D. M., ISODISPLACE: An Internet Tool for Exploring Structural Distortions. *J. Appl. Cryst.* **39**, 607-614 (2006)
[173] Farrow, C. L., *et al.* "PDFfit2 and PDFgui: computer programs for studying nanostructure in crystals." *J. Phys.: Condens. Mat.* **19**, 335219. (2007)
[174] Edwards, P. M., Origin 7.0: scientific graphing and data analysis software. *J Chem Inf Comp Sci* **42**, 1270-1271. (2002)
[175] Starykh, O. A., "Unusual ordered phases of highly frustrated magnets: a review". *Rep. Prog. Phys.* **78**, 052502 (2015).
[176] Jin, S., and Wang, C. "Synthesis and first investigation of excellent lithium storage performances of $Fe_2GeO_4$/reduced graphene oxide nanocomposite". *Nano Energy* **7**, 63-71. (2014)
[177] Han, J., *et al.* "Ultrasmall $Fe_2GeO_4$ nanodots anchored on interconnected carbon nanosheets as high-performance anode materials for lithium and sodium ion batteries". *Appl. Surf. Sci.* **427**, 670-679. (2018).
[178] Strobel, P., Koffyberg, F. P., and Wold, A., "Electrical and optical properties of high-purity p-type single crystals of $GeFe_2O_4$". *J. Solid State Chem.* **31**, 209-216 (1980).
[179] Blasse, G. and Fast, J. F., "Néel temperatures of some antiferromagnetic oxides with spinel structure", *Philips Res. Rep.* **18**, 393 (1963).

[180] Vandenberghe, R. E., and De Grave, E., "Mössbauer effect studies of oxidic spinels". In Mössbauer spectroscopy applied to inorganic chemistry (pp. 59-182). Springer US (1989).
[181] Chaix, L. *et al*., "Frustration induced complex phase diagram in the spinel $GeFe_2O_4$" *Poster abstract P.088, ICNS* (2013).
http://www.icns2013.org/IOP/media/uploaded/EVIOP/event_192/A%20-%20Magnetic%20oxides.pdf
[182] Zou, T. *et al*., "Spin Glass Behavior and Field Induced Anisotropic Magnetic Ordering in S = 2 Frustrated Spinel" *Abstract K5.009, APS March Meeting* (2016).
http://absimage.aps.org/image/MAR16/MWS_MAR16-2015-006763.pdf
[183] Barton, P. T. *et al.*, "Structural distortion below the Néel temperature in spinel $GeCo_2O_4$," *Phys. Rev. B* **90**, 064105 (2014).
[184] Ringwood, A. E. "The constitution of the mantle—II: Further data on the olivine-spinel transition" *Geochim. Cosmochim. Ac.* **15**, 18-29 (1958).
[185] Akimoto, S. and Fujisawa, H.,"Demonstration of the Electrical Conductivity Jump Produced by the Olivine-Spinel Transition" *J Geophys Res* 70, 443-449, (1965)
[186] Yamanaka, T., et al. "New structure of high-pressure body-centered orthorhombic $Fe_2SiO_4$". *Am. Mineral*. **100**, 1736-1743. (2015)
[187] Armentrout, M. and Kavner, A. "High pressure, high temperature equation of state for $Fe_2SiO_4$ ringwoodite and implications for the Earth's transition zone" *Geophys Res Lett* 38, L08309. (2011)
[188] Navrotsky, A. & Hughes, L. Thermodynamic relations among olivine, spinel, and phenacite structures in silicates and germanates. V. The system MgO-FeO-$GeO_2$. *J. Solid State Chem.* **16**, 185-188 (1976).
[189] Yong, W., Dachs, E., Withers, A. C. & Essene, E. J. Heat capacity of γ-$Fe_2SiO_4$ between 5 and 303 K and derived thermodynamic properties. *Phys. Chem. Miner.* **34**, 121-127 (2007)
[190] Derzsi, M., *et al.* Comparative ab initio study of lattice dynamics and thermodynamics of $Fe_2SiO_4$- and $Mg_2SiO_4$-spinels. *J. Phys.-Condens. Mat.* **23**, 105401 (2011).
[191] Sawaoka, A., Miyahara, S., and Akimoto, S. I. "Magnetic properties of several metasilicates and metagermanates with pyroxene structure". *J Phys Soc Jpn* **25**, 1253-1257. (1968)
[192] Redhammer, G. J., *et al*., "Magnetic and low-temperature structural behavior of clinopyroxene-type FeGeO3: A neutron diffraction, magnetic susceptibility, and 57Fe Mössbauer study." *Am. Mineral*. **97**, 694-706. (2012)

[193] Reehuis, M., Krimmel, A., Büttgen, N., Loidl, A. & Prokofiev, A. "Crystallographic and magnetic structure of $ZnV_2O_4$." *Eur. Phys. J. B* **35**, 311-316 (2003).
[194] Wills, A. S., Raju, N. P. & Greedan, J. E. "Low-Temperature Structure and Magnetic Properties of the Spinel $LiMn_2O_4$:  A Frustrated Antiferromagnet and Cathode Material." *Chem. Mater.* **11**, 1510-1518 (1999).
[195] Ortega-San-Martin, L., Williams, A. J., Gordon, C.D., Klemme, S. & Attfield, J.P., "Low temperature neutron diffraction study of $MgCr_2O_4$ spinel." *J. Phys.-Condens. Mat.* **20**, 104238 (2008).
[196] Diaz, S. *et al.*, "Magnetic frustration in the spinel compounds $GeCo_2O_4$ and $GeNi_2O_4$", *Phys. Rev. B* **74**, 092404 (2006).
[197] Pregelj, Zorko, M., A., Zaharko, O., Arcon, ,D., Komelj, M., Hillier, A. D. & Berger, H. "Persistent Spin Dynamics Intrinsic to Amplitude-Modulated Long-Range Magnetic Order" *Phys. Rev. Lett.* **109**, 227202 (2012).
[198] Stewart, J. R., Ehlers, G., Wills, A. S., Bramwell, S. T., & Gardner, J. S. "Phase transitions, partial disorder and multi-k structures in $Gd_2Ti_2O_7$." *J. Phys. Condens. Mat.* **16**, L321, (2004).
[199] Agrestini, S., et al. "Nature of the magnetic order in $Ca_3Co_2O_6$." *Phys. Rev. Lett.* **101**, 097207 (2008).
[200] Ringwood, A. E. "Olivine-spinel transition in fayalite". *Geol Soc Am Bull* **69**, 129-130. (1958)
[201] Ringwood, A. E. "The constitution of the mantle—II: further data on the olivine-spinel transition". *Geochim Cosmochim Ac* **15**, 18-29. (1958)
[202] Yagi, T., Akaogi, M., Shimomura, O., Suzuki, T., and Akimoto, S. I. "In situ observation of the olivine-spinel phase transformation in $Fe_2SiO_4$ using synchrotron radiation". *J Geophys Res-Sol Ea* **92**, 6207-6213. (1987)
[203] Yagi, T. "Crystal structures of spinel polymorphs of $Fe_2SiO_4$ and $Ni_2SiO_4$". *Amer. Mineral.* **59**, 486-490. (1974)
[204] Yamanaka, T. "Crystal structures of $Ni_2SiO_4$ and $Fe_2SiO_4$ as a function of temperature and heating duration". *Phys Chem Miner* **13**, 227-232. (1986)
[205] Chen, J., Weidner, D. J., Parise, J. B., Vaughan, M. T., and Raterron, P. "Observation of cation reordering during the olivine-spinel transition in fayalite by in situ synchrotron X-ray diffraction at high pressure and temperature". Phys. Rev. L **86**, 4072. (2001)
[206] Shtrikman, S. and E. Wohlfarth, "The theory of the Vogel-Fulcher law of spin glasses," *Phys. Lett. A* **8**, 467 – 470 (1981).
[207] Yong, W., Dachs, E., Withers, A. C., and Essene, E. J. "Heat capacity of $\gamma$-$Fe_2SiO_4$ between 5 and 303 K and derived thermodynamic properties." *Phys Chem Miner* ***34***, 121-127.
[208] Gopal, E. S. R. "Specific Heats at Low Temperatures" in *International Cryogenics Monograph Series*. (1966)
[209] Singh, S., *et al*. "Ordered spin-ice state in the geometrically frustrated metallic ferromagnet $Sm_2Mo_2O_7$." *Phys. Rev. B* **77**, 020406. (2008)
[210] Yasui, Y., *et al*. "Magnetic structure of $Nd_2Mo_2O_7$". *J Phys Soc Jpn* **70**, 284-289. (2001)
[211] MacDougall, G. J., Garlea, V. O., Aczel, A. A., Zhou, H. D., and Nagler, S. E. "Magnetic order and ice rules in the multiferroic spinel $FeV_2O_4$." *Phys. Rev. B* **86**, 060414. (2012)
[212] Marezio, M., and Dernier, P. D. "The crystal structure of $Ti_4O_7$, a member of the homologous series $Ti_nO_{2n-1}$." *J. Solid State Chem.* **3**, 340-348."(1971)
[213] Marezio, M., McWhan, D. B., Dernier, P. D., and Remeika, J. P. "Structural aspects of the metal-insulator transitions in $Ti_4O_7$". *J. Solid State Chem.* **6**, 213-221. (1973).
[214] Le Page, Y., and Marezio, M. "Structural chemistry of magnéli phases $Ti_nO_{2n-1}$ ($4 \leq n \leq 9$): IV. Superstructure in $Ti_4O_7$ at 140 K." *J. Solid State Chem.* **53**, 13-21 (1984)
[215] Koch, M., Woodland, A. B., and Angel, R. J. "Stability of spinelloid phases in the system $Mg_2SiO_4$–$Fe_2SiO_4$–$Fe_3O_4$ at 1100 C and up to 10.5 GPa." *Phys Earth Planet In* **143**, 171-183. (2004)
[216] Tellefsen, M., Kershaw, R., Dwight, K., and Wold, A. "The dependence of magnetic properties on structure in the system $Fe_2Ge_xSi_{1-x}O4$." *J. Solid State Chem.* **46**, 328-335. (1983)

# APPENDIX

## A. Appendix to Chapter 3

### A1. Natural magnetite

**Appendix Table 1 – Summary of experimental and refinement details for structure analysis of the natural magnetite grain in the monoclinic Cc phase at 90 K, below the Verwey transition.**

| | |
|---|---|
| **Crystal Data** | |
| Chemical Formula | $Fe_3O_4$ |
| Cell setting, Space group | Cc |
| Temperature (K) | 90.00(2) |
| a,b,c (Å) | 11.8801(17), 11.8457(17), 16.7773(30) |
| β (°) | 90.267(9) |
| Volume ($Å^3$) | 2361.01(7) |
| $D_c$(g $cm^{-3}$) | 5.238 |
| X-ray wavelength (Å) | 0.15842(1) |
| μ ($mm^{-1}$) | 0.19 |
| Crystal form | Approximately spherical |
| Crystal size (mm) | r = 0.062, 0.05, 0.025 |
| **Data Collection** | |
| Diffractometer | ID11@ESRF, Huber Omega and phi axis |
| Data collection method | ω |
| Absorption correction | none |
| No. of observed, symmetry unique reflections | 180686, 45904 |
| $θ_{max}$ (°) | 15.36 |
| $R_{int}$ | 0.0422 |
| Range of h,k,l | -39 → h → 39 |
| | -39 → k → 39 |
| | -55 → l → 55 |
| **Refinement** | |
| Refine on | $F^2$ |
| R($F^2$), R[$F^2$ > 4 sigma], wR($F^2$), S | 0.0416, 0.0359, 0.0890, 1.014 |
| Cutoff: I >σ | none |
| No. of reflections | 93108 |
| No. of parameters | 507 |

| | |
|---|---|
| Weighting scheme | Weight = 1 / [ sigma$^2$(Fo$^2$) + (0.0194 * P)$^2$ + 1.10 * P ] where P = (Max ( Fo$^2$, 0 ) + 2 * Fc$^2$ ) / 3 |
| (Δ/α)mean | 0.001 |
| (Δ/α)max | 0.007 |
| Δρmax, Δρmin (e Å$^{-3}$) | 5.88, -5.03 |
| Twin law | (0 -1 0) (1 0 0) (0 0 -1) Applied three times to account for *a/b, a/-a* and *a/-b* |
| Twin fractions: | 0.0280(4) *a/b*, 0.0294(6) *a/-a,* 0.0235(4) *a/-b* |

**Appendix Table 2 – Fractional coordinates and equivalent isotropic thermal parameters for natural magnetite at 90 K.**

| SITES | X | Y | Z | UEQUIVALENT (Å$^2$) |
|---|---|---|---|---|
| **A11** | 0.87525(2) | 0.75138(2) | 0.06523(2) | 0.00229(2) |
| **A12** | 0.87803(2) | 0.25212(2) | 0.06490(2) | 0.00216(1) |
| **A13** | 0.62485(2) | 0.75223(2) | 0.43791(2) | 0.00241(2) |
| **A14** | 0.62669(2) | 0.25361(2) | 0.43780(2) | 0.00232(2) |
| **A21** | 0.87470(2) | 0.50440(2) | 0.19017(2) | 0.00218(2) |
| **A22** | 0.88065(2) | 0.00072(2) | 0.18839(2) | 0.00215(2) |
| **A23** | 0.62540(2) | 0.50148(2) | 0.31125(2) | 0.00248(2) |
| **A24** | 0.62907(2) | 0.00475(2) | 0.31273(2) | 0.00243(2) |
| **B1A1** | 0.75081(2) | -0.00164(3) | 0.00153(2) | 0.00281(1) |
| **B1A2** | 0.75133(2) | 0.49905(3) | 0.0005(2) | 0.00266(1) |
| **B1B1** | 0.00221(2) | 0.50026(3) | 0.50159(2) | 0.00298(1) |
| **B1B2** | -0.00250(2) | 0.00051(2) | 0.49693(2) | 0.00251(1) |
| **B2A1** | 0.74812(2) | 0.75606(2) | 0.25244(2) | 0.00261(1) |
| **B2A2** | 0.75903(2) | 0.25194(2) | 0.25345(2) | 0.00241(2) |
| **B2B1** | 0.00249(3) | 0.74409(2) | 0.75120(2) | 0.00291(1) |
| **B2B2** | 0.00217(3) | 0.24621(2) | 0.75129(2) | 0.00246(1) |
| **B31** | 0.87667(2) | 0.87864(2) | 0.37924(2) | 0.00313(2) |
| **B32** | 0.87634(2) | 0.38689(2) | 0.38042(2) | 0.00281(2) |
| **B33** | 0.62647(2) | 0.88608(2) | 0.12176(2) | 0.00262(1) |
| **B34** | 0.62854(2) | 0.37465(2) | 0.12317(2) | 0.00257(2) |
| **B41** | 0.87610(2) | 0.62510(2) | 0.37643(2) | 0.00259(2) |
| **B42** | 0.87560(2) | 0.13092(2) | 0.37423(2) | 0.00280(2) |
| **B43** | 0.62602(2) | 0.62727(2) | 0.12570(2) | 0.00253(1) |
| **B44** | 0.62788(2) | 0.12528(3) | 0.12614(2) | 0.00280(1) |
| **O11** | 0.8755(1) | 0.8782(1) | -0.00018(8) | 0.00432(1) |

| | | | | |
|---|---|---|---|---|
| **O12** | 0.8755(1) | 0.3789(1) | -0.00170(8) | 0.0038(1) |
| **O13** | 0.6261(1) | 0.8827(1) | 0.50454(7) | 0.00297(8) |
| **O14** | 0.6250(1) | 0.38391(9) | 0.50523(7) | 0.00272(8) |
| **O21** | 0.8764(1) | 0.6235(1) | 0.00032(8) | 0.0038(1) |
| **O22** | 0.8769(1) | 0.1242(1) | 0.00047(8) | 0.0038(1) |
| **O23** | 0.6234(1) | 0.6222(1) | 0.50416(8) | 0.0041(1) |
| **O24** | 0.6257(1) | 0.1240(1) | 0.50264(8) | 0.0037(1) |
| **O31** | 0.8777(1) | 0.86809(7) | 0.25346(7) | 0.00299(8) |
| **O32** | 0.8740(1) | 0.37387(9) | 0.25575(7) | 0.00371(9) |
| **O33** | 0.6294(1) | 0.87772(9) | 0.24655(7) | 0.00347(9) |
| **O34** | 0.6250(1) | 0.37171(9) | 0.24642(8) | 0.0044(1) |
| **O41** | 0.8767(1) | 0.63732(7) | 0.25440(6) | 0.00318(8) |
| **O42** | 0.8777(1) | 0.13236(8) | 0.25168(8) | 0.00365(9) |
| **O43** | 0.6286(1) | 0.63106(9) | 0.24630(8) | 0.0046(1) |
| **O44** | 0.6265(1) | 0.13583(9) | 0.24877(8) | 0.0045(1) |
| **O5A1** | 0.7437(1) | 0.75061(9) | 0.13004(6) | 0.00320(8) |
| **O5A2** | 0.7484(1) | 0.25600(9) | 0.12997(7) | 0.00348(9) |
| **O5A3** | 0.7531(1) | 0.7548(1) | 0.37202(7) | 0.0044(1) |
| **O5A4** | 0.7560(1) | 0.2570(1) | 0.37401(8) | 0.0047(1) |
| **O5B1** | 0.0097(1) | 0.7487(1) | 0.62877(7) | 0.00326(9) |
| **O5B2** | 0.0051(1) | 0.2458(1) | 0.63022(7) | 0.00365(9) |
| **O5B3** | -0.0053(1) | 0.7460(1) | 0.87181(7) | 0.0039(1) |
| **O5B4** | -0.0027(1) | 0.2438(1) | 0.87105(6) | 0.00371(9) |
| **O6A1** | 0.74311(9) | 0.5032(1) | 0.12558(7) | 0.00382(9) |
| **O6A2** | 0.7509(1) | 0.0007(1) | 0.12427(7) | 0.0044(1) |
| **O6A3** | 0.7526(1) | 0.5016(1) | 0.37612(6) | 0.00333(8) |
| **O6A4** | 0.7594(1) | 0.0033(1) | 0.37649(7) | 0.00349(9) |
| **O6B1** | 0.0110(1) | -0.0023(1) | 0.62355(7) | 0.00434(9) |
| **O6B2** | 0.0027(1) | 0.4990(1) | 0.62591(7) | 0.00439(9) |
| **O6B3** | -0.0028(1) | -0.0022(1) | 0.87641(7) | 0.00351(8) |
| **O6B4** | 0.0004(1) | 0.4982(1) | 0.87740(7) | 0.00363(8) |

**Appendix Table 3 – Anisotropic thermal parameters for natural magnetite at 90 K.**

| SITES | U11 (Å$^2$) | U22 (Å$^2$) | U33 (Å$^2$) | U23 (Å$^2$) | U13 (Å$^2$) | U12 (Å$^2$) |
|---|---|---|---|---|---|---|
| **A11** | 0.00280(3) | 0.00248(3) | 0.00157(3) | -0.00009(3) | 0.00010(2) | 0.0000(3) |
| **A12** | 0.00273(3) | 0.00224(3) | 0.00152(3) | -0.00009(3) | 0.00011(2) | 0.00006(3) |
| **A13** | 0.00298(4) | 0.00216(3) | 0.00209(3) | -0.00027(3) | 0.00039(3) | -0.00010(3) |
| **A14** | 0.00300(3) | 0.00182(3) | 0.00213(3) | -0.00024(3) | 0.00041(2) | 0.0000(3) |
| **A21** | 0.00274(4) | 0.00209(3) | 0.00172(3) | -0.00024(3) | 0.00020(2) | -0.00008(3) |
| **A22** | 0.00250(4) | 0.00184(3) | 0.00210(3) | 0.00004(2) | 0.00027(2) | 0.00003(2) |
| **A23** | 0.00300(3) | 0.00240(3) | 0.00203(3) | -0.00013(3) | 0.00032(3) | -0.00001(3) |
| **A24** | 0.00263(4) | 0.00255(3) | 0.00212(3) | -0.00027(3) | 0.00021(2) | 0.00002(3) |
| **B1A1** | 0.00339(3) | 0.00245(3) | 0.00259(2) | -0.00046(2) | -0.00004(2) | 0.00021(2) |
| **B1A2** | 0.00314(3) | 0.00249(3) | 0.00236(2) | -0.00038(2) | 0.00007(2) | 0.00037(2) |
| **B1B1** | 0.00372(3) | 0.00255(2) | 0.00269(3) | 0.00048(1) | 0.00111(2) | 0.00027(1) |
| **B1B2** | 0.00306(3) | 0.00234(2) | 0.00215(3) | 0.00019(3) | 0.00045(2) | 0.00002(2) |
| **B2A1** | 0.00364(3) | 0.00214(3) | 0.00206(3) | -0.00013(2) | 0.00014(2) | -0.00023(3) |
| **B2A2** | 0.00271(3) | 0.00251(3) | 0.00203(3) | -0.00012(2) | 0.00014(2) | 0.00017(2) |
| **B2B1** | 0.00417(2) | 0.00256(2) | 0.00201(2) | -0.00013(3) | 0.00049(2) | -0.00013(4) |
| **B2B2** | 0.00282(2) | 0.00254(2) | 0.00202(2) | -0.00015(3) | 0.00035(1) | -0.00008(3) |
| **B31** | 0.00348(3) | 0.00321(3) | 0.00271(4) | 0.00055(3) | 0.00081(3) | 0.00047(3) |
| **B32** | 0.00313(2) | 0.00300(3) | 0.00229(3) | 0.00017(3) | 0.00020(3) | -0.00008(3) |
| **B33** | 0.00313(3) | 0.00256(3) | 0.00217(3) | -0.00025(3) | 0.00020(3) | -0.00006(3) |
| **B34** | 0.00310(3) | 0.00237(3) | 0.00223(4) | -0.00020(3) | 0.00005(3) | 0.00014(3) |
| **B41** | 0.00291(3) | 0.00303(3) | 0.00184(4) | 0.0000(3) | 0.0001(3) | 0.00012(3) |
| **B42** | 0.00362(3) | 0.00227(3) | 0.00253(4) | -0.00050(3) | 0.00084(3) | -0.00041(3) |
| **B43** | 0.00311(3) | 0.00246(3) | 0.00202(3) | -0.00018(2) | 0.00034(2) | -0.00004(2) |
| **B44** | 0.00297(3) | 0.00304(3) | 0.00239(3) | -0.00047(2) | 0.00043(2) | 0.00026(3) |
| **O11** | 0.0051(2) | 0.0037(2) | 0.0043(2) | 0.0019(2) | 0.0005(2) | -0.0005(2) |
| **O12** | 0.0044(2) | 0.0027(2) | 0.0041(2) | 0.0014(1) | 0.0006(2) | -0.0004(2) |
| **O13** | 0.0042(2) | 0.0022(2) | 0.0025(2) | -0.0001(1) | -0.0001(1) | 0.0001(1) |
| **O14** | 0.0044(2) | 0.0017(1) | 0.0021(2) | -0.0005(1) | 0.0004(1) | 0.0005(1) |
| **O21** | 0.0045(2) | 0.0039(2) | 0.0031(2) | -0.0015(1) | 0.0002(1) | 0.0005(2) |
| **O22** | 0.0051(2) | 0.0032(2) | 0.0032(2) | -0.0017(1) | 0.0000(2) | 0.0007(1) |
| **O23** | 0.0057(2) | 0.0033(2) | 0.0033(2) | -0.0002(1) | 0.0010(2) | -0.0002(2) |
| **O24** | 0.0048(2) | 0.0031(2) | 0.0033(2) | -0.0003(1) | 0.0005(2) | 0.0004(2) |
| **O31** | 0.0044(2) | 0.0009(1) | 0.0037(2) | -0.0007(2) | 0.0002(1) | 0.0002(1) |
| **O32** | 0.0042(2) | 0.0040(2) | 0.0029(2) | 0.0004(1) | -0.0004(1) | -0.0001(2) |
| **O33** | 0.0046(2) | 0.0021(1) | 0.0037(2) | -0.0008(1) | 0.0003(1) | 0.0004(1) |
| **O34** | 0.0047(2) | 0.0046(2) | 0.0040(2) | -0.0002(2) | 0.0004(2) | 0.0004(2) |
| **O41** | 0.0050(2) | 0.0020(1) | 0.0028(2) | -0.0011(1) | 0.0004(1) | 0.0001(1) |
| **O42** | 0.0048(2) | 0.0022(2) | 0.0039(2) | 0.0001(1) | 0.0000(1) | -0.0001(1) |

| | | | | | | |
|---|---|---|---|---|---|---|
| **O43** | 0.0053(2) | 0.0046(2) | 0.0040(2) | -0.0007(1) | 0.0002(1) | 0.0004(2) |
| **O44** | 0.0038(2) | 0.0057(2) | 0.0040(2) | -0.0003(2) | 0.0002(1) | 0.0004(2) |
| **O5A1** | 0.0043(2) | 0.0029(1) | 0.0024(1) | -0.0003(1) | 0.0007(1) | 0.0001(1) |
| **O5A2** | 0.0044(2) | 0.0032(2) | 0.0029(2) | -0.0004(1) | 0.0005(1) | 0.0008(1) |
| **O5A3** | 0.0034(2) | 0.0059(2) | 0.0040(2) | -0.0004(2) | 0.0004(1) | 0.0004(2) |
| **O5A4** | 0.0043(2) | 0.0050(2) | 0.0048(2) | 0.0001(1) | 0.0008(1) | -0.0001(1) |
| **O5B1** | 0.0036(2) | 0.0036(2) | 0.0025(2) | 0.0001(1) | 0.0002(1) | -0.0001(1) |
| **O5B2** | 0.0034(2) | 0.0044(2) | 0.0032(2) | 0.0007(1) | 0.0000(1) | -0.0003(1) |
| **O5B3** | 0.0039(2) | 0.0039(2) | 0.0038(2) | -0.0004(1) | -0.0004(1) | 0.0002(1) |
| **O5B4** | 0.0044(2) | 0.0036(2) | 0.0032(2) | -0.0010(1) | -0.0003(1) | -0.0004(1) |
| **O6A1** | 0.0034(2) | 0.0038(2) | 0.0042(2) | 0.0003(2) | -0.0006(1) | -0.0002(2) |
| **O6A2** | 0.0041(2) | 0.0053(2) | 0.0038(2) | 0.0001(2) | 0.0001(1) | 0.0001(2) |
| **O6A3** | 0.0039(2) | 0.0034(2) | 0.0027(1) | -0.0003(1) | -0.0002(1) | -0.0001(1) |
| **O6A4** | 0.0034(2) | 0.0038(2) | 0.0033(1) | 0.0003(2) | 0.0002(1) | -0.0003(2) |
| **O6B1** | 0.0040(2) | 0.0043(2) | 0.0047(2) | -0.0004(2) | 0.0008(1) | 0.0001(1) |
| **O6B2** | 0.0040(2) | 0.0055(2) | 0.0036(2) | -0.0001(2) | 0.0008(1) | 0.0000(2) |
| **O6B3** | 0.0044(2) | 0.0031(2) | 0.0031(2) | -0.0001(1) | 0.0005(1) | 0.0002(1) |
| **O6B4** | 0.0047(2) | 0.0029(2) | 0.0033(2) | 0.0001(2) | 0.0003(1) | 0.0000(2) |

Appendix Table 4 – B-B distances from a given site and their deviation from the global average (dB). Divalent-like sites are colour coded in blue, trivalent-like sites are in yellow.

| Site | <Fe-Fe> | Fe-Fe bond lenghts and dBB from the global average organised by opposite pairs. First pair is perpendicular to the short JT axis | | | | | | | | | | | | | | | | | |
|---|---|---|---|---|---|---|---|---|---|---|---|---|---|---|---|---|---|---|---|
| B1B1 | 2.9253881 | B32 | 2.8538461 | -0.1125544 | B33 | 2.8334908 | -0.1329096 | B44 | 2.9627048 | -0.0036956 | B41 | 2.9684178 | 0.0020173 | B1A1 | 2.9533718 | -0.0130287 | B1A2 | 2.9804971 | 0.0140966 |
| B31 | 2.9590408 | B2A1 | 2.9893337 | 0.0229333 | B1B2 | 2.8314024 | -0.134998 | B41 | 3.0037943 | 0.0373939 | B42 | 2.9896267 | 0.0232262 | B2B2 | 3.0081033 | 0.0417029 | B1A1 | 2.9319846 | -0.0344158 |
| B32 | 2.9373382 | B1B1 | 2.8538461 | -0.1125544 | B2A2 | 3.0012953 | 0.0348949 | B42 | 3.0338712 | 0.0674708 | B41 | 2.8225696 | -0.1438309 | B2B1 | 3.0632497 | 0.0968492 | B1A2 | 2.8491976 | -0.1172029 |
| B1A1 | 2.9402982 | B31 | 2.9319846 | -0.0344158 | B33 | 2.8368751 | -0.1295253 | B1B1 | 2.9533718 | -0.0130287 | B1B2 | 2.9321426 | -0.0342578 | B42 | 3.0222245 | 0.0558241 | B44 | 2.9651904 | -0.0012101 |
| B1A2 | 2.9531778 | B34 | 2.9262997 | -0.0401008 | B32 | 2.8491976 | -0.1172029 | B1B1 | 2.9804971 | 0.0140966 | B1B2 | 3.0158457 | 0.0494453 | B41 | 2.9532107 | -0.0131898 | B43 | 2.9940163 | 0.0276159 |
| B33 | 2.9432041 | B44 | 2.834503 | -0.1318974 | B43 | 3.0664907 | 0.1000902 | B1B1 | 2.8334908 | -0.1329096 | B2A1 | 3.0394458 | 0.0730453 | B1A1 | 2.8368751 | -0.1295253 | B2B1 | 3.0484193 | 0.0820188 |
| B41 | 2.9585806 | B31 | 3.0037943 | 0.0373939 | B32 | 2.8225696 | -0.1438309 | B1B1 | 2.9684178 | 0.0020173 | B2A1 | 3.0026748 | 0.0362743 | B2B2 | 3.0008167 | 0.0344162 | B1A2 | 2.9532107 | -0.0131898 |
| B2A1 | 2.9925569 | B2B1 | 2.9181462 | -0.0482542 | B2B2 | 3.0183996 | 0.0519991 | B43 | 2.9873412 | 0.0209407 | B31 | 2.9893337 | 0.0229333 | B33 | 3.0394458 | 0.0730453 | B41 | 3.0026748 | 0.0362743 |
| B34 | 2.986688 | B1B2 | 3.010887 | 0.0444865 | B2A2 | 3.0433568 | 0.0769563 | B44 | 2.9543825 | -0.012018 | B43 | 2.9929252 | 0.0265247 | B2B2 | 2.9922771 | 0.0258766 | B1A2 | 2.9262997 | -0.0401008 |
| B1B2 | 2.963602 | B34 | 3.010887 | 0.0444865 | B31 | 2.8314024 | -0.134998 | B42 | 2.9484962 | -0.0179043 | B43 | 3.0428378 | 0.0764373 | B1A1 | 2.9321426 | -0.0342578 | B1A2 | 3.0158457 | 0.0494453 |
| B43 | 3.0122072 | B34 | 2.9929252 | 0.0265247 | B33 | 3.0664907 | 0.1000902 | B2A1 | 2.9873412 | 0.0209407 | B1B2 | 3.0428378 | 0.0764373 | B2B1 | 2.989632 | 0.0232316 | B1A2 | 2.9940163 | 0.0276159 |
| B2B2 | 3.0114639 | B44 | 2.9975276 | 0.0311272 | B31 | 3.0081033 | 0.0417029 | B2A1 | 3.0183996 | 0.0519991 | B2A2 | 3.0516593 | 0.0852588 | B34 | 2.9922771 | 0.0258766 | B41 | 3.0008167 | 0.0344162 |
| B44 | 2.9581826 | B34 | 2.9543825 | -0.012018 | B33 | 2.834503 | -0.1318974 | B1B1 | 2.9627048 | -0.0036956 | B2A2 | 3.034787 | 0.0683865 | B2B2 | 2.9975276 | 0.0311272 | B1A1 | 2.9651904 | -0.0012101 |
| B42 | 2.9651334 | B1B2 | 2.9484962 | -0.0179043 | B2A2 | 2.8378265 | -0.1285739 | B31 | 2.9896267 | 0.0232262 | B32 | 3.0338712 | 0.0674708 | B2B1 | 2.9587553 | -0.0076451 | B1A1 | 3.0222245 | 0.0558241 |
| B2B1 | 2.9785458 | B2A2 | 2.8930724 | -0.0733281 | B2A1 | 2.9181462 | -0.0482542 | B32 | 3.0632497 | 0.0968492 | B43 | 2.989632 | 0.0232316 | B33 | 3.0484193 | 0.0820188 | B42 | 2.9587553 | -0.0076451 |
| B2A2 | 2.9769995 | B32 | 3.0012953 | 0.0348949 | B44 | 3.034787 | 0.0683865 | B34 | 3.0433568 | 0.0769563 | B42 | 2.8378265 | -0.1285739 | B2B2 | 3.0516593 | 0.0852588 | B2B1 | 2.8930724 | -0.0733281 |

## A2. Off-stoichiometric magnetite

**Appendix Table 5 – Summary of experimental and refinement details for structure analysis of the off-stoichiometric magnetite grain in the monoclinic Cc phase at 90 K, below the Verwey transition.**

| | |
|---|---|
| **Crystal Data** | |
| Chemical Formula | $Fe_{3-\delta}O_4$ with 3δ = 0.012 |
| Cell setting, Space group | *Cc* |
| Temperature (K) | 90.00(2) |
| a,b,c (Å) | 11.8874(2), 11.8656(2), 16.7887(3) |
| β ($^{o}$) | 90.162(9) |
| Volume (Å$^3$) | 2368.06(7) |
| $D_c$(g cm$^{-3}$) | 5.238 |
| X-ray wavelength (Å) | 0.15815 |
| μ (mm$^{-1}$) | 0.19 |
| Crystal form | Approximately spherical |
| Crystal size (mm) | r ≈ 0.05 |
| **Data Collection** | |
| Diffractometer | ID11@ESRF, Huber Omega and phi axis |
| Data collection method | ω |
| Absorption correction | none |
| No. of observed, symmetry unique reflections | 113655, 95338 |
| $\theta_{max}$ ($^{o}$) | 32.75 |
| $R_{int}$ | 0.0533 |
| Range of h,k,l | -42 → h → 42 |
| | -42 → k → 42 |
| | -59 → l → 59 |
| **Refinement** | |
| Refine on | $F^2$ |
| R($F^2$), R[$F^2$ > 4 sigma], wR($F^2$), S | 0.0533, 0.0373, 0.0955, 1.068 |
| Cutoff: I >σ | none |
| No. of reflections | 113655 |
| No. of parameters | 508 |
| Weighting scheme | Weight = 1 / [ sigma$^2$($Fo^2$) + (0.0201 * P)$^2$ + 1.48 * P] where P = (Max ( $Fo^2$, 0 ) + 2 * $Fc^2$ ) / 3 |
| (Δ/α)mean | 0.001 |
| (Δ/α)max | 0.007 |
| Δρmax, Δρmin (e Å$^{-3}$) | 5.88, -5.03 |
| Twin law | (0 -1 0) (1 0 0) (0 0 -1)<br>Applied three times to account for *a/b, a/-a* |
| Twin fractions: | 0.0436 (6) *a/b*, 0.4652(7) *a/-a,*<br>0.0404(6) *a/-b* |

**Appendix Table 6 – Fractional coordinates and equivalent isotropic thermal parameters for off-stoichiometric magnetite at 90 K.**

| SITES | X | Y | Z | UEQUIVALENT (Å$^2$) |
|---|---|---|---|---|
| **A11** | 0.8746(7) | 0.75159(3) | 0.06474(2) | 0.00184(3) |
| **A12** | 0.8772(7) | 0.25233(3) | 0.06459(2) | 0.00185(3) |
| **A13** | 0.6259(7) | 0.75108(3) | 0.43812(2) | 0.00263(2) |
| **A14** | 0.6272(7) | 0.25245(3) | 0.43778(2) | 0.00246(2) |
| **A21** | 0.8740(7) | 0.50296(4) | 0.19005(2) | 0.00190(3) |
| **A22** | 0.8796(7) | 0.00126(4) | 0.18836(2) | 0.00229(3) |
| **A23** | 0.6263(7) | 0.50064(3) | 0.31189(2) | 0.00270(2) |
| **A24** | 0.6286(6) | 0.00446(3) | 0.31267(2) | 0.00233(2) |
| **B1A1** | 0.7515(9) | -0.00047(6) | 0.00133(3) | 0.00284(4) |
| **B1A2** | 0.7514(9) | 0.50041(6) | 0.00087(3) | 0.00303(4) |
| **B1B1** | 0.002(1) | 0.49937(7) | 0.50130(3) | 0.00361(3) |
| **B1B2** | -0.0019(9) | 0.00021(6) | 0.49786(3) | 0.00300(3) |
| **B2A1** | 0.7487(8) | 0.75502(4) | 0.25195(3) | 0.00261(3) |
| **B2A2** | 0.7572(8) | 0.25230(4) | 0.25284(4) | 0.00280(4) |
| **B2B1** | 0.003(1) | 0.74562(4) | 0.75114(3) | 0.00377(3) |
| **B2B2** | 0.0009(1) | 0.24704(4) | 0.75140(3) | 0.00303(3) |
| **B31** | 0.880(1) | 0.87676(5) | 0.37815(3) | 0.00528(4) |
| **B32** | 0.8777(8) | 0.38287(4) | 0.37979(3) | 0.00360(3) |
| **B33** | 0.6259(6) | 0.88608(2) | 0.12225(2) | 0.00240(2) |
| **B34** | 0.62725(7) | 0.37553(3) | 0.12379(2) | 0.00273(2) |
| **B41** | 0.8773(8) | 0.62561(4) | 0.37636(3) | 0.00320(2) |
| **B42** | 0.8776(8) | 0.12862(4) | 0.37496(3) | 0.00347(4) |
| **B43** | 0.6260(8) | 0.62811(3) | 0.12638(2) | 0.00282(3) |
| **B44** | 0.6266(7) | 0.12476(3) | 0.12601(2) | 0.00250(2) |
| **O11** | 0.8771(2) | 0.8820(2) | -0.0008(1) | 0.00361(1) |
| **O12** | 0.8777(2) | 0.3817(2) | -0.0011(1) | 0.0034(2) |
| **O13** | 0.6292(3) | 0.8796(1) | 0.50458(9) | 0.0036(1) |
| **O14** | 0.6260(3) | 0.3809(1) | 0.50509(9) | 0.0038(2) |
| **O21** | 0.8764(2) | 0.6212(2) | 0.0005(1) | 0.0026(1) |
| **O22** | 0.8791(2) | 0.1242(2) | -0.0005(1) | 0.0032(2) |
| **O23** | 0.6265(3) | 0.6220(2) | 0.5043(1) | 0.0052(2) |
| **O24** | 0.6249(3) | 0.1242(2) | 0.5027(1) | 0.0042(2) |
| **O31** | 0.8798(2) | 0.8718(2) | 0.2540(1) | 0.0051(2) |
| **O32** | 0.8764(2) | 0.3750(1) | 0.2559(1) | 0.0032(1) |
| **O33** | 0.6304(2) | 0.8741(1) | 0.2471(1) | 0.0048(2) |
| **O34** | 0.6268(2) | 0.3684(1) | 0.2477(1) | 0.0033(1) |
| **O41** | 0.8768(2) | 0.6359(1) | 0.2545(1) | 0.0031(1) |

| | | | | |
|---|---|---|---|---|
| **O42** | 0.8782(1) | 0.1299(2) | 0.2519(1) | 0.0044(2) |
| **O43** | 0.6298(2) | 0.6321(1) | 0.2473(1) | 0.0038(1) |
| **O44** | 0.6278(2) | 0.1362(1) | 0.2484(1) | 0.0040(1) |
| **O5A1** | 0.7440(2) | 0.7517(2) | 0.1294(1) | 0.0032(2) |
| **O5A2** | 0.7481(2) | 0.2570(2) | 0.1291(1) | 0.0031(1) |
| **O5A3** | 0.7553(2) | 0.7513(2) | 0.3727(1) | 0.0035(2) |
| **O5A4** | 0.7559(2) | 0.2538(2) | 0.3736(1) | 0.0044(2) |
| **O5B1** | 0.0107(2) | 0.7479(2) | 0.6294(1) | 0.0026(1) |
| **O5B2** | 0.0051(2) | 0.2460(2) | 0.6311(1) | 0.0035(2) |
| **O5B3** | -0.0026(2) | 0.7467(2) | 0.8727(2) | 0.0061(2) |
| **O5B4** | -0.0024(2) | 0.2458(2) | 0.8720(1) | 0.0053(2) |
| **O6A1** | 0.7441(2) | 0.5017(2) | 0.1259(1) | 0.0030(1) |
| **O6A2** | 0.7514(2) | 0.0025(2) | 0.1250(1) | 0.0031(1) |
| **O6A3** | 0.7547(2) | 0.5006(2) | 0.3769(2) | 0.0047(2) |
| **O6A4** | 0.7593(2) | 0.0037(2) | 0.3773(1) | 0.0036(1) |
| **O6B1** | 0.0108(1) | -0.0026(2) | 0.6230(1) | 0.0035(2) |
| **O6B2** | 0.0039(1) | 0.5005(2) | 0.6251(1) | 0.0032(1) |
| **O6B3** | -0.0015(2) | -0.0012(3) | 0.8776(1) | 0.0050(2) |
| **O6B4** | -0.0001(2) | 0.4981(2) | 0.8767(1) | 0.0049(1) |

**Appendix Table 7 – Anisotropic thermal parameters for off-stoichiometric magnetite at 90 K.**

| SITES | U11 (Å$^2$) | U22 (Å$^2$) | U33 (Å$^2$) | U23 (Å$^2$) | U13 (Å$^2$) | U12 (Å$^2$) |
|---|---|---|---|---|---|---|
| **A11** | 0.00137(5) | 0.00218(6) | 0.00197(6) | 0.00020(4) | 0.00025(5) | 0.00007(6) |
| **A12** | 0.00242(7) | 0.00134(5) | 0.00179(6) | 0.00016(4) | 0.00049(5) | 0.00003(6) |
| **A13** | 0.00206(5) | 0.00291(5) | 0.00293(4) | -0.00006(4) | -0.00025(6) | 0.00007(8) |
| **A14** | 0.00196(5) | 0.00250(5) | 0.00291(5) | 0.00017(4) | -0.00016(6) | -0.00019(8) |
| **A21** | 0.00099(5) | 0.00257(5) | 0.00212(5) | -0.00012(4) | 0.00008(4) | 0.00004(6) |
| **A22** | 0.00231(7) | 0.00200(5) | 0.00255(6) | 0.00071(4) | 0.00018(5) | -0.00014(6) |
| **A23** | 0.00287(5) | 0.00209(4) | 0.00315(6) | 0.00008(4) | 0.00021(7) | -0.00015(8) |
| **A24** | 0.00215(6) | 0.00198(4) | 0.00287(5) | 0.00019(4) | -0.00030(6) | -0.00050(6) |
| **B1A1** | 0.00227(4) | 0.00323(6) | 0.00302(9) | -0.00050(7) | -0.00047(5) | 0.00005(8) |
| **B1A2** | 0.00183(4) | 0.00310(6) | 0.0041(1) | -0.00018(7) | -0.00078(5) | 0.00018(7) |
| **B1B1** | 0.00425(6) | 0.00217(5) | 0.00443(8) | 0.00050(6) | 0.00135(6) | 0.00081(6) |
| **B1B2** | 0.00318(7) | 0.00231(5) | 0.00350(7) | -0.00016(6) | -0.00006(5) | 0.00009(6) |
| **B2A1** | 0.00252(7) | 0.00224(6) | 0.00308(7) | -0.00008(4) | 0.00027(6) | -0.00005(5) |
| **B2A2** | 0.00298(7) | 0.00234(6) | 0.00307(7) | -0.00067(4) | 0.00044(6) | -0.00040(5) |
| **B2B1** | 0.00569(7) | 0.00307(6) | 0.00256(6) | 0.00037(5) | 0.00018(6) | 0.00119(7) |
| **B2B2** | 0.00332(6) | 0.00304(5) | 0.00274(5) | 0.00045(5) | -0.00009(5) | 0.00053(6) |

| | | | | | | |
|---|---|---|---|---|---|---|
| **B31** | 0.00252(7) | 0.00780(9) | 0.00552(8) | 0.00340(8) | 0.00053(6) | 0.00085(7) |
| **B32** | 0.00256(7) | 0.00523(7) | 0.00301(6) | 0.00060(6) | -0.00028(5) | -0.00153(6) |
| **B33** | 0.00211(5) | 0.00228(3) | 0.00281(4) | 0.00006(4) | -0.00061(5) | 0.00085(6) |
| **B34** | 0.00306(5) | 0.00190(3) | 0.00323(5) | -0.00008(4) | -0.00038(7) | -0.00067(6) |
| **B41** | 0.00215(7) | 0.00563(9) | 0.00183(6) | -0.00019(5) | -0.00092(5) | 0.00029(6) |
| **B42** | 0.00330(8) | 0.00404(9) | 0.00307(7) | -0.00162(5) | 0.00076(6) | -0.00144(6) |
| **B43** | 0.00219(5) | 0.00201(4) | 0.00424(6) | 0.00022(4) | -0.00022(8) | -0.00073(6) |
| **B44** | 0.00220(5) | 0.00182(4) | 0.00348(5) | -0.00061(3) | 0.00008(7) | -0.00031(6) |
| **O11** | 0.0015(3) | 0.0029(3) | 0.0064(4) | 0.0007(3) | -0.0002(3) | -0.0005(3) |
| **O12** | 0.0035(4) | 0.0014(2) | 0.0053(4) | 0.00003(3) | 0.0003(3) | -0.0007(3) |
| **O13** | 0.0037(3) | 0.0050(3) | 0.0022(2) | -0.0003(2) | -0.0006(3) | 0.0009(4) |
| **O14** | 0.0058(4) | 0.0037(3) | 0.0019(2) | -0.0005(1) | -0.0008(3) | 0.0000(4) |
| **O21** | 0.0016(3) | 0.0034(3) | 0.0029(4) | 0.0001(3) | 0.00001(3) | 0.0003(3) |
| **O22** | 0.0041(4) | 0.0032(2) | 0.0022(4) | -0.0005(2) | -0.00003(3) | -0.0006(3) |
| **O23** | 0.0068(3) | 0.0030(3) | 0.0057(2) | 0.0010(2) | 0.0025(3) | -0.0003(4) |
| **O24** | 0.0051(4) | 0.0024(3) | 0.0051(2) | 0.0009(1) | 0.0007(3) | 0.0006(4) |
| **O31** | 0.0038(3) | 0.0072(3) | 0.0042(3) | 0.0019(2) | 0.0016(3) | 0.0002(2) |
| **O32** | 0.0057(4) | 0.0005(3) | 0.0032(3) | -0.0004(2) | -0.0010(3) | 0.0006(3) |
| **O33** | 0.0016(4) | 0.0072(2) | 0.0054(3) | -0.0010(2) | 0.0011(4) | 0.0008(5) |
| **O34** | 0.0033(4) | 0.0008(2) | 0.0058(3) | 0.0003(2) | -0.0010(4) | -0.0014(4) |
| **O41** | 0.0040(4) | 0.0014(4) | 0.0040(3) | -0.0012(3) | -0.0007(3) | 0.0006(3) |
| **O42** | 0.0048(4) | 0.0031(2) | 0.0054(3) | -0.0001(2) | -0.0013(3) | -0.0003(2) |
| **O43** | 0.0034(3) | 0.0032(3) | 0.0047(3) | -0.0002(3) | 0.0004(3) | -0.0016(3) |
| **O44** | 0.0030(3) | 0.0057(2) | 0.0034(3) | 0.0009(3) | -0.0001(3) | -0.0002(3) |
| **O5A1** | 0.0017(3) | 0.0043(3) | 0.0036(3) | 0.0003(3) | 0.0011(2) | 0.0002(2) |
| **O5A2** | 0.0044(3) | 0.0021(3) | 0.0027(3) | -0.0001(2) | 0.0007(2) | 0.0019(2) |
| **O5A3** | 0.0039(4) | 0.0014(3) | 0.0051(4) | -0.0014(3) | -0.0001(3) | 0.0003(3) |
| **O5A4** | 0.0044(4) | 0.0054(4) | 0.0033(4) | 0.0002(3) | 0.0005(3) | 0.0007(3) |
| **O5B1** | 0.0019(3) | 0.0030(3) | 0.0030(3) | -0.0003(2) | -0.0004(2) | 0.0001(2) |
| **O5B2** | 0.0026(3) | 0.0046(3) | 0.0031(3) | -0.0010(2) | -0.0008(2) | -0.0013(3) |
| **O5B3** | 0.0044(4) | 0.0085(5) | 0.0055(5) | -0.0003(4) | 0.0000(3) | -0.0001(4) |
| **O5B4** | 0.0035(4) | 0.0063(5) | 0.0062(5) | -0.0016(4) | -0.0006(3) | -0.0019(3) |
| **O6A1** | 0.0019(3) | 0.0029(3) | 0.0042(3) | 0.0010(3) | -0.0007(2) | 0.0001(3) |
| **O6A2** | 0.0036(3) | 0.0025(3) | 0.0031(3) | 0.0006(3) | -0.0009(3) | -0.0007(3) |
| **O6A3** | 0.0034(3) | 0.0043(3) | 0.0064(4) | -0.0007(4) | 0.0005(3) | -0.0010(4) |
| **O6A4** | 0.0033(3) | 0.0023(3) | 0.0052(3) | 0.0008(3) | -0.0001(2) | -0.0003(3) |
| **O6B1** | 0.0027(2) | 0.0036(3) | 0.0043(3) | -0.0016(3) | 0.0008(2) | 0.0005(3) |
| **O6B2** | 0.0035(3) | 0.0026(2) | 0.0036(2) | -0.0014(3) | -0.0007(2) | -0.0002(3) |
| **O6B3** | 0.0054(4) | 0.0066(4) | 0.0031(3) | -0.0007(4) | 0.0001(3) | 0.0021(4) |
| **O6B4** | 0.0024(3) | 0.0086(4) | 0.0039(3) | -0.0018(4) | 0.0001(2) | -0.0001(3) |

Appendix Table 8 – B-B distances from a given site and their deviation from the global average (dB). Divalent-like sites are colour coded in blue, trivalent-like sites are in yellow.

| Site | <Fe-Fe> | Fe-Fe bond lenghts and dBB from the global average organised by opposite pairs. First pair is perpendicular to the short JT axis | | | | | | | | | | | | | | | | | |
|---|---|---|---|---|---|---|---|---|---|---|---|---|---|---|---|---|---|---|---|
| B1B1 | 2.9253881 | B32 | 2.8538461 | -0.1125544 | B33 | 2.8334908 | -0.1329096 | B44 | 2.9627048 | -0.0036956 | B41 | 2.9684178 | 0.0020173 | B1A1 | 2.9533718 | -0.0130287 | B1A2 | 2.9804971 | 0.0140966 |
| B31 | 2.9590408 | B2A1 | 2.9893337 | 0.0229333 | B1B2 | 2.8314024 | -0.134998 | B41 | 3.0037943 | 0.0373939 | B42 | 2.9896267 | 0.0232262 | B2B2 | 3.0081033 | 0.0417029 | B1A1 | 2.9319846 | -0.0344158 |
| B32 | 2.9373382 | B1B1 | 2.8538461 | -0.1125544 | B2A2 | 3.0012953 | 0.0348949 | B42 | 3.0338712 | 0.0674708 | B41 | 2.8225696 | -0.1438309 | B2B1 | 3.0632497 | 0.0968492 | B1A2 | 2.8491976 | -0.1172029 |
| B1A1 | 2.9402982 | B31 | 2.9319846 | -0.0344158 | B33 | 2.8368751 | -0.1295253 | B1B1 | 2.9533718 | -0.0130287 | B1B2 | 2.9321426 | -0.0342578 | B42 | 3.0222245 | 0.0558241 | B44 | 2.9651904 | -0.0012101 |
| B1A2 | 2.9531778 | B34 | 2.9262997 | -0.0401008 | B32 | 2.8491976 | -0.1172029 | B1B1 | 2.9804971 | 0.0140966 | B1B2 | 3.0158457 | 0.0494453 | B41 | 2.9532107 | -0.0131898 | B43 | 2.9940163 | 0.0276159 |
| B33 | 2.9432041 | B44 | 2.834503 | -0.1318974 | B43 | 3.0664907 | 0.1000902 | B1B1 | 2.8334908 | -0.1329096 | B2A1 | 3.0394458 | 0.0730453 | B1A1 | 2.8368751 | -0.1295253 | B2B1 | 3.0484193 | 0.0820188 |
| B41 | 2.9585806 | B31 | 3.0037943 | 0.0373939 | B32 | 2.8225696 | -0.1438309 | B1B1 | 2.9684178 | 0.0020173 | B2A1 | 3.0026748 | 0.0362743 | B2B2 | 3.0008167 | 0.0344162 | B1A2 | 2.9532107 | -0.0131898 |
| B2A1 | 2.9925569 | B2B1 | 2.9181462 | -0.0482542 | B2B2 | 3.0183996 | 0.0519991 | B43 | 2.9873412 | 0.0209407 | B31 | 2.9893337 | 0.0229333 | B33 | 3.0394458 | 0.0730453 | B41 | 3.0026748 | 0.0362743 |
| B34 | 2.986688 | B1B2 | 3.010887 | 0.0444865 | B2A2 | 3.0433568 | 0.0769563 | B44 | 2.9543825 | -0.012018 | B43 | 2.9929252 | 0.0265247 | B2B2 | 2.9922771 | 0.0258766 | B1A2 | 2.9262997 | -0.0401008 |
| B1B2 | 2.963602 | B34 | 3.010887 | 0.0444865 | B31 | 2.8314024 | -0.134998 | B42 | 2.9484962 | -0.0179043 | B43 | 3.0428378 | 0.0764373 | B1A1 | 2.9321426 | -0.0342578 | B1A2 | 3.0158457 | 0.0494453 |
| B43 | 3.0122072 | B34 | 2.9929252 | 0.0265247 | B33 | 3.0664907 | 0.1000902 | B2A1 | 2.9873412 | 0.0209407 | B1B2 | 3.0428378 | 0.0764373 | B2B1 | 2.989632 | 0.0232316 | B1A2 | 2.9940163 | 0.0276159 |
| B2B2 | 3.0114639 | B44 | 2.9975276 | 0.0311272 | B31 | 3.0081033 | 0.0417029 | B2A1 | 3.0183996 | 0.0519991 | B2A2 | 3.0516593 | 0.0852588 | B34 | 2.9922771 | 0.0258766 | B41 | 3.0008167 | 0.0344162 |
| B44 | 2.9581826 | B34 | 2.9543825 | -0.012018 | B33 | 2.834503 | -0.1318974 | B1B1 | 2.9627048 | -0.0036956 | B2A2 | 3.034787 | 0.0683865 | B2B2 | 2.9975276 | 0.0311272 | B1A1 | 2.9651904 | -0.0012101 |
| B42 | 2.9651334 | B1B2 | 2.9484962 | -0.0179043 | B2A2 | 2.8378265 | -0.1285739 | B31 | 2.9896267 | 0.0232262 | B32 | 3.0338712 | 0.0674708 | B2B1 | 2.9587553 | -0.0076451 | B1A1 | 3.0222245 | 0.0558241 |
| B2B1 | 2.9785458 | B2A2 | 2.8930724 | -0.0733281 | B2A1 | 2.9181462 | -0.0482542 | B32 | 3.0632497 | 0.0968492 | B43 | 2.989632 | 0.0232316 | B33 | 3.0484193 | 0.0820188 | B42 | 2.9587553 | -0.0076451 |
| B2A2 | 2.9769995 | B32 | 3.0012953 | 0.0348949 | B44 | 3.034787 | 0.0683865 | B34 | 3.0433568 | 0.0769563 | B42 | 2.8378265 | -0.1285739 | B2B2 | 3.0516593 | 0.0852588 | B2B1 | 2.8930724 | -0.0733281 |

# A3. Zn-doped magnetite

**Appendix Table 9 – Summary of experimental and refinement details for structure analysis of the Zn-doped magnetite grain in the monoclinic Cc phase at 80 K, below the Verwey transition.**

| | |
|---|---|
| **Crystal Data** | |
| Chemical Formula | $Fe_{3-x}Zn_xO_4$ with x = 0.03 |
| Cell setting, Space group | *Cc* |
| Temperature (K) | 80.00(2) |
| a,b,c (Å) | 11.8795(2), 11.8566(2), 16.7899(3) |
| β ($^{o}$) | 90.172(9) |
| Volume (Å$^3$) | 2364.863(7) |
| $D_c$(g cm$^{-3}$) | 5.203 |
| X-ray wavelength (Å) | 0.15815 |
| μ (mm$^{-1}$) | 7.31 |
| Crystal form | Approximately spherical |
| Crystal size (mm) | r ≈ 0.05 |
| **Data Collection** | |
| Diffractometer | ID11@ESRF, Huber Omega and phi axis |
| Data collection method | ω |
| Absorption correction | none |
| No. of observed, symmetry unique reflections | 421461, 103873 |
| $\theta_{max}$ ($^{o}$) | 32.82 |
| $R_{int}$ | 0.0662 |
| Range of h,k,l | -42 → h → 42 |
| | -42 → k → 42 |
| | -59 → l → 59 |
| **Refinement** | |
| Refine on | $F^2$ |
| R($F^2$), R[$F^2$ > 4 sigma], wR($F^2$), S | 0.0767, 0.0726, 0.1848, 1.079 |
| Cutoff: I >σ | none |
| No. of reflections | 103873 |
| No. of parameters | 512 |
| Weighting scheme | Weight = 1 / [ sigma$^2$($F_o^2$) + (0.0489 * P)$^2$ + 6.53 * P] where P = (Max ( $F_o^2$, 0 ) + 2 * $F_c^2$ ) / 3 |
| (Δ/α)mean | 0.001 |
| (Δ/α)max | 0.007 |
| Δρmax, Δρmin (e Å$^{-3}$) | 5.88, -5.03 |
| Twin law | 0 1 0 -1 0 0 0 0 1 -8 |
| Twin fractions: | 0.00(1), 0.02(1), 0.17(1), 0.32(1), 0.16(1), 0.01(1), -0.01(1) |

**Appendix Table 10 – Fractional coordinates and equivalent isotropic thermal parameters for Zn-doped magnetite at 80 K.**

| SITES | X | Y | Z | UEQUIVALENT (Å$^2$) |
|---|---|---|---|---|
| **A23** | 0.13347(3) | 0.00066(3) | 0.31334(2) | 0.00222(2) |
| **A13** | 0.13443(4) | 0.25081(3) | 0.43792(2) | 0.00287(3) |
| **A14** | 0.13616(4) | 0.24779(3) | 0.93767(2) | 0.00261(3) |
| **A24** | 0.13592(3) | 0.50311(3) | 0.31343(2) | 0.00282(2) |
| **A21** | 0.38305(3) | 0.00290(4) | 0.19021(2) | 0.00283(3) |
| **A11** | 0.38500(4) | 0.25126(3) | 0.06420(2) | 0.00287(3) |
| **A12** | 0.38676(4) | 0.24834(3) | 0.56398(2) | 0.00268(3) |
| **A22** | 0.38746(3) | 0.50074(4) | 0.18955(2) | 0.00311(3) |
| **B2B1** | 0.01012(6) | 0.25405(2) | 0.25118(3) | 0.00365(2) |
| **B2B2** | 0.00990(5) | 0.24775(2) | 0.75118(3) | 0.00323(2) |
| **B1B1** | 0.01320(4) | 0.49987(5) | 0.00302(3) | 0.00364(3) |
| **B43** | 0.13531(4) | 0.12781(4) | 0.12679(3) | 0.00338(3) |
| **B34** | 0.13610(4) | 0.12459(4) | 0.62468(2) | 0.00411(4) |
| **B33** | 0.13514(4) | 0.38433(4) | 0.12254(2) | 0.00389(3) |
| **B44** | 0.13567(4) | 0.37531(4) | 0.62567(2) | 0.00344(3) |
| **B1A2** | 0.26055(4) | 0.00014(5) | 0.00109(3) | 0.00360(2) |
| **B2A1** | 0.25533(4) | 0.25298(3) | 0.25000(2) | 0.00353(3) |
| **B2A2** | 0.26250(4) | 0.24769(3) | 0.75072(2) | 0.00412(4) |
| **B1A1** | 0.25977(4) | 0.49974(4) | 0.00176(3) | 0.00336(2) |
| **B41** | 0.38474(4) | 0.12545(4) | 0.37621(2) | 0.00320(3) |
| **B32** | 0.38511(4) | 0.11818(5) | 0.87909(2) | 0.00445(4) |
| **B31** | 0.38386(4) | 0.37561(5) | 0.37797(2) | 0.00419(4) |
| **B42** | 0.38470(4) | 0.37235(5) | 0.87564(3) | 0.00384(3) |
| **B1B2** | 0.50923(5) | 0.50009(6) | 0.50128(3) | 0.00454(3) |
| **O6B1** | 0.0168(2) | 0.0012(2) | 0.1239(1) | 0.0050(2) |
| **O5B1** | 0.0165(2) | 0.2523(2) | 0.1300(1) | 0.0039(2) |
| **O5B2** | 0.0146(2) | 0.2466(2) | 0.6309(1) | 0.0034(2) |
| **O6B2** | 0.0115(2) | 0.5002(2) | 0.1274(1) | 0.0028(1) |
| **O14** | 0.1351(2) | 0.1192(2) | 0.0028(1) | 0.0037(2) |
| **O23** | 0.1345(2) | 0.1214(2) | 0.5029(1) | 0.0045(2) |
| **O43** | 0.1349(2) | 0.1316(2) | 0.2486(1) | 0.0037(2) |
| **O34** | 0.1334(2) | 0.1308(2) | 0.7476(1) | 0.0032(1) |
| **O24** | 0.1350(2) | 0.3766(2) | 0.0037(1) | 0.0035(2) |
| **O33** | 0.1360(2) | 0.3732(2) | 0.2487(1) | 0.0053(2) |
| **O13** | 0.1351(2) | 0.3785(2) | 0.5047(1) | 0.0034(2) |
| **O44** | 0.1347(2) | 0.3655(2) | 0.7502(1) | 0.0044(2) |
| **O6A1** | 0.2530(1) | 0.0021(2) | 0.1249(1) | 0.0030(1) |

| | | | | |
|---|---|---|---|---|
| **O6A3** | 0.2620(1) | 0.0015(2) | 0.3786(1) | 0.0027(1) |
| **O5A1** | 0.2545(2) | 0.2507(2) | 0.1290(1) | 0.0041(2) |
| **O5A2** | 0.2576(2) | 0.2446(2) | 0.6294(1) | 0.0033(1) |
| **O5A3** | 0.2644(2) | 0.2518(2) | 0.3726(1) | 0.0049(2) |
| **O5A4** | 0.2669(2) | 0.2471(2) | 0.8734(1) | 0.0046(2) |
| **O6A2** | 0.2581(2) | 0.4998(2) | 0.1273(1) | 0.0062(2) |
| **O6A4** | 0.2676(2) | 0.5024(2) | 0.3772(1) | 0.0041(2) |
| **O41** | 0.3840(2) | 0.1347(2) | 0.2550(1) | 0.0039(2) |
| **O12** | 0.3849(2) | 0.1176(2) | 0.4992(1) | 0.0033(1) |
| **O32** | 0.3828(2) | 0.1259(2) | 0.7555(1) | 0.0034(1) |
| **O21** | 0.3855(2) | 0.1216(2) | 1.0004(1) | 0.0039(2) |
| **O31** | 0.3854(2) | 0.3710(2) | 0.2538(1) | 0.0042(2) |
| **O22** | 0.3868(2) | 0.3770(2) | 0.4980(1) | 0.0046(2) |
| **O42** | 0.3849(2) | 0.3696(2) | 0.7538(1) | 0.0042(2) |
| **O11** | 0.3855(2) | 0.3812(2) | 0.9966(1) | 0.0046(2) |
| **O6B4** | 0.5051(2) | 0.0017(2) | 0.3794(1) | 0.0039(2) |
| **O5B4** | 0.5062(2) | 0.2539(2) | 0.3728(1) | 0.0046(2) |
| **O5B3** | 0.5028(2) | 0.2492(2) | 0.8734(1) | 0.0037(2) |
| **O6B3** | 0.5036(2) | 0.5015(2) | 0.3786(1) | 0.0042(2) |

### Appendix Table 11 – Anisotropic thermal parameters for Zn-doped magnetite at 80 K.

| SITES | U11 (Å$^2$) | U22 (Å$^2$) | U33 (Å$^2$) | U23 (Å$^2$) | U13 (Å$^2$) | U12 (Å$^2$) |
|---|---|---|---|---|---|---|
| **A23** | 0.00226(5) | 0.00242(5) | 0.00196(3) | -0.00011(5) | -0.00077(3) | 0.00001(5) |
| **A13** | 0.00320(7) | 0.00310(6) | 0.00232(5) | -0.00040(4) | -0.00035(5) | 0.00017(5) |
| **A14** | 0.00236(6) | 0.00286(5) | 0.00261(5) | -0.00046(4) | -0.00007(4) | 0.00047(5) |
| **A24** | 0.00290(6) | 0.00248(5) | 0.00307(4) | -0.00012(5) | -0.00047(4) | 0.00049(5) |
| **A21** | 0.00215(5) | 0.00380(6) | 0.00255(5) | 0.00006(5) | 0.00028(4) | 0.00017(5) |
| **A11** | 0.00348(8) | 0.00255(6) | 0.00258(5) | 0.00025(4) | -0.00022(5) | 0.00003(5) |
| **A12** | 0.00272(6) | 0.00261(5) | 0.00269(5) | -0.00003(4) | 0.00013(4) | -0.00025(5) |
| **A22** | 0.00328(6) | 0.00248(5) | 0.00359(6) | 0.00019(6) | 0.00111(4) | 0.00012(5) |
| **B2B1** | 0.00456(4) | 0.00336(3) | 0.00302(3) | 0.00000(6) | -0.00026(3) | 0.00036(7) |
| **B2B2** | 0.00323(3) | 0.00317(3) | 0.00329(3) | 0.00003(6) | -0.00039(3) | -0.00019(6) |
| **B1B1** | 0.00395(6) | 0.00292(4) | 0.00406(5) | -0.00033(3) | 0.00145(4) | -0.00020(3) |
| **B43** | 0.00336(6) | 0.00368(6) | 0.00309(5) | 0.00082(5) | -0.00012(5) | -0.00026(6) |
| **B34** | 0.00334(7) | 0.00523(8) | 0.00375(7) | 0.00197(7) | -0.00054(6) | -0.00049(7) |
| **B33** | 0.00369(6) | 0.00457(7) | 0.00342(6) | -0.00056(5) | 0.00006(5) | 0.00060(5) |
| **B44** | 0.00309(6) | 0.00434(6) | 0.00291(5) | -0.00017(4) | 0.00042(5) | -0.00067(5) |
| **B1A2** | 0.00361(5) | 0.00380(5) | 0.00340(4) | -0.00031(5) | -0.00108(4) | 0.00025(6) |
| **B2A1** | 0.00408(7) | 0.00290(5) | 0.00362(5) | 0.00083(4) | 0.00029(5) | 0.00073(4) |
| **B2A2** | 0.00449(8) | 0.00410(7) | 0.00379(6) | 0.00014(5) | 0.00115(6) | -0.00116(5) |

| | | | | | | |
|---|---|---|---|---|---|---|
| **B1A1** | 0.00385(5) | 0.00265(5) | 0.00356(4) | -0.00037(5) | -0.00026(3) | 0.00046(5) |
| **B41** | 0.00267(6) | 0.00355(6) | 0.00338(5) | 0.00004(4) | -0.00068(5) | 0.00033(4) |
| **B32** | 0.00210(6) | 0.00703(9) | 0.00422(7) | -0.00239(6) | -0.00064(5) | 0.00004(5) |
| **B31** | 0.00295(7) | 0.00521(8) | 0.00441(8) | 0.00098(6) | 0.00102(6) | 0.00092(6) |
| **B42** | 0.00299(7) | 0.00501(8) | 0.00354(6) | 0.00081(5) | 0.00100(5) | 0.00080(6) |
| **B1B2** | 0.00495(6) | 0.00347(4) | 0.00523(6) | -0.00024(2) | 0.00252(5) | -0.00036(2) |
| **O6B1** | 0.0040(3) | 0.0051(4) | 0.0059(3) | 0.0002(4) | 0.0020(2) | -0.0001(4) |
| **O5B1** | 0.0041(4) | 0.0043(3) | 0.0032(3) | -0.0016(2) | 0.0008(2) | -0.0003(2) |
| **O5B2** | 0.0018(3) | 0.0051(4) | 0.0032(3) | -0.0005(2) | 0.0003(2) | -0.0005(2) |
| **O6B2** | 0.0032(3) | 0.0029(3) | 0.0023(2) | 0.0005(2) | 0.0005(2) | 0.0001(2) |
| **O14** | 0.0048(4) | 0.0031(3) | 0.0033(3) | 0.0001(2) | -0.0008(3) | -0.0002(2) |
| **O23** | 0.0038(4) | 0.0061(4) | 0.0036(3) | 0.0012(2) | -0.0019(3) | 0.0000(3) |
| **O43** | 0.0043(4) | 0.0035(3) | 0.0032(3) | 0.0002(2) | 0.0005(3) | 0.0001(3) |
| **O34** | 0.0041(3) | 0.0034(3) | 0.0022(2) | -0.0005(2) | 0.0001(2) | -0.0003(2) |
| **O24** | 0.0043(4) | 0.0017(2) | 0.0045(3) | -0.0015(2) | -0.0013(3) | 0.0004(2) |
| **O33** | 0.0041(4) | 0.0055(3) | 0.0061(4) | -0.0008(3) | -0.0010(3) | 0.0010(3) |
| **O13** | 0.0027(3) | 0.0039(3) | 0.0037(3) | -0.0001(2) | -0.0012(2) | -0.0003(2) |
| **O44** | 0.0041(3) | 0.0049(3) | 0.0040(3) | 0.0011(2) | 0.0007(2) | 0.0000(3) |
| **O6A1** | 0.0016(2) | 0.0044(3) | 0.0031(2) | 0.0008(3) | -0.0005(2) | -0.0002(3) |
| **O6A3** | 0.0014(2) | 0.0038(3) | 0.0029(2) | -0.0010(2) | 0.0002(2) | 0.0003(2) |
| **O5A1** | 0.0033(4) | 0.0059(4) | 0.0030(3) | 0.0001(2) | 0.0005(3) | 0.0002(2) |
| **O5A2** | 0.0030(3) | 0.0042(3) | 0.0027(2) | 0.0005(2) | 0.0000(2) | -0.0004(2) |
| **O5A3** | 0.0046(4) | 0.0046(4) | 0.0055(4) | -0.0014(3) | -0.0001(3) | 0.0004(3) |
| **O5A4** | 0.0041(4) | 0.0038(2) | 0.0058(4) | -0.0007(2) | -0.0005(3) | 0.0009(2) |
| **O6A2** | 0.0068(4) | 0.0036(2) | 0.0081(4) | 0.0000(3) | 0.0007(3) | 0.0004(3) |
| **O6A4** | 0.0038(3) | 0.0035(2) | 0.0050(3) | 0.0003(3) | -0.0008(2) | 0.0000(3) |
| **O41** | 0.0035(3) | 0.0047(3) | 0.0035(3) | -0.0014(2) | 0.0001(2) | -0.0001(3) |
| **O12** | 0.0054(4) | 0.0022(2) | 0.0024(2) | -0.0011(2) | 0.0008(2) | 0.0003(2) |
| **O32** | 0.0033(3) | 0.0037(3) | 0.0033(2) | -0.0007(2) | 0.0007(2) | -0.0006(2) |
| **O21** | 0.0051(4) | 0.0048(4) | 0.0017(2) | 0.0003(2) | 0.0009(2) | 0.0009(3) |
| **O31** | 0.0046(4) | 0.0026(3) | 0.0055(3) | 0.0012(2) | -0.0001(3) | -0.0003(3) |
| **O22** | 0.0066(4) | 0.0027(3) | 0.0046(3) | -0.0008(2) | 0.0017(3) | 0.0000(3) |
| **O42** | 0.0046(4) | 0.0033(3) | 0.0047(3) | 0.0003(3) | -0.0012(3) | -0.0014(3) |
| **O11** | 0.0043(4) | 0.0058(4) | 0.0038(3) | -0.0002(3) | -0.0001(3) | 0.0011(3) |
| **O6B4** | 0.0029(3) | 0.0071(4) | 0.0017(2) | -0.0004(2) | 0.0009(2) | 0.0006(2) |
| **O5B4** | 0.0047(4) | 0.0046(4) | 0.0044(3) | 0.0000(3) | -0.0012(3) | 0.0015(3) |
| **O5B3** | 0.0026(3) | 0.0045(4) | 0.0040(3) | 0.0016(2) | -0.0008(2) | 0.0015(2) |
| **O6B3** | 0.0043(3) | 0.0035(3) | 0.0047(3) | -0.0007(3) | 0.0001(2) | -0.0003(3) |

Appendix Table 12 – B-B distances from a given site and their deviation from the global average (dB). Divalent-like sites are colour coded in blue, trivalent-like sites are in yellow.

| | | | | | | | | | | | | | | | | | | | |
|---|---|---|---|---|---|---|---|---|---|---|---|---|---|---|---|---|---|---|---|
| B1B1 | 2.9361507 | B32 | 2.9316088 | -0.0360167 | B33 | 2.8256876 | -0.1419379 | B44 | 2.9204483 | -0.0471772 | B41 | 3.0084605 | 0.0408351 | B1A1 | 2.9291949 | -0.0384306 | B1A2 | 3.0015043 | 0.0338788 |
| B31 | 2.9738398 | B2A1 | 3.0069958 | 0.0393703 | B1B2 | 2.9436105 | -0.024015 | B41 | 2.9662204 | -0.0014051 | B42 | 2.988629 | 0.0210036 | B2B2 | 2.9886078 | 0.0209823 | B1A1 | 2.9489753 | -0.0186502 |
| B32 | 2.9610101 | B2B1 | 3.0218557 | 0.0542302 | B1A2 | 2.8917816 | -0.0758439 | B1B1 | 2.9316088 | -0.0360167 | B2A2 | 3.0176274 | 0.0500019 | B42 | 3.0141711 | 0.0465456 | B41 | 2.8890158 | -0.0786097 |
| B1A1 | 2.9423531 | B31 | 2.9489753 | -0.0186502 | B33 | 2.8626038 | -0.1050217 | B1B1 | 2.9291949 | -0.0384306 | B1B2 | 2.963541 | -0.0040845 | B42 | 2.9978114 | 0.0301859 | B44 | 2.9519924 | -0.0156331 |
| B1A2 | 2.9653505 | B34 | 2.9490168 | -0.0186087 | B32 | 2.8917816 | -0.0758439 | B1B1 | 3.0015043 | 0.0338788 | B1B2 | 2.9855187 | 0.0178933 | B43 | 2.996318 | 0.0286925 | B41 | 2.9679636 | 0.0003382 |
| B33 | 2.9384377 | B2B1 | 3.0456217 | 0.0779963 | B1A1 | 2.8626038 | -0.1050217 | B1B1 | 2.8256876 | -0.1419379 | B2A1 | 3.0041355 | 0.0365101 | B43 | 3.0422524 | 0.0746269 | B44 | 2.8503254 | -0.1173001 |
| B41 | 2.9723994 | **B31** | 2.9662204 | -0.0014051 | **B32** | 2.8890158 | -0.0786097 | B1B1 | 3.0084605 | 0.0408351 | B2A1 | 3.0200174 | 0.0523919 | B2B2 | 2.9827186 | 0.0150931 | B1A2 | 2.9679636 | 0.0003382 |
| B2A1 | 2.9805678 | B33 | 3.0041355 | 0.0365101 | B41 | 3.0200174 | 0.0523919 | B2B1 | 2.9130767 | -0.0545488 | B2B2 | 3.024239 | 0.0566135 | B43 | 2.9149421 | -0.0526833 | B31 | 3.0069958 | 0.0393703 |
| B34 | 2.9712112 | B43 | 2.9928388 | 0.0252133 | B44 | 2.9728163 | 0.0051909 | B1B2 | 2.9536641 | -0.0139614 | B2A2 | 2.9739049 | 0.0062794 | B2B2 | 2.9850264 | 0.0174009 | B1A2 | 2.9490168 | -0.0186087 |
| B1B2 | 2.9708228 | B34 | 2.9536641 | -0.0139614 | B31 | 2.9436105 | -0.024015 | B42 | 2.9844799 | 0.0168544 | B43 | 2.9941227 | 0.0264972 | B1A1 | 2.963541 | -0.0040845 | B1A2 | 2.9855187 | 0.0178933 |
| B43 | 2.9854088 | B34 | 2.9928388 | 0.0252133 | B33 | 3.0422524 | 0.0746269 | B2A1 | 2.9149421 | -0.0526833 | B1B2 | 2.9941227 | 0.0264972 | B2B1 | 2.9719788 | 0.0043533 | B1A2 | 2.996318 | 0.0286925 |
| B2B2 | 2.9963292 | B34 | 2.9850264 | 0.0174009 | B41 | 2.9827186 | 0.0150931 | B2A1 | 3.024239 | 0.0566135 | B2A2 | 3.0007687 | 0.0331433 | B44 | 2.9966149 | 0.0289895 | B31 | 2.9886078 | 0.0209823 |
| B44 | 2.9472813 | B34 | 2.9728163 | 0.0051909 | B33 | 2.8503254 | -0.1173001 | B1B1 | 2.9204483 | -0.0471772 | B2A2 | 2.9914906 | 0.0238651 | B2B2 | 2.9966149 | 0.0289895 | B1A1 | 2.9519924 | -0.0156331 |
| B42 | 2.984208 | **B1B2** | 2.9844799 | 0.0168544 | **B2A2** | 2.9450039 | -0.0226216 | B2B1 | 2.975153 | 0.0075275 | B1A1 | 2.9978114 | 0.0301859 | B31 | 2.988629 | 0.0210036 | B32 | 3.0141711 | 0.0465456 |
| B2B1 | 2.9782261 | B2A1 | 2.9130767 | -0.0545488 | B2A2 | 2.9416708 | -0.0259547 | B32 | 3.0218557 | 0.0542302 | B43 | 2.9719788 | 0.0043533 | B33 | 3.0456217 | 0.0779963 | B42 | 2.975153 | 0.0075275 |
| B2A2 | 2.9784111 | B32 | 3.0176274 | 0.0500019 | B44 | 2.9914906 | 0.0238651 | B34 | 2.9739049 | 0.0062794 | B42 | 2.9450039 | -0.0226216 | B2B2 | 3.0007687 | 0.0331433 | B2B1 | 2.9416708 | -0.0259547 |

# A4. Pair Distribution Function analysis

**Appendix Table 13 – Metrically cubic cell with cubic undistorted positions in supercell of dimensions equivalent to the ones of the monoclinic Cc. This model corresponds to Verwey shift $x_V$ = 0 and represents a perfectly undistorted cubic spinel. The high-resolution structural model for pure magnetite at 130 K from Ref[138] was used for the atomic positions and relative standard deviations.**

| *Atom label* | Occupancy | x | y | z |
|---|---|---|---|---|
| *A11* | 1 | 0.627 | 0 | 0.8135 |
| *A12* | 1 | 0.127 | 0 | 0.8135 |
| *A13* | 1 | 0.877 | 0.25 | 0.0635 |
| *A14* | 1 | 0.877 | 0.25 | 0.5635 |
| *A21* | 1 | 0.377 | 0 | 0.6885 |
| *A22* | 1 | 0.877 | 0 | 0.6885 |
| *A23* | 1 | 0.627 | 0.25 | 0.9385 |
| *A24* | 1 | 0.627 | 0.25 | 0.4385 |
| *B1A1* | 1 | 0.002 | 0 | 0.001 |
| *B1A2* | 1 | 0.502 | 0 | 0.001 |
| *B1B1* | 1 | 0.252 | 0.25 | 0.251 |
| *B1B2* | 1 | 0.252 | 0.25 | 0.751 |
| *B2A1* | 1 | 0.127 | 0.125 | 0.626 |
| *B2A2* | 1 | 0.127 | 0.125 | 0.126 |
| *B2B1* | 1 | 0.627 | 0.125 | 0.626 |
| *B2B2* | 1 | 0.627 | 0.125 | 0.126 |
| *B31* | 1 | 0.377 | 0.375 | 0.876 |
| *B32* | 1 | 0.377 | 0.375 | 0.376 |
| *B33* | 1 | 0.877 | 0.375 | 0.876 |
| *B34* | 1 | 0.877 | 0.375 | 0.376 |
| *B41* | 1 | 0.252 | 0 | 0.001 |
| *B42* | 1 | 0.752 | 0 | 0.001 |
| *B43* | 1 | 0.502 | 0.25 | 0.251 |
| *B44* | 1 | 0.502 | 0.25 | 0.751 |
| *O11* | 1 | 0.75690(3) | 0.00000(3) | 0.87845(15) |
| *O12* | 1 | 0.25690(3) | 0.00000(3) | 0.87845(15) |
| *O13* | 1 | 0.00690(3) | 0.25000(3) | 0.12845(15) |
| *O14* | 1 | 0.00690(3) | 0.25000(3) | 0.62845(15) |
| *O21* | 1 | 0.12700(3) | 0.37010(3) | 0.74855(15) |
| *O22* | 1 | 0.12700(3) | 0.37010(3) | 0.24855(15) |
| *O23* | 1 | 0.62700(3) | 0.37010(3) | 0.74855(15) |
| *O24* | 1 | 0.62700(3) | 0.37010(3) | 0.24855(15) |
| *O31* | 1 | 0.87700(3) | 0.12010(3) | 0.99855(15) |
| *O32* | 1 | 0.87700(3) | 0.12010(3) | 0.49855(15) |

| | | | | |
|---|---|---|---|---|
| O33 | 1 | 0.37700(3) | 0.12010(3) | 0.99855(15) |
| O34 | 1 | 0.37700(3) | 0.12010(3) | 0.49855(15) |
| O41 | 1 | 0.49710(3) | 0.00000(3) | 0.87845(15) |
| O42 | 1 | 0.99710(3) | 0.00000(3) | 0.87845(15) |
| O43 | 1 | 0.74710(3) | 0.25000(3) | 0.12845(15) |
| O44 | 1 | 0.74710(3) | 0.25000(3) | 0.62845(15) |
| O5A1 | 1 | 0.24710(3) | 0.00000(3) | 0.62355(15) |
| O5A2 | 1 | 0.74710(3) | 0.00000(3) | 0.62355(15) |
| O5A3 | 1 | 0.49710(3) | 0.25000(3) | 0.87355(15) |
| O5A4 | 1 | 0.49710(3) | 0.25000(3) | 0.37355(15) |
| O5B1 | 1 | 0.62700(3) | 0.37990(3) | 0.00345(15) |
| O5B2 | 1 | 0.62700(3) | 0.37990(3) | 0.50345(15) |
| O5B3 | 1 | 0.12700(3) | 0.37990(3) | 0.00345(15) |
| O5B4 | 1 | 0.12700(3) | 0.37990(3) | 0.50345(15) |
| O6A1 | 1 | 0.37700(3) | 0.12990(3) | 0.25345(15) |
| O6A2 | 1 | 0.37700(3) | 0.12990(3) | 0.75345(15) |
| O6A3 | 1 | 0.87700(3) | 0.12990(3) | 0.25345(15) |
| O6A4 | 1 | 0.87700(3) | 0.12990(3) | 0.75345(15) |
| O6B1 | 1 | 0.00690(3) | 0.00000(3) | 0.62355(15) |
| O6B2 | 1 | 0.50690(3) | 0.00000(3) | 0.62355(15) |
| O6B3 | 1 | 0.25690(3) | 0.25000(3) | 0.87355(15) |
| O6B4 | 1 | 0.25690(3) | 0.25000(3) | 0.37355(15) |

**Appendix Table 14 – Metrically cubic cell with monoclinic distorted positions in supercell of dimensions equivalent to the ones of the monoclinic Cc. This model corresponds to Verwey shift $x_V$ = 1 and represents a fully distorted monoclinic ground state. The high-resolution structural model for pure magnetite at 90 K from Ref[26] was used for the atomic positions and relative standard deviations.**

| *Atom label* | Occupancy | x | y | z | Biso (Å$^2$) |
|---|---|---|---|---|---|
| A11 | 1 | 0.62943(2) | 0.00502(2) | 0.81268(13) | 0.00187 |
| A12 | 1 | 0.12546(2) | 0.00162(2) | 0.81099(13) | 0.00172 |
| A13 | 1 | 0.87529(2) | 0.24867(2) | 0.06528(13) | 0.0019 |
| A14 | 1 | 0.87834(2) | 0.25204(2) | 0.56495(13) | 0.00186 |
| A21 | 1 | 0.37481(18) | 0.00477(2) | 0.69019(11) | 0.00189 |
| A22 | 1 | 0.88092(18) | 0.00074(2) | 0.68841(11) | 0.00183 |
| A23 | 1 | 0.62680(19) | 0.25398(2) | 0.93773(10) | 0.00185 |
| A24 | 1 | 0.62495(18) | 0.24724(19) | 0.43778(11) | 0.00179 |
| B1A1 | 1 | -0.00237(3) | 0.00076(3) | -0.00317(14) | 0.00232 |
| B1A2 | 1 | 0.50207(3) | 0.00050(3) | 0.00160(14) | 0.0022 |
| B1B1 | 1 | 0.25949(3) | 0.24780(3) | 0.25357(15) | 0.0024 |
| B1B2 | 1 | 0.24778(2) | 0.25639(2) | 0.75250(13) | 0.00206 |
| B2A1 | 1 | 0.12586(2) | 0.12776(15) | 0.62574(14) | 0.00209 |
| B2A2 | 1 | 0.12898(2) | 0.12538(16) | 0.12301(13) | 0.00186 |

| | | | | | |
|---|---|---|---|---|---|
| *B2B1* | 1 | 0.62808(3) | 0.12601(10) | 0.62642(18) | 0.00243 |
| *B2B2* | 1 | 0.62683(3) | 0.11338(10) | 0.12168(17) | 0.00194 |
| *B31* | 1 | 0.37714(2) | 0.37945(17) | 0.87971(13) | 0.00223 |
| *B32* | 1 | 0.37563(2) | 0.36913(16) | 0.37427(13) | 0.00191 |
| *B33* | 1 | 0.87664(2) | 0.38747(15) | 0.88065(12) | 0.00208 |
| *B34* | 1 | 0.87619(2) | 0.37518(18) | 0.37661(13) | 0.00198 |
| *B41* | 1 | 0.25136(2) | 0.00135(2) | 0.00100(14) | 0.00214 |
| *B42* | 1 | 0.75077(2) | 0.00212(2) | 0.00217(15) | 0.00244 |
| *B43* | 1 | 0.50275(2) | 0.24372(2) | 0.25178(15) | 0.00197 |
| *B44* | 1 | 0.50234(3) | 0.25412(3) | 0.75181(16) | 0.00228 |
| *O11* | 1 | 0.75982(12) | 0.00477(12) | 0.87660(8) | 0.00303 |
| *O12* | 1 | 0.25259(12) | 0.00327(11) | 0.87642(8) | 0.00277 |
| *O13* | 1 | 0.00537(13) | 0.24490(11) | 0.13070(8) | 0.00327 |
| *O14* | 1 | 0.01026(13) | 0.25207(12) | 0.62899(8) | 0.00337 |
| *O21* | 1 | 0.12962(13) | 0.37691(12) | 0.74564(8) | 0.0037 |
| *O22* | 1 | 0.12728(13) | 0.36320(13) | 0.24915(9) | 0.004 |
| *O23* | 1 | 0.62512(12) | 0.36980(11) | 0.74557(8) | 0.00307 |
| *O24* | 1 | 0.62958(13) | 0.36784(11) | 0.24671(8) | 0.00303 |
| *O31* | 1 | 0.87601(12) | 0.11957(10) | 1.00004(8) | 0.00319 |
| *O32* | 1 | 0.87718(13) | 0.12378(11) | 0.49993(8) | 0.0035 |
| *O33* | 1 | 0.37627(12) | 0.11928(11) | 0.99826(7) | 0.00304 |
| *O34* | 1 | 0.37656(12) | 0.12353(10) | 0.49962(7) | 0.00283 |
| *O41* | 1 | 0.50088(11) | 0.00176(10) | 0.87730(8) | 0.00297 |
| *O42* | 1 | 0.99736(12) | 0.00223(11) | 0.87619(8) | 0.00347 |
| *O43* | 1 | 0.74370(13) | 0.24950(11) | 0.13020(8) | 0.00367 |
| *O44* | 1 | 0.74874(12) | 0.25644(10) | 0.63025(7) | 0.00323 |
| *O5A1* | 1 | 0.24335(12) | 0.00275(11) | 0.62571(7) | 0.00305 |
| *O5A2* | 1 | 0.75123(13) | -0.00040(11) | 0.62466(7) | 0.0031 |
| *O5A3* | 1 | 0.49746(13) | 0.25561(12) | 0.87114(8) | 0.0036 |
| *O5A4* | 1 | 0.49505(13) | 0.24641(11) | 0.37207(8) | 0.00336 |
| *O5B1* | 1 | 0.62576(12) | 0.38280(11) | 0.00569(8) | 0.00317 |
| *O5B2* | 1 | 0.62372(13) | 0.37670(12) | 0.50330(8) | 0.0037 |
| *O5B3* | 1 | 0.12711(13) | 0.38186(11) | 0.00490(7) | 0.0031 |
| *O5B4* | 1 | 0.12595(12) | 0.37526(11) | 0.50168(7) | 0.00278 |
| *O6A1* | 1 | 0.37440(11) | 0.12398(11) | 0.25502(7) | 0.00331 |
| *O6A2* | 1 | 0.37752(11) | 0.13749(12) | 0.75466(7) | 0.00317 |
| *O6A3* | 1 | 0.87800(11) | 0.13034(13) | 0.25258(7) | 0.00335 |
| *O6A4* | 1 | 0.87821(11) | 0.13169(11) | 0.75170(6) | 0.00301 |
| *O6B1* | 1 | 0.01119(11) | 0.00229(12) | 0.62362(7) | 0.00369 |
| *O6B2* | 1 | 0.50298(11) | 0.00130(13) | 0.62598(7) | 0.00328 |
| *O6B3* | 1 | 0.25291(11) | 0.25518(13) | 0.87214(7) | 0.00332 |
| *O6B4* | 1 | 0.25606(11) | 0.24263(13) | 0.37410(7) | 0.00386 |

**Appendix Table 15 – Refinement output for $x_V$ = 0 at multiple temperatures.**

| T (K) | CELL (Å) | Uiso_FeA (Å$^2$) | Uiso_FeB (Å$^2$) | Uiso_O (Å$^2$) | $\delta_1$ (Å) | Rw (%) |
|---|---|---|---|---|---|---|
| **90** | 16.780(3) | 0.0017(3) | 0.0041(4) | 0.014(1) | 1.5(2) | 14.73 |
| **100** | 16.780(3) | 0.0017)3) | 0.0042(4) | 0.014(1) | 1.5(2) | 14.61 |
| **110** | 16.781(3) | 0.0018(3) | 0.0042(4) | 0.014(1) | 1.5(2) | 14.54 |
| **120** | 16.778(3) | 0.0017(3) | 0.0041(4) | 0.013(1) | 1.5(2) | 14.11 |
| **130** | 16.777(3) | 0.0017(3) | 0.0040(4) | 0.013(1) | 1.4(2) | 13.89 |
| **140** | 16.777(3) | 0.0018(3) | 0.0041(4) | 0.013(1) | 1.4(2) | 13.66 |
| **150** | 16.780(3) | 0.0019(3) | 0.0042(4) | 0.013(1) | 1.4(2) | 13.65 |
| **160** | 16.779(3) | 0.0020(3) | 0.0042(4) | 0.013(1) | 1.4(2) | 13.45 |
| **170** | 16.780(3) | 0.0021(3) | 0.0043(4) | 0.014(1) | 1.4(2) | 13.41 |
| **180** | 16.780(3) | 0.0022(3) | 0.0044(4) | 0.014(1) | 1.4(2) | 13.31 |
| **190** | 16.781(4) | 0.0023(4) | 0.0045(5) | 0.014(1) | 1.4(2) | 13.22 |
| **200** | 16.783(4) | 0.0024(4) | 0.0047(5) | 0.014(1) | 1.4(2) | 13.18 |
| **210** | 16.783(4) | 0.0025(4) | 0.0048(5) | 0.014(1) | 1.4(2) | 13.07 |
| **220** | 16.785(4) | 0.0026(4) | 0.0049(5) | 0.015(1) | 1.4(2) | 13.04 |
| **230** | 16.785(4) | 0.0027(4) | 0.0050(5) | 0.015(1) | 1.4(2) | 12.96 |
| **240** | 16.786(4) | 0.0028(4) | 0.0052(4) | 0.015(1) | 1.4(2) | 12.90 |
| **250** | 16.788(4) | 0.0029(4) | 0.0053(5) | 0.015(1) | 1.4(2) | 12.94 |
| **264** | 16.791(4) | 0.0031(4) | 0.0055(5) | 0.016(1) | 1.4(2) | 12.76 |
| **270** | 16.791(4) | 0.0031(4) | 0.0055(5) | 0.016(1) | 1.4(2) | 12.73 |
| **280** | 16.793(4) | 0.0032(4) | 0.0056(5) | 0.016(1) | 1.3(2) | 12.69 |
| **290** | 16.794(4) | 0.0033(5) | 0.0057(6) | 0.016(2) | 1.3(2) | 12.65 |
| **300** | 16.795(5) | 0.0035(5) | 0.0059(6) | 0.016(2) | 1.3(2) | 12.52 |
| **310** | 16.796(5) | 0.0036(5) | 0.0060(6) | 0.016(2) | 1.3(2) | 12.55 |
| **320** | 16.800(5) | 0.0037(5) | 0.0062(6) | 0.017(2) | 1.3(2) | 12.66 |
| **330** | 16.802(5) | 0.0038(5) | 0.0063(6) | 0.017(2) | 1.3(2) | 12.60 |
| **340** | 16.807(5) | 0.0039(5) | 0.0065(7) | 0.018(2) | 1.3(2) | 12.68 |
| **350** | 16.808(5) | 0.0040(5) | 0.0066(7) | 0.018(2) | 1.3(2) | 12.62 |
| **360** | 16.808(5) | 0.0041(5) | 0.0067(7) | 0.018(2) | 1.3(2) | 12.58 |
| **370** | 16.811(5) | 0.0042(6) | 0.0069(7) | 0.018(2) | 1.3(2) | 12.60 |
| **380** | 16.812(5) | 0.0043(6) | 0.0070(7) | 0.019(2) | 1.3(2) | 12.55 |
| **390** | 16.813(5) | 0.0044(6) | 0.0071(7) | 0.019(2) | 1.3(2) | 12.55 |
| **400** | 16.814(5) | 0.0045(6) | 0.0072(7) | 0.019(2) | 1.3(2) | 12.49 |
| **498** | 16.831(6) | 0.0060(7) | 0.0087(9) | 0.019(2) | 1.2(2) | 13.78 |
| **548** | 16.839(7) | 0.0065(8) | 0.009(1) | 0.020(2) | 1.2(2) | 13.62 |
| **598** | 16.849(7) | 0.0071(9) | 0.010(1) | 0.022(2) | 1.3(2) | 13.47 |
| **648** | 16.858(8) | 0.008(1) | 0.011(2) | 0.024(2) | 1.3(2) | 13.36 |
| **698** | 16.867(8) | 0.008(1) | 0.012(1) | 0.025(3) | 1.3(2) | 13.29 |
| **748** | 16.880(9) | 0.009(1) | 0.013(1) | 0.027(3) | 1.3(2) | 13.25 |
| **798** | 16.89(1) | 0.009(1) | 0.013(1) | 0.029(3) | 1.3(2) | 13.24 |
| **848** | 16.91(1) | 0.010(1) | 0.014(2) | 0.031(4) | 1.4(2) | 13.24 |
| **923** | 16.92(1) | 0.011(2) | 0.015(2) | 0.033(4) | 1.4(2) | 13.33 |

**Appendix Table 16 – Refinement output for $x_V$ = 0.2 at multiple temperatures.**

| T (K) | CELL (Å) | Uiso_FeA (Å²) | Uiso_FeB (Å²) | Uiso_O (Å²) | $\delta_1$ (Å) | Rw (%) |
|---|---|---|---|---|---|---|
| **90** | 16.780(3) | 0.0016(3) | 0.0040(4) | 0.014(1) | 1.5(2) | 14.63 |
| **100** | 16.780(3) | 0.0017(3) | 0.0041(4) | 0.014(1) | 1.5(2) | 14.52 |
| **110** | 16.781(3) | 0.0017(3) | 0.0041(3) | 0.014(1) | 1.5(2) | 14.44 |
| **120** | 16.778(3) | 0.0017(3) | 0.0040(4) | 0.013(1) | 1.5(2) | 14.03 |
| **130** | 16.777(3) | 0.0017(3) | 0.0040(4) | 0.013(1) | 1.5(2) | 13.82 |
| **140** | 16.777(3) | 0.0018(3) | 0.0040(4) | 0.013(1) | 1.4(2) | 13.60 |
| **150** | 16.780(3) | 0.0019(3) | 0.0041(4) | 0.013(1) | 1.4(2) | 13.59 |
| **160** | 16.779(3) | 0.0020(3) | 0.0041(4) | 0.013(1) | 1.4(2) | 13.39 |
| **170** | 16.780(3) | 0.0021(3) | 0.0042(4) | 0.014(1) | 1.4(2) | 13.36 |
| **180** | 16.780(3) | 0.0022(3) | 0.0043(4) | 0.014(1) | 1.4(2) | 13.26 |
| **190** | 16.781(3) | 0.0022(4) | 0.0045(4) | 0.014(1) | 1.4(2) | 13.17 |
| **200** | 16.783(4) | 0.0023(4) | 0.0046(5) | 0.014(1) | 1.4(2) | 13.14 |
| **210** | 16.783(4) | 0.0024(4) | 0.0047(5) | 0.014(1) | 1.4(2) | 13.02 |
| **220** | 16.785(4) | 0.0025(4) | 0.0048(5) | 0.015(1) | 1.4(2) | 13.00 |
| **230** | 16.785(4) | 0.0026(4) | 0.0049(5) | 0.015(1) | 1.4(2) | 12.92 |
| **240** | 16.786(4) | 0.0027(4) | 0.0051(5) | 0.015(1) | 1.4(2) | 12.86 |
| **250** | 16.788(4) | 0.0028(4) | 0.0052(5) | 0.015(1) | 1.4(2) | 12.90 |
| **264** | 16.791(4) | 0.0031(4) | 0.0054(5) | 0.016(1) | 1.4(2) | 12.72 |
| **270** | 16.791(4) | 0.0031(4) | 0.0054(5) | 0.016(1) | 1.4(2) | 12.69 |
| **280** | 16.793(4) | 0.0032(4) | 0.0055(5) | 0.016(1) | 1.3(2) | 12.65 |
| **290** | 16.794(4) | 0.0033(5) | 0.0056(5) | 0.016(1) | 1.3(2) | 12.61 |
| **300** | 16.795(5) | 0.0035(5) | 0.0058(6) | 0.016(1) | 1.3(2) | 12.49 |
| **310** | 16.796(5) | 0.0036(5) | 0.0059(6) | 0.016(1) | 1.3(2) | 12.51 |
| **320** | 16.800(5) | 0.0037(5) | 0.0061(6) | 0.017(2) | 1.3(2) | 12.62 |
| **330** | 16.802(5) | 0.0038(5) | 0.0062(6) | 0.017(2) | 1.3(2) | 12.57 |
| **340** | 16.807(5) | 0.0039(5) | 0.0064(7) | 0.018(2) | 1.3(2) | 12.64 |
| **350** | 16.808(5) | 0.0040(5) | 0.0065(7) | 0.018(2) | 1.3(2) | 12.58 |
| **360** | 16.808(5) | 0.0041(5) | 0.0067(7) | 0.018(2) | 1.3(2) | 12.55 |
| **370** | 16.811(5) | 0.0042(6) | 0.0068(7) | 0.018(2) | 1.3(2) | 12.56 |
| **380** | 16.812(5) | 0.0043(6) | 0.0069(7) | 0.019(2) | 1.3(2) | 12.52 |
| **390** | 16.813(5) | 0.0044(6) | 0.0070(7) | 0.019(2) | 1.3(2) | 12.52 |
| **400** | 16.814(5) | 0.0045(6) | 0.0071(7) | 0.019(2) | 1.3(2) | 12.46 |
| **498** | 16.831(6) | 0.0059(7) | 0.0086(9) | 0.019(2) | 1.2(2) | 13.75 |
| **548** | 16.839(7) | 0.0064(8) | 0.009(1) | 0.020(2) | 1.2(2) | 13.60 |
| **598** | 16.849(7) | 0.0070(9) | 0.010(1) | 0.022(2) | 1.3(2) | 13.45 |
| **648** | 16.858(8) | 0.008(1) | 0.011(1) | 0.024(2) | 1.3(1) | 13.35 |
| **698** | 16.867(9) | 0.008(1) | 0.011(1) | 0.025(3) | 1.3(2) | 13.28 |
| **748** | 16.880(9) | 0.009(1) | 0.013(1) | 0.027(3) | 1.3(2) | 13.25 |
| **798** | 16.89(1) | 0.009(1) | 0.013(2) | 0.029(3) | 1.3(2) | 13.24 |
| **848** | 16.91(1) | 0.010(1) | 0.014(2) | 0.031(3) | 1.4(2) | 13.24 |
| **923** | 16.92(1) | 0.011(2) | 0.015(2) | 0.033(4) | 1.4(2) | 13.34 |

**Appendix Table 17 – Refinement output for $x_V$ = 0.4 at multiple temperatures.**

| T (K) | CELL (Å) | Uiso_FeA (Å$^2$) | Uiso_FeB (Å$^2$) | Uiso_O (Å$^2$) | $\delta_1$ (Å) | Rw (%) |
|---|---|---|---|---|---|---|
| **90** | 16.780(3) | 0.0016(3) | 0.0037(4) | 0.014(1) | 1.6(2) | 14.34 |
| **100** | 16.780(3) | 0.0016(3) | 0.0038(4) | 0.014(1) | 1.5(2) | 14.24 |
| **110** | 16.781(3) | 0.0017(3) | 0.0039(4) | 0.014(1) | 1.5(2) | 14.17 |
| **120** | 16.778(3) | 0.0016(3) | 0.0038(4) | 0.013(1) | 1.5(2) | 13.81 |
| **130** | 16.777(3) | 0.0016(3) | 0.0037(4) | 0.013(1) | 1.4(2) | 13.65 |
| **140** | 16.777(3) | 0.0017(3) | 0.0037(4) | 0.013(1) | 1.4(2) | 13.44 |
| **150** | 16.780(3) | 0.0018(3) | 0.0038(4) | 0.013(1) | 1.4(2) | 13.44 |
| **160** | 16.779(3) | 0.0019(3) | 0.0039(4) | 0.013(1) | 1.4(2) | 13.26 |
| **170** | 16.780(3) | 0.0020(3) | 0.0040(4) | 0.0131) | 1.4(2) | 13.24 |
| **180** | 16.780(3) | 0.0021(3) | 0.0041(4) | 0.013(1) | 1.4(2) | 13.14 |
| **190** | 16.781(3) | 0.0022(4) | 0.0042(4) | 0.014(1) | 1.4(2) | 13.06 |
| **200** | 16.783(4) | 0.0023(4) | 0.0043(5) | 0.014(1) | 1.4(2) | 13.03 |
| **210** | 16.783(4) | 0.0024(4) | 0.0044(5) | 0.014(1) | 1.4(2) | 12.91 |
| **220** | 16.785(4) | 0.0025(4) | 0.0045(5) | 0.014(1) | 1.4(2) | 12.90 |
| **230** | 16.785(4) | 0.0026(4) | 0.0047(5) | 0.015(1) | 1.4(2) | 12.83 |
| **240** | 16.786(4) | 0.0027(4) | 0.0048(5) | 0.015(1) | 1.4(2) | 12.76 |
| **250** | 16.788(4) | 0.0028(4) | 0.0049(5) | 0.015(1) | 1.3(2) | 12.81 |
| **264** | 16.791(4) | 0.0030(4) | 0.0051(5) | 0.015(1) | 1.4(2) | 12.63 |
| **270** | 16.791(4) | 0.0030(4) | 0.0051(5) | 0.016(1) | 1.4(2) | 12.59 |
| **280** | 16.793(4) | 0.0031(4) | 0.0053(5) | 0.016(1) | 1.3(2) | 12.56 |
| **290** | 16.794(4) | 0.0032(5) | 0.0054(6) | 0.016(1) | 1.3(2) | 12.53 |
| **300** | 16.795(4) | 0.0034(5) | 0.0055(6) | 0.016(1) | 1.3(2) | 12.41 |
| **310** | 16.796(5) | 0.0035(5) | 0.0056(6) | 0.016(1) | 1.3(2) | 12.42 |
| **320** | 16.800(5) | 0.0036(5) | 0.0058(6) | 0.017(1) | 1.3(2) | 12.53 |
| **330** | 16.802(5) | 0.0037(5) | 0.0060(6) | 0.017(2) | 1.3(2) | 12.47 |
| **340** | 16.807(5) | 0.0038(5) | 0.0061(7) | 0.017(2) | 1.3(2) | 12.55 |
| **350** | 16.808(5) | 0.0039(5) | 0.0062(7) | 0.018(2) | 1.3(2) | 12.49 |
| **360** | 16.808(5) | 0.0040(5) | 0.0064(7) | 0.018(2) | 1.3(2) | 12.47 |
| **370** | 16.811(5) | 0.0041(6) | 0.0065(7) | 0.018(2) | 1.3(2) | 12.48 |
| **380** | 16.812(5) | 0.0042(6) | 0.0066(7) | 0.018(2) | 1.3(2) | 12.44 |
| **390** | 16.813(5) | 0.0043(6) | 0.0067(7) | 0.019(2) | 1.3(2) | 12.44 |
| **400** | 16.814(5) | 0.0044(6) | 0.0068(7) | 0.019(2) | 1.3(2) | 12.38 |
| **498** | 16.831(6) | 0.0058(7) | 0.0083(9) | 0.019(2) | 1.2(2) | 13.69 |
| **548** | 16.839(7) | 0.0063(8) | 0.009(2) | 0.020(2) | 1.2(2) | 13.55 |
| **598** | 16.849(7) | 0.0069(9) | 0.010(1) | 0.022(2) | 1.3(2) | 13.41 |
| **648** | 16.859(8) | 0.007(1) | 0.011(1) | 0.023(2) | 1.3(2) | 13.32 |
| **698** | 16.867(8) | 0.008(1) | 0.011(1) | 0.025(3) | 1.3(2) | 13.26 |
| **748** | 16.880(9) | 0.009(1) | 0.012(1) | 0.027(3) | 1.3(2) | 13.23 |
| **798** | 16.89(1) | 0.009(1) | 0.013(2) | 0.029(3) | 1.3(2) | 13.23 |
| **848** | 16.91(1) | 0.010(2) | 0.014(2) | 0.031(4) | 1.4(2) | 13.25 |
| **923** | 16.92(2) | 0.011(2) | 0.015(2) | 0.032(4) | 1.4(2) | 13.35 |

**Appendix Table 18 – Refinement output for $x_V$ = 0.6 at multiple temperatures.**

| T (K) | CELL (Å) | Uiso_FeA (Å²) | Uiso_FeB (Å²) | Uiso_O (Å²) | $\delta_1$ (Å) | Rw (%) |
|---|---|---|---|---|---|---|
| **90** | 16.780(3) | 0.0014(3) | 0.0033(4) | 0.013(1) | 1.6(2) | 13.96 |
| **100** | 16.780(3) | 0.0015(3) | 0.0034(4) | 0.013(1) | 1.5(2) | 13.87 |
| **110** | 16.781(3) | 0.0016(3) | 0.0034(4) | 0.013(1) | 1.5(2) | 13.82 |
| **120** | 16.778(3) | 0.0015(3) | 0.0033(4) | 0.013(1) | 1.5(2) | 13.55 |
| **130** | 16.778(3) | 0.0015(3) | 0.0033(4) | 0.012(1) | 1.4(2) | 13.48 |
| **140** | 16.777(3) | 0.0016(3) | 0.0033(4) | 0.012(1) | 1.4(2) | 13.29 |
| **150** | 16.780(3) | 0.0017(3) | 0.0034(4) | 0.013(1) | 1.4(2) | 13.31 |
| **160** | 16.779(3) | 0.0018(3) | 0.0035(4) | 0.013(1) | 1.4(2) | 13.15 |
| **170** | 16.780(3) | 0.0019(3) | 0.0036(4) | 0.013(1) | 1.4(2) | 13.14 |
| **180** | 16.780(3) | 0.0020(3) | 0.0036(4) | 0.013(1) | 1.4(2) | 13.06 |
| **190** | 16.781(3) | 0.0021(4) | 0.0038(4) | 0.013(1) | 1.4(2) | 13.00 |
| **200** | 16.783(4) | 0.0022(4) | 0.0039(4) | 0.014(1) | 1.4(2) | 12.97 |
| **210** | 16.783(4) | 0.0023(4) | 0.0040(5) | 0.014(1) | 1.4(2) | 12.85 |
| **220** | 16.785(4) | 0.0024(4) | 0.0041(5) | 0.014(1) | 1.3(2) | 12.85 |
| **230** | 16.785(4) | 0.0025(4) | 0.0042(5) | 0.014(1) | 1.3(2) | 12.77 |
| **240** | 16.786(4) | 0.0025(4) | 0.0044(5) | 0.014(1) | 1.3(2) | 12.70 |
| **250** | 16.788(4) | 0.0026(4) | 0.0045(5) | 0.015(1) | 1.3(2) | 12.77 |
| **264** | 16.791(4) | 0.0029(4) | 0.0047(5) | 0.015(1) | 1.3(2) | 12.58 |
| **270** | 16.791(4) | 0.0029(4) | 0.0047(5) | 0.015(1) | 1.3(2) | 12.53 |
| **280** | 16.793(4) | 0.0030(4) | 0.0048(5) | 0.015(1) | 1.3(2) | 12.51 |
| **290** | 16.795(4) | 0.0031(5) | 0.0049(6) | 0.015(1) | 1.3(2) | 12.48 |
| **300** | 16.795(4) | 0.0033(5) | 0.0051(6) | 0.016(1) | 1.3(2) | 12.36 |
| **310** | 16.796(5) | 0.0034(5) | 0.0052(6) | 0.016(1) | 1.3(2) | 12.36 |
| **320** | 16.800(5) | 0.0034(5) | 0.0054(6) | 0.016(2) | 1.3(2) | 12.47 |
| **330** | 16.803(5) | 0.0036(5) | 0.0055(6) | 0.017(2) | 1.3(2) | 12.41 |
| **340** | 16.807(5) | 0.0037(5) | 0.0057(6) | 0.017(2) | 1.3(2) | 12.49 |
| **350** | 16.808(5) | 0.0037(5) | 0.0058(7) | 0.017(2) | 1.3(2) | 12.43 |
| **360** | 16.808(5) | 0.0039(6) | 0.0059(7) | 0.017(2) | 1.3(2) | 12.41 |
| **370** | 16.811(5) | 0.0040(6) | 0.0060(7) | 0.018(2) | 1.3(2) | 12.41 |
| **380** | 16.813(5) | 0.0040(6) | 0.0061(7) | 0.018(2) | 1.3(2) | 12.39 |
| **390** | 16.813(5) | 0.0041(6) | 0.0062(7) | 0.018(2) | 1.3(2) | 12.39 |
| **400** | 16.814(5) | 0.0042(6) | 0.0064(7) | 0.018(2) | 1.2(2) | 12.34 |
| **498** | 16.831(6) | 0.0057(7) | 0.0079(9) | 0.018(2) | 1.2(2) | 13.65 |
| **548** | 16.839(7) | 0.0062(8) | 0.009(1) | 0.020(2) | 1.2(2) | 13.53 |
| **598** | 16.849(7) | 0.0068(9) | 0.009(1) | 0.021(2) | 1.3(2) | 13.40 |
| **648** | 16.859(8) | 0.007(1) | 0.010(1) | 0.023(2) | 1.3(2) | 13.32 |
| **698** | 16.867(8) | 0.008(1) | 0.011(1) | 0.024(3) | 1.3(2) | 13.26 |
| **748** | 16.880(9) | 0.008(1) | 0.012(1) | 0.026(3) | 1.3(2) | 13.25 |
| **798** | 16.89(1) | 0.009(1) | 0.012(1) | 0.028(3) | 1.3(2) | 13.26 |
| **848** | 16.91(1) | 0.010(1) | 0.013(2) | 0.030(4) | 1.4(2) | 13.30 |
| **923** | 16.92(1) | 0.011(2) | 0.014(2) | 0.03(4) | 1.4(2) | 13.41 |

**Appendix Table 19 – Refinement output for $x_V$ = 0.8 at multiple temperatures.**

| T (K) | CELL (Å) | Uiso_FeA (Å$^2$) | Uiso_FeB (Å$^2$) | Uiso_O (Å$^2$) | $\delta_1$ (Å) | Rw (%) |
|---|---|---|---|---|---|---|
| **90** | 16.780(3) | 0.0013(3) | 0.0027(4) | 0.013(1) | 1.5(2) | 13.66 |
| **100** | 16.780(3) | 0.0014(3) | 0.0028(4) | 0.013(1) | 1.5(2) | 13.59 |
| **110** | 16.781(3) | 0.0014(3) | 0.0029(4) | 0.013(1) | 1.5(2) | 13.56 |
| **120** | 16.778(3) | 0.0014(3) | 0.0028(4) | 0.012(1) | 1.4(2) | 13.43 |
| **130** | 16.778(3) | 0.0014(3) | 0.0027(4) | 0.012(1) | 1.4(2) | 13.49 |
| **140** | 16.777(3) | 0.0015(3) | 0.0028(4) | 0.012(1) | 1.3(2) | 13.34 |
| **150** | 16.780(3) | 0.0016(3) | 0.0028(4) | 0.012(1) | 1.3(2) | 13.39 |
| **160** | 16.779(3) | 0.0016(3) | 0.0029(4) | 0.012(1) | 1.3(3) | 13.25 |
| **170** | 16.780(3) | 0.0017(3) | 0.0030(4) | 0.012(1) | 1.3(3) | 13.24 |
| **180** | 16.780(3) | 0.0018(3) | 0.0031(4) | 0.012(1) | 1.3(3) | 13.18 |
| **190** | 16.781(3) | 0.0019(4) | 0.0032(4) | 0.013(1) | 1.3(3) | 13.13 |
| **200** | 16.783(4) | 0.0020(4) | 0.0033(4) | 0.013(1) | 1.3(2) | 13.12 |
| **210** | 16.783(4) | 0.0021(4) | 0.0034(4) | 0.013(1) | 1.3(2) | 12.99 |
| **220** | 16.785(4) | 0.0022(4) | 0.0035(5) | 0.013(1) | 1.3(2) | 12.99 |
| **230** | 16.785(4) | 0.0023(4) | 0.0037(5) | 0.014(1) | 1.3(2) | 12.92 |
| **240** | 16.787(4) | 0.0024(4) | 0.0038(5) | 0.014(1) | 1.3(2) | 12.84 |
| **250** | 16.788(4) | 0.0025(4) | 0.0039(5) | 0.014(1) | 1.3(3) | 12.92 |
| **264** | 16.791(4) | 0.0027(4) | 0.0041(5) | 0.014(1) | 1.3(2) | 12.71 |
| **270** | 16.792(4) | 0.0027(4) | 0.0041(5) | 0.015(1) | 1.3(2) | 12.67 |
| **280** | 16.793(4) | 0.0028(4) | 0.0042(5) | 0.015(1) | 1.3(2) | 12.65 |
| **290** | 16.795(4) | 0.0029(5) | 0.0043(6) | 0.015(1) | 1.3(2) | 12.61 |
| **300** | 16.796(4) | 0.0031(5) | 0.0045(6) | 0.015(1) | 1.3(2) | 12.50 |
| **310** | 16.796(5) | 0.0032(5) | 0.0046(6) | 0.015(1) | 1.3(2) | 12.48 |
| **320** | 16.800(5) | 0.0033(5) | 0.0048(6) | 0.016(2) | 1.3(2) | 12.57 |
| **330** | 16.803(5) | 0.0034(5) | 0.0049(6) | 0.016(2) | 1.3(2) | 12.52 |
| **340** | 16.807(5) | 0.0035(5) | 0.0051(6) | 0.016(2) | 1.3(2) | 12.60 |
| **350** | 16.808(5) | 0.0036(5) | 0.0052(6) | 0.017(2) | 1.3(2) | 12.52 |
| **360** | 16.809(5) | 0.0037(6) | 0.0053(7) | 0.017(2) | 1.2(2) | 12.52 |
| **370** | 16.811(5) | 0.0038(6) | 0.0054(7) | 0.017(2) | 1.2(2) | 12.50 |
| **380** | 16.813(5) | 0.0038(6) | 0.0055(7) | 0.017(2) | 1.2(2) | 12.49 |
| **390** | 16.813(5) | 0.0040(6) | 0.0056(7) | 0.018(2) | 1.2(2) | 12.49 |
| **400** | 16.814(5) | 0.0040(6) | 0.0058(7) | 0.018(2) | 1.2(2) | 12.43 |
| **498** | 16.831(6) | 0.0055(7) | 0.0072(9) | 0.018(2) | 1.2(2) | 13.73 |
| **548** | 16.839(7) | 0.0060(8) | 0.008(1) | 0.019(2) | 1.2(2) | 13.61 |
| **598** | 16.849(7) | 0.006(1) | 0.009(1) | 0.021(2) | 1.2(2) | 13.49 |
| **648** | 16.859(8) | 0.007(1) | 0.009(1) | 0.023(2) | 1.3(2) | 13.41 |
| **698** | 16.868(8) | 0.008(1) | 0.010(1) | 0.024(3) | 1.3(2) | 13.35 |
| **748** | 16.880(9) | 0.008(1) | 0.011(1) | 0.026(3) | 1.3(2) | 13.35 |
| **798** | 16.89(1) | 0.009(1) | 0.012(1) | 0.028(3) | 1.3(2) | 13.38 |
| **848** | 16.91(1) | 0.010(1) | 0.013(2) | 0.030(4) | 1.3(2) | 13.43 |
| **923** | 16.92(1) | 0.010(2) | 0.013(2) | 0.031(4) | 1.4(2) | 13.54 |

**Appendix Table 20 – Refinement output for $x_V$ = 1 at multiple temperatures.**

| T (K) | CELL (Å) | Uiso_FeA (Å²) | Uiso_FeB (Å²) | Uiso_O (Å²) | $\delta_1$ (Å) | Rw (%) |
|---|---|---|---|---|---|---|
| **90** | 16.780(3) | 0.0011(3) | 0.0021(4) | 0.012(1) | 1.4(3) | 13.68 |
| **100** | 16.781(3) | 0.0012(3) | 0.0021(4) | 0.012(1) | 1.4(3) | 13.63 |
| **110** | 16.781(3) | 0.0013(3) | 0.0022(4) | 0.012(1) | 1.4(3) | 13.62 |
| **120** | 16.779(3) | 0.0012(3) | 0.0021(4) | 0.011(1) | 1.3(3) | 13.68 |
| **130** | 16.778(3) | 0.0012(3) | 0.0021(4) | 0.011(1) | 1.2(3) | 13.89 |
| **140** | 16.777(3) | 0.0013(3) | 0.0021(4) | 0.011(1) | 1.2(3) | 13.78 |
| **150** | 16.780(3) | 0.0014(3) | 0.0022(4) | 0.011(1) | 1.2(3) | 13.85 |
| **160** | 16.779(3) | 0.0015(3) | 0.0022(4) | 0.011(1) | 1.1(3) | 13.74 |
| **170** | 16.780(3) | 0.0016(3) | 0.0023(4) | 0.011(1) | 1.1(3) | 13.73 |
| **180** | 16.780(3) | 0.0017(3) | 0.0024(4) | 0.011(1) | 1.1(3) | 13.69 |
| **190** | 16.782(4) | 0.0017(4) | 0.0025(4) | 0.012(1) | 1.1(3) | 13.66 |
| **200** | 16.784(4) | 0.0018(4) | 0.0026(4) | 0.012(1) | 1.2(3) | 13.64 |
| **210** | 16.784(4) | 0.0019(4) | 0.0028(4) | 0.012(1) | 1.2(3) | 13.50 |
| **220** | 16.786(4) | 0.0020(4) | 0.0029(4) | 0.012(1) | 1.2(3) | 13.52 |
| **230** | 16.786(4) | 0.0021(4) | 0.0030(5) | 0.013(1) | 1.1(3) | 13.43 |
| **240** | 16.787(4) | 0.0022(4) | 0.0031(5) | 0.013(1) | 1.2(3) | 13.34 |
| **250** | 16.789(4) | 0.0023(4) | 0.0032(5) | 0.013(1) | 1.1(3) | 13.43 |
| **264** | 16.791(4) | 0.0025(4) | 0.0034(5) | 0.014(1) | 1.2(3) | 13.21 |
| **270** | 16.792(4) | 0.0025(4) | 0.0034(5) | 0.014(1) | 1.2(3) | 13.16 |
| **280** | 16.793(4) | 0.0026(4) | 0.0036(5) | 0.014(1) | 1.2(3) | 13.13 |
| **290** | 16.795(4) | 0.0027(5) | 0.0037(5) | 0.014(1) | 1.2(3) | 13.08 |
| **300** | 16.796(4) | 0.0029(5) | 0.0038(5) | 0.014(1) | 1.2(3) | 12.98 |
| **310** | 16.796(5) | 0.0030(5) | 0.0039(6) | 0.014(1) | 1.2(3) | 12.93 |
| **320** | 16.800(5) | 0.0030(5) | 0.0041(6) | 0.015(1) | 1.2(3) | 13.00 |
| **330** | 16.803(5) | 0.0032(5) | 0.0042(6) | 0.015(2) | 1.2(3) | 12.95 |
| **340** | 16.807(5) | 0.0032(5) | 0.0044(6) | 0.015(2) | 1.2(3) | 13.01 |
| **350** | 16.808(5) | 0.0033(5) | 0.0045(6) | 0.016(2) | 1.2(3) | 12.93 |
| **360** | 16.809(5) | 0.0034(6) | 0.0046(7) | 0.016(2) | 1.2(3) | 12.92 |
| **370** | 16.811(5) | 0.0035(6) | 0.0047(7) | 0.016(2) | 1.2(3) | 12.88 |
| **380** | 16.813(5) | 0.0036(6) | 0.0048(7) | 0.017(2) | 1.2(3) | 12.89 |
| **390** | 16.813(5) | 0.0037(6) | 0.0049(7) | 0.017(2) | 1.1(3) | 12.88 |
| **400** | 16.814(5) | 0.0038(6) | 0.0050(7) | 0.017(2) | 1.1(3) | 12.82 |
| **498** | 16.831(6) | 0.0052(7) | 0.0065(9) | 0.017(2) | 1.2(2) | 14.05 |
| **548** | 16.839(7) | 0.0057(8) | 0.007(1) | 0.018(2) | 1.2(2) | 13.91 |
| **598** | 16.849(7) | 0.0063(9) | 0.008(1) | 0.020(2) | 1.2(2) | 13.78 |
| **648** | 16.859(8) | 0.007(1) | 0.009(1) | 0.022(2) | 1.2(2) | 13.69 |
| **698** | 16.868(8) | 0.007(1) | 0.009(1) | 0.023(3) | 1.3(2) | 13.63 |
| **748** | 16.880(9) | 0.008(1) | 0.010(1) | 0.025(3) | 1.3(2) | 13.63 |
| **798** | 16.89(1) | 0.009(1) | 0.011(1) | 0.027(3) | 1.3(2) | 13.65 |
| **848** | 16.91(1) | 0.009(1) | 0.01(2) | 0.029(4) | 1.3(2) | 13.71 |
| **923** | 16.92(1) | 0.010(1) | 0.013(1) | 0.031(4) | 1.4(2) | 13.82 |

Appendix Table 21 – Refinement output for $x_V$ = 1.2 at multiple temperatures.

| T (K) | CELL (Å) | Uiso_FeA (Å$^2$) | Uiso_FeB (Å$^2$) | Uiso_O (Å$^2$) | $\delta_1$ (Å) | Rw (%) |
|---|---|---|---|---|---|---|
| **90** | 16.781(3) | 0.0009(3) | 0.0013(4) | 0.010(1) | 1.1(4) | 14.21 |
| **100** | 16.781(3) | 0.0010(3) | 0.0014(4) | 0.010(1) | 1.1(4) | 14.19 |
| **110** | 16.782(3) | 0.0011(3) | 0.0015(4) | 0.011(1) | 1.1(4) | 14.20 |
| **120** | 16.779(3) | 0.0010(3) | 0.0014(4) | 0.010(1) | 0.9(4) | 14.45 |
| **130** | 16.778(3) | 0.0010(3) | 0.0013(4) | 0.010(1) | 0.8(5) | 14.82 |
| **140** | 16.778(3) | 0.0011(3) | 0.0014(4) | 0.010(1) | 0.8(5) | 14.75 |
| **150** | 16.781(3) | 0.0012(3) | 0.0014(4) | 0.010(1) | 0.8(5) | 14.83 |
| **160** | 16.780(3) | 0.0012(3) | 0.0015(4) | 0.010(1) | 0.8(4) | 14.75 |
| **170** | 16.781(3) | 0.0013(3) | 0.0016(4) | 0.010(1) | 0.8(4) | 14.73 |
| **180** | 16.781(3) | 0.0014(3) | 0.0017(4) | 0.010(1) | 0.8(4) | 14.70 |
| **190** | 16.782(4) | 0.0015(4) | 0.0018(4) | 0.010(1) | 0.8(4) | 14.68 |
| **200** | 16.784(4) | 0.0016(4) | 0.0019(4) | 0.011(1) | 0.8(4) | 14.65 |
| **210** | 16.784(4) | 0.0017(4) | 0.0020(4) | 0.011(1) | 0.9(4) | 14.51 |
| **220** | 16.786(4) | 0.0017(4) | 0.0021(4) | 0.011(1) | 0.9(4) | 14.52 |
| **230** | 16.786(4) | 0.0018(4) | 0.0022(4) | 0.011(1) | 0.9(4) | 14.42 |
| **240** | 16.787(4) | 0.0019(4) | 0.0024(5) | 0.012(1) | 0.9(4) | 14.32 |
| **250** | 16.789(4) | 0.0020(4) | 0.0025(5) | 0.012(1) | 0.9(4) | 14.40 |
| **264** | 16.792(4) | 0.0022(4) | 0.0027(5) | 0.012(1) | 1.0(3) | 14.17 |
| **270** | 16.792(4) | 0.0022(4) | 0.0027(5) | 0.012(1) | 1.0(3) | 14.12 |
| **280** | 16.794(4) | 0.0023(4) | 0.0028(5) | 0.013(1) | 1.0(3) | 14.08 |
| **290** | 16.795(4) | 0.0024(5) | 0.0029(5) | 0.013(1) | 1.0(3) | 14.01 |
| **300** | 16.796(5) | 0.0026(5) | 0.0031(5) | 0.013(1) | 1.0(3) | 13.91 |
| **310** | 16.796(5) | 0.0027(5) | 0.0032(6) | 0.013(1) | 1.0(3) | 13.84 |
| **320** | 16.800(5) | 0.0027(5) | 0.0033(6) | 0.014(1) | 1.0(3) | 13.87 |
| **330** | 16.803(5) | 0.0028(5) | 0.0035(6) | 0.014(1) | 1.0(3) | 13.81 |
| **340** | 16.807(5) | 0.0029(5) | 0.0036(6) | 0.014(1) | 1.0(3) | 13.86 |
| **350** | 16.808(5) | 0.0030(5) | 0.0037(6) | 0.015(2) | 1.0(3) | 13.76 |
| **360** | 16.809(5) | 0.0031(6) | 0.0038(6) | 0.015(2) | 1.0(3) | 13.76 |
| **370** | 16.811(5) | 0.0032(6) | 0.0039(6) | 0.015(2) | 1.0(3) | 13.68 |
| **380** | 16.813(5) | 0.0033(6) | 0.0041(7) | 0.015(2) | 1.0(3) | 13.70 |
| **390** | 16.813(5) | 0.0034(6) | 0.0042(7) | 0.016(2) | 1.0(3) | 13.68 |
| **400** | 16.814(5) | 0.0035(6) | 0.0043(7) | 0.016(2) | 1.0(3) | 13.61 |
| **498** | 16.831(6) | 0.0049(8) | 0.0057(9) | 0.016(2) | 1.1(3) | 14.72 |
| **548** | 16.839(7) | 0.0054(8) | 0.0064(9) | 0.017(2) | 1.1(3) | 14.55 |
| **598** | 16.849(7) | 0.0060(9) | 0.007(2) | 0.019(2) | 1.2(2) | 14.38 |
| **648** | 16.859(8) | 0.007(1) | 0.008(1) | 0.021(2) | 1.2(2) | 14.27 |
| **698** | 16.867(8) | 0.007(1) | 0.008(1) | 0.022(3) | 1.2(2) | 14.17 |
| **748** | 16.88(1) | 0.008(1) | 0.009(1) | 0.024(3) | 1.3(2) | 14.15 |
| **798** | 16.89(1) | 0.008(1) | 0.010(1) | 0.026(3) | 1.3(2) | 14.15 |
| **848** | 16.91(1) | 0.009(1) | 0.011(2) | 0.028(4) | 1.3(2) | 14.21 |
| **923** | 16.92(1) | 0.010(2) | 0.012(2) | 0.030(4) | 1.3(2) | 14.31 |

**Appendix Table 22 – Weighted average of refinement output for min-Rw $x_V$ at multiple temperatures.**

| T (K) | CELL (Å) | Uiso_FeA (Å$^2$) | Uiso_FeB (Å$^2$) | Uiso_O (Å$^2$) | MIN-Rw $x_V$ |
|---|---|---|---|---|---|
| **90** | 16.780(3) | 0.0012(3) | 0.0023(4) | 0.012(1) | 0.92 |
| **100** | 16.781(3) | 0.0013(3) | 0.0024(4) | 0.012(1) | 0.91 |
| **110** | 16.781(3) | 0.0014(3) | 0.0026(4) | 0.012(1) | 0.89 |
| **120** | 16.778(3) | 0.0014(3) | 0.0028(4) | 0.012(1) | 0.80 |
| **130** | 16.778(3) | 0.0015(3) | 0.0030(4) | 0.012(1) | 0.70 |
| **140** | 16.777(3) | 0.0016(3) | 0.0031(4) | 0.012(1) | 0.66 |
| **150** | 16.780(3) | 0.0017(3) | 0.0033(4) | 0.013(1) | 0.64 |
| **160** | 16.779(3) | 0.0018(3) | 0.0034(4) | 0.013(1) | 0.61 |
| **170** | 16.780(3) | 0.0019(3) | 0.0036(4) | 0.013(1) | 0.60 |
| **180** | 16.780(3) | 0.0020(3) | 0.0037(4) | 0.013(1) | 0.59 |
| **190** | 16.781(3) | 0.0021(4) | 0.0038(4) | 0.013(1) | 0.57 |
| **200** | 16.783(4) | 0.0022(4) | 0.0040(4) | 0.014(1) | 0.56 |
| **210** | 16.783(4) | 0.0023(4) | 0.0041(5) | 0.014(1) | 0.56 |
| **220** | 16.785(4) | 0.0024(4) | 0.0042(5) | 0.014(1) | 0.55 |
| **230** | 16.785(4) | 0.0025(4) | 0.0043(5) | 0.014(1) | 0.55 |
| **240** | 16.786(4) | 0.0026(4) | 0.0045(5) | 0.015(1) | 0.56 |
| **250** | 16.788(4) | 0.0027(4) | 0.0046(5) | 0.015(1) | 0.54 |
| **264** | 16.791(4) | 0.0029(4) | 0.0048(5) | 0.015(1) | 0.55 |
| **270** | 16.791(4) | 0.0029(4) | 0.0048(5) | 0.015(1) | 0.56 |
| **280** | 16.793(4) | 0.0030(4) | 0.0049(5) | 0.015(1) | 0.55 |
| **290** | 16.794(4) | 0.0031(5) | 0.0050(5) | 0.016(1) | 0.55 |
| **300** | 16.795(4) | 0.0033(5) | 0.0052(6) | 0.016(1) | 0.54 |
| **310** | 16.796(4) | 0.0034(5) | 0.0053(6) | 0.016(1) | 0.57 |
| **320** | 16.800(5) | 0.0035(5) | 0.0054(6) | 0.016(2) | 0.58 |
| **330** | 16.802(5) | 0.0036(5) | 0.0056(6) | 0.017(2) | 0.58 |
| **340** | 16.807(5) | 0.0037(5) | 0.0057(6) | 0.017(2) | 0.58 |
| **350** | 16.808(5) | 0.0038(5) | 0.0058(7) | 0.017(2) | 0.59 |
| **360** | 16.808(5) | 0.0039(6) | 0.0060(7) | 0.018(2) | 0.58 |
| **370** | 16.811(5) | 0.0040(6) | 0.0060(7) | 0.018(2) | 0.60 |
| **380** | 16.812(5) | 0.0041(6) | 0.0062(7) | 0.018(2) | 0.57 |
| **390** | 16.813(5) | 0.0042(6) | 0.0063(7) | 0.018(2) | 0.57 |
| **400** | 16.814(5) | 0.0043(6) | 0.0064(7) | 0.019(2) | 0.57 |
| **498** | 16.831(6) | 0.0057(7) | 0.0079(9) | 0.018(2) | 0.58 |
| **548** | 16.839(7) | 0.0062(8) | 0.009(1) | 0.020(2) | 0.56 |
| **598** | 16.849(7) | 0.0068(9) | 0.009(1) | 0.022(2) | 0.53 |
| **648** | 16.859(8) | 0.007(1) | 0.010(1) | 0.023(2) | 0.51 |
| **698** | 16.867(8) | 0.008(1) | 0.011(1) | 0.025(3) | 0.49 |
| **748** | 16.880(9) | 0.009(1) | 0.012(1) | 0.027(3) | 0.42 |
| **798** | 16.89(1) | 0.009(1) | 0.013(2) | 0.029(3) | 0.35 |
| **848** | 16.91(1) | 0.010(1) | 0.014(2) | 0.030(4) | 0 |
| **923** | 16.92(1) | 0.011(2) | 0.015(2) | 0.030(4) | 0 |

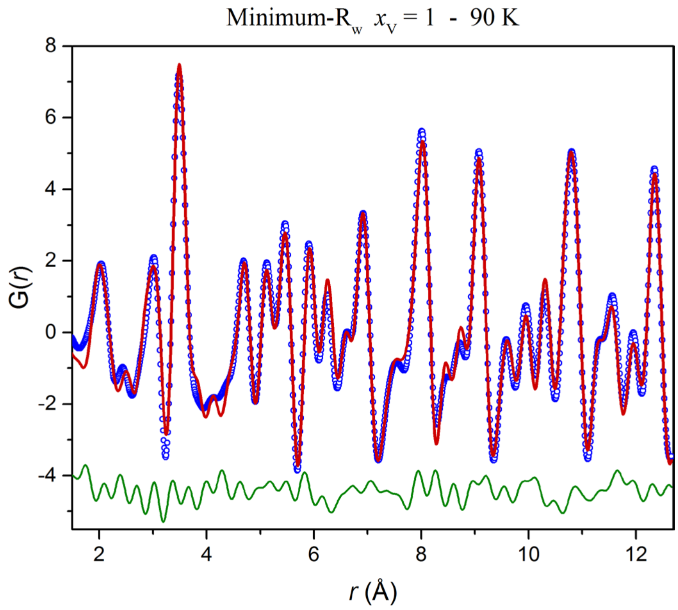


Appendix Figure 1 – Fits to the PDF at 90 K with the closes minimum-Rw $x_V$ = 1.

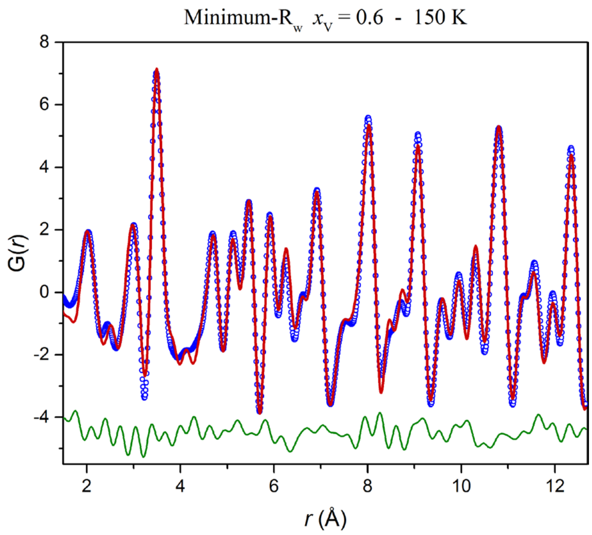


Appendix Figure 2 – Fits to the PDF at 150 K with the closes minimum-Rw $x_V$ = 0.6.

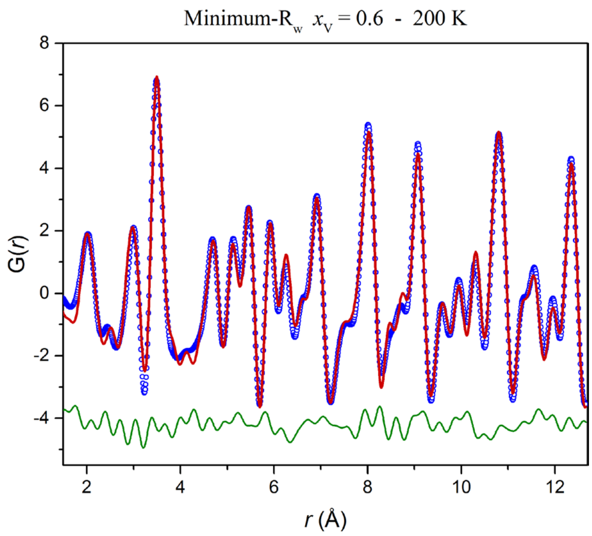


Appendix Figure 3 – Fits to the PDF at 200 K with the closes minimum-Rw $x_V$ = 0.6.

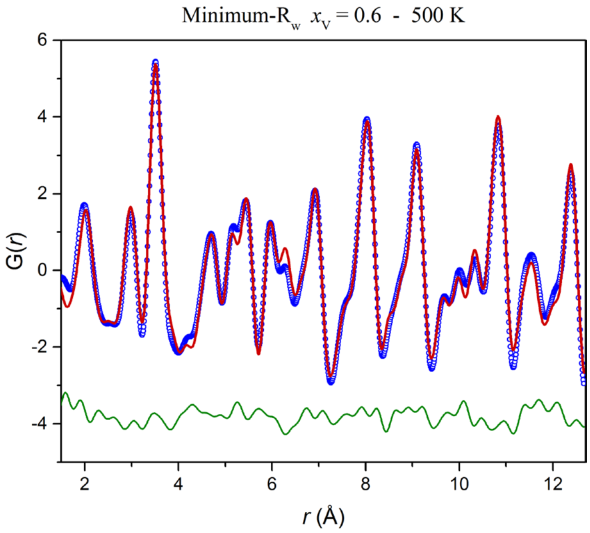


Appendix Figure 4 – Fits to the PDF at 500 K with the closes minimum-Rw $x_V$ = 0.6.

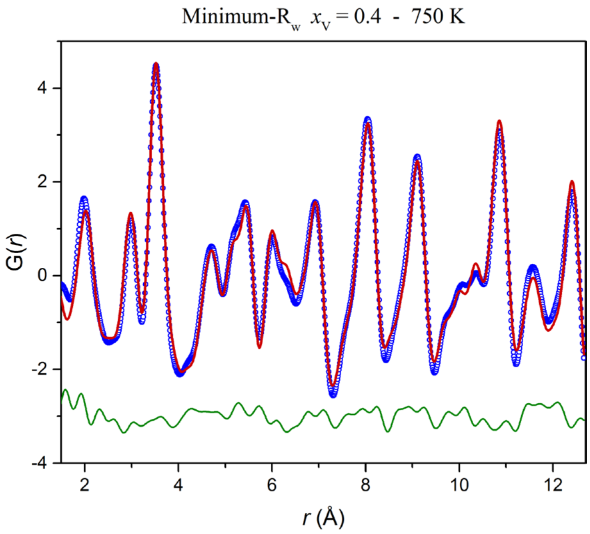


Appendix Figure 5 – Fits to the PDF at 750 K with the closes minimum-Rw $x_V$ = 0.4.

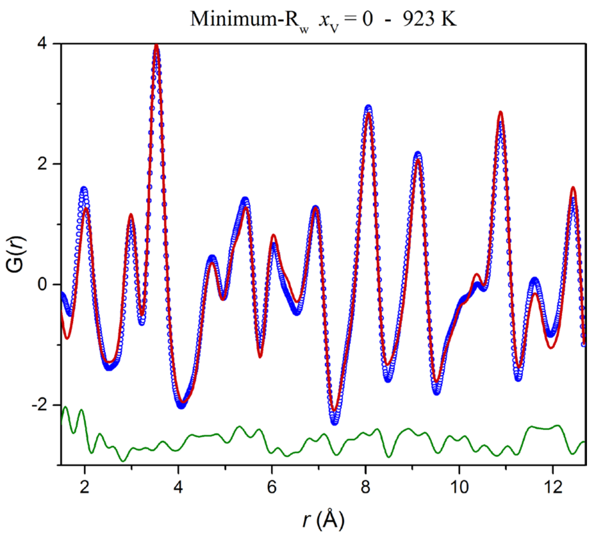


Appendix Figure 6 – Fits to the PDF at 923 K with the closes minimum-Rw $x_V$ = 0.

# B. Appendix to Chapter 4

## B1. $Fe_2GeO_4$

**Appendix Table 1 – Irreducible representations and basis vectors (BV) for $Fe_2GeO_4$ with propagation vectors $k_1 = (\frac{2}{3}+\delta_1\ -\frac{2}{3}-\delta_1\ 0)$. The two magnetically independent atoms are Fe1 at (½,½,½) and Fe2 at (¾,0,¼). Symmetry-related positions are generated by the operators 1: (x,y,z), 2: (x+ ¼ ,y+ ¾ ,-z+ ½ ) for Fe1 and 1: (x,y,z), 2: (-y+1,-x+1,-z) for Fe2. The sublattice of Fe2 is not refined with this propagation vector, thus referred to as $k_{1\_1}$. The irreducible representations for atom Fe1 are in Table 13, this table lists only the Fe2 Γ.**

| Propagation vector $\mathbf{k_{1\_1}}$ | | | | | |
|---|---|---|---|---|---|
| Irreps | $\Gamma_1$ | | $\Gamma_2$ | | |
| BV | $\psi_1$ | | $\psi_1$ | | $\psi_2$ |
| Atom | $m_x$ | $m_x$ | $m_x$ | $m_y$ | $m_z$ |
| Fe2_1 | 1 | 1 | 1 | -1 | 1 |
| Fe2_2 | -1 | -1 | 0 | 0 | 0 |
| Irreps | $\Gamma_3$ | | $\Gamma_4$ | | |
| BV | $\psi_1$ | | $\psi_1$ | | $\psi_2$ |
| Atom | $m_x$ | $m_x$ | $m_x$ | $m_y$ | $m_z$ |
| Fe2_1 | 1 | 1 | 1 | -1 | 1 |
| Fe2_2 | 1 | 1 | 0 | 0 | 0 |

**Appendix Table 24 – Irreducible representations and basis vectors (BV) for $Fe_2GeO_4$ with propagation vectors $k_1 = (\frac{2}{3}+\delta_1\ \frac{2}{3}+\delta_1\ 0)$. The two magnetically independent atoms are Fe1 at (½,½,½) and Fe2 at (¾,0,¼). Symmetry-related positions are generated by the operators 1: (x,y,z), 2: (y+ ¾ ,x+ ¼ ,-z+ ½ ) for Fe1 and 1: (x,y,z), 2: (x+ ¼ ,y+ ¾ ,-z+ ½ ) for Fe2.The sublattice of Fe1 is not refined with this propagation vector, thus referred to as $k_{1\_2}$. The irreducible representations for atom Fe1 are in Table 14, this table lists only the Fe1 Γ.**

| Propagation vector $\mathbf{k_{1\_2}}$ | | | | | | | |
|---|---|---|---|---|---|---|---|
| Irreps | $\Gamma_1$ | | $\Gamma_2$ | | | | |
| BV | $\psi_1$ / $\psi_2$ | | $\psi_1$ | | $\psi_2$ | | $\psi_2$ |
| Atom | $m_x$ | $m_x$ | $m_x$ | $m_y$ | $m_x$ | $m_y$ | $m_z$ |
| Fe1_1 | 1 | 1 | 1 | -1 | -1 | 1 | 1 |
| Fe1_2 | $\frac{1}{2}-\frac{i\sqrt{3}}{2}$ | $\frac{1}{2}-\frac{i\sqrt{3}}{2}$ | $\frac{1}{2}-\frac{i\sqrt{3}}{2}$ | $-\frac{1}{2}+\frac{i\sqrt{3}}{2}$ | $-\frac{1}{2}+\frac{i\sqrt{3}}{2}$ | $\frac{1}{2}-\frac{i\sqrt{3}}{2}$ | $-\frac{1}{2}+\frac{i\sqrt{3}}{2}$ |
| Irreps | $\Gamma_3$ | | $\Gamma_4$ | | | | |
| BV | $\psi_1$ / $\psi_2$ | | $\psi_1$ | | $\psi_1$ | | $\psi_2$ |
| Atom | $m_x$ | $m_x$ | $m_x$ | $m_y$ | $m_x$ | $m_y$ | $m_z$ |
| Fe1_1 | 1 | 1 | 1 | -1 | -1 | 1 | 1 |
| Fe1_2 | $-\frac{1}{2}+\frac{i\sqrt{3}}{2}$ | $-\frac{1}{2}+\frac{i\sqrt{3}}{2}$ | $-\frac{1}{2}+\frac{i\sqrt{3}}{2}$ | $\frac{1}{2}-\frac{i\sqrt{3}}{2}$ | $\frac{1}{2}-\frac{i\sqrt{3}}{2}$ | $-\frac{1}{2}+\frac{i\sqrt{3}}{2}$ | $\frac{1}{2}-\frac{i\sqrt{3}}{2}$ |

**Appendix Table 25 – Refinement results at multiple temperatures. D20, 90° take-off. λ = 2.41 Å.**

| T (K) | $R_{WP}$ (%) | $R_{mag}$ (%) | a (Å) | $B_{Fe}$ (Å$^2$) | $B_{Ge}$ (Å$^2$) | $B_O$ (Å$^2$) | C1_ki1 (μB) | C3_ki2 (μB) | δ1 |
|---|---|---|---|---|---|---|---|---|---|
| 1.8 | 14.1 | 5.73 | 8.38582(8) | 1.93(9) | 1.73(9) | 2.98(7) | 2.77(3) | 0.94(9) | 0.0254(8) |
| 2.5 | 14.2 | 5.78 | 8.38589(8) | 1.96(9) | 1.74(9) | 3.01(7) | 2.76(4) | 0.94(9) | 0.0253(8) |
| 10 | 13.9 | - | 8.38588(8) | 2.10(9) | 1.78(9) | 3.60(7) | - | - | - |
| 12 | 13.9 | - | 8.38590(8) | 1.83(9) | 2.11(9) | 3.61(7) | - | - | - |
| 15 | 13.9 | - | 8.38585(8) | 1.83(9) | 2.11(9) | 3.59(7) | - | - | - |
| 25 | 13.9 | - | 8.38592(9) | 1.83(8) | 2.11(8) | 3.61(7) | - | - | - |
| 50 | 13.7 | - | 8.38609(8) | 1.84(8) | 2.12(8) | 3.61(7) | - | - | - |

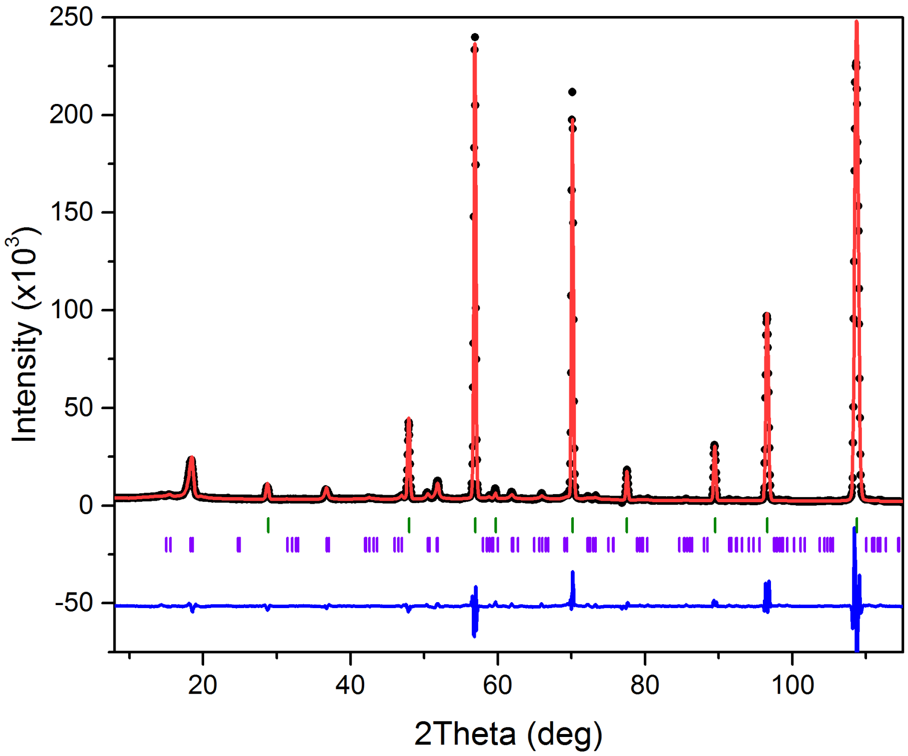


**Appendix Figure 7 – Data refinement for $Fe_2GeO_4$ in D20, 90 degree take-off. Temperature = 1.8 K. In this figure and all the following figures, Bragg reflections are in green, magnetic reflections are in purple (when present).**

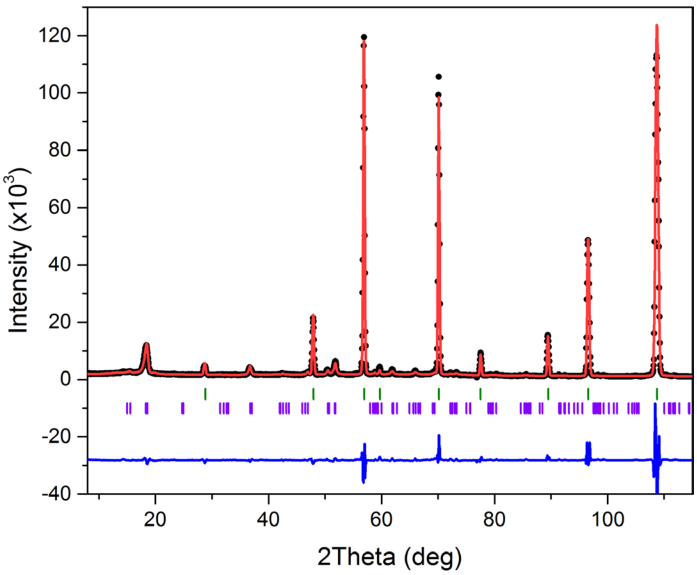


Appendix Figure 8 – Data refinement for $Fe_2GeO_4$ in D20, 90° take-off. T = 2.5 K.

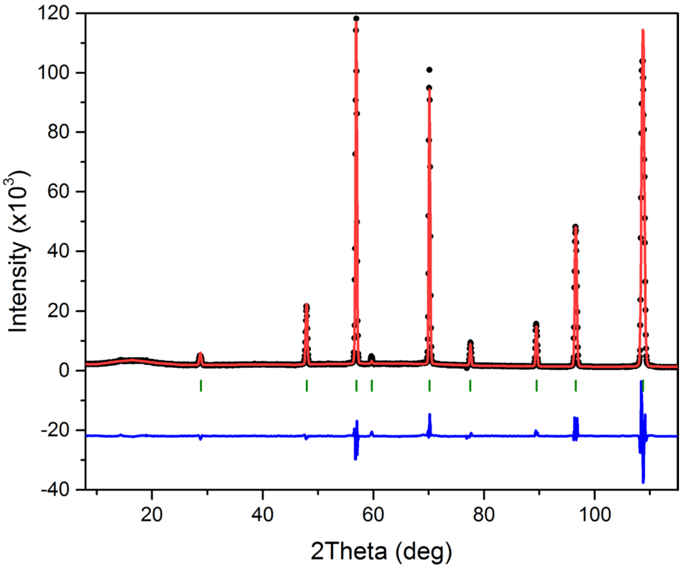


Appendix Figure 9 – Data refinement for $Fe_2GeO_4$ in D20, 90° take-off. T = 10 K.

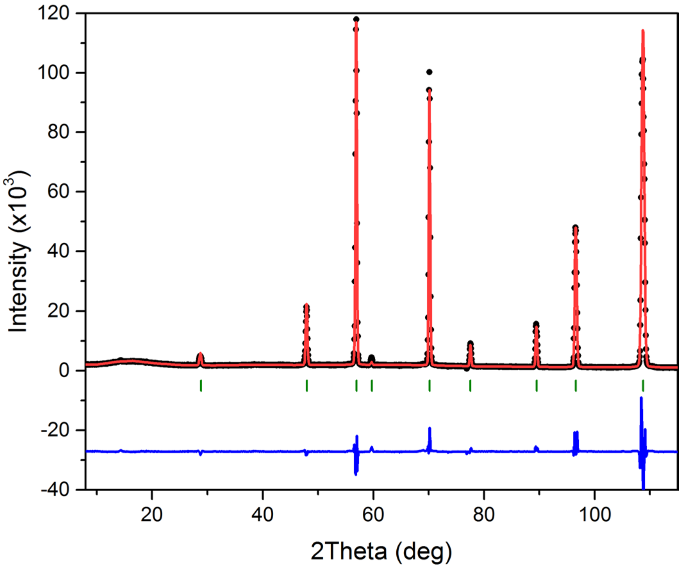


Appendix Figure 10 – Data refinement for $Fe_2GeO_4$ in D20, 90° take-off. T = 12 K.

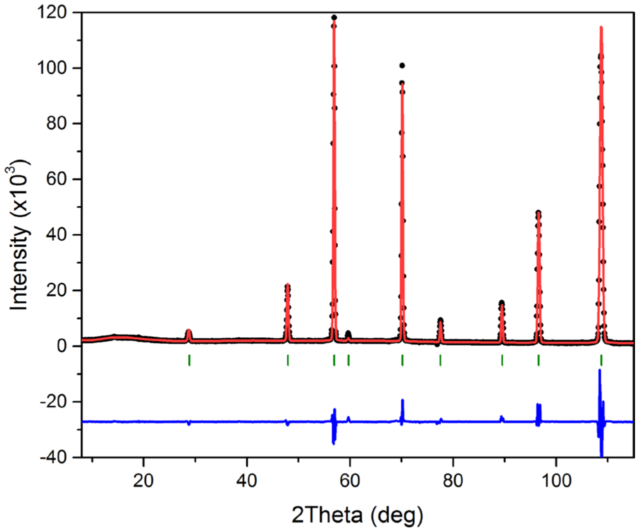


Appendix Figure 11 – Data refinement for $Fe_2GeO_4$ in D20, 90° take-off. T = 15 K.

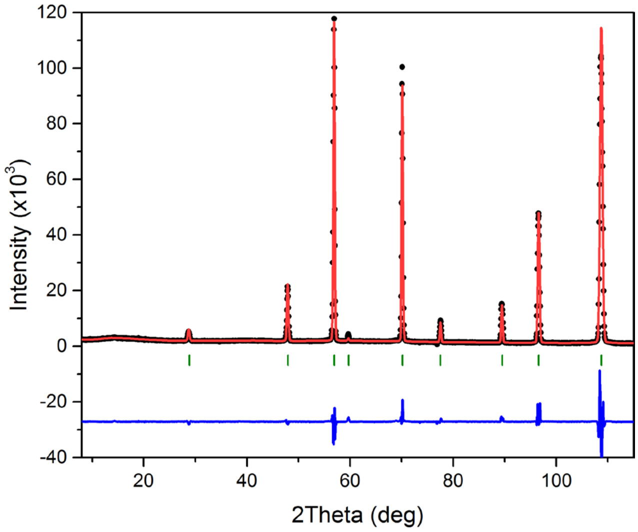


Appendix Figure 12 – Data refinement for $Fe_2GeO_4$ in D20, 90° take-off. T = 25 K.

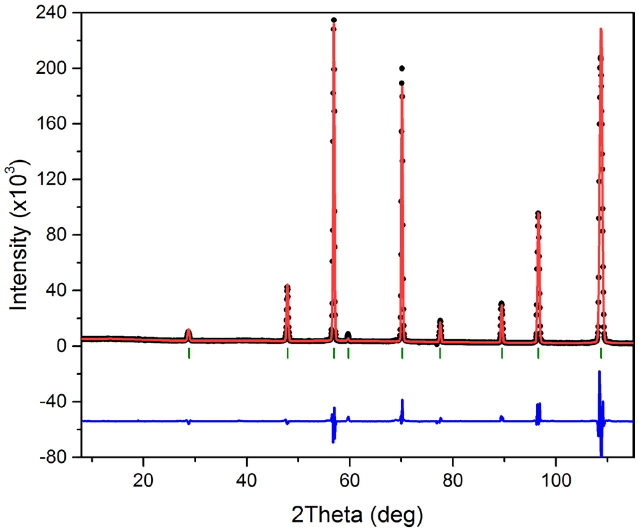


Appendix Figure 13 – Data refinement for $Fe_2GeO_4$ in D20, 90° take-off. T = 50 K.

**Appendix Table 26 – Refinement results at multiple temperatures. D20, 42° take-off. λ = 2.41 Å.**

| T (K) | $R_{WP}$ (%) | $R_{mag}$ (%) | a (Å) | $B_{Fe}$ (Å²) | $B_{Ge}$ (Å²) | $B_O$ (Å²) | C1_ki1 (μB) | C3_ki2 (μB) | δ1 |
|---|---|---|---|---|---|---|---|---|---|
| 1.8 | 14.2 | 4.41 | 8.3867(8) | 0.4(9) | 0.5(8) | 0.6(3) | 2.81(4) | 0.84(8) | 0.0244(9) |
| 2.5 | 14.2 | 4.14 | 8.3866(8) | 0.4(2) | 0.5(8) | 0.7(2) | 2.79(4) | 0.84(8) | 0.0244(9) |
| 12 | 14.8 | - | 8.3866(8) | 1.2(3) | 0.9(9) | 1.4(3) | - | - | - |
| 15 | 14.8 | - | 8.3865(8) | 1.2(3) | 0.9(9) | 1.4(3) | - | - | - |
| 25 | 14.4 | - | 8.3865(8) | 1.1(3) | 1.0(9) | 1.3(3) | - | - | - |

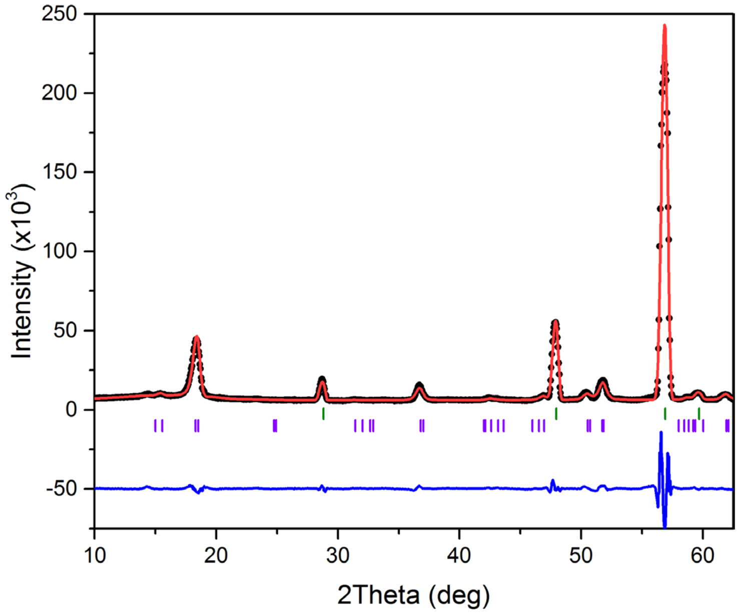


Appendix Figure 14 – Data refinement for $Fe_2GeO_4$ in D20, 42° take-off. T = 1.8 K.

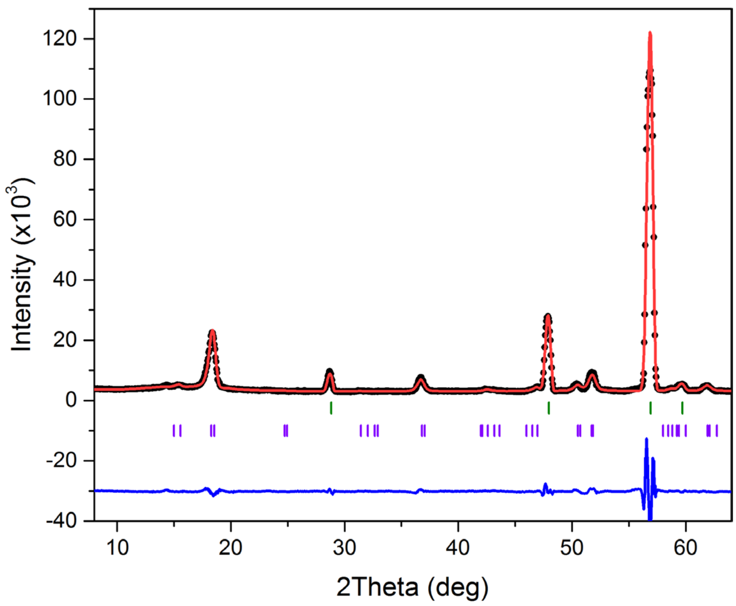


Appendix Figure 15 – Data refinement for $Fe_2GeO_4$ in D20, 42° take-off. T = 2.5 K.

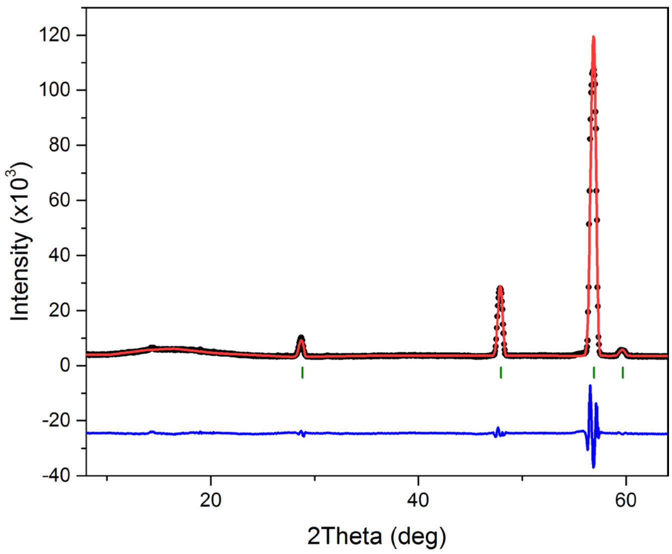


Appendix Figure 16 – Data refinement for $Fe_2GeO_4$ in D20, 42° take-off. T = 12 K.

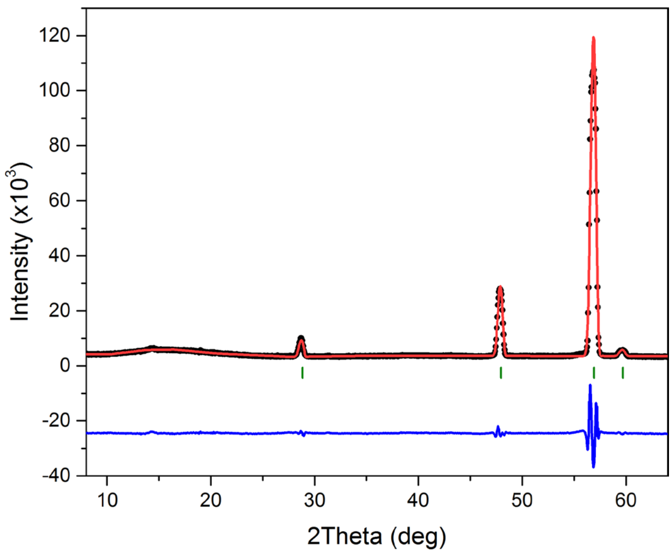


Appendix Figure 17 – Data refinement for $Fe_2GeO_4$ in D20, 42° take-off. T = 15 K.

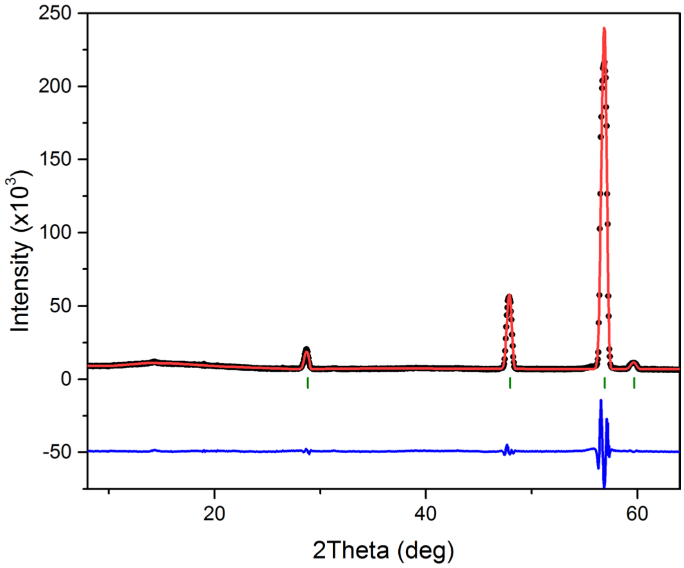


Appendix Figure 18 – Data refinement for $Fe_2GeO_4$ in D20, 42° take-off. T = 25 K.

**Appendix Table 27 – Refinement results at multiple temperatures. D2B. λ = 1.59475 Å.**

| T (K) | $R_{WP}$ (%) | $R_{mag}$ (%) | a (Å) | $B_{Fe}$ (Å$^2$) | $B_{Ge}$ (Å$^2$) | $B_O$ (Å$^2$) | C1_ki1 (μB) | C3_ki2 (μB) | δ1 |
|---|---|---|---|---|---|---|---|---|---|
| 2 | 10.5 | 13.3 | 8.40987(5) | 0.10(2) | 0.09(1) | 0.32(2) | 2.85(6) | 1.1(8) | 0.0237(7) |
| 2 COL | 11.6 | 11.8 | 8.40984(5) | 0.14(2) | 0.13(2) | 0.36(2) | 2.64(6) | 0.98(4) | 0.0392(7) |
| 6 | 10.5 | 14.7 | 8.40989(5) | 0.11(2) | 0.10(1) | 0.33(2) | 2.94(8) | 0.84(5) | 0.0245(7) |
| 10 | 12.1 | - | 8.40988(6) | 0.08(2) | 0.06(2) | 0.38(2) | - | - | - |
| 100 | 10.9 | - | 8.41071(5) | 0.12(2) | 0.10(2) | 0.41(2) | - | - | - |
| 200 | 10.7 | - | 8.41376(5) | 0.2(2) | 0.19(2) | 0.52(1) | - | - | - |
| 300 | 11.5 | - | 8.41819(6) | 0.31(2) | 0.32(2) | 0.65(2) | - | - | - |

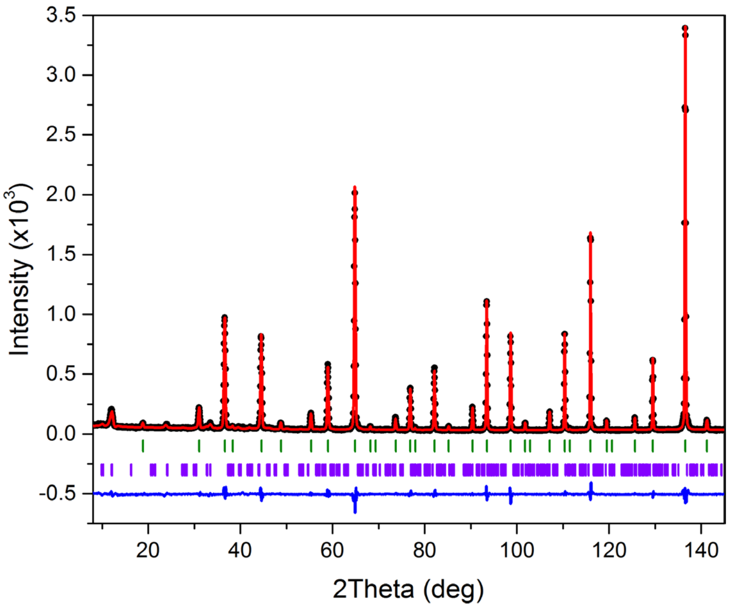


Appendix Figure 19 – Data refinement for $Fe_2GeO_4$ in D2B, T = 2 K.

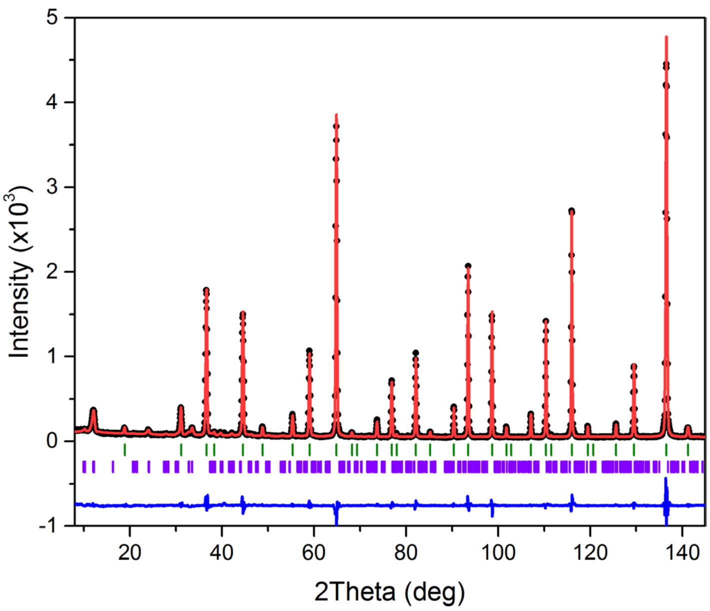


Appendix Figure 20 – Data refinement for $Fe_2GeO_4$ in D2B, with 10’ collimator T = 2 K.

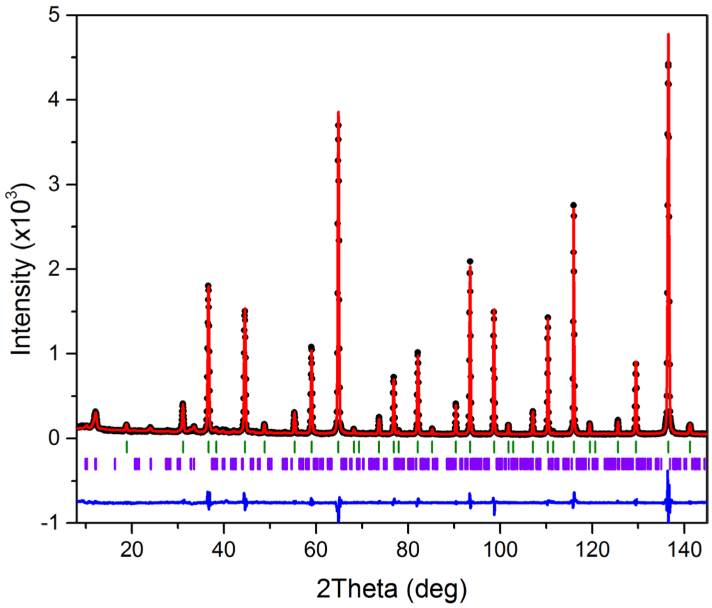


Appendix Figure 21 – Data refinement for $Fe_2GeO_4$ in D2B- T = 6 K.

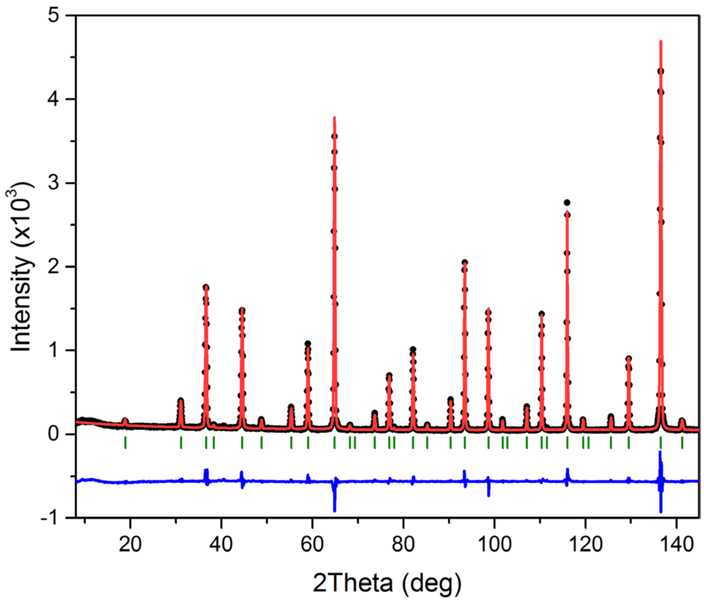


Appendix Figure 22 – Data refinement for $Fe_2GeO_4$ in D2B- T = 10 K.

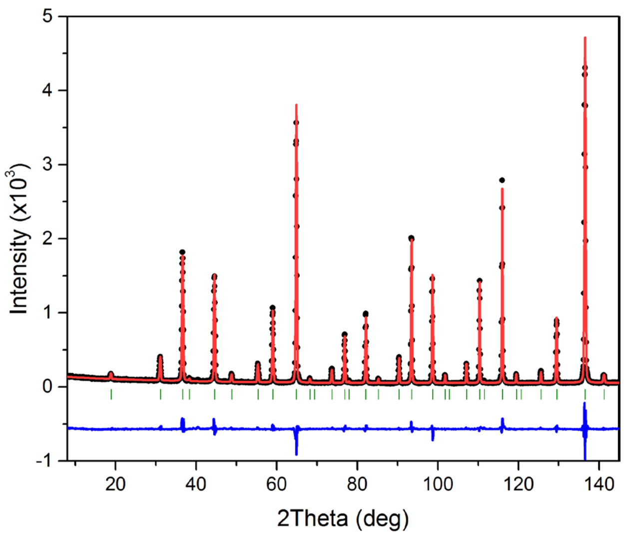


Appendix Figure 23 – Data refinement for $Fe_2GeO_4$ in D2B- T = 100 K.

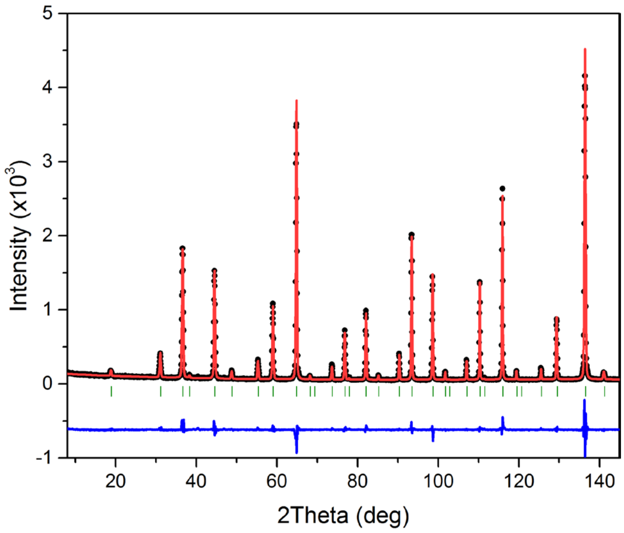


Appendix Figure 24 – Data refinement for $Fe_2GeO_4$ in D2B- T = 200 K.

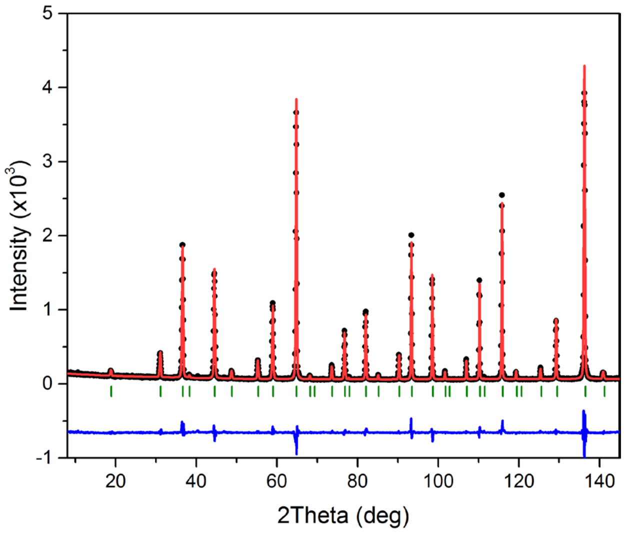


Appendix Figure 25 – Data refinement for $Fe_2GeO_4$ in D2B- T = 300 K.

# B2. γ-$Fe_2SiO_4$

**Appendix Table 28 – Full Irreducible representations and basis vectors (BV) for γ-$Fe_2SiO_4$ with propagation vectors $k_1$ = (¾+$\delta_1$ -¾-$\delta_1$ 0). The two magnetically independent atoms are Fe1 at (½,½,½) and Fe2 at (¾,0,¼). Symmetry-related positions are generated by the operators 1: (x,y,z), 2: (x+ ¼ ,y+ ¾ ,-z+ ½ ). The sublattice of Fe2 is not refined with this propagation vector, thus referred to as $k_{1\_1}$.**

| Propagation vector $\mathbf{k_{1\_1}}$ | | | | | |
|---|---|---|---|---|---|
| Irreps | $\Gamma_1$ | | $\Gamma_2$ | | |
| BV | $\psi_1$ | | $\psi_1$ | | $\psi_2$ |
| Atom | $m_x$ | $m_x$ | $m_x$ | $m_y$ | $m_z$ |
| Fe1_1 | 1 | -1 | 1 | 1 | 1 |
| Fe1_2 | $-\frac{\sqrt{2}}{2}+\frac{i\sqrt{2}}{2}$ | $\frac{\sqrt{2}}{2}-\frac{i\sqrt{2}}{2}$ | $-\frac{\sqrt{2}}{2}+\frac{i\sqrt{2}}{2}$ | $-\frac{\sqrt{2}}{2}+\frac{i\sqrt{2}}{2}$ | $\frac{\sqrt{2}}{2}-\frac{i\sqrt{2}}{2}$ |
| Irreps | $\Gamma_3$ | | $\Gamma_4$ | | |
| BV | $\psi_1$ | | $\psi_1$ | | $\psi_2$ |
| Atom | $m_x$ | $m_x$ | $m_x$ | $m_y$ | $m_z$ |
| Fe1_1 | 1 | -1 | 1 | 1 | 1 |
| Fe1_2 | $\frac{\sqrt{2}}{2}-\frac{i\sqrt{2}}{2}$ | $-\frac{\sqrt{2}}{2}+\frac{i\sqrt{2}}{2}$ | $\frac{\sqrt{2}}{2}-\frac{i\sqrt{2}}{2}$ | $\frac{\sqrt{2}}{2}-\frac{i\sqrt{2}}{2}$ | $-\frac{\sqrt{2}}{2}+\frac{i\sqrt{2}}{2}$ |
| Irreps | $\Gamma_1$ | | $\Gamma_2$ | | |
| BV | $\psi_1$ | | $\psi_1$ | | $\psi_2$ |
| Atom | $m_x$ | $m_x$ | $m_x$ | $m_y$ | $m_z$ |
| Fe2_1 | 1 | 1 | 1 | -1 | 1 |
| Fe2_2 | $-i$ | $-i$ | $i$ | $-i$ | $-i$ |
| Irreps | $\Gamma_3$ | | $\Gamma_4$ | | |
| BV | $\psi_1$ | | $\psi_1$ | | $\psi_2$ |
| Atom | $m_x$ | $m_x$ | $m_x$ | $m_y$ | $m_z$ |
| Fe2_1 | 1 | 1 | 1 | -1 | 1 |
| Fe2_2 | $i$ | $i$ | $-i$ | $i$ | $i$ |

**Appendix Table 29 – Full Irreducible representations and basis vectors (BV) for γ-$Fe_2SiO_4$ with propagation vectors $k_1 = (\frac{3}{4}+\delta_1\ \frac{3}{4}+\delta_1\ 0)$. The two magnetically independent atoms are Fe1 at (½,½,½) and Fe2 at (¾,0,¼). Symmetry-related positions are generated by the operators 1: (x,y,z), 2: (x+ ¼ ,y+ ¾ ,-z+ ½ ). The sublattice of Fe1 is not refined with this propagation vector, thus referred to as $k_{1\_2}$.**

| Propagation vector $\mathbf{k_{1\_2}}$ | | | | | |
|---|---|---|---|---|---|
| Irreps | $\Gamma_1$ | | $\Gamma_2$ | | |
| BV | $\psi_1$ | | $\psi_1$ | | $\psi_2$ |
| Atom | $m_x$ | $m_x$ | $m_x$ | $m_y$ | $m_z$ |
| Fe1_1 | 1 | -1 | 1 | 1 | 1 |
| Fe1_2 | $i$ | $-i$ | $-i$ | $-i$ | $i$ |
| Irreps | $\Gamma_3$ | | $\Gamma_4$ | | |
| BV | $\psi_1$ | | $\psi_1$ | | $\psi_2$ |
| Atom | $m_x$ | $m_x$ | $m_x$ | $m_y$ | $m_z$ |
| Fe1_1 | 1 | -1 | 1 | 1 | 1 |
| Fe1_2 | $-i$ | $i$ | $i$ | $i$ | $-i$ |
| Irreps | $\Gamma_1$ | | $\Gamma_2$ | | |
| BV | $\psi_1$ | | $\psi_1$ | | $\psi_2$ |
| Atom | $m_x$ | $m_x$ | $m_x$ | $m_y$ | $m_z$ |
| Fe2_1 | 1 | 1 | 1 | -1 | 1 |
| Fe2_2 | $-i$ | $-i$ | $-i$ | $i$ | $i$ |
| Irreps | $\Gamma_3$ | | $\Gamma_4$ | | |
| BV | $\psi_1$ | | $\psi_1$ | | $\psi_2$ |
| Atom | $m_x$ | $m_x$ | $m_x$ | $m_y$ | $m_z$ |
| Fe2_1 | 1 | 1 | 1 | -1 | 1 |
| Fe2_2 | $i$ | $i$ | $i$ | $-i$ | $-i$ |

**Appendix Table 30 – Refinement results at multiple temperatures. D20, 90° take-off. λ = 1.54 Å.**

| T (K) | $R_{WP}$ (%) | $R_{mag}1$ (%) | $R_{mag}2$ (%) | a (Å) | C2_ki1 (µB) | C3_ki1 (µB) | δ1 | C4_k2 (µB) | C5_k2 (µB) |
|---|---|---|---|---|---|---|---|---|---|
| 1.8 | 17.3 | 11.7 | 11.6 | 8.2095(1) | 0.5(4) | 2.2(3) | 0.028(7) | 0.6(4) | 0.45(5) |
| 25 | 16.2 | - | - | 8.2102(1) | - | - | - | - | - |
| 50 | 16.3 | - | - | 8.2104(1) | - | - | - | - | - |

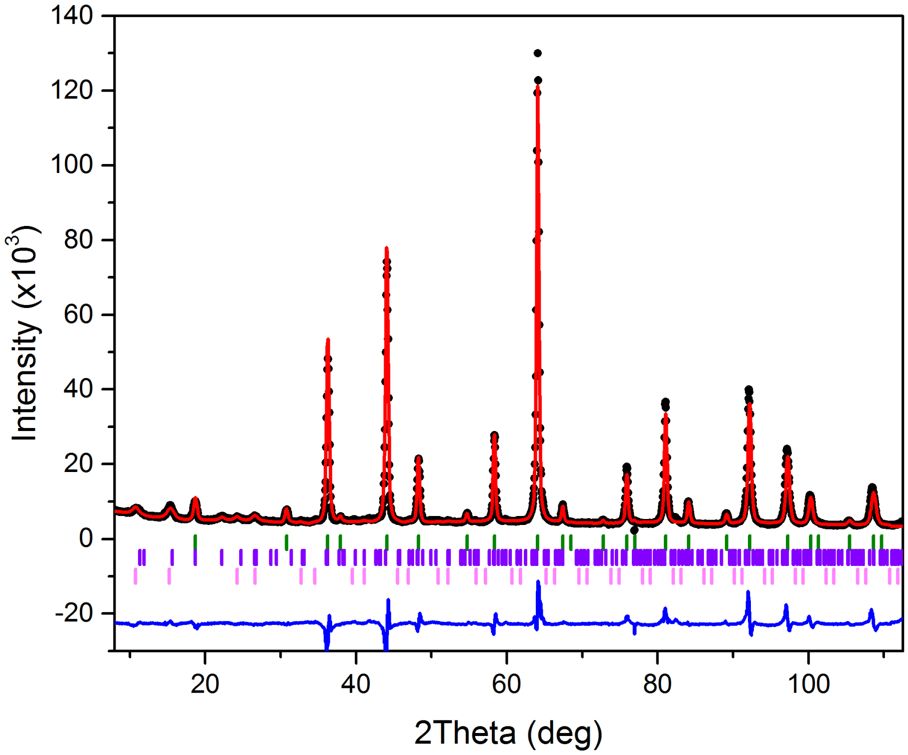


**Appendix Figure 26 – Data refinement for γ-$Fe_2SiO_4$ in D20, 90$^o$ take-off, λ = 1.54 Å. Temperature = 1.8 K. In this figure and all the following figures, Bragg reflections are in green, magnetic reflections (when present) are in purple for the k1 phase and pink for the k2 phase.**

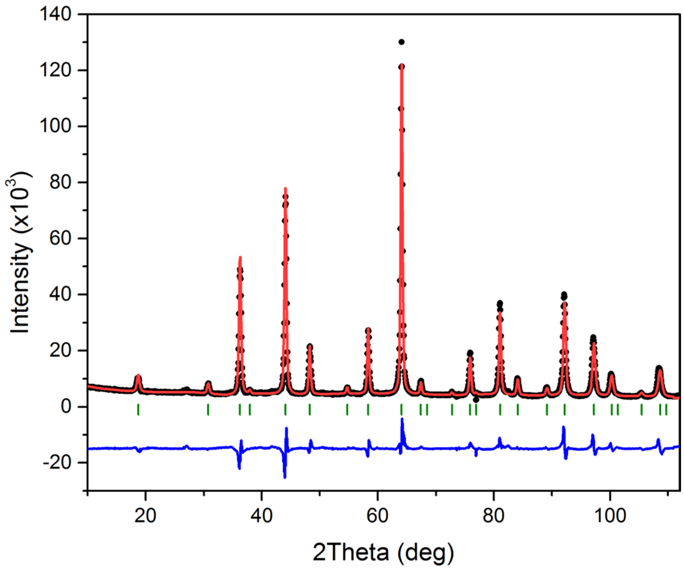


Appendix Figure 27 – Data refinement for γ-$Fe_2SiO_4$ in D20, 90$^o$ take-off. Temperature = 25 K. λ = 1.54 Å.

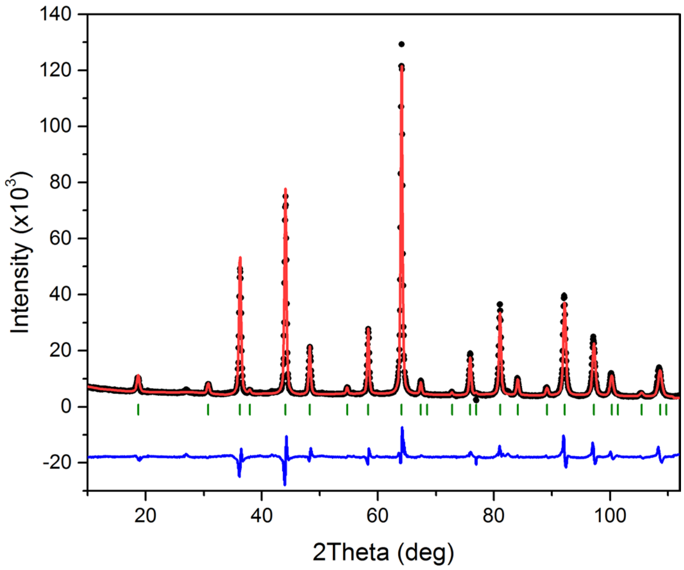


Appendix Figure 28 – Data refinement for γ-$Fe_2SiO_4$ in D20, 90$^o$ take-off. Temperature = 50 K. λ = 1.54 Å.

**Appendix Table 31 – Refinement results at multiple temperatures. D20, 90$^o$ take-off. λ = 2.41 Å.**

| T (K) | $R_{WP}$ (%) | $R_{mag}1$ (%) | $R_{mag}2$ (%) | a (Å) | C2_ki1 (µB) | C3_ki1 (µB) | δ1 | C4_k2 (µB) | C5_k2 (µB) |
|---|---|---|---|---|---|---|---|---|---|
| 1.8 | 9.70 | 5.75 | 8.57 | 8.2015(1) | 0.82(4) | 2.34(7) | 0.027(1) | 0.87(3) | 0.61(2) |
| 2.5 | 10.1 | 5.79 | 8.49 | 8.2015(2) | 0.80(4) | 2.32(7) | 0.025(2) | 0.90(3) | 0.63(2) |
| 5 | 10.1 | 6.42 | 9 | 8.2014(1) | 0.77(4) | 2.28(5) | 0.028(1) | 0.87(3) | 0.62(2) |
| 7 | 9.72 | 6.08 | 7.02 | 8.2017(1) | 0.90(2) | 2.45(5) | 0.022(1) | 0.51(2) | 0.36(5) |
| 9 | 9.63 | 5.24 | - | 8.2017(1) | 0.81(2) | 2.31(4) | 0.022(9) | - | - |
| 11 | 9.83 | 7.42 | | 8.2017(1) | 0.58(3) | 1.68(5) | 0.009(2) | - | - |
| 25 | 10.3 | - | - | 8.2017(1) | - | - | - | - | - |

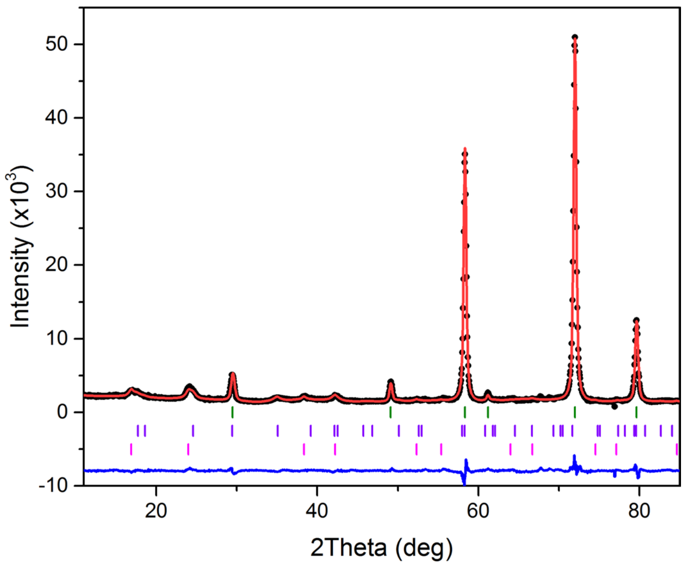


Appendix Figure 29 – Data refinement for γ-$Fe_2SiO_4$ in D20, 90$^o$ take-off.
Temperature = 2 K.
λ = 2.41 Å.

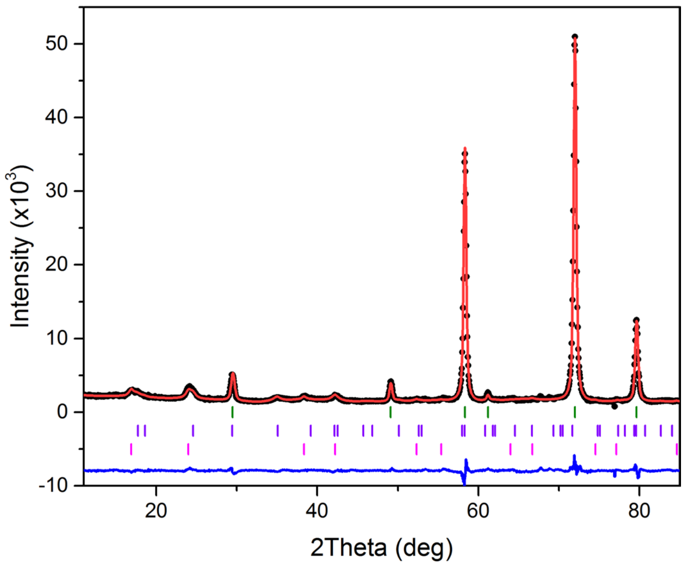


Appendix Figure 30 – Data refinement for γ-$Fe_2SiO_4$ in D20, 90$^o$ take-off.
Temperature = 3 K.
λ = 2.41 Å.

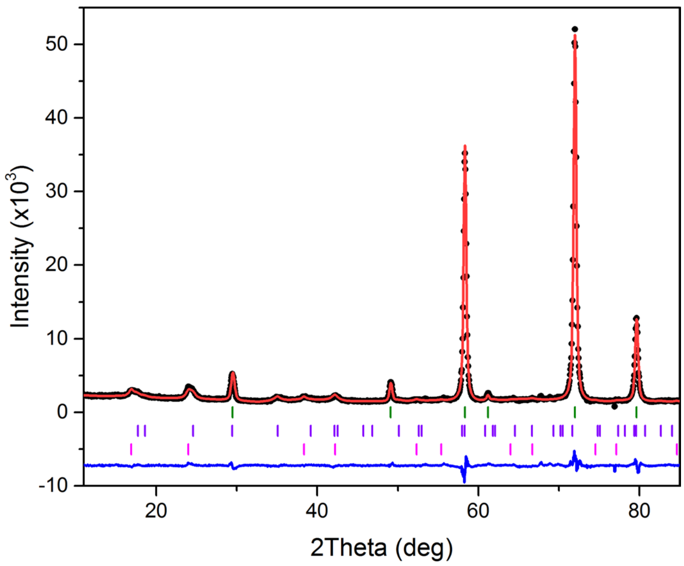


Appendix Figure 31 – Data refinement for γ-$Fe_2SiO_4$ in D20, 90$^o$ take-off.
Temperature = 5 K.
λ = 2.41 Å.

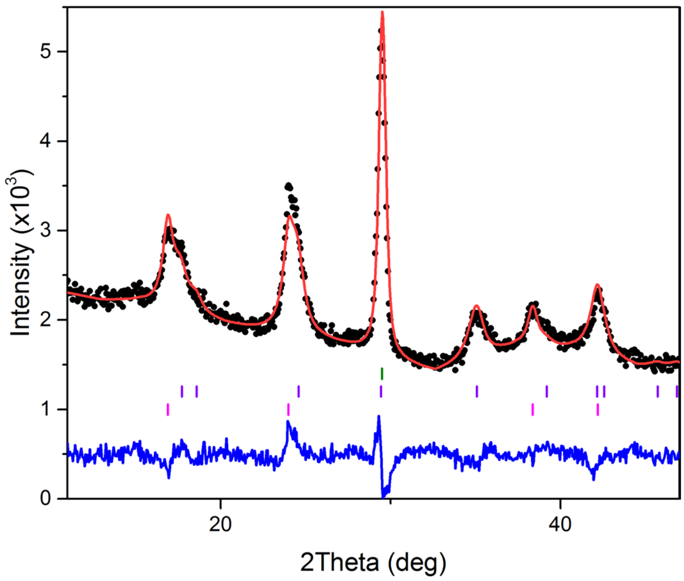


Appendix Figure 32 – Data refinement for γ-$Fe_2SiO_4$ in D20, 90$^o$ take-off. Temperature = 5 K. λ = 2.41 Å.
Focus on the low angle region with both magnetic phases.

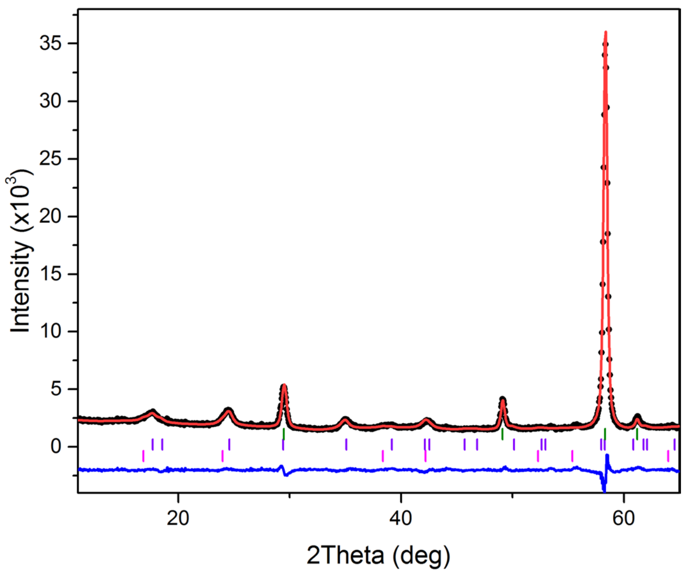


Appendix Figure 33 – Data refinement for γ-$Fe_2SiO_4$ in D20, 90$^o$ take-off. Temperature = 7 K. λ = 2.41 Å.

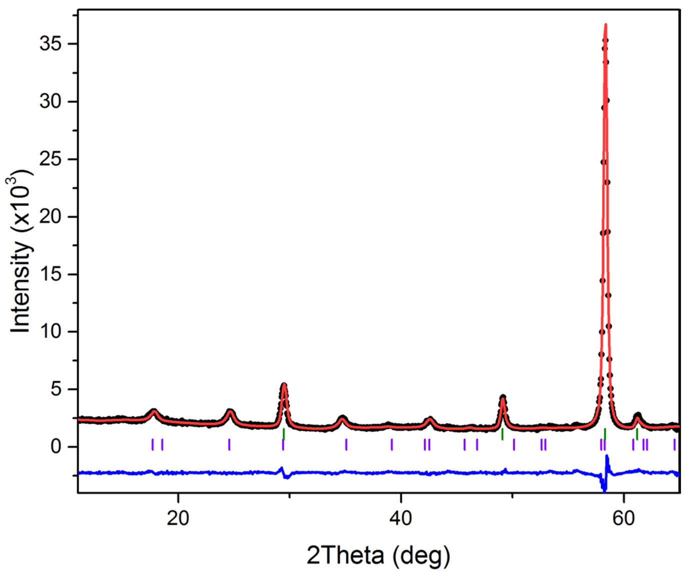


Appendix Figure 34 – Data refinement for γ-$Fe_2SiO_4$ in D20, 90$^o$ take-off. Temperature = 9 K. λ = 2.41 Å.

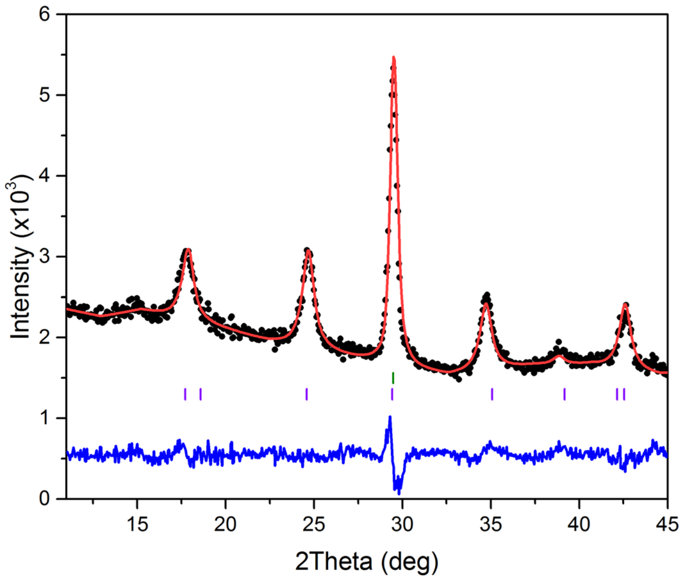


Appendix Figure 35 – Data refinement for γ-$Fe_2SiO_4$ in D20, 90$^o$ take-off. Temperature = 9 K. λ = 2.41 Å.
Focus on the low angle region, with only k1 reflections before the appearance of the k2 phase

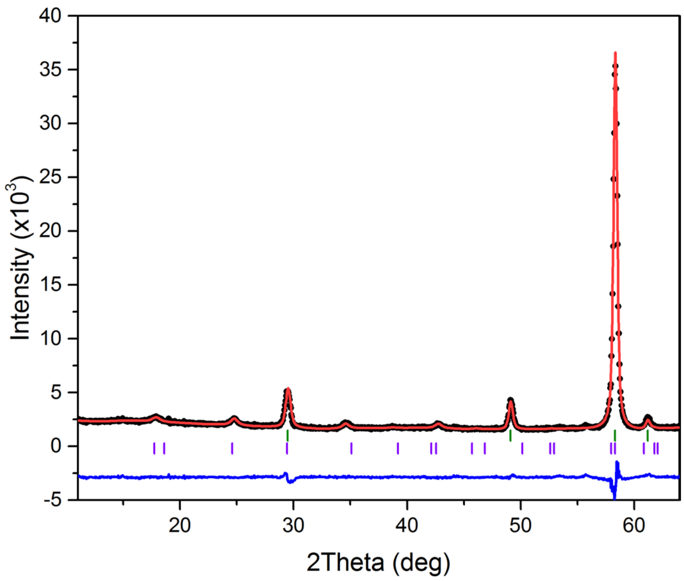


Appendix Figure 36 – Data refinement for γ-$Fe_2SiO_4$ in D20, 90$^o$ take-off. Temperature = 11 K. λ = 2.41 Å.

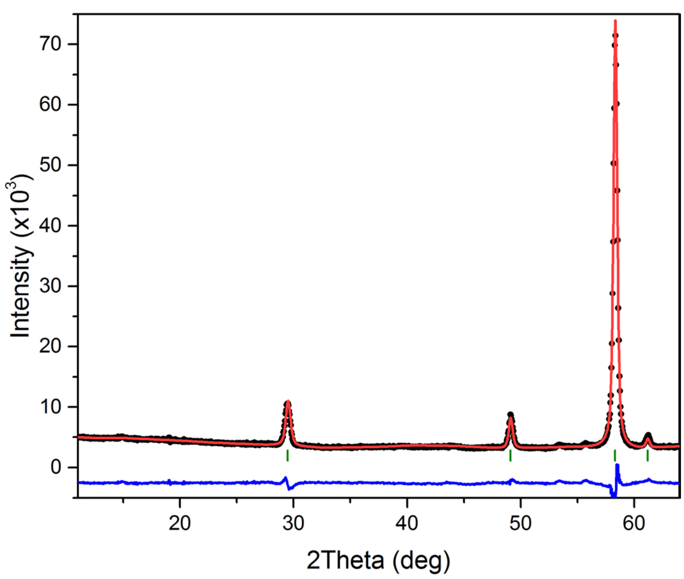


Appendix Figure 37 – Data refinement for γ-$Fe_2SiO_4$ in D20, 90$^o$ take-off. Temperature = 25 K. λ = 2.41 Å.

**Appendix Table 32 – Refinement results at multiple temperatures. D20, 42° take-off. λ = 2.41 Å.**

| T (K) | $R_{WP}$ (%) | $R_{mag}1$ (%) | $R_{mag}2$ (%) | a (Å) | C2_ki1 (µB) | C3_ki1 (µB) | δ1 | C4_k2 (µB) | C5_k2 (µB) |
|---|---|---|---|---|---|---|---|---|---|
| 1.8 | 9.29 | 4.23 | 6.69 | 8.2080(3) | 0.86(4) | 2.49(7) | 0.030(1) | 0.91(3) | 0.65(2) |
| 7 | 9.11 | 5.04 | 5.44 | 8.2080(3) | 0.91(3) | 2.47(6) | 0.034(1) | 0.71(4) | 0.50(3) |
| 25 | 10.5 | - | - | 8.2082(4) | - | - | - | - | - |

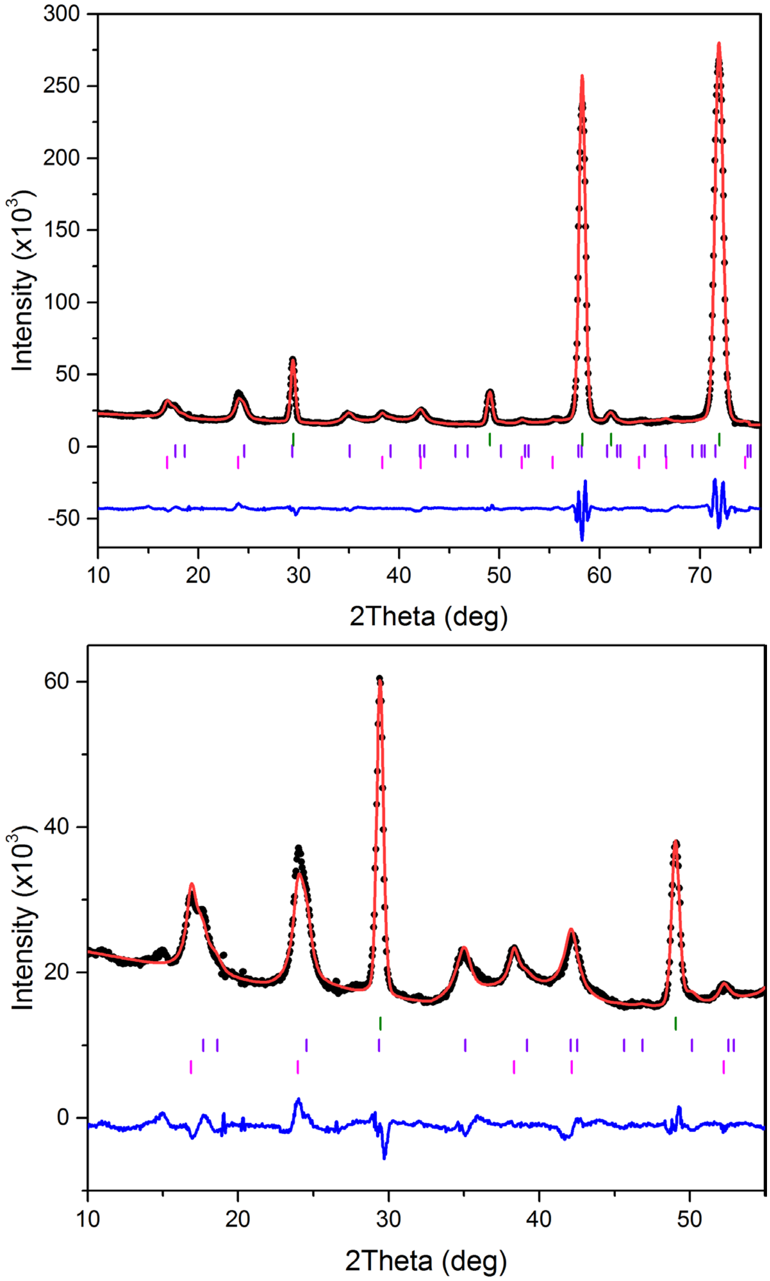


Appendix Figure 38 – Data refinement for γ-$Fe_2SiO_4$ in D20, 42° take-off. Temperature = 2 K. λ = 2.41 Å.
Focus on the low angle region, with reflections of k1 and k2 phases at saturation.

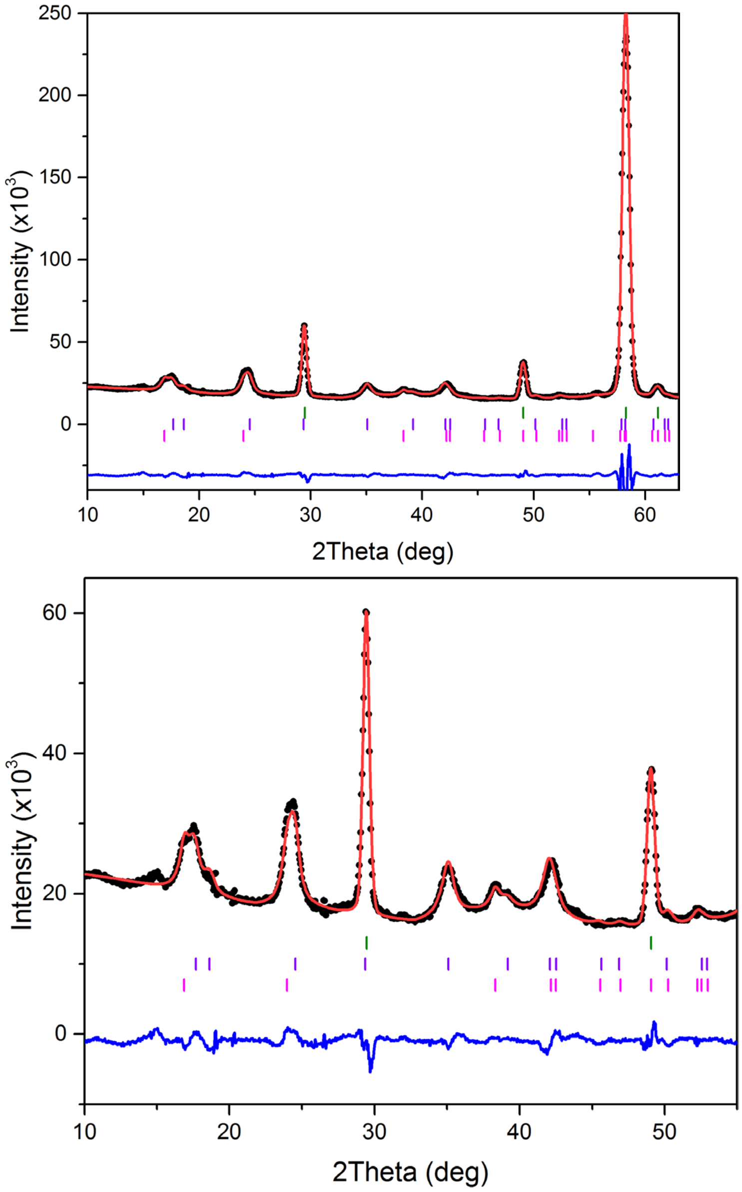


Appendix Figure 39 – Data refinement for γ-$Fe_2SiO_4$ in D20, 42$^o$ take-off. Temperature = 2 K. λ = 2.41 Å.
Focus on the low angle region, with reflections of k1 and k2 phases at the point of first appearance of the k2 phase.

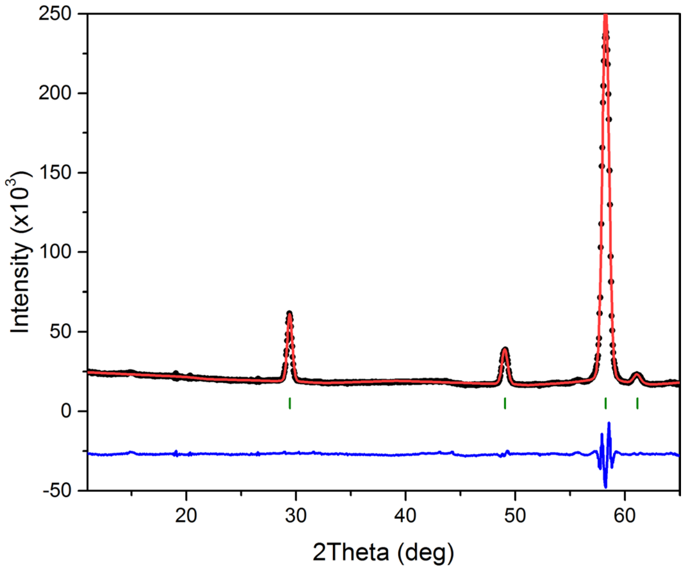


Appendix Figure 40 – Data refinement for γ-$Fe_2SiO_4$ in D20, 42$^o$ take-off. Temperature = 25 K. λ = 2.41 Å.

# REPRINT OF PUBLICATIONS

**The Verwey structure of a natural magnetite**

Giuditta Perversi, James Cumby, Elise Pachoud, Jon P. Wright and J. Paul Attfield

Reprinted with permission from Chemical Communications, 2016, 52, 4864-4867.



DOI: 10.1039/C5CC10495E

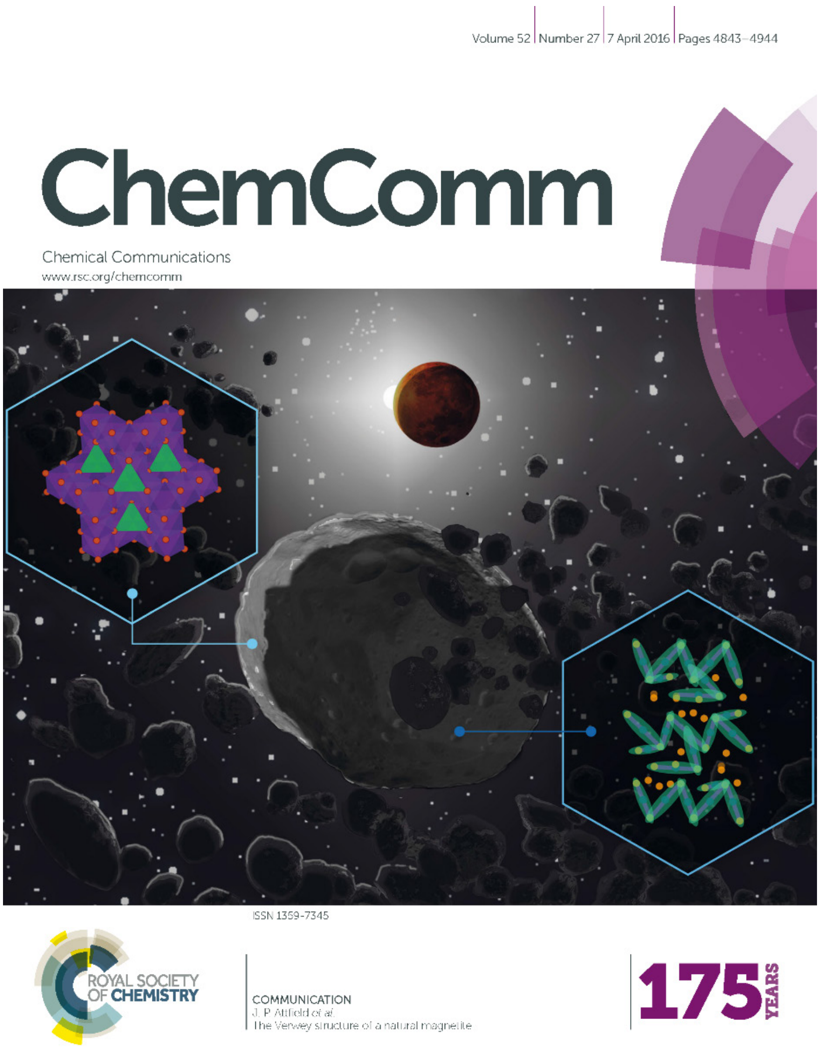

ChemComm

COMMUNICATION

View Article Online
View Journal | View Issue



# The Verwey structure of a natural magnetite†

Cite this: *Chem. Commun.*, 2016, 52, 4864

Received 22nd December 2015, Accepted 19th February 2016

DOI: 10.1039/c5cc10495e

www.rsc.org/chemcomm

G. Perversi,[a] J. Cumby,[a] E. Pachoud,[a] J. P. Wright[b] and J. P. Attfield*[a]

**A remarkably complex electronic order of $Fe^{2+}$/$Fe^{3+}$ charges, $Fe^{2+}$ orbital states, and weakly metal–metal bonded $Fe_3$ units known as trimerons, was recently discovered in stoichiometric magnetite ($Fe_3O_4$) below the 125 K Verwey transition. Here, the low temperature crystal structure of a natural magnetite from a mineral sample has been determined using the same microcrystal synchrotron X-ray diffraction method. Structure refinement demonstrates that the natural sample has the same complex electronic order as pure synthetic magnetite, with only minor reductions of orbital and trimeron distortions. Chemical analysis shows that the natural sample contains dopants such as Al, Si, Mg and Mn at comparable concentrations to extraterrestrial magnetites, for example, as reported in the Tagish Lake meteorite. Much extraterrestrial magnetite exists at temperatures below the Verwey transition and hence our study demonstrates that the low temperature phase of magnetite represents the most complex long-range electronic order known to occur naturally.**

Magnetite, $Fe_3O_4$, is the original magnetic material and is technologically important in magnetic applications and as the parent phase for spinel ferrites. At ambient temperatures magnetite is ferrimagnetic and has the cubic spinel structure (space group $Fd\bar{3}m$) with inverse charge distribution $Fe^{3+}(Fe^{2.5+})_2O_4$ over the cation sites of the $AB_2O_4$ spinel lattice. Early low temperature experiments revealed changes in magnetism, conductivity, and other properties at the Verwey transition, which occurs at $T_V \approx 125$ K in pure $Fe_3O_4$ samples.[1] In 1939, Verwey proposed that the transition is driven by charge ordering of $Fe^{2+}$ and $Fe^{3+}$ ions on the octahedral B-sites. However, this order was not verified during the early years of study, and the ground state structure proved controversial for many decades.[2–11]

The structure of magnetite below the Verwey transition has an acentric monoclinic $\sqrt{2} \times \sqrt{2} \times 2$ supercell (space group $Cc$) of the high temperature cubic $Fd\bar{3}m$ spinel arrangement. A full solution of the $Cc$ supercell of highly stoichiometric magnetite was recently achieved through use of microcrystal X-ray diffraction.[12] $Fe^{2+}$/$Fe^{3+}$ charge ordering and orbital ordering of high-spin $3d^6$ $Fe^{2+}$ states (evidenced by Jahn–Teller distortions of the $Fe^{2+}O_6$ octahedra) were found from analysis of the observed Fe–O distances, confirming that the Verwey charge ordering hypothesis is correct to a useful first approximation. However, additional structural distortions in which B site Fe–Fe distances within linear Fe–Fe–Fe units are anomalously shortened showed that electrons are not fully localised as $Fe^{2+}$ states, but are instead spread over the three sites resulting in highly structured three-site polarons known as trimerons (Fig. 1).

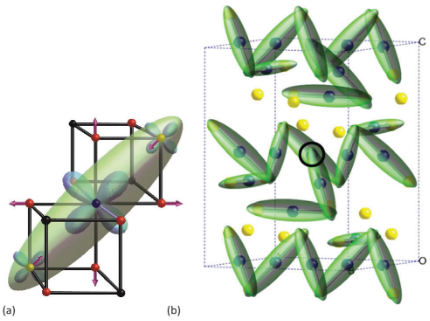


Fig. 1 (a) A trimeron unit showing the bonding electron density as an ellipsoid with approximate atomic populations indicated by the sizes of the $t_{2g}$ orbitals. The atomic displacement arrows show how orbital order at the central $Fe^{2+}$ site elongates the four Fe–O bonds perpendicular to the local Jahn–Teller axis while weak Fe–Fe bonding shortens the distances to the two adjacent cations. (b) Distribution of charge states (with $Fe^{2+}$/$Fe^{3+}$ states shown as blue/yellow spheres) and trimerons in the low temperature $Cc$ structure of magnetite. Most trimerons are terminated by a $Fe^{3+}$-type site, but one trimeron ends with $Fe^{2+}$ (circled).

[a] *Centre for Science at Extreme Conditions (CSEC) and School of Chemistry, University of Edinburgh, Edinburgh EH9 3FD, UK. E-mail: j.p.attfield@ed.ac.uk*
[b] *European Synchrotron Radiation Facility, Grenoble, France*

† Electronic supplementary information (ESI) available: Further experimental information and structural results. Open data for this article are at http://dx.doi.org/10.7488/ds/1318. See DOI: 10.1039/c5cc10495e

These are an example of orbital molecules, weakly-bonded clusters of orbitally-ordered cations.[13,14]

Charge and orbital orders are known in many transition metal oxides,[15] for example, manganite perovskites such as $La_{0.5}Ca_{0.5}MnO_3$.[16] However the charge, orbital and trimeron orders of magnetite stand out as perhaps the most complex electron ordered ground state known, and also because magnetite occurs naturally as a common mineral. However, natural magnetites are impure and commonly contain other metals or silicon as dopants that may suppress the electronic order. Previous studies showed that the Verwey transition is very sensitive to non-stoichiometry in $Fe_{3(1-\delta)}O_4$ and $Fe_{3-x}M_xO_4$ (M = Zn, Ti) cation-doped samples.[17–19] Heat capacity and electrical measurements on single crystals showed that the transition is first order for zero or small impurity levels, and $T_V$ falls from 122 K in pure $Fe_3O_4$ to 108 K at $3\delta$ or $x$ = 0.012. A broader second order transition is observed above this value where $T_V$ decreases from 101 K to 83 K at the $3\delta$ or $x \approx 0.035$ upper limit for observation of the Verwey anomaly. Here we investigate whether the long range charge, orbital, and trimeron order previously observed in highly pure $Fe_{3(1-\delta)}O_4$ ($\delta < 0.0001$)[12] is maintained in natural samples with multiply-doped compositions comparable to those of extra-terrestrial magnetites that exist in the Verwey state.

A natural octahedral magnetite crystal of approximate width 1 cm was obtained from the locality of Ouro Preto, Brazil. The crystal was crushed and microcrystal fragments were screened for diffraction quality at room temperature on beamline ID11 at the ESRF synchrotron. A grain of approximate dimensions 60 × 50 × 25 μm was selected for further study. Electron Probe Microanalysis (EPMA) gave cation contents as shown in Table 1. The sample has a relatively low dopant content (<0.5% total impurities) typical of magnetites of hydrothermal origin, with Al, Si, Mg and Mn as the observed dopants. The microcrystal fragment has a similar composition to the bulk.

The Verwey transition of the natural magnetite sample was characterised using SQUID magnetisation and single crystal X-ray diffraction measurements (Fig. 2). The microcrystal shows a sharp magnetisation transition at $T_V$ = 119 K. The bulk powdered sample gives a broader Verwey transition at 116–120 K (shown in ESI†), demonstrating that the microcrystal is representative of the bulk in agreement with the chemical analysis.

A magnetic field was applied to minimise microtwinning of domains while the selected microcrystal was cooled through the Verwey transition, and diffraction images were acquired at

Table 1 Cation compositions from EPMA elemental analysis of the bulk natural magnetite crystal and the microcrystal fragment used for structural study. Compositions are normalised to 3 cations per formula unit and standard deviations in parentheses show compositional variations for the dopants

| Element | Bulk | Microcrystal |
|---|---|---|
| Fe | 2.9866 | 2.9888 |
| Al | 0.0066(4) | 0.0054(4) |
| Si | 0.0030(3) | 0.0017(3) |
| Mg | 0.0020(2) | 0.0022(2) |
| Mn | 0.0018(6) | 0.0019(5) |

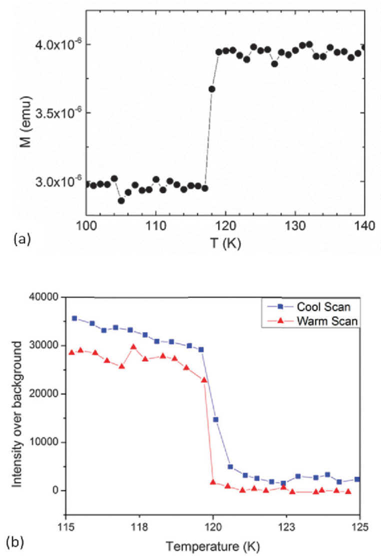


Fig. 2 Thermal variations of (a) magnetisation in a field of 500 Oe, and (b) intensity of a superstructure reflection, during cooling and warming scans, for the magnetite microcrystal around the Verwey transition.

90 K. The presence of a long range structural Verwey transition was revealed by the appearance of sharp superstructure peaks in detector images on cooling, and the temperature evolution of a superstructure intensity shown in Fig. 2(b) confirms the transition at $T_V$ = 119 K. The natural sample was found to have a monoclinic $Cc$ unit cell with parameters $a$ = 11.8801(17) Å, $b$ = 11.8457(17) Å, $c$ = 16.7773(30) Å and $\beta$ = 90.267(9)° at 90 K. These are similar to those of pure magnetite at the same temperature ($a$ = 11.88881(3) Å, $b$ = 11.84940(3) Å, $c$ = 16.77515(14) Å and $\beta$ = 90.2363(2)°)[12] and show that the natural sample has a comparable monoclinic distortion despite impurity doping. The full 90 K data set consists of 45 904 symmetry unique reflections out to a resolution of 0.30 Å. This enabled coordinates and anisotropic thermal parameters to be refined for all atoms. Domain proportions were also refined and parent domain fraction was found to be 91.9%, with 2.9% of $a/-a$, 2.8% of $a/b$, and 2.3% of $a/-b$ twin domains also present. The overall quality of the natural microcrystal is thus very good and comparable to that of pure synthetic magnetite microcrystals studied previously.[12,20] The low level of microtwinning of the natural sample may reflect a long annealing period during crystallisation resulting in low residual strains. Further refinement details and results are given as ESI.†

Structural evidence for charge ordering of $Fe^{2+}/Fe^{3+}$ and orbital ordering of $Fe^{2+}$ states is obtained from the local distortion modes of the B site $FeO_6$ octahedra in the low temperature structure.[12] The amplitude of the radial expansion or breathing mode

$Q_{Rad} = \sum(d_i - d_{av})/\sqrt{6}$ (summed over the six Fe–O distances $d_i$ in each octahedron, where $d_{av}$ is the global average bond distance) with $A_{1g}$ symmetry is sensitive to charge order, as $Fe^{2+}$ has a larger ionic radius than $Fe^{3+}$. $Q_{Rad}$ correlates with Bond Valence Sum (BVS) which estimates the formal Fe oxidation state. BVS's were calculated using a standard method[21] and interpolation formula.[7] The $E_g$ distortion is doubly degenerate and the amplitudes of the orthorhombic and tetragonal modes were calculated following the procedure used previously.[12] The tetragonal $E_g$ mode with amplitude $Q_{JT}$ describes the compressive Jahn–Teller distortion associated with orbital order of $Fe^{2+}$, while the non-degenerate $3d^5$ configuration of $Fe^{3+}$ is not Jahn–Teller active.

Fig. 3a shows a plot of tetragonal Jahn–Teller $Q_{JT}$ *versus* breathing $Q_{Rad}$ amplitudes for the 16 crystallographically distinct B sites in the *Cc* structure of the natural magnetite and the previously-studied highly stoichiometric sample.[12] This enabled the $Fe^{2+}/Fe^{3+}$ charge order and $Fe^{2+}$ orbital order to be discovered in the latter material, as the 8 $Fe^{2+}$-like sites have large $Q_{Rad}$ and significantly negative $Q_{JT}$ values, while the 8 $Fe^{3+}$-like sites have small $Q_{Rad}$ and near-zero $Q_{JT}$. The domains of these distributions, shown by the rectangular boxes on Fig. 3a, are very similar for the natural sample, showing that the charge and orbital orders are still present. The $Q_{Rad}$ ranges for the $Fe^{2+}$ and $Fe^{3+}$ like states in the two structures are very similar. However, the $Q_{JT}$ values for the $Fe^{2+}$ and $Fe^{3+}$ like states are more similar to each other in the natural sample than in the stoichiometric material, demonstrating that the orbital order is more sensitive than the charge order to the presence of dopants. Hence this plot shows that while low temperature charge and orbital order in magnetite is sensitive to low levels of doping (<0.5%), long range electronic order is still preserved.

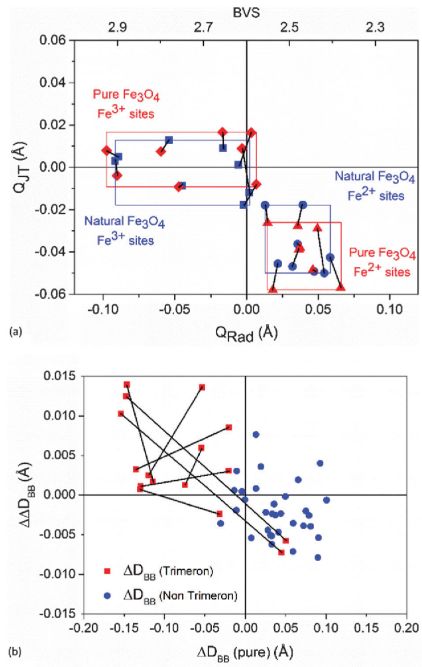


Fig. 3 (a) Distortion amplitudes of the tetragonal Jahn–Teller (orbital order) mode plotted against the radial (charge order) mode for the 16 octahedral B sites in the *Cc* structure of the present natural sample and of pure magnetite.[12] Points for the same B-site in the two structures are connected by lines. Domains of the 8 $Fe^{2+}$-like and 8 $Fe^{3+}$-like sites are shown as rectangles. An approximate BVS scale is shown at the top of the plot. (b) Plot of $\Delta\Delta D_{BB} = \Delta D_{BB}$(natural) − $\Delta D_{BB}$(pure) against $\Delta D_{BB}$(pure), showing changes in the B–B distances relative to those in the pure sample. Different symbols are used for trimeron and non-trimeron distances, and pairs of distances in the same trimeron are connected.

The previous study of a pure magnetite microcrystal at 90 K revealed structural distortions in addition to those from charge and orbital ordering, where distances from $Fe^{2+}$ states to their two B site neighbours (usually $Fe^{3+}$ ions) in the local orbital ordering plane are anomalously shortened due to trimeron formation. 14 of the expected 16 trimeron Fe–Fe contacts are shorter than the average B–B distance. This effect is quantified by the changes $\Delta D_{BB}$(natural) of nearest neighbour B–B distances relative to the global average value of 2.9614 Å in the natural sample. To show differences between B–B distances in the natural and pure samples, we plot $\Delta\Delta D_{BB} = \Delta D_{BB}$(natural) − $\Delta D_{BB}$(pure) against $\Delta D_{BB}$(pure) in Fig. 3b. This plot demonstrates that the trimeron bonding in the natural magnetite sample is very similar to that in the pure sample, with the same pattern of short and long Fe–Fe distances. The magnitude of differences between the two structures ($-0.010 < \Delta\Delta D_{BB} < 0.015$ Å) is only ~10% of the overall B–B shifts ($-0.20 < \Delta D_{BB}$(pure) $< 0.10$ Å). Relatively large positive values of $\Delta\Delta D_{BB}$ for trimeron distances show that Fe–Fe bonds which are very short in the pure sample are slightly elongated in the natural material due to the doping effects of impurities. Changes in the non-trimeron B–B distances are smaller and are a consequence of changes in the trimerons.

These structural results demonstrate that the complex electronic order of $Fe^{2+}/Fe^{3+}$ charges, $Fe^{2+}$ orbital states, and Fe–Fe–Fe trimerons discovered in pure synthetic magnetite below the Verwey transition is also present in a microcrystal fragment obtained from a natural crystal typical of aqueous mineralisation. Small differences are observed between the two crystal structures, notably a loss of $Fe^{2+}$ orbital distortions and elongated Fe–Fe trimeron distances in the natural sample due to the dopants. However, the overall long range electronic order is still preserved over a domain scale of a few tens of microns, as observed in microcrystals of the pure sample. This finding is significant because it demonstrates that the long range electronic order will be present in magnetites of similar chemical compositions at temperatures below the ~120 K Verwey transition. Although minerals on Earth are not exposed to temperatures below this limit, much magnetite on other planets, moons, meteors and in grains of space dust is routinely below 120 K. For example, magnetite has recently been identified in a regolith breccia from the Moon, where diurnal temperature variations commonly span $T_V$.[22]

Magnetites that reach Earth in meteorites have varying levels of chemical purity, leading to variations in $T_V$. Verwey transitions of magnetites from several carbonaceous chondrites (meteorites with high oxide and silicate content, and sometimes also containing water and organic molecules) have been reported from magnetisation measurements.[23] Magnetite from the Tagish Lake meteorite (which has provided a rare example of very primitive solar system materials) was found to have a sharp transition at 122 K which is above that of the natural sample used in this study (with $T_V$ = 119 K) and close to that of stoichiometric synthetic material. Hence magnetite within the Tagish Lake meteorite would have been in the electronically-ordered Verwey state prior to falling to Earth. Material from the Orgueil meteorite had a broader transition at $T_V \approx 118$ K but this is also well within the range for long range electronic order. These relatively pure magnetites may have been formed by aqueous alteration within asteroids[24] leading to similar dopant levels to terrestrial hydrothermal magnetites such as our Ouro Preto sample. However, magnetites from the Murchison and Allende meteorites showed no distinct Verwey transition due to relatively high contents of impurities such as Cr that suppress the electronic order.[25] Another consequence of the Verwey transition is that the lattice distortion from cubic to monoclinic symmetry gives rise to anisotropic lattice strains.[26] Hence, the stresses resulting from natural magnetites being cycled through the transition may contribute to mechanical weathering on some planetary bodies.

In summary, the present study shows that long range electronic order is present in slightly doped natural magnetites produced by aqueous processes. Although coupled orders of electronic charges, orbital states and spins are known in many synthetic transition metal compounds, the long-range order within the Verwey state is perhaps the most complex known example and is certainly without comparison amongst naturally occurring substances. The Verwey phase of magnetite thus represents the most complex electronic order known to occur naturally. On a cosmic scale, the Verwey phase is likely to exist widely in cold (<120 K) atomic matter ranging from planets to micron-sized dust particles, given the relatively high abundances of Fe and O.

We thank ERC for funding and STFC for provision of beamtime at ESRF.

## Notes and references


1 E. J. W. Verwey, *Nature*, 1939, **144**, 327.
2 M. Iizumi, T. F. Koetzle, G. Shirane, S. Chikazumi, M. Matsui and S. Todo, *Acta Crystallogr., Sect. B: Struct. Crystallogr. Cryst. Chem.*, 1982, **38**, 2121.
3 J. P. Wright, J. P. Attfield and P. G. Radaelli, *Phys. Rev. Lett.*, 2001, **87**, 266401.
4 J. P. Wright, J. P. Attfield and P. G. Radaelli, *Phys. Rev. B: Condens. Matter Mater. Phys.*, 2002, **66**, 214422.
5 F. Walz, *J. Phys.: Condens. Matter*, 2002, **14**, R285.
6 R. J. Goff, J. P. Wright, J. P. Attfield and P. G. Radaelli, *J. Phys.: Condens. Matter*, 2005, **17**, 7633.
7 E. Nazarenko, J. E. Lorenzo, Y. Joly, J. L. Hodeau, D. Mannix and C. Marin, *Phys. Rev. Lett.*, 2006, **97**, 056403.
8 Y. Joly, J. E. Lorenzo, E. Nazarenko, J. L. Hodeau, D. Mannix and C. Marin, *Phys. Rev. B: Condens. Matter Mater. Phys.*, 2008, **78**, 134110.
9 J. E. Lorenzo, C. Mazzoli, N. Jaouen, C. Detlefs, D. Mannix, S. Grenier, Y. Joly and C. Marin, *Phys. Rev. Lett.*, 2008, **101**, 226401.
10 J. Blasco, J. Garcia and G. Subias, *Phys. Rev. B: Condens. Matter Mater. Phys.*, 2011, **83**, 104105.
11 J. P. Attfield, *J. Jpn. Soc. Powder Powder Metall.*, 2014, **61**, S43.
12 M. S. Senn, J. P. Wright and J. P. Attfield, *Nature*, 2012, **481**, 173.
13 M. S. Senn, I. Loa, J. P. Wright and J. P. Attfield, *Phys. Rev. B: Condens. Matter Mater. Phys.*, 2012, **85**, 125119.
14 J. P. Attfield, *APL Mater.*, 2015, **3**, 041510.
15 J. P. Attfield, *Solid State Sci.*, 2006, **8**, 861.
16 R. J. Goff and J. P. Attfield, *Phys. Rev. B: Condens. Matter Mater. Phys.*, 2004, **70**, 140404.
17 J. M. Honig, *J. Alloys Compd.*, 1995, **229**, 24.
18 J. P. Shepherd, J. W. Koenitzer, R. Aragón, C. J. Sandberg and J. M. Honig, *Phys. Rev. B: Condens. Matter Mater. Phys.*, 1985, **31**, 1107.
19 J. P. Shepherd, J. W. Koenitzer, R. Aragón, J. Spal and J. M. Honig, *Phys. Rev. B: Condens. Matter Mater. Phys.*, 1991, **43**, 8461.
20 M. S. Senn, J. P. Wright, J. Cumby and J. P. Attfield, *Phys. Rev. B: Condens. Matter Mater. Phys.*, 2015, **92**, 024104.
21 I. D. Brown and D. Altermatt, *Acta Crystallogr., Sect. B: Struct. Sci.*, 1985, **41**, 244.
22 K. H. Joy, C. Visscher, M. E. Zolensky, T. Mikouchi, K. Hagiya, K. Ohsumi and D. A. Kring, *Meteorit. Planet. Sci.*, 2015, **50**, 1157.
23 A. N. Thorpe, F. E. Senftle and J. R. Grant, *Meteorit. Planet. Sci.*, 2002, **37**, 763.
24 J. F. Kerridge, A. L. Mackay and W. V. Boynton, *Science*, 1979, **205**, 395.
25 B. G. Choi, K. D. McKeegan, L. A. Leshin and J. T. Wasson, *Earth Planet. Sci. Lett.*, 1997, **146**, 337.
26 R. S. Coe, R. Egli, S. A. Gilder and J. P. Wright, *Earth Planet. Sci. Lett.*, 2012, **319**, 207.